Doctoral Dissertation
Doctoral Program in Energetics (36^{th}cycle)

Ducted Fuel Injection: a mixing-enhancement strategy to abate soot emissions in compression-ignition engines

By

Cristiano Segatori

******

Supervisor(s):
Prof. Federico Millo, Supervisor
Dr. Andrea Piano, Co-Supervisor

Doctoral Examination Committee:
Prof. Tommaso Lucchini, Referee, Politecnico di Milano
Dr. Charles Mueller, Referee, Sandia National Laboratories
Prof. Marco Badami, Politecnico di Torino
Dr. Eric Pomraning, Convergent Science
Prof. Carlos Micó Reche, Universitat Politècnica de València

Politecnico di Torino
2024

Declaration

I hereby declare that, the contents and organization of this dissertation constitute my own original work and does not compromise in any way the rights of third parties, including those relating to the security of personal data.

Cristiano Segatori
2024

* This dissertation is presented in partial fulfillment of the requirements for **Ph.D. degree** in the Graduate School of Politecnico di Torino (ScuDo).

A mia moglie Chiara,
per l'amore che mi dona.
Sono profondamente grato.

Acknowledgements

I feel the need to wholeheartedly express my gratitude to the people who, directly or otherwise, have contributed to this research work and, more generally, to the attainment of my PhD.

First of all, I would like to acknowledge my supervisor, Prof. Federico Millo, for having always believed in me and for his excellent leadership of our research group. Likewise, a special thanks goes to Dr. Andrea Piano who, during this years, has been much more than a simple co-supervisor for me. I feel profoundly grateful to have experienced his guidance, not only at work. In addition, I would like to thank all the members of the *e3 research group* with whom I have had the opportunity to share my daily office life over the past 4 years, experiencing valuable technical discussions and, more importantly, fun life vibes together. In particular, I would like to thank Dr. Benedetta Peiretti Paradisi for developing part of the research work together, and for her constant, loving, and rare kindness.

Then, I also wish to thank Andrea Bianco from *GammaTech Engineering* (formerly, *POWERTECH Engineering*) for his availability in sharing his valuable expertise in CFD modelling.

I would like to acknowledge *DUMAREY Automotive Italia* (formerly, *PUNCH Torino*) for the fruitful collaboration regarding the DFI technology. In particular, I wish to convey my gratitude to Dr. Francesco C. Pesce, Dr. Alberto L. Vassallo, and Dr. Francesco Accurso.

Thanks to Prof. Lucio Postrioti and his research group at the *Università degli Studi di Perugia* for performing the extensive experimental analysis.

I am grateful to the reviewers of my doctoral thesis, Dr. Charles Mueller and Prof. Tommaso Lucchini, for their comments and time.

Last but not least, on a personal note, I want to mention the most important people in my life: my wife Chiara; my little daughter Priscilla; my dad Roberto; my

mom Rosanna; my sister Eugenia; the good friends who strongly believed in me, one above all my best friend Jacopo; the passionate teachers who have contributed to my education, one above all Roberta Rosa. This achievement is also thanks to them.

* * *

Convergent Science provided CONVERGE licenses and technical support for this work.

For large eddy simulations (LES), I acknowledge the CINECA award under the ISCRA initiative, for the availability of high-performance computing resources and support.

For RANS simulations, computational resources were provided by HPC@POLITO, a project of Academic Computing within the Department of Control and Computer Engineering at the Politecnico di Torino (http://www.hpc.polito.it).

Abstract

The compression-ignition (CI) engine powered by diesel fuel, also known as *Diesel engine*, is a leader technology in freight road transportation and shipping sectors, and will remain so for the next decades. This technology is based on the diesel combustion process, in which the injected high-reactivity fuel in a high-pressure-temperature environment spontaneously ignites at locally fuel-rich composition, thus leading to the formation of incomplete combustion products such as soot (or *black carbon*). For this reason, diesel engines are today among the major anthropogenic emission sources of soot, which is toxic for the human health and a major short-lived climate forcer. Therefore, it is of paramount importance pushing nowadays research for a low-soot diesel combustion process. For this purpose, strategies that can reduce the fuel-to-air ratio composition before the auto-ignition region (or lift-off length, LOL) have been widely studied and, among them, one of the most promising is the ducted fuel injection (DFI) concept, patented by Sandia National Laboratories few years ago. DFI is based on injecting fuel down the axis of a small cylindrical pipe in the combustion chamber, placed at a small distance from the injector orifice exit, in order to improve the mixture quality at the LOL. In the scientific literature, there is experimental evidence that DFI can abate soot formation in both constant-volume and CI engine conditions. However, although several studies have focused on DFI from both a fundamental physics-based and an implementation-based point of views, a key knowledge gap is still present regarding the understanding of its working principles, the impact of duct design and operating conditions, and the real feasibility of its integration on series-production engines working on the whole operating map. In light of this, the present PhD work aims to contribute in bridging the open knowledge gap towards the complete success of this new concept.

Thanks to a collaboration with *Università degli Studi di Perugia*, an extensive experimental campaign has been carried out to collect data related to both free and ducted sprays under several non-reacting constant-volume conditions, considering a single-hole injector configuration which can be relevant for heavy-duty applica-

tions. The experimental data have been then exploited to develop a high-fidelity 3-dimensional computational fluid dynamics (3D-CFD) virtual test rig for the investigation of DFI concept. In particular, large eddy simulations coupled with statistical analysis were primarily used to obtain a robust knowledge on DFI working mechanisms under non-reacting conditions, such as entrainment and turbulent mixing enhancement. This high-fidelity (>80% resolved turbulent structures) dataset was then used as a target to assess a RANS model for the same case study, in order to extend the number of analyses at an affordable computational cost. The RANS model has proven reliability, at least in terms of major trends, thus a further step was the integration of combustion and emissions models, based on detailed chemistry solver and detailed soot modelling. Combustion simulations provided robust results, in line with the available data from the literature. After that, the validated RANS combustion model was used for understanding the impact of the main duct geometrical features, figuring out an optimal duct design, and engine parameters, defining preliminary DFI-oriented calibration requirements.

Finally, in collaboration with *PUNCH Torino S.p.A.*, the potential benefits coming from DFI implementation on a series-production diesel engine for light duty applications were explored, firstly, through 3D-CFD simulations, secondly, through optical engine analyses. Even though DFI capability to reduce soot formation was confirmed, some criticalities were observed regarding soot oxidation, highlighting the need for combustion system optimization and engine calibration.

Contents

List of Figures

List of Tables

Nomenclature

Roman Symbols

$\dot{m}$	Mass flow rate
CO	Carbon monoxide
CO_2	Carbon dioxide
d_{hole}	Injector hole diameter
dt	Time-step
dx	Grid size
f	Grid refinement factor
HC	Unburned hydrocarbons
N-C_7H_{16}	Normal-heptane
NO_x	Nitrogen oxides
O_2	Oxygen
P	Pressure
Re	Reynolds number
T	Temperature
Y_m	Mass fraction of species m
y_+	Non-dimensional wall distance
D	Duct diameter

G Duct stand-off distance

KL Soot optical thickness

L Duct length

Z Axial distance from the injector orifice

Greek Symbols

χ_{st} Stoichiometric scalar dissipation rate

$\dot{\omega}$ Reaction rate

η Kolmogorov turbulent length scale

κ Turbulent kinetic energy

ω Specific turbulent dissipation rate

ϕ Equivalence ratio

ρ Density

ε Turbulent dissipation rate

Other Symbols

$\bar{}$ Reynolds averaging

$\langle\,\rangle$ Ensemble average operator

$\tilde{}$ Favre averaging

Acronyms / Abbreviations

2D 2-dimensional

3D 3-dimensional

AMR Adaptive mesh refinement

aSOI After start of injection

ATS Aftertreatment system

BMEP Brake mean effective pressure

CA Crank angle

CD Combustion duration

CDC Conventional diesel combustion

CFD Computational fluid dynamics

CFL Courant-Friedrichs-Lewy

CI Compression-ignition

COV Coefficient of variation

CVV Constant-volume vessel

DES Detached eddy simulation

DFI Ducted fuel injection

DNS Direct numerical simulation

DoE Design of experiments

DOI Injection duration

DPF Diesel particulate filter

ECN Engine Combustion Network

EGR Exhaust gas recirculation

EOC End of combustion

EOI End of injection

ET Energizing time

EVM Eddy viscosity model

EVO Exhaust valve opening

HRR Heat release rate

ID Ignition delay

IMAP Intake manifold ambient pressure

IMEPg Gross indicated mean effective pressure

IMT Intake manifold ambient temperature

KH-RT Kelvin-Helmholtz Rayleigh-Taylor

LES Large eddy simulation

LES-NWM Large eddy simulation with near wall modelling

LES-NWR Large eddy simulation with near wall resolution

LLFC Leaner lifted-flame combustion

LNT Lean-NO_x trap

LOL Lift-off length

LSR Length scale resolution

LTC Low temperature combustion

MC Mixing-controlled

MSI Magnitude similarity index

NL Natural luminosity

NZE Net zero emissions by 2050

PAH Poly-cyclic aromatic hydrocarbon

PDA Phase doppler anemometry

PM Particle mass

PN Particle number

RANS Reynolds-averaged Navier-Stokes

RMS Root mean square

RNG Re-normalization group

SCORE Sandia compression-ignition optical research engine

SCR Selective catalytic reduction

SGS Sub-grid scale

SMD Sauter mean diameter

SOC Start of combustion

SOI Start of injection

SSI Structure similarity index

TCI Turbulence-chemistry interaction

TDCf Top dead center firing

TKE Turbulent kinetic energy

TRI Turbulence resolution index

VLES Very large eddy simulation

WSR Well-stirred reactor

Chapter 1

Introduction

1.1 Background information

"The massive diesel engines that power cargo ships [...] are more important to the global economy than any corporate structure or international trade agreement" [1]. Indeed, the compression-ignition (CI) engine powered by diesel or biodiesel fuel is a leader technology in freight road transportation and shipping sectors, and will remain so for the next decades. In 2022, the European market share of new trucks was composed for 96.6% by diesel trucks [2] and, even in a net zero emissions by 2050 (NZE) scenario, more than 60% of 2030 heavy trucks global sales will not adopt battery electric or fuel cell alternatives [3, Figure 7.3]. Assuming that the typical lifetime is about 9-17 years [4], diesel trucks are expected to play a major role for many years to come. This argument is even more relevant for maritime shipping, whose NZE scenario forecasts an oil demand almost unvaried in the period 2021-2030 and a reduced shipping fuel demand in 2050, since partly substituted by biofuels [3, Table 7.1 and Figure 7.8]. Therefore, assuming that typical ship lifetime is between 20 and 35 years [3], the reader can appreciate the importance of pushing current research for the development of environmentally cleaner CI engine propulsion systems, minimizing direct and indirect pollutant emissions.

1.2 Diesel combustion process and need for low-soot operation

CI engines convert fuel energy in mechanical energy through the diesel combustion process [5], whose physical comprehension is today well-established thanks to the pioneering work of Dec [6]. The diesel fuel injected at high pressure in high reactivity conditions spontaneously ignites at locally rich mixture fraction composition, under the so-called premixed combustion phase. Then, a standing, fuel-rich premixed autoignition zone stabilizes in the upstream region of the diesel flame, whereas the downstream region of the diesel flame is a pseudo-stationary diffusive flame characterized by a thin external layer at high temperature and approximately stoichiometric conditions. This is the so-called mixing-controlled (MC) combustion phase. These characteristics are the points of strength of the conventional diesel combustion (CDC) which guarantee high efficiencies, given the possibility to work with high compression ratios and low global fuel-to-air ratios; high controllability, ensured by the possibility to control the ignition timing by means of the fuel injection timing; fuel-flexibility, reducing the cost associated with fuel processing and enabling the possibility to use fuels deriving from scrap materials; robustness and durability. Nonetheless, the fuel rich premixed autoignition zone leads to the formation of soot (or black carbon) particles, while the diffusion flame creates the conditions under which nitrogen oxides (NO_x) can easily form. In other words, considering a temperature - fuel-to-air ratio (or equivalence ratio) diagram, also known as Kamimoto-Bae diagram [7], the local conditions typical of the CDC fall in both the soot and NO_x formation areas. Moreover, the strategies that can be adopted, varying either injection or ambient conditions, to curtail NO_x emissions, typically have an opposite effect on soot emissions, obeying to the well-known soot/NO_x trade-off [8]. Therefore, even though aftertreatment systems (ATSs)[1] are continuously under development in order to comply with more and more stringent emissions standards [10], on-road and off-road diesel engines are today among the major sources of anthropogenic soot emissions [11], for which the whole transportation sector (including international shipping) contributes about 25% worldwide [12]. In the scientific literature, there is well-documented evidence that exposure to soot has adverse effects on human beings [13–15]. Furthermore, soot is classified as a short-lived climate pollutant,

[1]The particulate matter originating from soot is typically captured through the diesel particulate filter (DPF) , while NO_x emissions are controlled through selective catalytic reduction (SCR) or lean-NO_x trap (LNT) systems [9].

whose reduction could play a crucial role in the mitigation of the near-term climate change [16]. In particular, soot is estimated to have a global warming potential 3200 times higher than carbon dioxide (CO_2) over a 20-year time frame [17]. In this scenario, it can be clearly perceived the urgency of mitigating the soot emissions from the diesel engines. Hence, significant research efforts in the diesel combustion community are focused on the in-cylinder combustion process to prevent the formation of soot, reducing the amount of ATS required to meet the legislative targets[2]. Advanced diesel combustion strategies aiming at enhancing the charge premixing to the extent of lowering both the equivalence ratio and the combustion temperatures are an interesting option for simultaneous soot and NO_x reduction. However, these strategies, collected under the generic name of low temperature combustion (LTC) [18, 19], work by the decoupling of fuel injection and fuel ignition timings, resulting in hard controllability, high combustion noise and difficulties to operate at high load. Thereby, the usage of the MC combustion coupled with low-soot operation, simultaneously breaking the above mentioned soot/NO_x trafe-off, remains desirable.

The formation of soot under MC combustion conditions is regulated by the equivalence ratio value in the stabilized autoignition region, conventionally defined as lift-off length (LOL) . Equivalence ratio values lower than 2 in the LOL region are demonstrated to provide a soot-free combustion [20]. In light of this, an advanced MC combustion concept named leaner lifted-flame combustion (LLFC) , defined as "mixing-controlled combustion that does not produce soot because it occurs at equivalence ratios less than or equal to approximately 2" [21], emerged in the last decades. The LLFC can be pursued by increasing the LOL, thus increasing the amount of air entering the fuel spray plume before the ignition location as well as the mixing extent. In this way, it has been demonstrated that soot formation can effectively be prevented even at a high level of charge dilution, giving the opportunity of decreasing NO_x formation without any detrimental effect on the combustion process [20]. Early investigations in a heavy-duty CI engine using conventional diesel fuel showed that this approach can be adopted at low loads (<4 bar gross indicated mean effective pressure, IMEPg) coupled with small orifices (110 μm) and high injection pressures (approx. 2400 bar), but unfortunately, when load increases and injectors with more than two orifices are employed, re-entrainment of hot combustion products and spray-to-spray interaction nullify the LLFC regime due to shortening of the LOL [21]. By using a blend of diesel and oxygenated fuels

[2]On the contrary, relying on ATSs effectiveness means a high complexity degree, additional costs and fuel-economy penalties.

coupled with the same orifices diameter and injection pressure level, the LLFC could be sustained with a 6-hole injector tip at slightly higher loads (up to 6 bar IMEPg) [22]. Therefore, in order to achieve a further increase in the peak load limit of LLFC, the mentioned studies highlight the need for a new strategy capable to enhance the mixing upstream of the LOL.

During the last few years, the ducted fuel injection (DFI) concept was patented by Sandia National Laboratories [23] drawing inspiration from the Bunsen burner [24], typically used in chemistry labs to obtain minimum luminosity non-sooting flames by controlling the amount of air mixed with fuel before combustion. DFI is based on injecting fuel down the axis of a small cylindrical pipe in the combustion chamber in order to improve the mixture quality at the LOL to enable and sustain the LLFC. This small duct is placed at a small distance, named stand-off distance, from the injector orifice exit and coaxial to it, imitating the working principles of a series of devices which can fall under the name of eductors (e.g., ejectors [25], jet pumps [26], confined turbulent jets [27], etc.). In Fig. 1.1, a schematic of the DFI concept in comparison with the CDC, taken from [28], is reported.

Ideally, the presence of the duct changes the entrainment, evaporation, mixing and reactivity conditions in a way to reach leaner conditions in the autoignition region, indicated in red in Fig. 1.1 (a), compared to the CDC, thus producing little to no soot. The experimental reproduction of this concept is in Fig. 1.1 (b), where the white color manifests the presence of incandecent hot soot on the CDC left side, while the blue represents soot-free combustion (i.e., no soot natural luminosity) on the DFI right side.

1.3 Ducted fuel injection (DFI) proof-of-concept

The experimental DFI proof-of-concept was carried out by Sandia National Laboratories researchers in [29] by comparing the soot natural luminosity (NL) of DFI with respect to the free spray (i.e., conventional spray configuration without duct) considering constant-volume Engine Combustion Network (ECN) spray A conditions [30] and using a reference duct with a 3 mm inner diameter, a 14 mm length, and a 2 mm stand-off distance. The experiments showed an impressive soot abatement over a large air temperature range, being the soot NL reduced by more than one order of magnitude when the duct was used, as shown in Fig. 1.2, taken from [29]. Moreover,

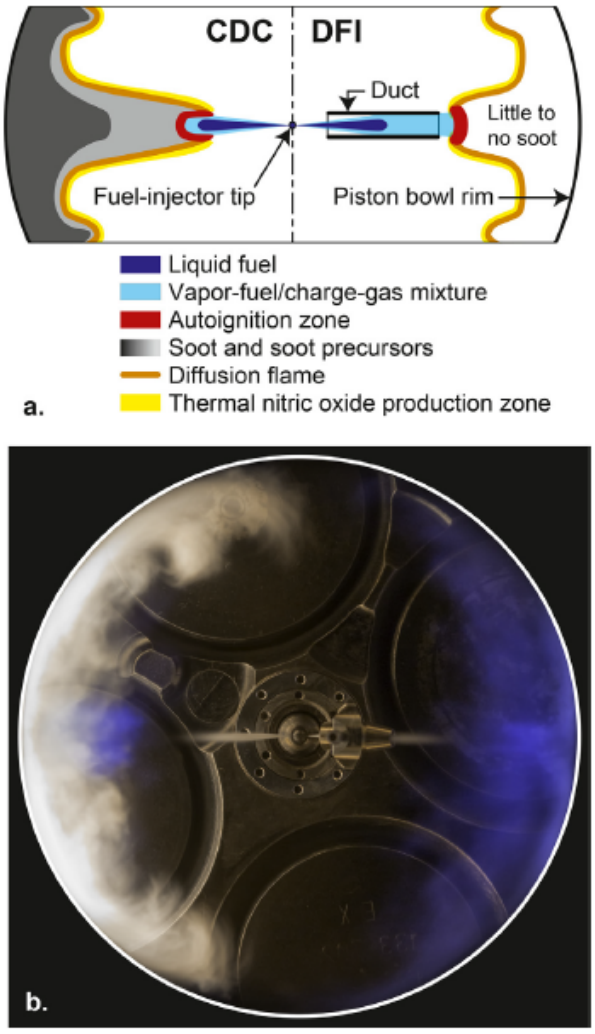

Fig. 1.1 Reproduced from [28]. (a) Schematic of the ducted fuel injection (DFI) concept (right side) against the conventional diesel combustion (CDC, left side); (b) color experimental picture representing a combustion event like that depicted in the schematic.

a notable LOL extension was observed as well as a longer ignition delay (ID) and a shorter combustion duration (CD) .

A subsequent work [31] moved to the evaluation of the soot mass (instead of the NL) throughout the combustion event by means of optical thickness (KL) measurements in similar working conditions, extending the ambient temperature range of the analysis. As can be seen in Fig. 1.3, the DFI capability to dramatically attenuate the soot mass formation in comparison with the free spray was confirmed, using a duct with a 2 mm inner diameter, a 16 mm length, a 1.4 mm stand-off distance, rounded inlet and tapered outer wall at the outlet. Moreover, different

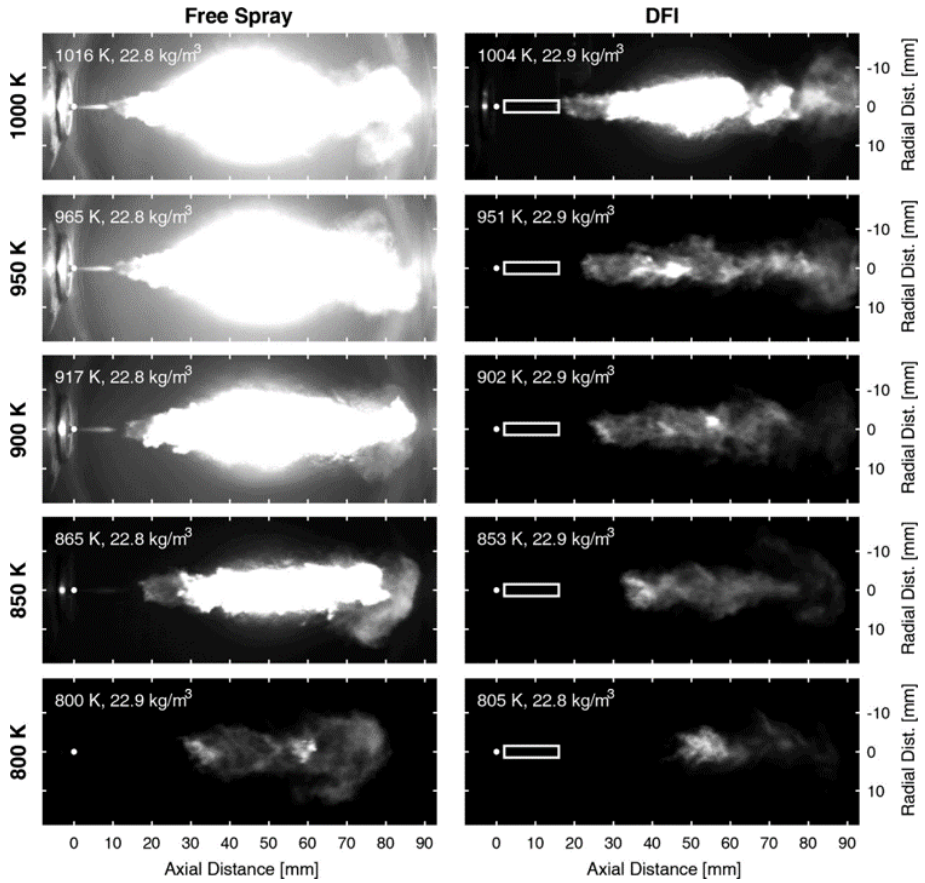

Fig. 1.2 Reproduced from [29]. Soot natural luminosity associated with free spray (left) and DFI (right) combustion. The nominal ambient temperature and density are indicated at the top-left of each image. The injector orifice exit is at the origin (white dot); the duct inner geometry is indicated by a white rectangle.

ambient densities (14.8 and 22.8 kg/m^3) and oxygen concentrations (15% and 21%) were tested, and several duct geometries were examined, maintaining the DFI soot mitigation advantage, up to more than an order of magnitude in all the tested conditions.

As observable in these experimental campaigns, the DFI was capable to highly attenuate the soot even at high temperatures (>1000 K). Of particular significance is the case at 1000 K in Fig. 1.2, since the LOL was anchored at the duct exit, but the soot was still strongly reduced, manifesting that some mechanisms are enabled upstream of the duct outlet, as explicitly commented by Sandia researchers: “the 1000-K DFI case clearly shows lower NL signal levels than the 1000-K, 950-K, and even 900-K free-spray cases, despite the fact that the free-spray cases have longer axial distances over which entrainment into the spray can occur. Hence, it

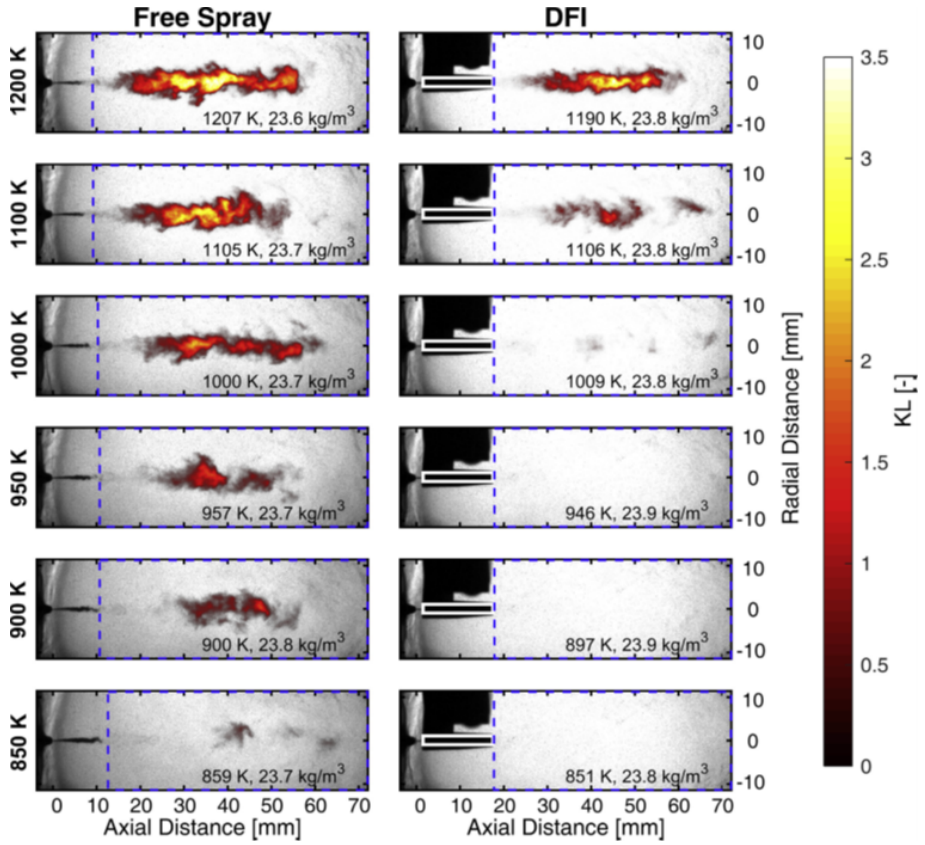

Fig. 1.3 Reproduced from [31]. Soot optical thickness (KL) associated with free spray (left) and DFI (right) combustion. The nominal ambient temperature and density are indicated at the bottom-right of each image. The duct inner geometry is indicated by a white rectangle.

appears that the duct either increases the entrainment rate into the spray, enhances the fuel/charge-gas mixing via a different mechanism, or both" [29]. The fact that the LOL extension, and the related higher entrainment into the fuel spray, is not the only mechanism through which DFI suppresses soot is also visible for the cases at 1100K and 1200K in Fig. 1.3, as again explicitly commented by Sandia researchers: "Finally, at 1100 K, although the soot in the DFI case begins to be noticeably higher at this temperature, there is still $\sim$ 2/3 less soot by using the duct, despite the fact that G [i.e., stand-off distance] in this case was small and H [i.e., LOL] was within a millimeter of the end of the duct, such that there is almost no area for entrainment that is not confined by the duct" [31]. These comments make it clear that, even though these experimental observations highlight the high potential of this innovative concept for soot mitigation throughout the diesel combustion process, the physical mechanisms enabled by the duct adoption are not fully clear and several research gaps have to be covered towards the implementation of DFI technology on series-

production diesel engines. These gaps define several research areas which have been object of attention for several academic, governmental and industrial groups across the world in the last few years, growing the number of scientific publications about DFI, as can be seen in Fig. 1.4 which highlights the increasing interest in this promising concept.

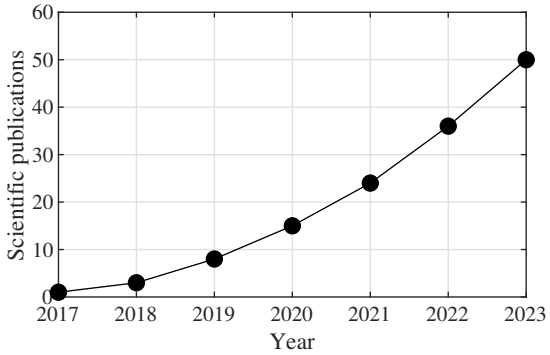

Fig. 1.4 Number of scientific publications on journal about DFI concept over the last years. Updated to November 2023.

The main outcomes emerging from the scientific literature for each area of research are reviewed in the following sections.

1.4 Literature review on DFI concept

1.4.1 Research for DFI physics understanding

One of the major area of research on DFI concerns the understanding of its working principles, basically addressing the question: why does DFI reduce the soot formation? In other words, as commented above regarding the basics of the diesel combustion process, answering this question means to identify the key mechanisms enabling a much lower fuel-to-air ratio at the LOL than the CDC. Moreover, as just seen, this issue must be addressed considering that the simple LOL extension, and its underlying physical reasons, cannot explain everything alone but other physical mechanisms are involved. Therefore, several researchers have committed themselves to the study and identification of the phenomena that could explain the DFI soot mitigation performance, through both experiments and computational fluid dynamics (CFD) . In this context, CFD played the major role, thanks to its capability to compute where the experiments cannot measure, of course taking into account that

the accuracy of the results can be an open point. Different computational approaches, Reynolds-averaged Navier-Stokes (RANS) simulations and large eddy simulations (LES) , were employed providing different levels of detail at different computational costs. It follows a summary of the main outcomes emerged from a literature review in this area of research, focusing on the effect of the duct on spray global characteristics, air entrainment into the fuel spray plume, mixing between air and fuel, and main combustion parameters.

Spray global characteristics

Several research works studied the DFI global spray characteristics, such as spray penetration, spray cone angle, spray area/volume, Sauter mean diameter (SMD), etc., comparatively to the free spray. In this subject, there are not significant controversial opinions about the way DFI works and the major trends are summarized in Table 1.1.

Table 1.1 Summary of DFI effect on the main spray global characteristics

Effect of DFI on:		
Spray penetration	$\Uparrow$	[31–48]
Spray cone angle	$\Uparrow$	[34–36, 38, 39, 42, 48]
Spray area	$\Uparrow$	[34–36, 38, 42, 48]
SMD	$\Downarrow$ or $\simeq$	[49, 39]
Nº droplets	$\Downarrow$	[39]

The duct presence in front of the injector tip tends to increase the penetration of the spray due to the higher velocity inside the duct, guaranteed by the lower jet cross-sectional area, being confined by the duct wall [31–36, 38, 37, 39–42, 44, 45, 43, 46, 48, 47]. In particular, transient penetration tends to be higher for both liquid and vapor phase, despite the higher evaporation rate at the duct exit can lead to a lower stabilized liquid length for DFI [50, 45].

The spray cone angle, which is computed after the duct exit for DFI, tends to be higher [34–36, 38, 39, 42, 48], as well as the spray area [34–36, 38, 42, 48]. Concerning the shape of the spray tip, the DFI plume typically features a peculiar mushroom-shaped head, as discussed in [36, 38, 39, 49, 48, 51].

Finally, the droplet average size (or SMD) after the duct exit is typically similar between free spray and DFI [39, 49], slightly lower for the latter thanks to the higher

evaporation rate. The droplet count was also evaluated in [39], showing that, even though the SMD is very similar for several injection pressure levels, the number of droplets is significantly lower for DFI, consistently with the presumed higher evaporation rate.

Of course, the discussed trends can be smoothed by the variation of the duct design. As a rule of thumb, these behaviours are less pronounced for geometries that tend to reduce the interaction between spray and duct wall (e.g., larger duct diameter).

Air entrainment

Several works investigated the possibility that the duct presence can increase the amount of entrained air into the fuel spray. Given the presence of the duct wall that eliminates a portion of spray surface available for entrainment, this can happen only in the near-nozzle region (i.e., upstream of the duct) and/or in the region between the duct exit and the LOL (i.e., downstream of the duct). Many CFD studies highlighted that DFI enhances the air entrainment upstream of the duct due to a sort of pumping effect [50, 40, 52, 49, 42, 46, 47, 51], or jet pump effect, since a low-pressure region establishes inside the duct due to the higher velocity of the jet, as observable in Fig. 1.5, taken from [39]. The extent of this pressure difference between duct volume and test chamber, which drives the higher entraining air mass flow rate in the DFI near-nozzle region, depends on the injection and ambient conditions.

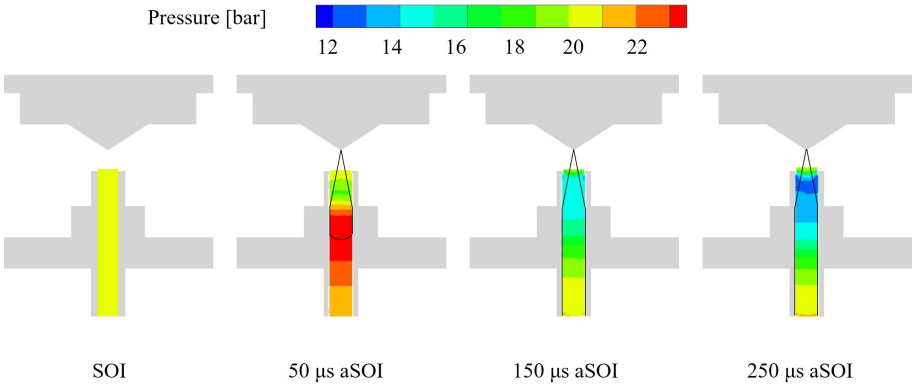

Fig. 1.5 Reproduced from [39]. Pressure distribution evolution within the duct, black line represents the jet profile. Operating conditions: rail pressure = 1200 bar, vessel pressure = 20 bar, vessel temperature = 573 K.

In [50][3], the upstream charge gas entrainment rate for DFI was increased by more than a factor of three relative to the free spray but was prevented along the length of the duct to such an extent that the global entrainment was reduced. Similar trends were observed in [43][4], where the upstream mass flux was slightly enhanced but the global one was reduced, and in [49][5], where the mass flow rate entering the duct inlet was six times higher than the corresponding free spray but remaining almost identical and 50% lower than free spray at the outlet.

The air mass flow rate into the spray plume upstream of the duct resulted approximately doubled for the DFI in [39][6], as well as the entrainment rate per unit of surface in [40][7]. In this second work, the entrainment rate resulted slightly higher for DFI also in the region between duct outlet and LOL, suggesting the potential to recover the amount of missed entrainment along the duct length. This becomes possible especially when the LOL is sufficiently extended by the duct adoption, as shown in [52][8], in which the computed downstream air entrainment was higher for the DFI in most of conditions, and in [51][9], in which a higher global entrainment was computed for DFI thanks to a higher entrainment rate in the downstream region and a longer LOL. The possibility to achieve a globally equal entrainment between free spray and DFI, enhancing the one close to the injector in the latter case, was also demonstrated in [53][10], even considering the limited dimension of a light-duty piston bowl. Other researchers [44, 45][11], achieved higher values for the DFI global entrainment or entrainment rate under the same operating conditions. However, [44] concluded that no pre-duct entrainment enhancement was observed as well as a significant in-duct pressure reduction. According to the Author's opinion, this conclusion is not supported by the data, since the comparison was not fair: the pre-duct entrainment was compared with the global free spray entrainment. Moreover,

[3]Test vessel, 90 μm single-hole injector, ECN Spray A inert conditions.

[4]Test vessel, 180 μm single-hole injector, rail pressure=400-1200 bar, vessel density=4.5-18.7 kg/m^3, vessel temperature=373-773 K.

[5]Test vessel, 120 μm single-hole injector, rail pressure=1200 bar, vessel density=68 kg/m^3, vessel temperature=308 K.

[6]Test vessel, 180 μm single-hole injector, rail pressure=1200 bar, vessel density=12.2 kg/m^3, vessel temperature=573 K.

[7]Test vessel, 180 μm single-hole injector, rail pressure=1200 bar, vessel density=22.8 kg/m^3, vessel temperature=900 K, oxygen concentration=21 %.

[8]Test vessel, 180 μm single-hole injector, rail pressure=800-2000 bar, vessel density=22.2-50 kg/m^3, vessel temperature=900 K, oxygen concentration=16.5-21 %.

[9]Test vessel, 180 μm single-hole injector, rail pressure=1200 bar, vessel density=9 kg/m^3, vessel temperature=773 K.

[10]CI engine, BMEP=6 bar.

[11]Test vessel, 90 μm single-hole injector, ECN Spray A reacting conditions.

the lower in-duct pressure drop compared to other studies can be justified by the relatively large duct diameter [40], as also stated by the Authors. This speculation was also confirmed by [46][12] that, considering the same case study, found the in-duct low-pressure region consistent with the Bernoulli's principle, as well as the enhanced upstream air entrainment for DFI consistent with formulations derived for jet pumps[13]. Other researchers, firstly, concluded from experimental pictures, thanks to a spray air entrainment model, that DFI enhances global entrainment in the middle and late stage of spray development under different injection pressure levels [48][14]; secondly, computed through CFD a more than doubled air entrainment at the duct inlet [47][15].

Even though a lot of works, as discussed, highlighted that DFI is capable to enhance entrainment at the duct inlet, it must be said that one early study stated an opposite opinion, suggesting that "up to the duct exit plane, the duct reduces entrainment, does not enhance mixing, and results in a richer, cooler, faster moving core" [32][16]. This statement was justified by the estimation of a bottom limit for the global fuel-to-air ratio (or ϕ_{global}) inside the duct, expressed in terms of ratio of fuel and air inflow rates, assuming that the air velocity (V_{air}) cannot be higher than fuel velocity (V_{fuel}), as in equation 1.1:

$$min(\phi_{global,in-duct}) = \frac{\rho_{fuel} V_{fuel} d_{hole}^2}{\rho_{air} max(V_{air})(D^2 - d_{hole}^2)} = \frac{\rho_{fuel} d_{hole}^2}{\rho_{air}(D^2 - d_{hole}^2)} \tag{1.1}$$

where ρ is the density, D is the duct diameter and d_{hole} is the nozzle diameter. Nevertheless, despite its correctness to assess a global limit value, this calculation does not provide any evidence regarding the difference in global entrainment with respect to the corresponding free spray, neither provides light on the local distribution,

[12]Test vessel, 90 μm single-hole injector, ECN Spray A reacting conditions.

[13]According to [54], the ratio between the mass flow rate of secondary fluid, $\dot{m}_s$, (i.e., charge gas) and primary fluid, $\dot{m}_p$, (i.e., fuel) can be expressed as follows:

$$\frac{\dot{m}_s}{\dot{m}_p} = \frac{-(1+\sigma)}{2\sigma} + \frac{D_{duct}}{D_p}\sqrt{\frac{1}{(1+C_L)\sigma}}$$

where σ is the ratio between the densities of primary and secondary fluids, D_{duct} is the duct diameter, D_p is the injector diameter, and C_L is the skin friction coefficient.

[14]Test vessel, 140 μm single-hole injector, rail pressure=1200-1600 bar, vessel density=46 kg/m^3, vessel temperature=303 K.

[15]Test vessel, 140 μm single-hole injector, rail pressure=1600 bar, vessel density=46 kg/m^3, vessel temperature=303 K.

[16]Test vessel, 138 μm single-hole injector, rail pressure=1000-2500 bar, vessel density=22-55 kg/m^3, vessel temperature=800-950 K, oxygen concentration=21 %.

that can be more homogeneous for DFI even with a globally richer mixture inside the duct. Moreover, it is worth noting that the assumption $max(V_{air}) \simeq V_{fuel}$ it could be not far from reality in the DFI case, due to the presence of the pumping effect, not analysed in that work.

Finally, a clearer understanding of the entrainment process with DFI was developed in the conceptual model (Fig. 1.6) proposed by [55][17], which suggests that, differently from the free spray which continuously decreases the mixture fraction moving farther from the nozzle, the DFI mixing process presents two stages: "(i) wall-confined mixing with enhanced pre-duct air entrainment, towards a globally-rich yet spatially-more-uniform mixture at the duct outlet; (ii) free-space mixing with secondary air entrainment, towards an even leaner mixture at the FLOL [i.e., flame lift-off length] to yield low-soot combustion" [55]. Furthermore, they concluded that the conditions at the duct outlet are critical, since a rich mixture should be maintained to avoid in-duct pre-ignition[18] as well as a lower mixture fraction in the spray core to facilitate a LLFC downstream of the duct. It is noteworthy that these considerations on the equivalence ratio field are in line with the distributions at the duct exit computed in the recent highly-detailed LES campaign under non-reacting conditions, reported in [51].

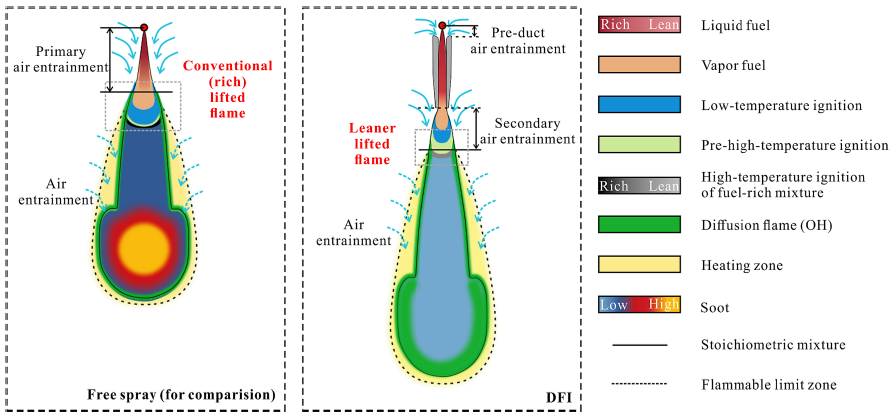

Fig. 1.6 Reproduced from [55]. DFI combustion conceptual model proposed by *Feng et al.*.

In conclusions, according to the evidences nowadays available in the scientific literature, the duct presence does not necessarily enhance or reduce the air entrainment into the fuel spray from a global point of view, but it changes the entrainment rate

[17] Test vessel, 90 μm single-hole injector, ECN Spray A reacting conditions.

[18] This claim seems not supported by ID measurements [56], indicating shorter IDs for richer mixtures. It is probable that the avoidance of in-duct pre-ignition is mainly driven by the higher mixture fraction gradients, perhaps promoted by the global richness at the duct exit.

distribution across the spray plume. In particular, the entrainment rate is enhanced close to the injector; it is inhibited along the duct wall, leading in general to a globally (not locally) richer mixture at the duct exit; it is similar to the free spray (or slightly higher) downstream of the duct, where the amount of LOL extension plays an important role to define if the total entrained mass is lower, equal or higher than the free spray.

Air/Fuel mixing

When air/fuel mixing is discussed, two aspects must be examined: on the one hand, the mixing intended as intensity of the turbulent structures inside the spray plume which can contribute to a better mixing between fuel and air; on the other hand, the equivalence ratio field, main parameter to determine the soot formation potential, which is determined by both the turbulent mixing itself and the already analyzed air entrainment.

Several works investigated the possibility that the duct presence can significantly increase the turbulent mixing compared to the free spray. In [32], the centerline turbulent kinetic energy (TKE) resulted slightly lower than free spray inside the duct, while an enhancement was present downstream of the duct. A lower turbulence inside the duct, then recovered downstream of it thanks to the longer LOL was also observed in [37, 53]. In [39], there was the first observation of a remarkably higher turbulent mixing in the DFI case compared to the free spray, by means of RANS simulations. In particular, the enhancement was observed both inside the duct (Fig. 1.8, taken from [39]), attributed to the establishment of a confined turbulent regime [19], and downstream of the duct (Fig. 1.7, taken from [39]), due to the high velocity and density gradients at the duct exit section. In this latter case, the high turbulence levels seemed triggered by the formation of vortex rings in the transient spray outflow phase, which were observed also during the experimental campaign as reported in Fig. 1.9, adapted from [39].

The impact of duct geometry and operating conditions on this 2-stage mixing process was then analysed in detail in two subsequent works considering the same 180 μm single-hole injector [40, 52]. It worth noting that the observed high turbulence originates from the duct wall in the DFI case (i.e., from the periphery of the jet), thus the evaluation of the centerline TKE only, as done in previous works,

[19] This was confirmed by the evaluation of the Reynolds number (Re) for pipe flows, largely above the laminar-to-turbulent transition threshold: $Re \simeq 2.4 \cdot 10^5 > 2300$

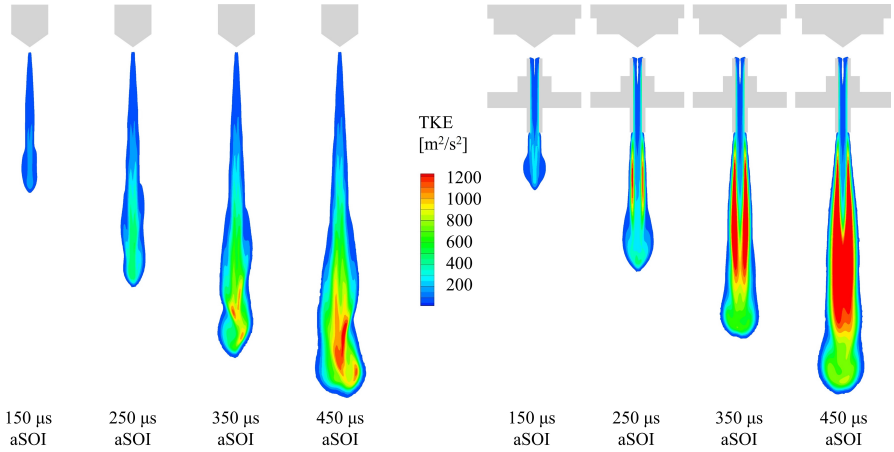

Fig. 1.7 Reproduced from [39]. Evolution of the TKE distribution comparing free spray and DFI configuration. Operating conditions: rail pressure= 1200 bar, vessel pressure= 20 bar, vessel temperature= 573 K.

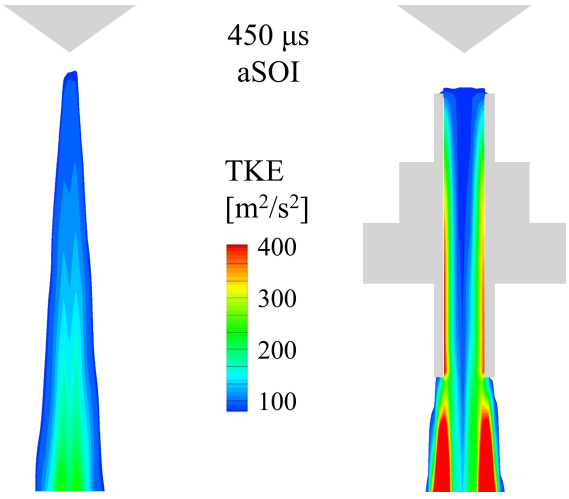

Fig. 1.8 Reproduced from [39]. Enlargement of the TKE distribution of Fig. 1.7 at nozzle tip comparing free spray and DFI configurations.

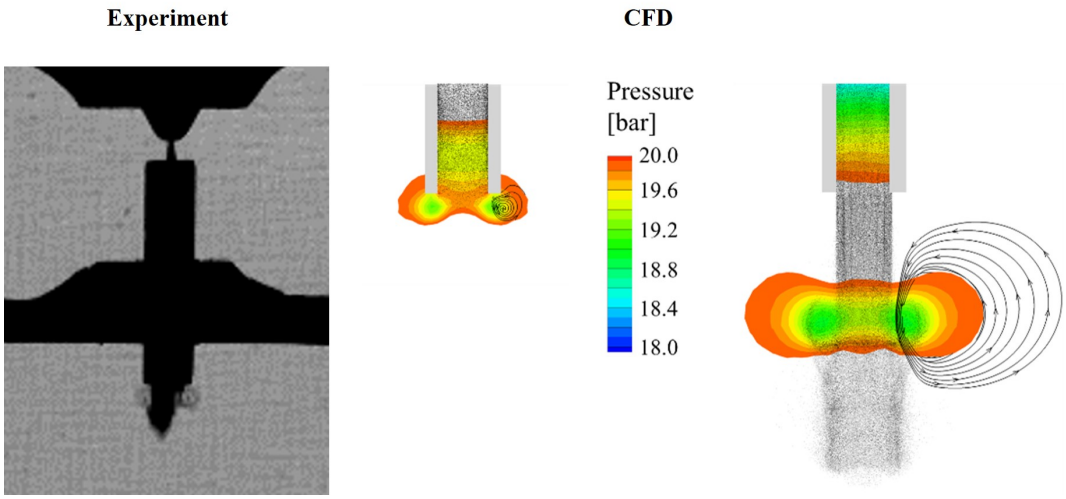

Fig. 1.9 Adapted from [39]. On the right, the pressure distribution and air flow streamlines at duct outlet computed through CFD, with black points representing the liquid fuel parcels. On the left, similar structures observed during the experimental campaign of the same work.

could be misleading. Similar conclusions were also achieved by [49, 42] through a single-realization LES with a relatively coarse grid, in which the TKE associated to the sub-grid scale (SGS) for the DFI was small in the spray axis, where the flow is relatively stable, and large near the duct wall and downstream of the duct, where the momentum transfer with the surrounding gas is higher than free spray. A single-realization LES with a more refined grid was also performed by [47], reporting again similar differences between DFI and free spray in terms of SGS TKE. Moreover, many small vortices were shown close to the duct inner wall, attributed to an adverse pressure gradient effect along with a strong shear force, and two larger vortices at the duct outlet promoting spray radial diffusion, similarly to Fig. 1.9. Researchers in [51] compared for the first time the resolved TKE field of DFI and free spray, by coupling LES with statistical analysis (20 samples for each configuration) and by resolving more than 80% of the turbulent energy spectrum (using a highly refined grid, never achieved in other studies on DFI). The two-stage turbulent mixing enhancement was confirmed, concluding in general that the turbulent energy cascade is spatially more advanced and highly turbulent areas are wider when duct is adopted, showing the importance of the turbulent mixing to achieve a lean mixture with DFI.

Moving to the evaluation of the equivalence ratio field which is determined by both the amount of entrained air into the fuel spray and the turbulent mixing, it is still not clear if the lower local values for DFI are achieved only at the LOL location or for the entire axial length of the spray. Controversial conclusions have been achieved,

suggesting that the answer depends on the ambient and injection conditions, which can make more or less relevant the importance of enhanced upstream entrainment, enhanced turbulent mixing and LOL extension relatively to the free spray.

The extension of the LOL resulted as the key enabler of a low-soot combustion according to the results in [32, 45], where the centerline equivalence ratio or the radial mixture fraction was higher for DFI at equal axial location, but much lower at the corresponding LOL.

More uncertain outcomes were instead obtained by other works. [37] showed lower equivalence ratio values at equal axial location for DFI, but attributed to a lower evaporation rate inside the duct, which could be an additional parameter to take into account to understand DFI physics. In [50], the equivalence ratio was lower than free spray at each axial location for a short duct, while became higher than free spray after the duct exit for longer ducts. In the end, the longer LOL guaranteed always lower values for DFI in the presumed autoignition region. In [53], the centerline equivalence ratio was lower at each axial location for DFI, despite a lower turbulent mixing than the free spray. In this case, it was concluded that the enhancement of the entrainment in a upstream position with respect to the free spray can play a crucial role, since this guarantees a longer available mixing length before the ignition. Moreover, the importance of the entrainment compared to the turbulent mixing phenomena can depend on the different ambient or injection conditions. A leaner and closer-to-stoichiometric average in-duct mixture was computed also by [46] which, anyway, attributed the decrease of soot production to the initial transient phase in which DFI shows a larger spatial regime of near-stoichiometric equivalence ratio values than the free spray.

Lower equivalence ratio values along the whole ducted spray plume was obtained in [39], which also highlighted the homogenization capability of DFI which showed a narrower distribution, due to the high levels of TKE (Fig. 1.7). This distribution was confirmed by [40] for several duct geometries, despite a larger portion of duct wall that inhibits air entrainment (e.g., by increasing duct length) can lead to a locally richer mixture at the duct exit. The importance of the enhanced turbulent mixing and entrainment to achieve this condition has been then highlighted by [52]: comparing combustion results of free spray and DFI in several operating conditions, it emerged that a remarkably lower amount of soot was formed at equal LOL, thus concluding that DFI cannot be classified only as a LOL-extender technology, in agreement with the comments to Figs. 1.2 and 1.3.

Several aspects were then clarified by two detailed LES analyses under different operating conditions. Firstly, according to the conceptual model in Fig. 1.6 presented by [55], global equivalence ratio values tend to be richer for DFI but spatially more uniform at an equal axial distance from the injector orifice (Z). Secondly, according to [51], the globally richer (in agreement with the air entraiment) but spatially more uniform mixture at the duct exit was confirmed, showing that the DFI core tends to be much leaner than the free spray but highly rich pockets are present at the duct wall due to the lack of entrainment. However, these rich pockets are immediately broken after the duct exit by the highly turbulent vortices, guaranteeing a much lower and uniform equivalence ratio distribution at each axial location downstream of the duct. These works show that the enhanced turbulent mixing can be desirable to achieve a better mixture for DFI in the whole domain but its relevance on the final outcome depends on the injection and ambient conditions. Nevertheless, despite turbulent mixing can be similar between free spray and DFI in some conditions, the generally higher spray velocities and mixture fraction gradients (or scalar dissipation rates; see next section) at the duct exit promote a longer LOL, thus lower equivalence ratio values in the autoignition region. Of course, the relative weight of entrainment, turbulent mixing, and LOL extension phenomena depends also on the duct design.

Combustion parameters

Regarding the fundamental characteristics of DFI combustion, there is consensus that the major trends are the ones observed during the proof-of-concept [29, 31], summarized in Table 1.2.

Table 1.2 Summary of DFI effect on the main combustion parameters

Effect of DFI on:		
Ignition delay	⇑	[28, 29, 31–33, 55, 57–63, 37, 39–41, 52, 53, 44–46]
Lift-off length	⇑	[29, 31–33, 58, 37, 40, 52, 41, 60, 53, 44–46, 61, 55]
Combustion duration	⇓	[29, 31, 57–59, 39, 40, 52, 41, 28, 45, 61, 62]
Flame temperature	⇑	[57, 40, 41, 44, 61, 46, 55]

The ID is generally higher for DFI and clear explanations for this effect were provided by evaluating the stoichiometric scalar dissipation rate (χ_{st}), the mixture fraction and the temperature at the duct exit. The χ_{st} quantifies the rate of micro-mixing in turbulent reacting flows, thus properly accounting the effects of turbulent mixing on ignition. In [45], increased values of χ_{st} were observed at the duct exit due

to strong mixture fraction gradients leading to an increased thermal runaway phase affecting the ignition delay, as discussed in [64]. This effect was also combined with a higher heat transfer inside the duct, leading to lower temperatures at the duct exit, even though a minor role was expected. In [55] (see conceptual model in Fig. 1.6), similar conclusions were achieved, being a clear correlation present between the higher ID for DFI and the increased values of χ_{st}, due to a globally richer mixture at the duct exit.

The same explanations apply to the flame LOL extension enabled by the duct adoption, which is also determined by the higher jet penetration previously discussed.

Moreover, the higher ID generally leads to a higher amount of fuel burning in a premixed phase, reducing the CD and increasing the flame temperature.

It is important to note that these trends are valid for DFI under proper working conditions. On the contrary, if abnormal operation is present, such as in-duct ignition or spray-duct misalignment, these trends can be significantly altered. Indeed, there is extensive evidence that, if combustion occurs inside the duct, the DFI soot mitigation potential is curtailed, leading typically to higher soot mass than the free spray [29, 32, 40, 52, 53, 44, 65]. An example of in-duct ignition event is reported in Fig. 1.10, adapted from [29]. The fact that DFI is not working properly can be immediately perceived by comparing this NL signal with the one obtained in Fig. 1.2 for the same temperature level.

1.4.2 Research for DFI implementation on CI engines

The area of research focused on the DFI implementation on CI engine aims at investigating the capability of DFI concept to effectively work and curtail soot when moved from the test vessel to the engine combustion chamber. This passage comes with several questions to be answered, regarding the operation of DFI on the whole engine map, at each load level, studying also the response of fuel conversion efficiency and other emissions to the duct presence. Moreover, since the possibility to implement a low-soot-emissions concept on the existing diesel circulating fleet and in the engines currently under series production would be desirable, it is also important to understand if DFI can be implemented with a direct retrofit approach or if requires an *ad hoc* combustion system design and calibration. All the studies nowadays falling in this area of research are summarised in Table 1.3, indicating the method of investigation, the engine type and displacement, the characteristics of the

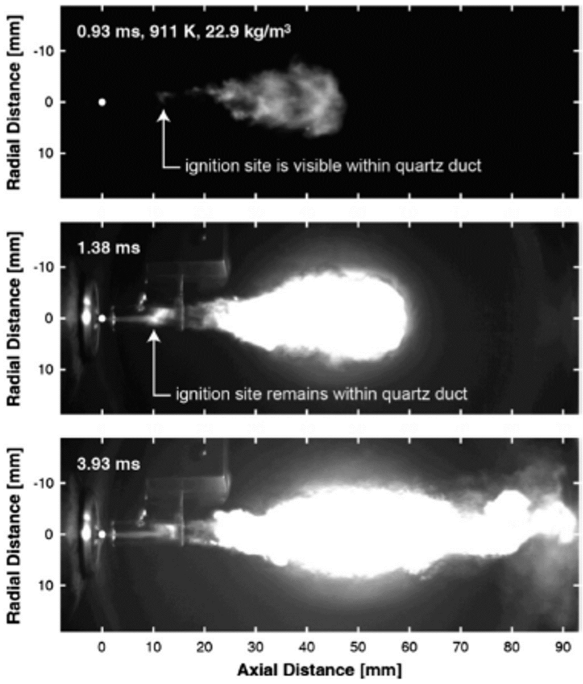

Fig. 1.10 Adapted from [29]. In-duct ignition event: soot natural luminosity associated to the D3L14G2 quartz-duct configuration. The nominal ambient temperature and density are indicated at the top-left of the first image.

injection system[20] , the investigated engine load levels, and the soot emissions trends when the duct is implemented compared to the CDC results.

In this context, most of the evidence comes from analyses on the Sandia compression-ignition optical research engine (SCORE) [21], a 1.72L single-cylinder version of a heavy-duty diesel engine, operated in skip-fire mode and properly modified to provide optical access to the combustion chamber through the fused-silica window of the piston, which features a flat bowl and a vertical side. The suitability of DFI implementation in CI engine combustion chambers maintaining similar effectiveness was firstly shown in [57] through experiments with a 2-holes injector at 2.6 bar IMEPg, demonstrating its potential of breaking the soot/NO_x trade-off with intake-mixture dilution (just considering two dilution levels), reducing engine-out soot emissions by approximately an order of magnitude relative to CDC, without significantly degrading the efficiency and the other regulated emissions. The breakage of the soot/NO_x

[20]For a correct and effective implementation of DFI in diesel engine combustion chamber, a proper design of the duct holder, its assembly on the injector or cylinder head, and the aligment procedure between ducts and injector orifices also play a crucial role. However, the discussion of these aspects is out of the scope for the present work. If interested, different solutions and details can be be found in [29, 57, 58, 66–70].

Table 1.3 Published research works focused on the DFI implementation in CI engines: main details and soot outcome compared to the corresponding CDC. Nomenclature: O=Optical engine; M=Metal engine; I=IMEPg; B=BMEP.

Investigator(s)	Method	Displacement L	Injector Nº holes x μm	Load bar	Δ(Soot)
Nilsen et al. [57]	EXP	1.72 (O)	2 x 110	2.6 (I)	$\Downarrow\Downarrow$
Tanno et al. [58]	EXP	/ (M)	4 x /	/	$\Downarrow\Downarrow$
Nilsen et al. [66]	EXP	1.72 (O)	4 x 110	$2.5 \div 8.7$ (I)	$\Downarrow\Downarrow$
Nilsen et al. [59]	EXP	1.72 (O)	4 x 110	$1 \div 10$ (I)	$\Downarrow\Downarrow$ or $\Downarrow$
Svensson et al. [67]	EXP	2.53 (M)	6 x 205	$16.9 \div 20.3$ (B)	$\Uparrow$
Mueller et al. [28]	EXP	1.72 (O)	2 x 110	2.6 (I)	$\Downarrow\Downarrow$
Nilsen et al. [41]	EXP	1.72 (O)	4 x 110, 175	$6.8 \div 13.4$ (I)	$\Downarrow\Downarrow$
Wilmer at al. [71]	EXP	1.72 (O)	4 x 175	13.3 (I)	$\Downarrow\Downarrow$
Piano et al. [53]	CFD	0.8 (M)	8 x 140	$6 \div 23$ (B)	$\simeq$ or $\Uparrow$
Dias et al. [68]	EXP	/ (M)	8 x 122	$4.7 \div 7.2$ (I)	$\Downarrow$
Sener [62]	CFD	2.44 (M)	6 x 259	13.9 (I)	$\Downarrow$
Sener [61]	CFD	2.44 (M)	6 x 259	$4.1 \div 13.8$ (I)	$\Downarrow$
Nyrenstedt et al. [72]	EXP	1.72 (O)	4 x 175	$1 \div 10$ (I)	$\Downarrow\Downarrow$
Sener et al. [63]	CFD	1.72L (O)	4 x 110	6.8 (I)	/
Buurman et al. [69]	EXP	1.72L (O)	4 x 221	$6 \div 22$ (I)	$\Downarrow\Downarrow$ or $\Downarrow$
Yraguen et al. [70]	EXP	1.72L (O)	2,4 x 110	$0.7 \div 8.7$ (I)	/
Liu et al. [65]	CFD	1.72L (O)	$4 \div 8$ x 175	10 (I)	/

trade-off with dilution was then confirmed in [66] using a 4-holes injector and considering a wider dilution range at 6.8 bar IMEPg, manifesting that DFI operation could meet the current on-road and off-road United States emissions standards on soot and NO_x, without any specific aftertreatment system using intake charge at 12% oxygen, as shown in Fig. 1.11 taken from [66]. Furthermore, a wide range of operating conditions were tested, considering sweeps of oxygen concentration, injection duration (DOI), start of combustion (SOC), injection pressure, intake manifold ambient pressure (IMAP) and temperature (IMT). At all these conditions DFI attenuated engine-out soot, up to two orders of magnitude under certain conditions. A slight reduction of fuel conversion efficiency with DFI was observed, attributable to higher heat losses with head, piston and cylinder liner compared to CDC at all dilution levels, as shown by the corresponding CFD simulations in [63].

The passage from 2-holes to 4-holes guaranteed also the possibility to reach higher engine loads (approximately 10 bar IMEPg) still attenuating engine-out soot emissions, as shown in [59]. However, even though at idle conditions the soot attenuation of DFI relative to CDC was higher than 90% across the entire dilution sweep, it was lower than expected at high load conditions (approx. -27%). This lower performance was related to a second spike (or late-cycle flare-up) in the spatial integral NL trace of DFI, probably due to re-entrainment of hot combustion products upstream of the LOL. This effect correlates with increased injection pressures and

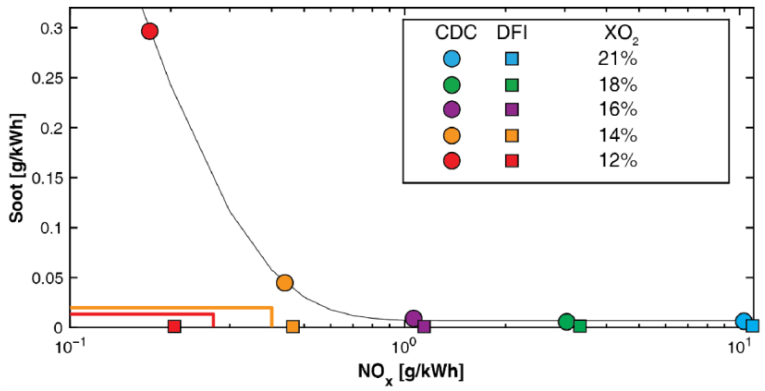

Fig. 1.11 Reproduced from [66]. Soot vs. NO_x plot for DFI and CDC in the oxygen concentration (XO_2) sweep at 6.8 bar IMEPg. The orange box represents the soot/NO_x limits for current off-road emissions in the USA; the red box shows the limits for the current on-road emissions in the USA.

longer DOI, that were used in this work to guarantee the load level despite the relatively small injector orifices. Therefore, better results could be achieved with a different calibration than CDC. In conjunction, the impact of having four ducts instead of two was explored by [70] with a side-by-side study of the DFI combustion, using the same injector orifices. In this context, the just mentioned late-cycle flare-up behaviours were examined, showing that they are increased by the 4-duct configuration and confirming that longer DOI, higher injection pressure and lower IMAP tend to favor them.

Given the possibility to reduce this undesirable phenomenon with larger injector orifices[21], in [41], researchers studied the impact on DFI performance of changing the injector nozzle diameter from 110 μm to 175 μm, which enabled a peak load of 13.4 IMEPg. Although, as expected, larger orifices increased the amount of soot formed per unit of power by both DFI and CDC, the former still guaranteed a reduction of more than 70% and the fuel conversion efficiency became higher for DFI with nearly each duct design tested. Furthermore, a possible interesting correlation emerged between duct diameter and injector orifice diameter, since better performances were achieved coupling the larger-orifice fuel injector with the larger-diameter ducts.

The same combination of injector and engine load was then further investigated in [71] to understand how DFI affects the particle number (PN) and the particle mass (PM) distributions, using an engine exhaust particle sizer and a photoacoustic analyzer (instead of the more conventional filter smoke number correlations). DFI

[21]The larger flow area associated to bigger injector orifices allows lowering injection pressure and DOI, engine load kept constant.

produced both lower PN and lower PM for particulate matter >23 nm in size. More in detail, under accumulation mode, the total solid particle concentration of DFI was 59% lower than CDC, while PM was reduced by 77%. This outcome can lower the particulate loading of DPF over a range of engine operating conditions, thus requiring less frequent active regeneration and thus lower specific fuel consumption.

The focus on the effect of DFI on the aftertreatment devices persisted also in [72], analysing the data collected on a low-load (1 bar IMEPg) and a mid-load (10 bar IMEPg) working points at several dilution levels, implementing the same 175 μm 4-holes injector. Combining DFI with low-lifecycle-CO_2 fuels[22], researchers provided several solutions to meet heavy-duty future on-road and off-road emissions regulations for California, without using some of the aftertreatment systems. As an example, focusing on the cases with diesel fuel, the usage of DFI enabled the compliance of off-road emissions regulations for 2028 without the DPF. The DFI working condition at 10 bar IMEPg with 16% oxygen concentration was then used as benchmark for the CFD study in [65], which investigated how engine parameter changes affect performance, defining some trends towards a DFI-oriented combustion system optimization. In particular, the effects of swirl ratio, piston geometry, compression ratio, number of injector orifices, split injection strategy, and exhaust gas recirculation (EGR) were investigated. As a general outcome, no particular limitations were found by varying compression ratio, piston geometry and number of orifices, suggesting that DFI can already work in existing engine geometries.

Finally, in [69], DFI operation was tested up to full load conditions (approx. 22 bar IMEPg) by using larger injector orifices (221 μm hole diameter) and increasing the IMAP up to 4.2 bar, given the relatively low compression ratio of the optical engine (equal to 12.5 against about 16.5 of typical modern diesel metal engines). DFI reduced engine-out soot by 38.1–63.1% compared to CDC without significant detrimental effects on other emission types, thus reducing the severity of the soot–NO_x trade-off at each load level. Nevertheless, this soot reduction was less remarkable than what observed in previous studies at low- and mid-load conditions, making it emerge that the employed DFI configuration was non-optimal in terms of injection and piston geometry. Therefore, combustion system optimization is fundamental for DFI success on the whole engine map.

[22]It is noteworthy that in a previous study [28], synergies were found between DFI and alternative oxygenated fuels in reducing soot, as discussed in section 1.4.4.

Moving to studies implementing DFI on engines other than SCORE, similar trends in terms of soot reduction were shown through experimental tests on metal engines in [58, 68]. Two CFD studies [61, 62] on a bigger 2.44L heavy-duty metal engine, implementing a 6-holes injector with larger orifices (259 μm), provided also similar trends in terms of soot reduction by the means of a detailed soot model. In particular, the soot was reduced up to 67% by the DFI, simultaneously decreasing *HC* and *CO* emissions and without compromising engine performance.

Nevertheless, some metal engine studies reported less promising results compared to the ones obtained on the SCORE. In [67], DFI was tested on a heavy-duty metal engine equipped with a 6-holes injector, comparing performance and emissions for DFI and CDC at high loads (up to 20 bar IMEPg) to evaluate whether DFI could be successfully retrofitted into a production-like combustion system. In this case study, DFI generally yielded higher engine-out soot emissions, and some speculations were done about the underlying reasons behind this countercurrent outcome: the LOL shortening, due to the re-entrainment of hot combustion products, and the poor soot oxidation, due to jet-jet interaction. Increased number of injector nozzles could also contribute to the worsening of DFI performances. High sensitivity to the injection timing was also found. In the end, they concluded that it cannot be assumed that DFI can be retrofitted onto existing engines, which are highly optimized to meet current emission regulations for CDC. On the contrary, the optimization of the combustion system should be considered also for DFI application. A following CFD study [53], based on detailed chemistry and detailed soot modelling, investigated further this aspect on a light-duty diesel engine implementing a 8-holes injector, to highlight the factors which can limit or facilitate DFI integration in existing combustion chambers. Considering a low load and a full load conditions, it was observed that DFI did not yield any significant advantage to engine-out soot emissions and fuel consumption with the existing combustion system. Although soot formation was generally reduced at low load, the soot oxidation process was partially inhibited by the adopted duct keeping fixed the engine calibration, suggesting the need for a complete optimization of the combustion system design. On the other hand, a preliminary variation of engine calibration highlighted several beneficial trends for DFI, whose operation was improved by a simplified injection strategy (i.e., no post-injection). At high load, the high density–high temperature conditions were prohibitive for the DFI configuration due to the occurrence of in-duct combustion, suggesting that a limit on the engine operating map could be needed, consistently with the soot mass outcome in [52] under high-density (50 kg/m^3) constant-volume conditions. Therefore, these results

indicated that DFI retrofit solutions without specific optimization of the combustion system design do not guarantee soot reduction. Nonetheless, it was also highlighted that there is much room for improvement in terms of DFI-targeted combustion chamber design and engine calibration to achieve the full success of this technology for soot-free CI engines.

1.4.3 Research for duct geometrical optimization

A clear understanding of the impact of each duct geometrical parameter on DFI combustion behaviours and performance would be of paramount importance for duct design optimization and integration in engine combustion systems, featuring a variety of characteristics and working conditions. Despite several works focused on this kind of analyses, it is Author's opinion that clear and simple trends are not yet established to obtain optimal duct design in terms of soot emissions reduction. This is mainly because the effect of each geometrical parameter cannot be decoupled by the setup in which DFI behaviour is explored. Injector characteristics, injection pressure and timings, ambient temperature and density, combustion chamber design, etc., are just some of the aspect that can drastically affect the main trends with duct geometry. This is especially true when the focus is the soot mass, since the final value depends on the very complex soot formation/oxidation process: geometrical changes that in certain conditions can improve the soot formation could have an opposite effect on soot oxidation. In other words, this is a multi-variable problem which hardly can be answered by a simple and clear solution. The studies which explored the impact of different duct designs on the soot mass under reacting conditions are summarized in Table 1.4. For the sake of clarity, stand-off distance (G), duct length (L), and duct diameter (D) are illustrated in Fig. 1.12. The duct names are established according to the herein used convention (D<diameter>L<length>G<stand-off distance>) which will be exploited for the whole text.

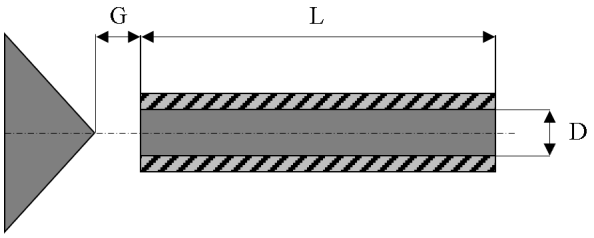

Fig. 1.12 Main duct geometrical parameters: stand-off distance (G), duct length (L), and duct diameter (D).

Table 1.4 Published research works focused on the impact of duct design on soot mass: main details and tested geometries. Nomenclature: CVCV=Constant-volume combustion vessel; HPTV=High-pressure-temperature vessel; CI=Compression-ignition engine; d_{hole}=Nozzle hole diameter; P_{rail}=Rail pressure; T_v=Vessel temperature; ρ_v=Vessel density; O_2=oxygen concentration.

Investigator(s)	Setup (Method)	Operating conditions	Duct geometries
Gehmlich et al. [31]	CVCV (EXP)	$d_{hole} = 90\mu m$ $P_{rail} = 1500bar$ $T_v = 850 \div 1200K$ $\rho_v = 14.8 \div 22.8kg/m^3$ $O_2 = 15 \div 21\%$	D1.5L6G(1.4,3.2) D2L8G3.8 D2L16G(1.4,3.8,5.9) D3L14G2
Fitzgerald et al. [32]	HTPV (EXP)	$d_{hole} = 138\mu m$ $P_{rail} = 1000 - 2500bar$ $T_v = 800 \div 950K$ $\rho_v = 22 \div 55kg/m^3$ $O_2 = 21\%$	D2L14G2 D3L7G4 D3L14G(2,9) D4L14G2
Svensson et al. [33]	HTPV (EXP)	$d_{hole} = 138\mu m$ $P_{rail} = 1000 - 2500bar$ $T_v = 800 \div 1000K$ $\rho_v = 20.9 \div 52.3kg/m^3$ $O_2 = 21\%$	D2L8G(0.1,4.5) D2L(10,12)G0.1 D2L14G(0.1,2.2,4,6)
Nilsen et al. [57]	CI (EXP)	$d_{hole} = 110\mu m$ $P_{rail} = 1800bar$ $O_2 = 16 \div 21\%$ $IMEP_g = 2.6bar$	D2L12G(1.6,3)
Millo et al. [40]	CVCV (CFD)	$d_{hole} = 180\mu m$ $P_{rail} = 1200bar$ $T_v = 900K$ $\rho_v = 22.2kg/m^3$ $O_2 = 21\%$	D1.5L8G1 D1.5L10G(0.1,1,2) D1.5L14G1 D2L8G1 D2L10G(0.1,1,2,4) D2L(14,16)G(1,2,4) D3L8G1 D3L10G(0.1,1,2) D3L14G1
Nilsen et al. [41]	CI (EXP)	$d_{hole} = 110 \div 175\mu m$ $P_{rail} = 1800bar$ $O_2 = 16\%$ $IMEP_g = 6.8 \div 13.4bar$	D(2,3)L(8,12,16)G3
Svensson et al. [60]	HTPV (EXP)	$d_{hole} = 150 \div 219\mu m$ $P_{rail} = 2500bar$ $T_v = 800 \div 1000K$ $\rho_v = 20.5 \div 25.3kg/m^3$ $O_2 = 21\%$	D1.6L14G(3,4.7) D1.85L14G(3,4.7) D2L14G3 D2.25L14G(3,4.7) D2.5L14G3 D3.2L14G(0.1,3)
Sener [62]	CI (CFD)	$d_{hole} = 259\mu m$ $P_{rail} = 900bar$ $IMEP_g = 13.9bar$	D1.5L8G4.8 D2L8G(3.2,4.8) D2L16G3.2 D3L8G4.8
Feng et al. [55]	CVCV (CFD)	$d_{hole} = 90\mu m$ $P_{rail} = 1500bar$ $T_v = 900 \div 1100K$ $\rho_v = 22.8kg/m^3$ $O_2 = 21\%$	D2L(12,16,20)G1.4

Less challenging is instead the definition of trends for other less complex physical quantities that affect the final combustion and soot outcome. Among them, spray-related quantities, such as penetration, cone angle, air entrainment, turbulent mixing, and combustion/flame-related quantities, such as ID and LOL, have been investigated when duct geometry varies. Even though simple answers are still far to be achieved also in this case, a summary of the main observed trends are reported in Table 1.5.

Table 1.5 Summary of duct geometry effects on the main spray and combustion quantities. ⇑ indicates positive correlation, ⇓ indicates negative correlation.

Spray penetration	D	⇓	[32, 35, 38, 41, 48]
	L	⇑	[33, 35, 40, 41]
	G	⇑	[33, 38]
Spray cone angle	D	≃	[35, 38, 48]
	L	⇑	[35, 40]
	G	⇓ or ≃	[38]
Upstream entrainment	D	⇑	[32, 40, 48]
	L	⇑	[50, 40, 55]
	G	⇑	[40]
Ignition delay	D	≃	[32, 41, 60, 62]
	L	⇑	[33, 41, 55]
	G	≃ or ⇓	[31] [33]
Lift-off length	D	⇓	[32, 40, 41]
	L	⇑	[31, 33, 40, 41, 55]
	G	≃ or ⇑	[31, 40, 33]

As can be seen, the spray penetration features clear correlations, being typically higher with lower duct diameters, longer duct lengths, and longer stand-off distances. In other words, as the portion of spray confined by the duct increase, the higher jet momentum conservation allows the spray to penetrate more. Less evident are instead the correlations between spray cone angle and duct geometrical features, which is slightly affected by duct diameter and stand-off distance, while features a certain correlation with the duct length.

The influence of the duct geometry on the upstream air entrainment is clear, being based only on mass flow rate considerations enabled by a pressure difference. Basically, the geometrical variations which increase the pressure difference (longer ducts and smaller diameters) and/or the flow area (longer stand-off distance and larger diameters) are beneficial for pre-duct entrainment, with the latter more impacting

than the former. The influence of duct geometry on turbulent mixing is not reported in the table, since this is much more complex and hardly classifiable with a positive or negative correlation. Indeed, as seen in section 1.4.1, it is a two-stage process, whose final outcome depends on a number of parameters, such as the duct exit location, the mixing intensity inside the duct and downstream of it, the LOL, etc., as discussed in [40]. Some preliminary details on the effect of duct geometry on turbulent mixing can be found in [32, 50, 40, 47, 55].

Moving to the combustion parameters, the ID is poorly affected by duct diameter and stand-off distance, while slightly increases with longer duct lengths, probably due to the reduced contact with the surrounding air given by the more extended duct wall. The LOL dependency on the duct geometry is mainly driven by the combined effect of penetration and ID. Therefore, the LOL is longer when the duct diameter decreases and the duct length increases, while it is little affected by variation of stand-off distances, featuring a weak positive correlation. However, it is worth noting that the usage of longer duct lengths to enhance the LOL extension can in the end cause a reduction of the so-called "effective LOL", namely the portion of ducted spray length really available for entrainment. Indeed, as shown in [40, 55], the distance between duct exit and autoignition region tends to be shorter when the duct length increases.

Some secondary importance geometrical variations were also investigated in the scientific literature. In particular, the effect of the duct inlet and outlet shape was object of attention of some studies. These different shapes can be mainly classified in 4 classes, as introduced in [31], whose picture is herein reproduced (Fig. 1.13). The α shape features sharp inlet and outlet section; the β shape features a full radius or a chamfer at the inlet of the duct; the γ shape features a tapered duct outer wall up to the outlet section; the δ shape is the combination of the last two.

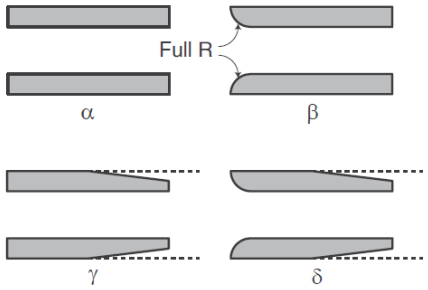

Fig. 1.13 Reproduced from [31]. Sketch of four different classes of duct shape: α, β, γ, δ.

The effect of these shapes was firstly studied in [31], where large benefits were found by using a rounded inlet section (i.e., moving from α to β) while slight benefits were associated to the tapered outlet (i.e., moving from α to γ). These effects were then combined in the δ shape that was defined as optimal, and extensively used in subsequent works by the same and other researchers [33, 57, 37, 50, 66, 59, 67, 28, 41, 71, 60, 45, 61, 62, 72, 63, 55, 70, 65].

Similar analyses were also executed in [40] through CFD, considering the α, β and γ shapes. The benefits of a chamfer at the duct inlet were confirmed, promoting higher upstream air entrainment and extending the LOL. On the contrary, the tapered outlet did not lead significant improvements in that conditions.

In conclusion, it must be said that also some unconventional duct geometries (e.g., convergent-divergent duct [48, 47]; conical duct [73], elliptical duct [74], internally threaded duct [42]) were explored by some research groups, but the available information is currently relatively low.

1.4.4 Research for DFI coupling with low-lifecycle-CO_2 fuels

In order to achieve a simultaneous low-soot low-lifecycle-CO_2 emissions diesel combustion, as needed in a decarbonized scenario considering a CI engine-based transportation, DFI technology must be coupled with low-lifecycle-CO_2 fuels. Therefore, some studies from Sandia National Laboratories researchers focused on this topic, aiming at investigating if DFI works effectively with fuels other than diesel suitable for CI engines, always employing the SCORE experimental setup.

In [28], two oxygenated blends were tested at low load (2.6 bar IMEPg) implementing a 2-holes injector, having as baseline the No. 2 emissions certification diesel (denoted CF_B). One oxygenated blend contained 25% in volume of methyl decanoate in CF_B (denoted MD25), while the other contained 25% in volume of tri-propylene glycol mono-methyl ether in CF_B (denoted T25). The 25% was chosen since representative of biodiesel blend levels commercially available in the United States. For the conditions investigated, synergies were found between DFI and oxygenated fuels in terms of soot formation reduction, indeed soot NL was curtailed by two orders of magnitude, one due to DFI and an additional one due to fuel oxygenation, as illustrated in Fig. 1.14 taken from [28]. It is worth noting that a two orders of magnitude higher camera relative gain (G_{rel}) was necessary to visualize the NL when DFI was coupled with the oxygenated blend (bottom right image). This goal was

achieved regardless of dilution level and without large effects on other emissions or efficiency.

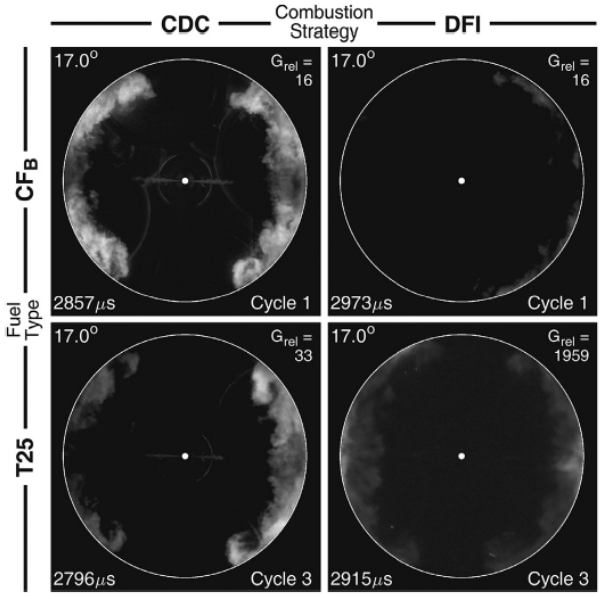

Fig. 1.14 Reproduced from [28]. Effect of fuel oxygenation and DFI on the in-cylinder natural luminosity at 16 mol% oxygen concentration near the middle of mixing-controlled combustion phase. The white dot shows the injector-tip position; the white circle shows location of piston bowl-rim. Relative camera gain (G_{rel}), time after actual start of injection, and fired-cycle number are shown in upper-right, lower-left, and lower-right corners, respectively, of each image frame.

These synergies were then examined by evaluating the different equivalence ratio at the LOL required for LLFC, that was significantly higher in the case of fuel oxygenation. Thus, assuming other factors are equal, it should be easier to achieve LLFC with oxygenated rather than non-oxygenated fuels and, given the fuel-flexibility of DFI, the combination with its physical working mechanisms can further facilitate the achievement of this target.

In [72], evidence was provided on the possibility to achieve future emissions regulations at an affordable aftertreatment cost and reduce at least 70% of lifecycle CO_2 emissions, combining DFI with low-lifecycle-CO_2 fuels. In particular, three low-lifecycle-CO_2 fuel blends were examined having as a petroleum-based (100% fossil carbon content) reference the No. 2 S15 diesel (denoted CF_C). Starting from a non-oxygenated blend from products of hydrothermal liquefaction of sewage sludge and ethanol-to-distillate conversion (denoted HEA00) featuring only 18.5% non-renewable carbon content, the alkoxyalkanoate (AOA) synthesis was added at 33% or 67% in volume (forming the HEA33 and HEA67 fuels) to provide further

soot reduction due to oxygen content, at the cost of a higher non-renewable carbon content of 24% and 29.5%, respectively. Analysing the soot-NO_x diagrams with dilution sweeps, considering a low-load (1 bar IMEPg) and a mid-load (10 bar IMEPg) working points, it was shown that the lower soot emissions when using DFI and/or oxygenated fuels enable higher dilution levels to be employed, facilitating simultaneous NO_x control. Indeed, the CDC with diesel fuel had soot up to 1323% and NO_x up to 492% higher than DFI coupled with HEA67, as shown in Fig. 1.15, adapted from [72]. Finally, they concluded that, by combining DFI with renewable fuels featuring a significant oxygenation level, the future off-road regulations for California could be even satisfied without a DPF or NO_x aftertreatment system.

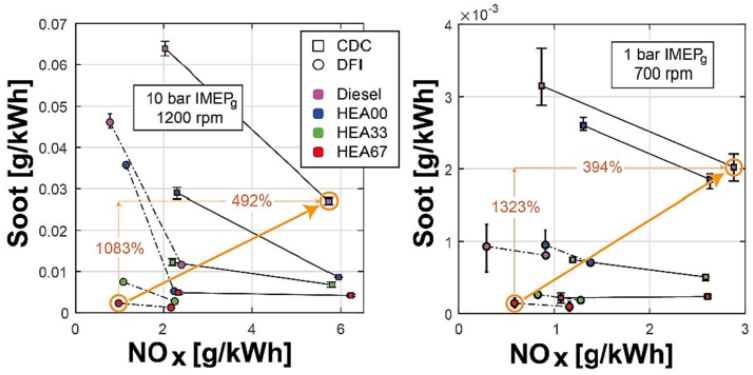

Fig. 1.15 Adapted from [72]. Soot-NO_x plots showing the effect of DFI with changed fuels and dilution at both low- and mid- loads.

In conclusion, given these previous positive insights, a low-lifecycle-CO_2 fuel consisting of 80% renewable diesel and 20% biodiesel was used in combination with DFI in [69] for the whole testing campaign on a wide range of engine load levels up to full load conditions (approx. from 6 to 22 bar IMEPg), whose main outcomes were already discussed in section 1.4.2. This is in line with the Co-Optima[23] project [75] aiming at proposing DFI with low-lifecycle-CO_2 fuels as a promising path to practical, clean, and sustainable machines powered by internal combustion engines.

1.5 This work: objectives and structure

The present work aims to cover several key knowledge gaps in the understanding of DFI, analysing in detail the entrainment and mixing mechanisms, the combustion and

[23]Co-Optimization of fuels and engines (Co-Optima) is a Consortium of the U.S. Department of Energy

emissions formation processes, as well as the impact that duct geometrical features and/or operating conditions have on them. Moreover, the application of DFI on a light-duty series-production CI engine is explored, to highlight the factors which can limit or facilitate its integration in existing combustion chambers. Therefore, the results of this research activity, that were already published and briefly presented to the reader throughout the broad literature review (section 1.4), contributes to several areas of research regarding the DFI concept: research for DFI physics understanding, research for DFI implementation on CI engines, research for duct geometrical optimization.

In particular, the PhD thesis is structured as follows. After having presented the reference data for 3D-CFD modelling validation coming from an extensive experimental campaign in constant-volume vessel for spray characterization (chapter 2), the DFI working mechanisms are explored through high-quality computationally-expensive LES combined with statistical analysis (chapter 3), considering non-reacting conditions. This numerical highly-detailed high-fidelity dataset is then employed as benchmark to validate a RANS model (chapter 4), that is exploited to investigate the DFI combustion and emissions formation processes at an affordable computer power request (chapter 5). The combustion modelling approach is also qualitatively validated against literature data. Hence, this robust RANS combustion model is used for understanding the impact of the main duct geometrical characteristics (chapter 6) and engine parameters (chapter 7) on DFI performance. Finally, as a side activity, the numerical and experimental results coming from the application of DFI concept on a series-production light-duty diesel engine are reported too (chapter 8).

Chapter 2

Experimental campaign

Part of the work described in this chapter was previously published in:

- Cristiano Segatori, "Ducted Fuel Injection: a Computational Fluid Dynamics analysis of soot formation mitigation mechanisms," Rel. Federico Millo, Andrea Piano, Politecnico di Torino, Corso di laurea magistrale in Ingegneria Meccanica, 2020, http://webthesis.biblio.polito.it/id/eprint/14575
- Millo, F., Piano, A., Peiretti Paradisi, B., Postrioti, L., Pieracci, L., Bianco, A., Pesce, F.C. and Vassallo, A.L., "Ducted Fuel Injection: Experimental and numerical investigation on fuel spray characteristics, air/fuel mixing and soot mitigation potential," *Fuel*, Volume 289, 2021, doi:1016/j.fuel.2023.128110.
- Millo, F., Piano, A., Peiretti Paradisi, B., Segatori, C., Postrioti, L., Pieracci, L., Bianco, A., Pesce, F.C. and Vassallo, A.L., "Ducted Fuel Injection: A Numerical Soot-Targeted Duct Geometry Optimization," *SAE Int. J. Engines* 15(2):2022, doi:10.4271/03-15-02-0014.

The CFD work object of this thesis is based on the data collected during an *ad hoc* experimental campaign carried out in the *SprayLAB* of the *Università degli Studi di Perugia*. This campaign aimed at characterizing the DFI jet in constant-volume non-reacting conditions in terms of spray shape, penetration, cone angle, drop sizing and velocity with respect to a corresponding free spray and, thus, providing reliable experimental data to support the validation of the 3D-CFD models. This chapter summarizes most of the information regarding the conducted experimental tests and the available data exploitable for the subsequent numerical activity. For further details, please refer to the cited publications.

2.1 Injection hydraulic characterization

A Bosch CRI1 solenoidal common rail injector featuring a single, in-axis 180 μm hole[1] (nozzle length/diameter ratio equal to 5) was used for all the investigations in high temperature and pressure conditions. The injector was fed with commercial diesel fuel pressurized by a static pressure generator (Loccioni Mobility Thor) and actuated by a programmable driver (Loccioni Mobility AEA006).

The hydraulic analysis of the tested prototype injection system was carried out by a proprietary Injection Analyzer based on the Zeuch Method [78], to derive simultaneously the shot-to-shot injection rate and injected volume. In order to measure the injection rate time-history in a given operating condition (defined by the injection pressure level and injector actuation strategy), the injection took place in a closed, constant volume chamber filled with the same injected fuel. At the injector actuation timing, the fuel pressure in the test chamber is constant at a "base level" typically ranging between 20 and 60 bar for diesel applications. During the injection process, a volume of fluid is forced to enter in the test chamber, causing the pressure to rise. More in detail, the volumetric injection rate (dV/dt) is proportional to the chamber pressure rise rate (dp/dt) according to equation 2.1:

$$\frac{dV}{dt} = \frac{V}{k}\frac{dp}{dt} \tag{2.1}$$

where V is the chamber volume, while k is the fluid bulk modulus, characterizing the compressibility of the fluid. Therefore, analyzing the chamber pressure time-history through a piezo-resistive pressure transducer [2] , it is possible to derive both the injection rate and the injected volume relevant to each single injection process. Nevertheless, since the main purpose of this process is the measurement of the injection rate shape, the fluid evacuated from the test chamber is metered by a Coriolis mass flow meter for a reliable measurement of the injected volume, thus overcoming the well-known difficulties related to the fluid bulk modulus dependence on pressure and temperature and allowing a continuous self-calibration of the instrument. In particular, at the end of the injection process, after a proper stabilization period, the

[1] It is worth noting that this nozzle hole diameter is similar to the ECN Spray D [76], thus is relevant for heavy duty applications [77].

[2] It is noteworthy that, given the rapidity of the phenomenon and the need to derive the pressure signal, amplifying the high-frequency noise, the digital acquisition system must be set with a high-enough sampling frequency and a well-designed low-pass filter. For this case study, each injection event was sampled with a frequency of $100kHz$ for an acquisition time of $10ms$; the resulting signal was filtered with a 2nd order low-pass filter featuring a cut-off frequency of $2kHz$.

measuring chamber pressure is reset to the initial level so to repeat the measurement for a consecutive injection event; to this end, a fast acting discharge valve evacuates the injected volume from the chamber by opening a port towards a large downstream volume maintained at the pressure base level. This sequence of events defines the instrument operating cycle that in the current release can be operated up to 100 Hz. In a given operating condition, a batch of identical injection events (e.g. 600) is repeated, the first part of which (e.g. 300) is used to obtain a thermal stabilization of the system, while during the remaining events of the batch all dynamic signals are recorded and analyzed to obtain the mean and individual events time-histories of injection rate and of the other acquired quantities. Further details about the used Injection Analyzer are reported in [79, 80].

For the herein experimental campaign, the injected volume and the injection rate measurements were carried out in the operating conditions reported in Table 2.1.

Table 2.1 Operating conditions for the injection hydraulic characterization

Test fluid		ISO4113		
Fluid temperature	K	$299 \div 309$		
Fluid density	kg/m^3	$823.4 \div 824.7$		
Nº injections		Single injection		
Nº of repetitions		300		
		Injection pressure bar		
		400	800	1200
Back pressure	bar	10	Energizing time μs	
		20		
		30	$250 \div 2000$	

The shot-to-shot dispersion of the injected volume was assessed in terms of coefficient of variation (COV) and EMI[3]-like curves. As an example, the mean injected volume and the related COV as function of the energizing time (ET) are reported in Fig. 2.1 for an injection pressure of 800 bar and a back pressure of 10 bar.

In general, the injected volume provided by the single-hole prototype injector was almost linear apart from the ballistic operation zone. Furthermore, the obtained shot-to-shot dispersion of injected volume was appreciably low, with COV values

[3]EMI stands for *Einspritzmengenindikator*, injection quantity indicator.

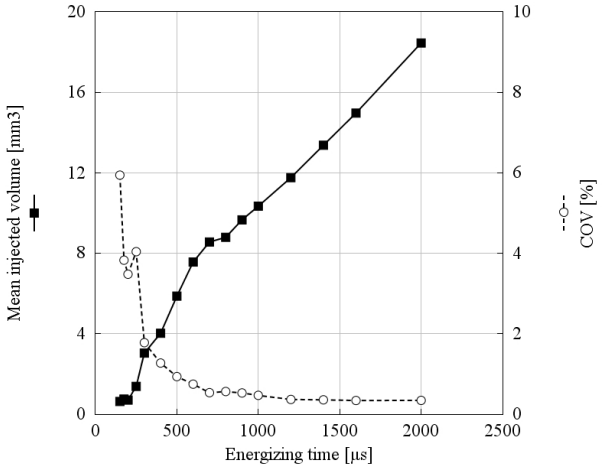

Fig. 2.1 EMI-like curve and coefficient of variation (COV) as a function of the energizing time for the the prototype single-hole injector. Injection pressure: 800 bar; back pressure: 10 bar. Adapted from [81].

below 0.5% in the linear operation zone for all the tested injection pressure levels. Consequently, for the optical spray evolution analysis in test vessel the $ET = 1000\mu s$ was assumed, and the related experimental injection rate are depicted in Fig. 2.2 for all the tested rail pressures.

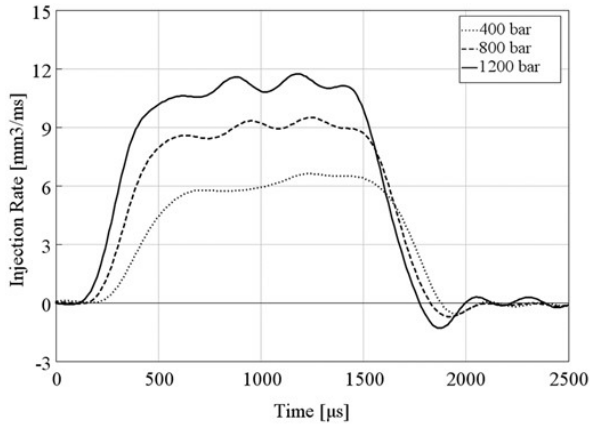

Fig. 2.2 Experimental injection rate measurements at different rail pressures and constant energizing time ($ET = 1000\mu s$).

As can be seen, the injection pressure increase causes a gradual reduction of the injection delay from the ET start, with less evident effects on the injector closing delay. The steady flow rate level is achieved for ET values between 400 and 500 μs depending on the injection pressure level, confirming the end of ballistic operation characterized by a relatively high shot-to-shot injected quantity dispersion. In order

to correctly simulate the spray evolution, the actual hydraulic start of injection (SOI) was estimated from the injection rate measurement following the procedure reported in [79]. According to this methodology the actual spray exit timing can be evaluated computing the injected volume as the injection rate time integral, and the actual SOI is coincident with the final zero-crossing event, as shown by the black vertical lines in Fig. 2.3. The corresponding injection rate level is assumed as the initial value of the liquid injection flow rate adopted in the 3D-CFD Lagrangian simulation of the spray evolution.

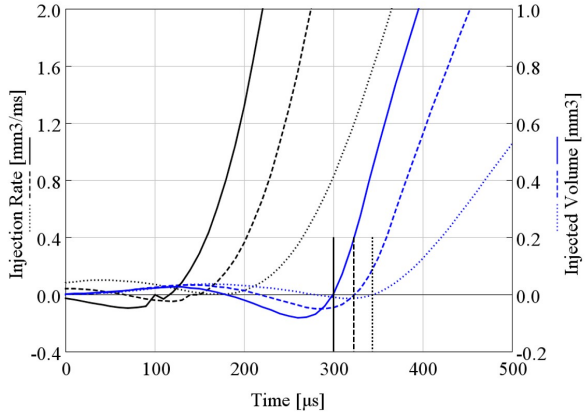

Fig. 2.3 Hydraulic start of injection (SOI) estimation: injection rate (black) and injected volume (blue) at different rail pressures and constant energizing time ($ET = 1000\mu s$), with vertical bars indicating the computed spray start timings.

After the injection starts, the hydraulic end of injection (EOI) is defined as the first time value corresponding to the injection rate equal to 0 mm^3/ms. The DOI is thus the difference between hydraulic EOI and SOI.

2.2 Optical analysis

2.2.1 Constant-volume vessel

The overall spray evolution and the drop sizing analyses in high temperature and pressure conditions were both carried out in a dedicated 4-liter constant-volume vessel (CVV, Fig. 2.4). The CVV features 3 rectangular optical accesses (50x100 mm) arranged in order to allow both a back-light optical layout for global spray imaging and a classical phase doppler anemometry (PDA) layout for drop velocimetry and sizing measurements (110 deg scattering angle).

Fig. 2.4 Photo of the constant-volume vessel used for the optical analysis.

The CVV was designed to operate up to 30 bar and 773 K thanks to a proper internal ceramic shield (Fig. 2.5) and to a continuous, compressed, hot air/nitrogen flow. The incoming flow (typically 90 l/min under normal conditions, nlpm) is heated by a 3.5 kW electric air gun installed on the vessel side shell; the heater input power was controlled in closed-loop with the vessel internal temperature measured 20 mm downstream the nozzle exit. The flow inlet is on the side of the CVV, the flow outlet at the bottom. The main specifications of the CVV are presented in Table 2.2.

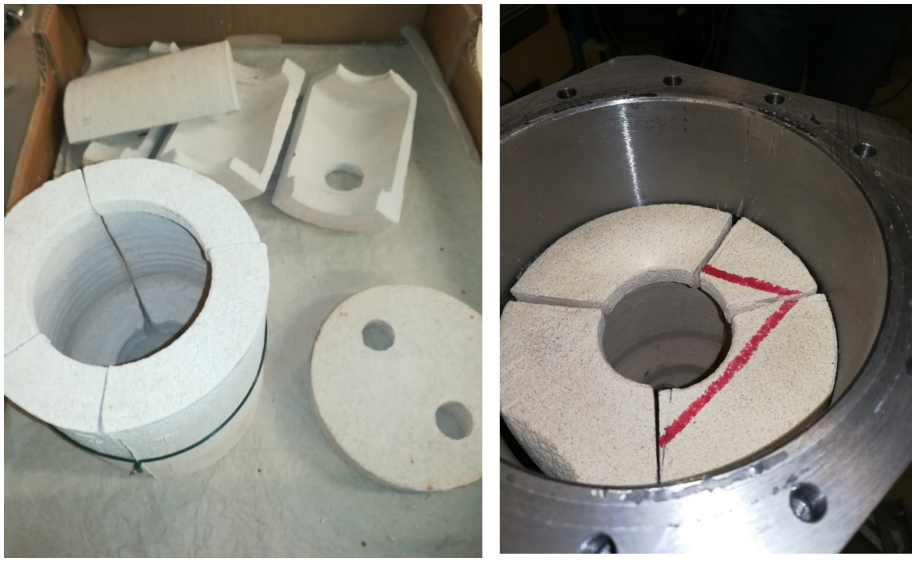

Fig. 2.5 Photo of the internal ceramic shield for the thermal insulation of the test vessel.

Table 2.2 Experimental constant-volume vessel specifications

Volume	l	4
Shape		Cylindrical
Material		Stainless steel
Maximum pressure	bar	30
Maximum temperature	K	773
Air mass flow rate	$nlpm$	90
Heaters type		Electric in-line
Heaters power	kW	3.5
Nº windows		3
Windows shape / material		Rectangular / Quartz
Windows dimensions / thickness	mm	50x100 / 30

The common rail injector is installed on the CVV top, with the single jet evolving downward along the vessel main axis. In order to investigate the interaction between the high pressure spray and a duct, the prototype nozzle was equipped with a stainless steel modular duct-holder (Fig. 2.6), designed to minimize its intrusiveness on the spray evolution and on the spray/duct interaction as well as to accommodate different duct designs at different distances from the nozzle hole (ranging from 0 to 4 mm). In this way, the effect of different lengths and/or stand-off distances on the ducted spray behaviour can be parametrically investigated.

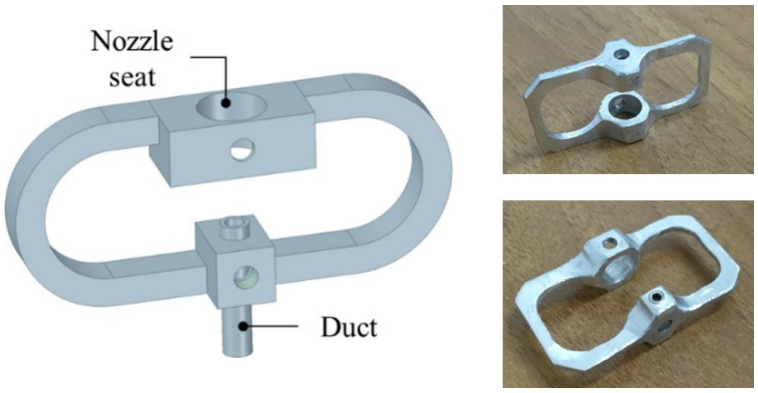

Fig. 2.6 Modular duct holder design: sketch (left) and photos (right).

In particular, three different duct geometries were tested during the experimental campaign, for a total of four configurations considering the free spray case, as summarized in Table 2.3. The standard duct configuration was taken as a reference, given the optimal soot reduction achieved in other works [32, 33]. Then, the effect of duct length (i.e., both short and shifted duct) and stand-off distance (i.e., shifted duct)

were considered; further, the distance from the nozzle hole to the duct outlet section was the same for standard and shifted duct configurations while it was significantly reduced for the short duct configuration.

Table 2.3 Geometrical configurations analysed through experiments. Duct wall thickness: 0.5 mm.

Configuration	D *mm*	L *mm*	G *mm*	Duct name
Free spray	-	-	-	-
Standard duct	2	14	2	D2L14G2
Shifted duct	2	12	4	D2L12G4
Short duct	2	10	2	D2L10G2

2.2.2 High speed imaging (Schlieren technique)

In Fig. 2.7, a detailed schematic of the spray imaging layout is depicted.

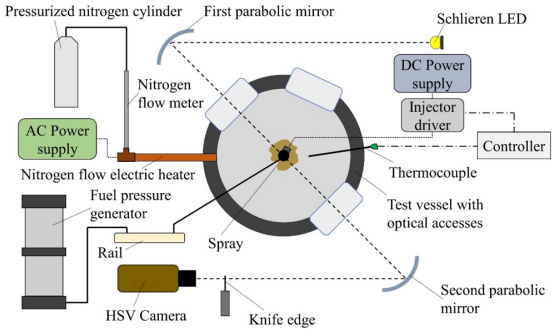

Fig. 2.7 Detailed schematic of the experimental apparatus for spray imaging.

The classical "Z-shaped" Schlieren configuration was used to allow the vapor phase visualization in low temperature, non-evaporating conditions in the CVV; removing the Schlieren knife the spray liquid phase could be visualized. In high temperature conditions, both liquid and vapor phases are clearly visible in simple backlight configuration. In particular, a high-power LED (Luminus CBT-140) was used as a steady light source, and two 6-inches parabolic mirrors were positioned to obtain a parallel light beam crossing the CVV, through the two opposite rectangular quartz windows, and re-focus on the knife edge. The spray evolution was finally acquired by a high-speed complementary metal-oxide-semiconductor (CMOS) camera (Vision Research Miro 310 C) operated at 50 kframe/s, with a 1 μs exposure time and

a 128 × 320 resolution, offering a 50-mm long field of view in the spray evolution plane. In each operating condition, 20 acquisitions were performed to account for the shot-to-shot dispersion. The 20 spray videos acquired in each tested operating condition were offline digitally analyzed by proprietary software developed in the LabVIEW™ Vision environment. By this procedure, single frames were extracted from the high-speed videos and binarized in order to locate the boundary of the spray liquid phase. The resulting 2-bit images were then further processed to compute the spray tip penetration and cone angle, according to the SAEJ2715 rule [82]. This procedure was repeated at different elapsed timings from the injector actuation start, so to build spray mean penetration and cone angle curves as a function of time along with the corresponding shot-to-shot dispersion. Further details about the image analysis procedure can be found in [83].

The operating conditions adopted for the high-speed imaging analysis of the free spray and the standard duct (see Table 2.3) in the herein experimental campaign are summarized in Table 2.4. The other geometrical configurations were tested only on narrower range of conditions.

Table 2.4 Operating conditions for the high-speed imaging analysis, free spray and standard duct configurations.

Test fluid			Diesel oil		
Nº injections			Single injection		
Energizing time	μs		1000		
Nº of repetitions			20		
			Injection pressure *bar*		
			400	800	1200
Vessel pressure	*bar*	10	Vessel temperature *K*		
		20	373, 573, 773		

Sample sequences of the spray evolution in different operating conditions are reported in Fig. 2.8. For the sake of brevity, only data pertaining to the 20 bar vessel pressure operating conditions are shown. The first two sequences were obtained in non-evaporative conditions (373 K) for both the free spray and the DFI with standard duct configuration. In the third and fourth sequences, the free spray and the DFI developed in fully evaporative conditions (773 K).

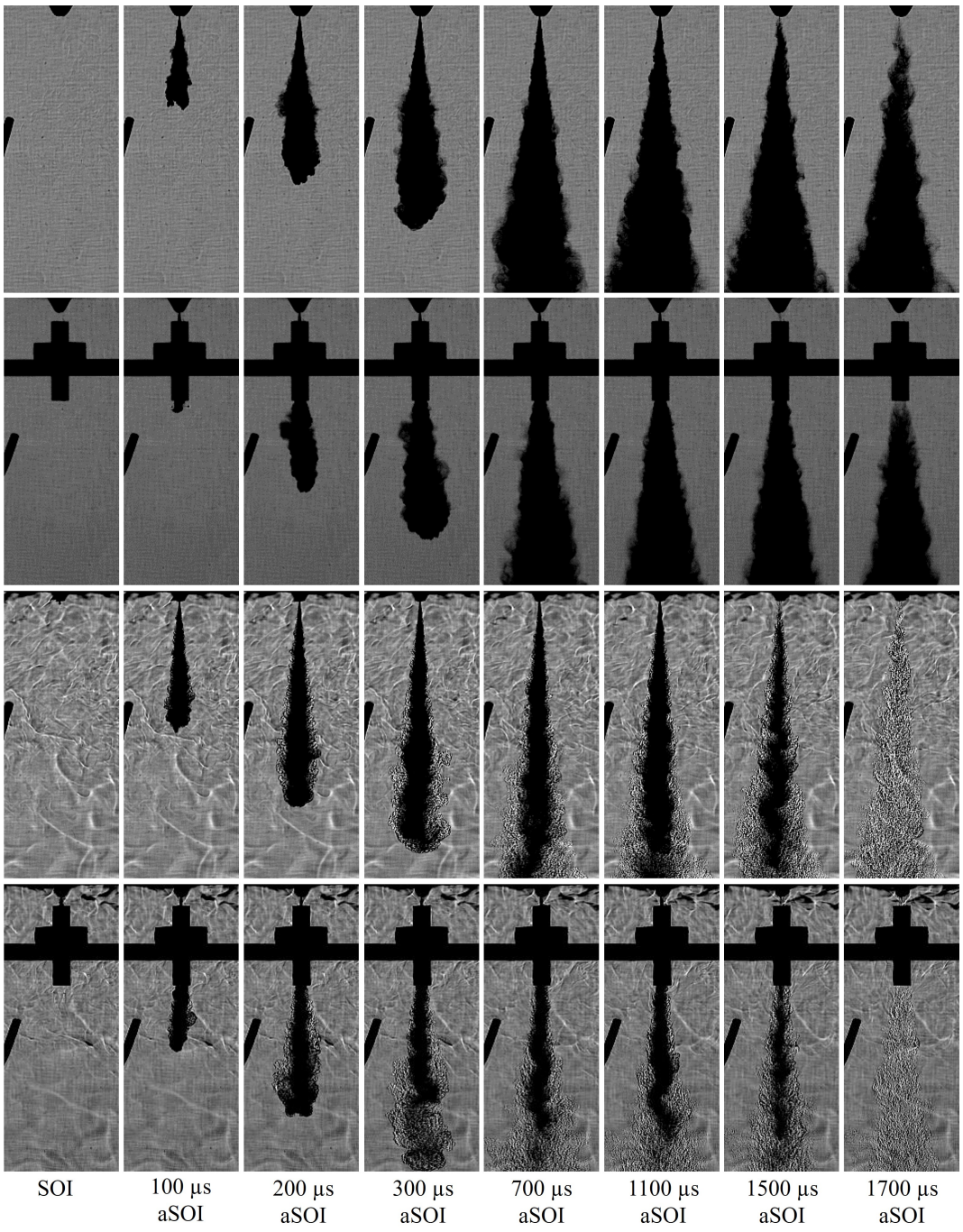

Fig. 2.8 Experimental spray evolution sequences, vessel pressure = 20 bar, rail pressure = 1200 bar, ET = 1000 μs. First row: free spray, vessel temperature = 373 K. Second row: DFI (Standard duct configuration), vessel temperature = 773 K. Third row: free spray, vessel temperature = 773 K. Fourth row: DFI (Standard duct configuration), vessel temperature = 773 K.

The quantitative analysis of the ducted spray evolution evidences significant differences with the free spray, as outlined in Fig. 2.9 for some of the examined operating conditions.

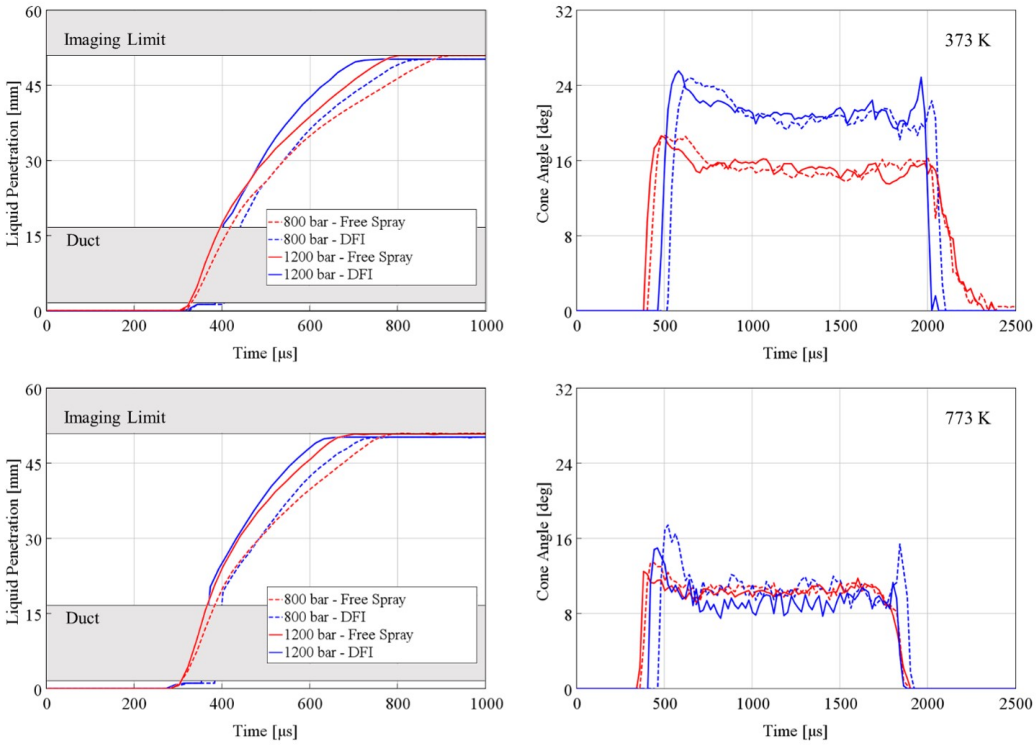

Fig. 2.9 Experimental liquid penetration (left) and global cone angle (right) for free spray and DFI (Standard duct configuration) at different rail pressures. Test conditions: vessel pressure = 20 bar, vessel temperature = 373 K (top) – 773 K (bottom), ET = 1000 μs.

The spray tip penetration velocity downstream the duct is generally higher for the ducted configuration, suggesting the missing momentum flux exchange with the surrounding air in the duct to prevail on the spray-duct wall dissipative interactions. In terms of liquid spray structure shape, in non-evaporative conditions the spray-duct interactions caused an evident increase of spray cone angle, from 15 to 20 deg, suggesting a more intense momentum flux exchange and air entrainment flux. Conversely, in high vessel temperature conditions the strong evaporation rate and the reduced air chamber density significantly thinned the liquid spray to such an extent that global cone angle values in the range 9 to 12 deg were measured in all operating conditions and configurations. In addition, it is worth pointing out that the liquid spray cone angle is affected by a higher fluctuation of the measured angle due to the duct insertion, which is also perceivable observing the third and fourth spray sequences reported in Fig. 2.8. In fact, in the last sequences (from 300 to

1500 μs aSOI), the internal liquid-portion of the spray appears thinner and more distorted, suggesting also the presence of enhanced evaporation and more intense radial velocity components related to air entrainment in high temperature conditions.

Concerning the other geometrical configurations reported in Table 2.3, the high-speed imaging analysis was applied only with the CVV conditions set at 20 bar and 773 K, with different rail pressure levels (400, 800 and 1200 bar). For sake of brevity, only the results obtained at 1200 bar rail pressure are reported in Fig. 2.10 in terms of penetration and cone angle for the spray liquid phase. In addition, Fig. 2.11 shows sample spray images captured 0.2 ms after SOI (aSOI) and in fully developed jet conditions for the analyzed duct configurations.

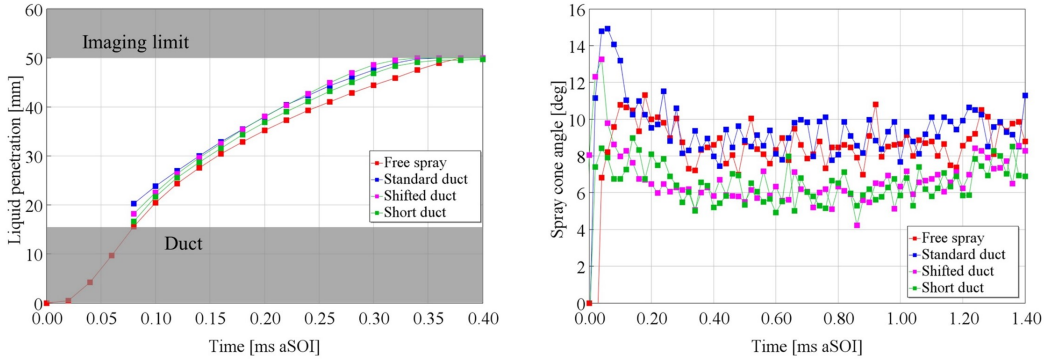

Fig. 2.10 Experimental liquid penetration (left) and global cone angle (right) for each geometrical configuration reported in Table 2.3. Test conditions: vessel pressure = 20 bar; vessel temperature = 773 K; rail pressure = 1200 bar; ET = 1000 μs.

The duct insertion evidently influences the spray global shape evolution. Considering the free spray (red) as a reference, the spray tip penetration (Fig. 2.10, left) is significantly enhanced by the standard configuration (blue), with a more moderate effect with the short design (green). Shifting downstream the duct inlet section so to obtain the shifted duct (magenta) results in an initially reduced penetration at the timing of the first appearance of the spray tip downstream the duct (80 μs aSOI), followed by an increased tip velocity in the following spray evolution with respect to the standard design. In other words, a significant reduction of the duct length (short vs standard duct) results in a drastic reduction of the duct effect, while shifting the duct inlet section with a moderate length reduction (shifted vs standard duct), the duct effect seems to be delayed and shifted downstream. In terms of spray cone angle (Fig. 2.10, right), the insertion of the standard duct does not seem to affect the spray evolution to a large extent, at high vessel temperature, while a slight cone angle decrease was observed for both the shifted and the short configurations. The

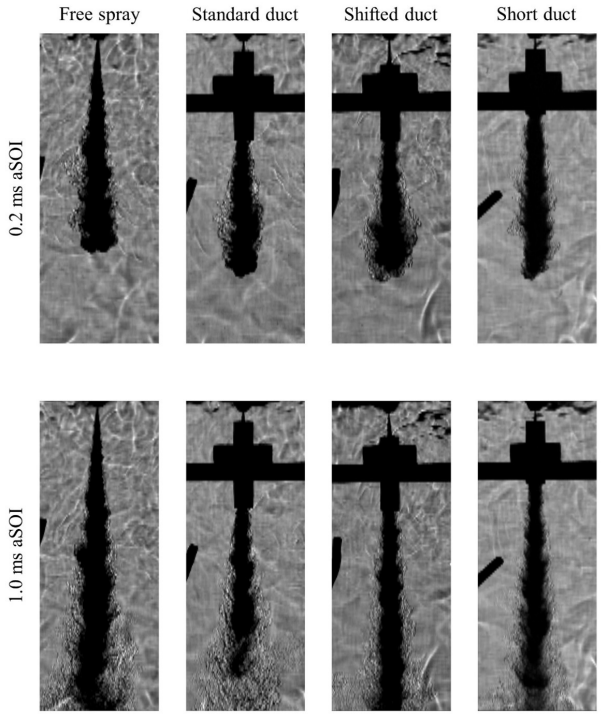

Fig. 2.11 Experimental spray evolution for each geometrical configuration reported in Table 2.3 at 0.2 ms (top) and 1.0 ms (bottom) aSOI. Test conditions: vessel pressure = 20 bar; vessel temperature = 773 K; rail pressure = 1200 bar; ET = 1000 μs.

relevance of small differences in the duct design can be better perceived by observing the fully developed spray appearance (Fig. 2.11, bottom). At the considered timing, the standard duct spray is completely different from the free spray structure: the inner liquid core (dark in the image) is significantly less extended and compact, suggesting a more intense evaporation process. Around the spray tip, large blobs of liquid fuel periodically seem to detach from the main spray structure being dissolved downstream, thus defining a region where the fuel is vaporized over the entire plume section (complete vaporization distance); for standard duct configuration, this distance is around 50 mm for the entire injection process duration. Conversely, with the shifted duct the complete vaporization takes place well downstream the 50 mm observation window. Finally, for the short duct configuration, the complete vaporization distance seems to be intermediate among the standard duct configuration and the shifted one: the geometrical inlet pattern for the spray and air streams is the same as the standard duct, while the sucking driving force produced by the spray evolution in the duct could be less effective, as explained in the numerical section.

2.2.3 Phase doppler anemometry (PDA)

In Fig. 2.12, a detailed schematic of the PDA layout is depicted.

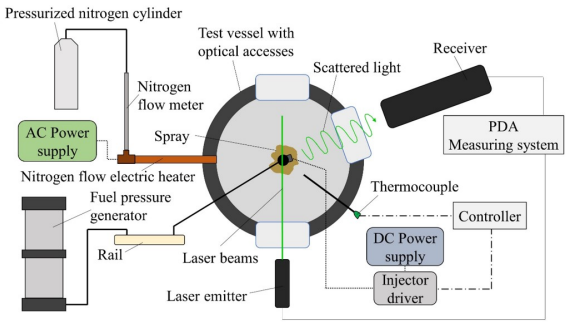

Fig. 2.12 Detailed schematic of the experimental apparatus for phase doppler anemometry (PDA).

The PDA system is based on a Dantec FlowLite 1D laser source (532 nm, 200 mW) coupled with a Dantec BSA P80 processor, a 112 mm Fiber PDA transmitter and a 112 mm Hi-Dense receiver, which is specifically designed to operate with dense spray such as diesel or gasoline direct-injection jets. Both the PDA transmitter and receiver are positioned by a 3-axis Cartesian traverse system, which allows the PDA measuring volume positioning in XY planes at different distances from the nozzle exit along the vertical, downward oriented Z-axis. Further details on the main features of the system are reported in [84].

In this experimental activity, the PDA system was used to detect drop sizing and vertical velocity components resulting from the spray evolution along a linear traverse along Y direction crossing the entire spray structure over a plane at 50 mm distance from the nozzle exit. The Y traverse was positioned at X = 2 mm coordinate where the maximum data rate was obtained in a preliminary scan. In each measurement station in the traverse, valid data pertaining to 150 consecutive shots were collected. Moreover, the spray boundaries were determined according the data count criterion suggested in [82]. This analysis was executed in both non-evaporative (373 K) and evaporative (773 K) conditions in the pressurized CVV (10 bar) for the free-evolving and the ducted spray configurations.

The operating conditions adopted for the PDA-based drop sizing and velocity measurements of the free spray and the standard duct (see Table 2.3) in the herein experimental campaign are summarized in Table 2.5. This kind of test was not executed for the other geometrical configurations.

Table 2.5 Operating conditions for the phase doppler anemometry (PDA) analysis, free spray and standard duct configurations.

Test fluid		ISO4113	
Nº injections		Single injection	
Energizing time	μs	1000	
Nº of repetitions		150	
Measure location	mm	$X = 2; Z = 50$	
		Injection pressure	
		bar	
		400	800 1200
		Vessel temperature	
Vessel pressure	bar	10	K
			373, 773

In Fig. 2.13, the raw results obtained in X=2, Y=0 in non-evaporative and evaporative conditions are reported for the free spray configuration, in which time axis values are referred to the ET start.

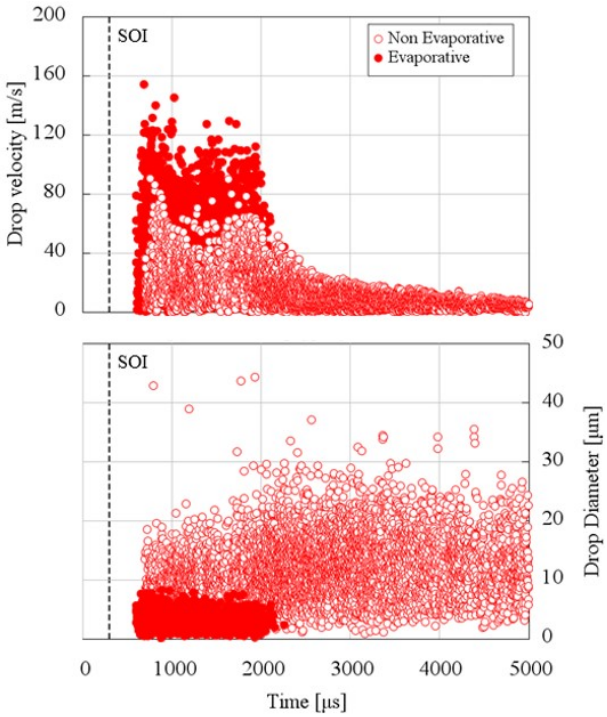

Fig. 2.13 Drop velocity (top) and sizing (bottom) data at X = 2, Y = 0, Z = 50 mm for the free spray configuration. Test conditions: Rail pressure = 1200 bar, vessel pressure = 10 bar, vessel temperatures = 373 K (non-evaporative conditions) - 773 K (evaporative conditions).

As can be observed, in non-evaporative conditions a large number of drops is detected after the EOI (1500 μs aSOI). These drops, passing through the considered measuring station after the EOI are progressively slowed down due to aerodynamic drag while their diameter tends to remain constant due to both very slow evaporation and weak breakup mechanisms. Conversely, at vessel temperature equal to 773 K, the spray evolution is completely different: drops are no longer detected in the measuring station later than 1900 μs aSOI (400 μs after the EOI) evidencing the drastic effect of evaporation mechanism in high temperature conditions. Further, in terms of drops axial velocity, the vessel temperature increase causes the spectrum of observed values to be significantly larger due to the reduced vessel air density and conversely the range of measured diameters is dramatically narrowed for both improved breakup and promoted drop evaporation velocity. The comparison between the free spray and the DFI (with standard duct configuration) in terms of mean count data and drop sizing for the tested conditions vessel pressure = 10 bar, vessel temperature = 773 K at different rail pressures is reported in Fig. 2.14.

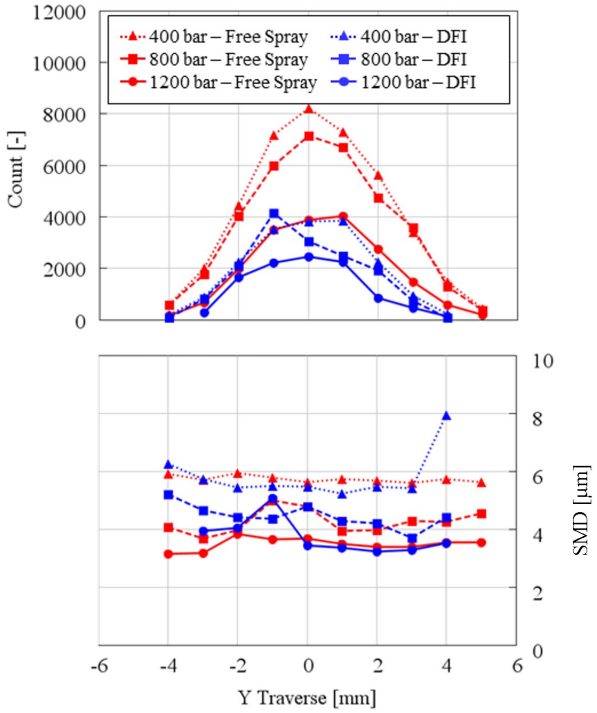

Fig. 2.14 Drop counting (top) and sizing (bottom) data at X = 2, Z = 50 mm for free spray and DFI (Standard duct configuration) at different rail pressures. Test conditions: vessel pressure = 10 bar, vessel temperature = 773 K.

The most evident result is the remarkable decrease of drops count (-58 % at 1200 bar of rail pressure) obtained for the ducted spray, in all the explored measuring

stations: this evidence seems to confirm the enhanced drop evaporation rate due to the duct presence. In terms of SMD of the droplets, only marginal reductions (lower than 0.5 μm) seem to be caused by the duct adoption, the most significant effect being the evident decrease in the residual drops number downstream the duct rather than substantial modification in the drop diameter statistical distribution.

Chapter 3

DFI physical understanding through large eddy simulation (LES): the reasons of low-soot operation

Part of the work described in this chapter was previously published in:

- Millo, F., Segatori, C., Piano, A., Peiretti Paradisi, B. and Bianco, A., "Large Eddy Simulations (LES) towards a comprehensive understanding of Ducted Fuel Injection concept in non-reacting conditions," Proceedings - *Thiesel 2022 Conference on Thermo- and Fluid Dynamics of Clean Propulsion Powerplants*, 2022, doi:10.4995/Thiesel.2022.632801.
- Segatori, C., Piano, A., Peiretti Paradisi, B., Millo, F. and Bianco, A., "Ensemble average method for runtime saving in Large Eddy Simulation of free and Ducted Fuel Injection (DFI) sprays," *Fuel*, Volume 344, 2023, doi:1016/j.fuel.2023.128110.
- Segatori, C., Piano, A., Peiretti Paradisi, B., Bianco, A. and Millo, F., "Exploiting the potential of large eddy simulation (LES) for ducted fuel injection investigation in non-reacting conditions," *International Journal of Multiphase Flow*, Volume 171, 2024, doi:10.1016/j.ijmultiphaseflow.2023.104686.

As a first detailed approach to the study of the DFI concept, this chapter presents a non-reacting numerical analysis through LES. In fact, it is well-known how, for highly turbulent case studies, a LES capable to satisfy the quality criteria guarantees

more accurate and reliable results with respect to the corresponding RANS simulation, with the drawback of a much higher computational cost [85, 86]. Therefore, considering that the turbulence plays a dominant role in DFI mixing process, the usage of LES increases in importance for a robust and detailed knowledge on the topic. Furthermore, another interesting characteristic of LES is its inherent dependency of the solution by very small fluctuations of the initial conditions, similarly to experiments [87], making it deserve the name of *numerical experiment*. As a consequence, run-to-run variability must be taken into account with this turbulence modelling approach.

Therefore, the aim of this part of work is to exploit the potential of LES combined with statistical analysis to explore the non-reacting spray of DFI configuration compared with the unconstrained spray towards its full comprehension. For this purpose, as discussed in the next sections, a highly refined grid was adopted to ensure a high-quality LES [88] together with a statistically significant sample size for both spray configurations. Then, a detailed analysis of the ducted spray turbulent characteristics was performed, improving its understanding to support DFI development and optimization.

3.1 Methodology

3.1.1 Reference operating conditions

The LES numerical analysis was conducted under the non-reacting ambient conditions and injection characteristics reported in Table 3.1. The ambient pressure and temperature values (determined by the limitations of the experimental setup; see section 2.2) led to an ambient density approximately equal to 9 kg/m^3, which is relatively low compared to the typical density values achievable by modern CI engines at the top dead center firing (TDCf). However, given the fundamental importance of having experimental data for validation in this part of the analysis, these conditions were considered acceptable. Predictive reacting simulations in chapter 5, 6 and 7 will assess the main findings under higher temperature and density values. For the DFI configuration, the D2L14G2 geometry (also named *standard duct* in Table 2.3) was used.

Table 3.1 Reference operating conditions (non-reacting)

Oxygen concentration	%	0
Vessel pressure	bar	20
Vessel temperature	K	773
Rail pressure	bar	1200
Injection duration	ms	1.5
Injected mass	mg	11.85

3.1.2 LES 3D-CFD setup

Overview

The numerical simulations were carried out on the commercially available software CONVERGE CFD 3.0.14 [89]. The post-processing of the 3D results was conducted on MATLAB R2021a [90].

The experimental cylindrical 1.5L test vessel, equipped with a co-axial prototype single-hole common rail injector featuring a nozzle diameter equal to 0.180 mm and injecting standard diesel fuel, was replicated in the 3D-CFD environment. Wall-type fixed-temperature (equal to the vessel temperature) boundary conditions were set for the whole CVV as well as the duct wall. The heat transfer was taken into account through the O'Rourke and Amsden model [91]. The domain was initialized with an almost quiescent flow based on the experimental test boundary conditions. Considering a SOI occurring 0.3 ms later than the start of the simulation, and the injection event simulated for 0.5 ms, the total simulation duration was set equal to 0.8 ms. This time window is sufficient for the spray to cover the whole length of the experimental optical access window (i.e., approx. 50 mm in the spray axis direction), thus achieving pseudo-stationary conditions in the spatial window of interest.

Concerning the numerical aspects, the flow field was solved by means of a finite volume method employing a second-order central difference scheme for spatial discretization. The pressure implicit with splitting of operators (PISO) algorithm [92] coupled with the Rhie-Chow scheme for pressure-velocity coupling [93] was adopted to solve the Navier-Stokes equations. The second-order, numerically stable, Crank-Nicolson method was adopted for the temporal discretization. A variable time-step was set, dynamically determined by the Courant-Friedrichs-Lewy (CFL) limits, to minimize the runtime maintaining the solution accuracy.

Spray model

The spray model was developed and calibrated in the RANS framework to enable more simulation attempts at an affordable computational cost. The spray model was then moved to LES and validated against experimental data, as documented in section 3.2. The underlying hypothesis is that the turbulence modelling approach, moving from RANS to LES, does not affect the liquid-related results to such an extent as to involve a modification of the spray sub-models selection and calibration.

The Lagrangian particle tracking approach was adopted for the spray modelling, injecting parcels with a diameter equal to the effective nozzle hole diameter according the blob injection model [94] and with a near spray cone angle accurately set according to the experimental spray imaging acquisitions. The number of injected parcels was chosen to guarantee a good balance between liquid and gas phase in each cell, avoiding overestimation of the penetration due to high liquid volume fraction [95]. This number was changed according to the minimum grid size. The primary and secondary breakup processes were described according to the Kelvin-Helmholtz Rayleigh-Taylor (KH-RT) model without breakup length [96]. The collision model was neglected for the present case study. The drop drag phenomenon was modelled as dynamic drop drag, in order to take into account the deformation of each droplet due to aerodynamic resistance [97]. Concerning the fuel physical characteristics, the liquid phase was represented by Diesel #2 liquid fuel, while the normal-heptane (N-C_7H_{16}) was selected as single species for the gas phase. The evaporation process occurred according to the Frossling model, considering also the boiling process [98]. All this information is summarised in Table 3.2.

Table 3.2 3D-CFD spray model summary

Injected fuel	Diesel #2
Evaporating species	N-Heptane ($N-C_7H16$)
Liquid injection	Blob model [94]
Droplet turbulent dispersion	O'Rourke model [98]
Spray breakup	Modified KH-RT model [96]
Evaporation	Frossling with boiling model [98]
Droplet drag	Dynamic drop drag [97]
Heat transfer	O'Rourke and Amsden model [91]

The calibration process was mainly focused on the time and size constants of the modified KH-RT breakup model (i.e., without the breakup length) and on the discharge coefficient, which was properly modified taking into consideration the

super-cavitation hypothesis deeply investigated in [99] for similar injector configurations.

DFI spray/wall interaction modelling

According to the results reported in [39], the spray model did not require any variation of the calibration constants to predict both free and DFI sprays. This was deemed as an important outcome of the model validation process and was achieved only if the spray/wall interaction, critical aspect when DFI is concerned (especially in non-reacting weakly evaporative conditions), was described with the rebound/slide model [100, 101].

This model, adopted in this work too, enables the drop impacting on the wall to just rebound or slide, according to the normal component of the Weber number [1] , without the formation of a wall film. Although it could seem too simplistic, it could be the most representative option for DFI spray/wall interaction characterization among the models nowadays available. In fact, DFI is a peculiar case due to short distance from injector (thus, high drop velocity at impact) and very low impact angle (i.e., <10-15 deg). In these conditions, typically used wall film models (e.g., O'Rourke model [102]; Kuhnke model [103]) led to a not negligible overestimation of splash and thermal breakup phenomena, causing unphysical drop size reduction downstream of the duct, and subsequent liquid penetration degradation. Vice versa, rebound/slide model led to very good penetration prediction and drop size reduction with respect to the free spray, consistent with experimental analysis reported in [39]. For the sake of completeness, a comparison among the experimental SMD reduction provided by the duct adoption and the one predicted by RANS simulations employing the abovementioned spray/wall interaction models (i.e., rebound/slide, O'Rourke, Kuhnke) are reported in Fig. 3.1. The SMD is evaluated on the spray axis, 50 mm downstream of the injector nozzle. The reference values are related to the models featuring the default coefficients, while the calibration effect refers to the maximum variation of SMD obtained conducting several simulation tests, varying for the DFI configuration the calibration constants of both the spray/wall interaction model and the secondary breakup model through their entire usable range. The

[1] $We = \frac{\rho_l U^2 D}{\sigma_l}$, non-dimensional parameter describing the competition between the inertial force and the surface tension in the droplet evolution. ρ_l is the liquid density; U is the characteristic velocity, D is the drop diameter and σ_l is the liquid surface tension.

parameters of the primary breakup model were kept unchanged since it is strictly related to the injector characteristics, which are unvaried among free spray and DFI.

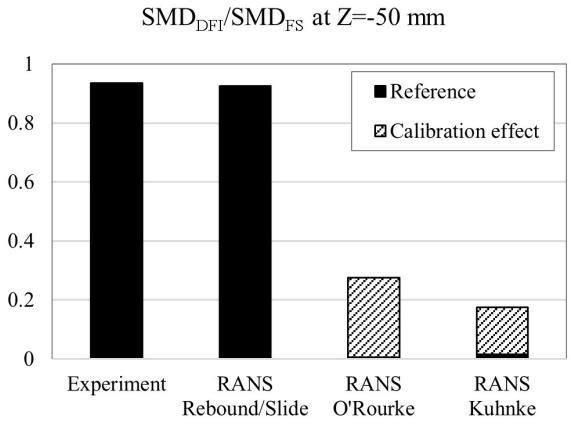

Fig. 3.1 DFI Sauter mean diameter (SMD) normalized with respect to the free spray one at Z=-50 mm: comparison among experiments (vessel pressure = 10 bar; vessel temperature = 773 K) and RANS simulations (operating conditions in Table 3.1) employing different spray/wall interaction models. Filled bar, reference values; patterned bar, maximum effect of spray/wall interaction model and secondary breakup model calibration

It is evident how the rebound/slide model outperforms the other spray/wall interaction models in the prediction of the SMD variation provided by the duct adoption, even if a calibration effort is considered.

Besides, the absence of a wall film could be physical for the DFI-like conditions, since the possibility of impingement is strongly affected by the dynamic conditions of drop/wall impact, drastically decreasing as the impact angle decreases [104, 105] (i.e., droplet motion direction quasi tangential to the wall). As stated, this could be caused by the dramatic reduction of the so-called dynamic Leidenfrost temperature and/or by aerodynamic effects playing a role in preventing drop/wall contact, due to the formation of an interposed gas layer according to the lubrication theory. Furthermore, an indirect demonstration of the absence of duct wall impingement is provided by Sandia researchers in [29]. According to their experiments, the luminosity associated with soot incandescence was not detected at the end of the injection, meaning the absence of locally fuel-rich regions related to liquid fuel droplets ripped out of the duct wall by the high-velocity spray. Therefore, “it is believed that liquid fuel did not impinge on the duct wall during injection for any of the studied conditions” [29], partly comparable to the present study in terms of vessel temperature.

In conclusion, the rebound/slide model was deemed as sufficiently motivated from both a practical and physical perspective among the state-of-the-art spray/wall interaction models. It must be specified that this model comes with some drawbacks. In particular, if the droplet dynamics falls in the conditions for a sliding output, the model does not predict any momentum degradation due to friction, leading to a probable overestimation of the velocity close to the duct wall.

Turbulence model and wall treatment

The turbulence was described by means of the LES approach, directly resolving the largest turbulent eddies from the Navier-Stokes equations, while modelling the smallest ones, more isotropic and less case dependent [106]. A spatial filter, defined through the minimum grid size, establishes the passage from solved to unsolved turbulent structures (i.e., sub-grid scale).

The SGS was modelled through the one-equation dynamic structure model [107]. This non-viscosity model, on one hand, does not require *a priori* knowledge of the flow coefficients that, instead, are dynamically determined as a function of time and space from the resolved field; on the other hand, provides a reliable estimation of the SGS TKE [108]. In particular, it directly estimates the stress tensor of the NS momentum equation, instead of modelling the viscosity term, and adds a transport equation for the SGS kinetic energy to provide scaling and enforce a budget on the energy flow between the resolved and the sub-grid scales [109].

Considering the present case study, the whole optical window was resolved through LES for the free spray. Instead, for the DFI configuration, the need to guarantee a physical solution at the duct wall provided additional complexity to the simulation setup. Two options were available for this purpose: LES with near wall resolution (LES-NWR) approach or LES with near wall modelling (LES-NWM) approach [85]. LES-NWR, meaning directly resolving the boundary layer, requires a non-dimensional wall distance (y_+) lower than 1 together with an almost isotropic mesh (i.e., flow field must be resolved in the streamwise and spanwise direction [110]). However, LES-NWR for this case study would lead to a prohibitive number of cells, increasing as a power of Reynolds number[2] [111], and thus a computational

[2]In his famous book on turbulent flows [85], prof. Pope states that "In LES with near wall resolution (LES-NWR), in order to resolve the near-wall motions, [...] it can be estimated that the number of grid nodes required increases as $Re^{1.76}$. As a consequence, LES-NWR is infeasible for high-Reynolds-number flows [...]."

cost similar to direct numerical simulation (DNS) [88] due to the high Reynolds number in the duct [3] [39, 34]. Therefore, LES-NWM approach [112] has been employed, meaning applying a wall function at the duct wall, adopting a first cell sufficiently large to include the whole viscous wall region. In particular, the Werner and Wengle wall function [113] was used and care was taken for its correct application, maintaining the y_+ in the suggested range ($30 < y_+ < 300$), as dealt with in the grid sensitivity analysis.

The application of a RANS-LES hybrid mode, like detached eddy simulation (DES) [114], might have been one of the options, allowing the description of the boundary layer, not requiring a high grid resolution in the direction tangential to the wall. However, it is worth noting that DES is mainly thought for aerodynamic highly detached external flows while features some issues when deals with internal flows [115–117], like the in-duct region of DFI. For this reason, it has been discarded.

Grid settings

The CVV was entirely meshed with a cartesian grid featuring a base grid of 2 mm and processing the cells at the wall according the patented cut-cell technique in [118]. Starting from the base grid size (dx_{base}), the mesh was gradually refined towards the spray main area by adopting several fixed refinement regions, according to the rule in equation 3.1:

$$dx_{ref} = \frac{dx_{base}}{2^f} \tag{3.1}$$

where f, the refinement factor, is an integer. The fixed refinement regions are illustrated in Fig. 3.2, together with the associated longitudinal dimension and refinement factor value.

As can be seen, each refinement was parametrically defined as a function of the same variable "r" (with $r > 2$), whose final value has been determined according to a grid sensitivity analysis, illustrated later in the text. In particular, three fixed refinement regions were employed: a first cylinder covering the whole optical access window; a second cylinder covering the near-spray region (i.e., twice the axial duct occupancy), and the volume inside the duct. The latter was not used for the free spray configuration. Moreover, the adaptive mesh refinement (AMR) based on local

[3] $Re = \frac{UD}{\nu} \simeq 2.2 \cdot 10^5$, assuming an average velocity inside the duct (U) equal to $300 m/s$, the duct diameter (D) equal to $2mm$, and the kinematic viscosity (ν) at the considered operating conditions equal to $2.7 m^2/s$. Considering the 1.76 exponent, this Reynolds number would approximately lead to more than $2 \cdot 10^9$ grid nodes for applying LES-NWR at the duct wall.

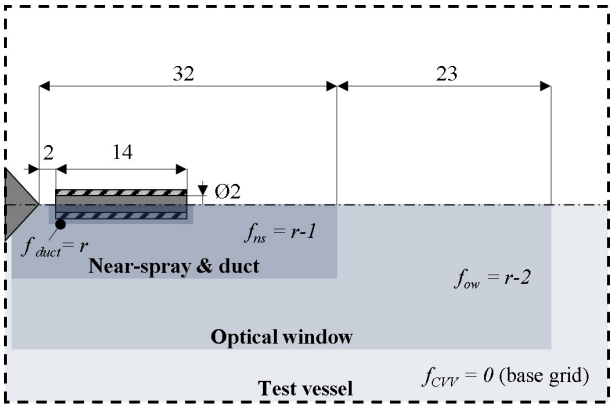

Fig. 3.2 Fixed refinement regions with the associated refinement factors (f) and dimensions for the DFI configuration. Main duct geometrical characteristics also provided.

velocity and temperature gradients was adopted to achieve the maximum refinement (i.e., $f = r$) where required in the whole domain, without unnecessary increment of the computational cost.

As far as the DFI configuration is concerned, since the analysis is based on the LES-NWM approach, the y_+ must be maintained in the optimal range for correct wall function application. For this purpose, a 1-layer inlaid mesh was extruded from the duct inner wall to enable an additional degree of freedom in structuring the grid. This choice was pursued for two main reasons: on one hand, the inlaid mesh is unrelated to the cartesian grid, thus the grid size at the duct wall can be optimized flexibly with respect to a fixed cartesian refinement; on the other hand, the extrusion from the wall avoids cell shape variation due to the cartesian cut-cell technique, ensuring cells homogeneity in the circumferential direction. In Fig. 3.3, a sketch of the 1-layer inlaid mesh region with the associated refinement factor is reported.

The refinement factor value was again parametrically defined as a function of the variable, i, approximately equal in radial, axial and circumferential direction to guarantee an almost isotropic mesh. Furthermore, the constraint in equation 3.2 was imposed to limit the number of cartesian/inlaid cell neighbours, thus maintaining a high mesh quality:

$$f_{duct} - 1 \leq f_{inlaid} \leq f_{duct} + 1 \tag{3.2}$$

which determines the relation in equation 3.3 for the parameters r and i.

$$r - 1 \leq i \leq r + 1 \tag{3.3}$$

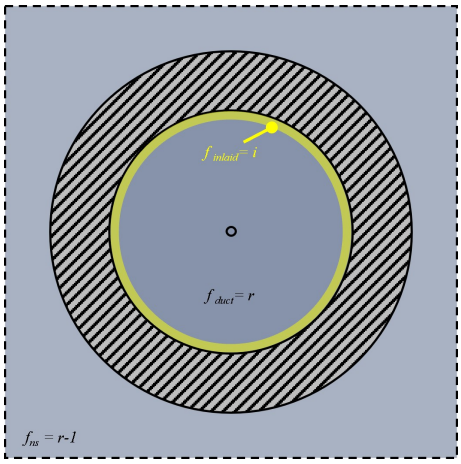

Fig. 3.3 Sketch of the 1-layer inlaid mesh with the associated refinement factors (f) in radial, circumferential and axial direction considering a duct cross-section

According to the grid settings and constraints defined above, a grid sensitivity analysis was performed aiming at figuring out the most appropriate grid size which, firstly, solves at least 80% of the turbulent structures in the whole domain, as suggested by [85, 88] for a high-quality LES, and, secondly, guarantees the desired y_+ at the duct wall. Indeed, it is worth noting that the local grid size acts as LES spatial filter (i.e., the smaller the grid, the smaller the turbulent structures directly resolved) and affects the y_+ (i.e., the smaller the grid at the wall, the lower the y_+). Since the latter presents a lower limit value, a compromise among the two criteria is needed at the duct wall.

The combination of the parameters r and i considered for the grid sensitivity analysis are reported in Table 3.3 with the associated minimum grid size in the whole domain and cell size in the inlaid mesh. The definitions “out of constraints” or “not done” indicate, respectively, the combinations of r and i which do not comply the constraints in equation 3.3 or which were not tested since out of interest. As far as the free spray configuration, the i parameter is not considered since the inlaid mesh not present, while the sweep of the r parameter was performed as in the DFI case.

The first two rows of Table 3.3 (i.e., r=4) concern the simulations carried out for the sensitivity analysis on the inlaid mesh at the duct wall. In Fig. 3.4, the y_+ values on the duct inner wall are illustrated as a function of the axial distance at a time instant featuring quasi stationary conditions inside the duct. Green bands are reported to highlight the optimal range ($30 < y_+ < 100$) and the acceptable range

Table 3.3 Grid sensitivity analysis: values of the refinement factor variables and associated inlaid and minimum grid size

r	i	dx_{min}	dx_{inlaid}
-	-	μm	μm
4	4	125	125
4	5	125	62.5
5	4	Not done	
5	5	62.5	62.5
6	4	Out of constraints	
6	5	31.25	62.5

($100 < y_+ < 300$) for proper wall function operation; the vertical grey dashed lines indicate the duct inlet and outlet locations.

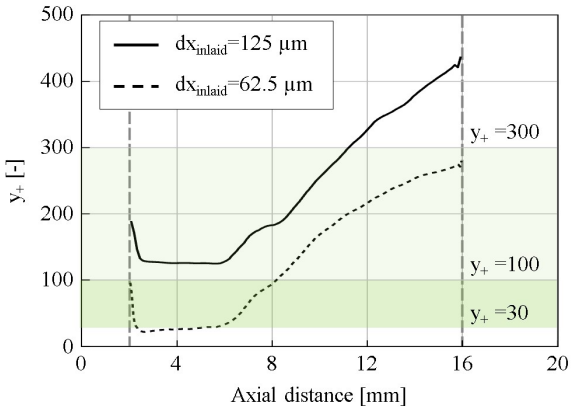

Fig. 3.4 Non-dimensional wall distance (y_+) values on the duct inner wall in quasi stationary conditions as a function of the axial distance (Z) for two different inlaid mesh sizes. Optimal and acceptable range for proper wall function operation highlighted with green bands; duct inlet and outlet locations highlighted with vertical dashed lines.

From an overall point of view, the 62.5 μm inlaid mesh (dashed line) performs much better than the 125 μm one (solid line), despite the y_+ values slightly lower than 30 for a small range at the duct entrance. In fact, it falls in the optimal range for almost half of the duct length and remains inside the acceptable range for the rest. On the contrary, the 125 μm inlaid mesh does not lie in the optimal range and comes out of the acceptable range for a substantial part of the duct length. Furthermore, the Werner and Wengle wall function utilizes a reliable blending function for y_+ values in between the viscous sub-layer ($y_+ < 1$) and the log-law region ($y_+ > 30$) [113],

thus a negligible error is expected at the duct entrance. Therefore, the refinement level $f_{inlaid} = i = 5$ has been chosen for the inlaid mesh.

Considering the rest of the domain, when LES is adopted, the best solution is approached as the grid size is reduced, since the spatial filter is gradually shifted towards smaller turbulent structures, increasing the resolved portion of the turbulent energy spectrum while reducing the influence of the SGS modelled part. Hence, once defined the refinement level for the inlaid mesh, a sensitivity analysis on the grid size was performed, following the data in Table 3.3, aiming at establishing the smallest resolved turbulent scales and, thus, the quality of the LES resolution as well as the computational cost required for the subsequent physical investigation. The maximum number of cells, the minimum time-step (dt_{min}), the number of injected parcels and the corresponding core hours on the available high-power computing (HPC) resources are reported in Table 3.4 for each step of the grid sensitivity analysis considering a single DFI simulation. Similar values, at least in terms of order of magnitude, were obtained for the free spray configuration [119].

Table 3.4 Computational details for a single DFI simulation as a function of the minimum grid size. Processors: x86 Intel Xeon Platinum 8276-8276L (2.4 GHz).

dx_{min} μm	Max N° cells -	dt_{min} s	N° inj. parcels -	Computational cost Core hours
125 (r=4)	$\simeq$ 2M	1.4e-07	2M	$\simeq$ 0.1k
62.5 (r=5)	$\simeq$ 13M	5.8e-08	8M	$\simeq$ 1.1k
31.25 (r=6)	$\simeq$ 87M	3.0e-08	21M	$\simeq$ 29.8k

As the grid is refined, the computational cost drastically increases even for a single simulation. This is due to the higher number of cells, the reduction of the minimum time-step to respect the CFL restrictions and the higher number of injected parcels to avoid any overestimation of the penetration related to an excessive liquid fraction in the computational cells. In this context, it is important to stress the fact that several realizations are needed for LES statistics, each one costing the just mentioned computational resources.

Concerning the resolved flow field associated with each minimum grid size (with $i = 5$), the equivalence ratio (ϕ)[4] fields of a single realization at 0.3 ms aSOI on a plane containing the spray axis are depicted in Fig. 3.5 for both free spray and DFI. The injector nozzle is located at r=0 mm, Z=0 mm.

[4]For the whole document, the ϕ is defined as the ratio of the current fuel-to-air mass ratio over the fuel-to-air mass ratio required for complete stoichiometric combustion. In particular, it is computed

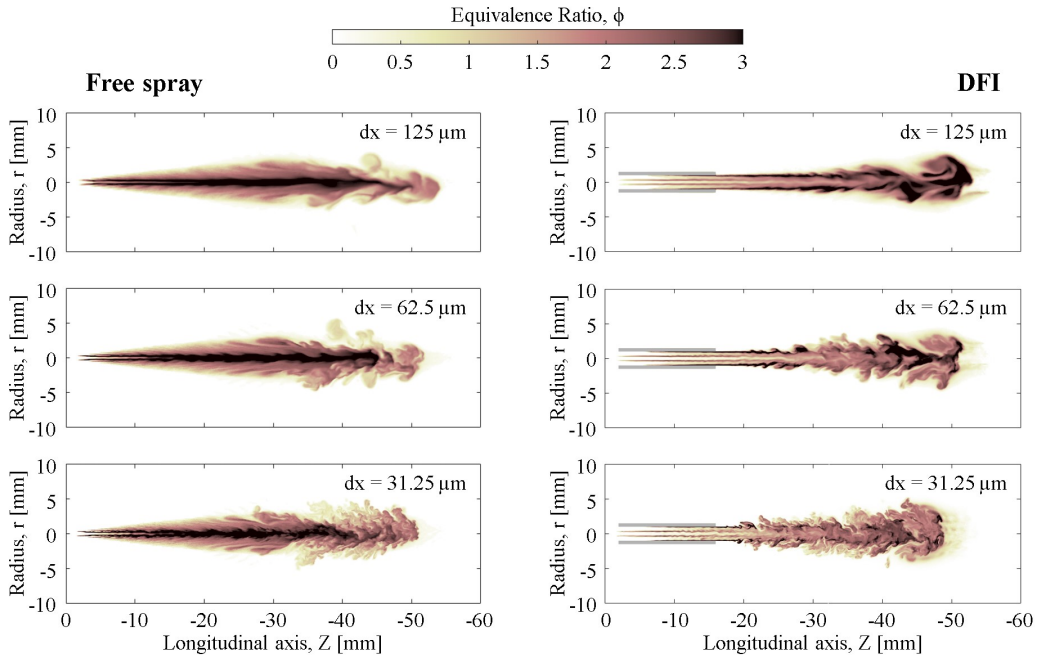

Fig. 3.5 Sensitivity analysis to the grid size: equivalence ratio distribution of a single realization on a plane containing the spray axis at 0.3 ms aSOI as a function of the minimum grid size for both free spray (left) and DFI (right) configurations.

Focusing on the free spray configuration (Fig. 3.5, left), from an overall perspective the intermediate grid size (62.5 μm) is close to the convergence, showing similar penetration and shape of the spray tip to the most refined grid (31.25 μm), while the coarsest one (125 μm) features a more stretched shape, overestimating the spray tip penetration. However, the rich core of the jet behaves differently also among the latter two grids. Indeed, the rich core depicted in saturated black color is less extended for the 31.25 μm grid, compared to the 62.5 μm one. This is due to the fact that the jet core is the part that interacts less effectively with the surrounding environment, and thus tends to be more compact unless the effect of the smallest length scales is well-described. For the 125 μm grid, the jet core does not show vortex structures up to Z = -40 mm, thus remaining more compact and characterized by high ϕ values up to Z = -50 mm. Some vortices are involved in the jet core when

as follows:

$$\phi = \frac{2n_C + \frac{1}{2}n_H}{n_O}$$

where n_C, n_H, and n_O are the numbers of carbon, hydrogen, and oxygen atoms, respectively [120]. For the sake of clarity, it is important to underline that this ϕ computation takes into account only the contribution of the vapor phase fuel in the computational cell. In other words, the amount of liquid fuel mass is not considered for this computation.

an intermediate grid size of 62.5 μm is considered, reducing this length of breakup to about 45 mm. Nevertheless, the most refined grid (31.25 μm) leads to a more detailed turbulent description of the rich jet core. According to these results, the 125 μm grid must be discarded for inaccuracy reasons, while the 62.5 μm grid emerged as a possible option, able to well predict the overall spray behaviour at a reasonable computational cost, forgoing an accurate quantification of certain local values, like the equivalence ratio in the core of the jet, for which 31.25 μm turbulent length scale resolution seems needed.

Moving to the DFI configuration (Fig. 3.5, right), as expected, from an overall perspective, the vortical structures are gradually smaller as the grid is refined. At the same time, from a local perspective, the smallest vortices in the domain are visibly advanced in terms of space, manifesting an anticipation of the turbulent energy cascade, causing a reduction of the ϕ value throughout the ducted spray plume. This is particularly observable looking at the spray tip and at the rich pockets' breakage close to the wall at the duct exit. In fact, the spray tip is gradually leaner as well as the rich pockets are gradually shorter further refining the grid, not showing any convergence of the solution before the finest grid is employed. Furthermore, also the spray shape is strongly affected by the grid, indeed, the spray tip progresses towards a mushroom-shaped head, typical of the DFI non-reacting spray [36], as the grid is refined. Therefore, the 31.25 μm minimum grid size seems strongly suggested to correctly capture the DFI behaviour.

According to this qualitative analysis, the DFI configuration seems characterized by more stringent requirements in terms of minimum grid size to obtain a high quality LES solution. This aspect emerges also by estimations based on the so-called length scale resolution (LSR) parameter, defined as the ratio between the resolved energy level and the corresponding lower limit of the inertial subrange (equation 3.4):

$$LSR = \frac{\Delta}{60\eta} \tag{3.4}$$

where Δ is the filter size, here coincident with the minimum grid size, while η is the Kolmogorov length scale which can be estimated as in equation 3.5 [85]:

$$\eta = \frac{L_0}{Re^{\frac{3}{4}}} \tag{3.5}$$

where L_0 is the characteristic dimension of the phenomenon. For the DFI, as discussed in the subsection 3.1.2, $Re_{DFI} \simeq 2.2 \cdot 10^5$ can be assumed inside the duct,

leading to an estimated Kolmogorov length scale $\eta_{DFI} \simeq 0.20\mu m$. For the free spray, considering the conditions encountered by the spray at $10mm$ from the injector nozzle (i.e., similar axial distance considered for the DFI), the characteristic dimension can be assumed equal to the corresponding spray diameter (approx. $2.7mm$). By assuming the average values of kinematic viscosity ($\nu \simeq 2.7 \cdot 10^{-6} m^2/s$) and velocity ($U \simeq 150 m/s$) on the spray cross-section, it can be estimated $Re_{FS} = 1.25 \cdot 10^5$, leading to $\eta_{FS} \simeq 0.41\mu m$. According to [121], a reasonable turbulence resolution is achieved when the LSR parameter (equation 3.4) is lower than 3, thus emerging the requirements in terms of filter size (i.e., minimum grid size) expressed in equations 3.6 and 3.7:

$$\Delta_{FS} < 3 \cdot 60 \cdot \eta_{FS} \simeq 73.8\mu m \tag{3.6}$$

$$\Delta_{DFI} < 3 \cdot 60 \cdot \eta_{DFI} \simeq 36\mu m \tag{3.7}$$

Since $\Delta_{DFI} < \Delta_{FS}$, the DFI requirements in terms of grid size are confirmed to be more stringent. Therefore, since the same dx_{min} was targeted for both free spray and DFI regardless of their own requirements to guarantee the same level of detail in the solution[5] , henceforth further more quantitative grid analyses will be applied only to the DFI case, which will determine the final choice in terms of grid. Please refer to [119] for more details on the grid sensitivity analysis applied to the free spray case, considering that the final simulation setup adopted the same r parameter for both free spray and DFI configurations.

To properly study the convergence of the solution as the grid is refined in the LES framework, the behaviour of the ensemble average field must be assessed instead of the instantaneous flow realization. Therefore, in Fig. 3.6, the ensemble-averaged ϕ and velocity magnitude fields on a semi-slice containing the spray axis are reported for DFI at 0.3 ms aSOI considering each minimum grid size. The ensemble average among 20 different samples was considered, using the ensemble average method analysed in section 3.1.3.

As can be seen, large variations of the ensemble-averaged solution are present moving from the 125 μm grid to the 62.5 μm grid, in terms of both spray shape and values, and significant variations are still present for the further grid refinement

[5]It is worth noting that, differently from RANS, the eddy viscosity introduced by LES tends to zero in the limit of very fine grid resolutions (i.e., the influence of the SGS LES model on the flow field progressively reduces), since the solution moves towards DNS [122, 108]. Therefore, adopting a finer grid than required to achieve the 80% turbulent eddies resolution target guarantees that a better solution is anyway approached. In other words, the further investment in computational cost for the free spray, due to the more stringent dx_{min} determined by the DFI configuration, is not useless.

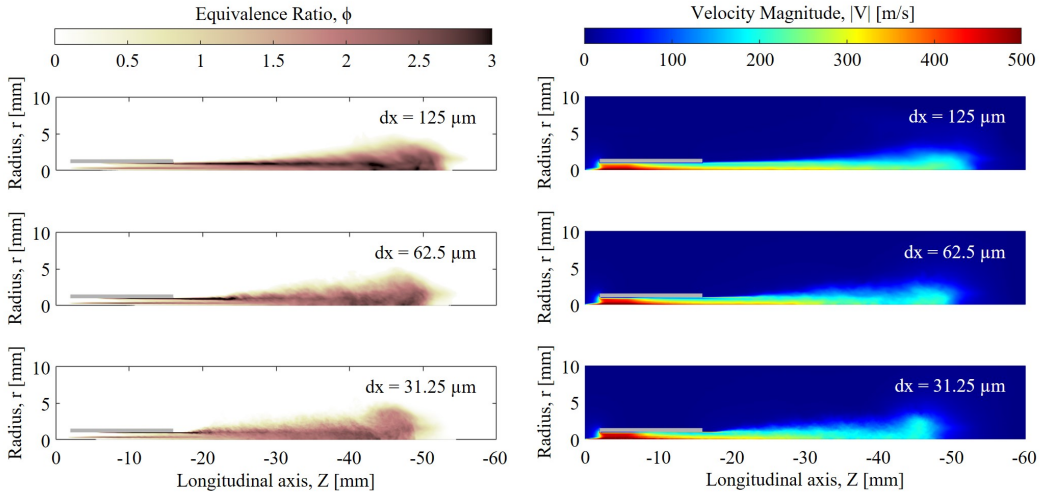

Fig. 3.6 Sensitivity analysis to the grid size for the DFI configuration: ensemble-averaged equivalence ratio (left) and velocity magnitude (right) distributions of the ensemble average among 20 samples on a semi-slice containing the spray axis at 0.3 ms aSOI as a function of the minimum grid size.

up to 31.25 μm. In particular, the rich pockets at the duct exit change in extension, since the flow detachment is predicted as more retarded if the grid is not sufficiently refined. This affects also the enlargement of the spray cone angle at the duct outlet, which is higher as the grid is refined. Furthermore, the penetration is progressively reduced as well as the ducted-spray tip shape changes towards a mushroom-shaped head, as discussed above. Finally, the refinement of the grid allows also a better prediction of the velocity magnitude values inside the duct. Therefore, in this case study, the adoption of a minimum grid size higher than 31.25 μm would lead to a not properly captured DFI behaviour and even a probable underestimation of its effectiveness in terms of mixing.

Finally, an additional check was carried out to determine the best grid settings: the turbulence resolution index (TRI) [119] was evaluated to indicate the local value of the ratio between the resolved TKE and the total TKE (i.e., resolved plus sub-grid scale TKE), as in equation 3.8:

$$TRI(X,Y,Z) = \frac{TKE_{resolved}}{TKE_{total}} = \frac{TKE_{resolved}}{TKE_{resolved} + TKE_{SGS}} \tag{3.8}$$

As abovementioned, a minimum amount of resolved turbulent structures equal to 80% was targeted to guarantee a high quality LES [85, 88], therefore a minimum value of 0.8 is imposed for the TRI, where 0 characterizes a RANS simulation

(completely modelled turbulence) and 1 characterizes a DNS (completely resolved turbulence). The resolved portion of the TKE field was computed based on the root mean square (RMS) of the velocity components fluctuations with respect to the average components, as in equations 3.9 and 3.10.

$$TKE_{resolved} = \frac{1}{2}\left(RMS_u^2 + RMS_v^2 + RMS_w^2\right) \tag{3.9}$$

$$RMS_{(u,v,w)} = \sqrt{\langle (u', v', w')^2 \rangle} \tag{3.10}$$

Each velocity fluctuation component (u', v' and w') is computed as the difference between the velocity value (u, v and w) of sample j and the ensemble-averaged value ($\langle u \rangle$, $\langle v \rangle$ and $\langle w \rangle$) considering all the available samples, as in equation 3.11:

$$\left(u', v', w'\right)_j = (u, v, w)_j - (\langle u \rangle, \langle v \rangle, \langle w \rangle) \tag{3.11}$$

In Fig. 3.7, the TRI fields for the DFI configuration at 0.3 ms aSOI are depicted on a semi-slice containing the spray axis for each considered grid size (with $i = 5$). As above, 20 samples were considered for the ensemble average and resolved TKE computation. In order to avoid areas at very low turbulence level, only the cells featuring ϕ>0.01 are represented to define the domain of interest.

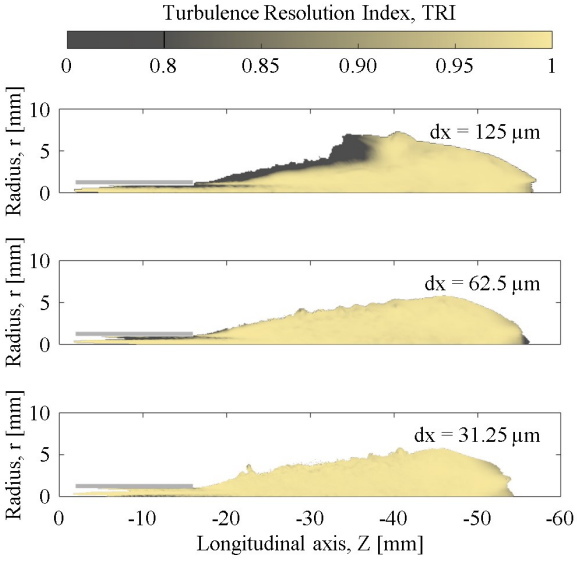

Fig. 3.7 Sensitivity analysis to the grid size for the DFI configuration: turbulence resolution index distribution of the ensemble average among 20 samples on a semi-slice containing the spray axis at 0.3 ms aSOI as a function of the minimum grid size.

According to the adopted colour scale, the saturated grey highlights the locations not satisfying the imposed minimum resolution requirements, while the light-yellow highlights the well-resolved locations. As can be seen, the 125 μm grid features a poor resolution both inside the duct and along the spray periphery. The latter deficiencies seem overcame by the 62.5 μm grid, sufficiently resolving most of the spray plume, but a poor resolution is still present inside the duct and immediately after the duct exit. This is consistent with the retarded rich pockets breakage at the duct outlet, previously described (Fig. 3.5, right) for this intermediate grid size. Finally, the 31.25 μm grid resolves the whole domain of interest with a TRI higher than 0.8.

Therefore, these results provide extensive evidence that the 31.25 μm grid is necessary for an accurate physical analysis of the DFI configuration under the considered operating conditions. According to this, the combination of the parameters $r = 6$, $i = 5$ (Table 3.3) was chosen, accepting to deal with a dramatically larger computational cost, affecting both runtime and postprocessing time, associated with the final grid configuration. This huge computational cost was partially reduced by means of the ensemble average methodology presented in section 3.1.3, enabling a lower number of simulations keeping constant the number of available samples for the average.

3.1.3 Statistical analysis

A single LES realization can be considered as a sort of *numerical experiment*, due to its capability to be locally affected by very small variations of initial conditions or random processes, as well as in experimental campaigns [87]. Therefore, as in experiments, a single realization cannot provide general results but spray-to-spray (i.e., run-to-run) variability must be taken into account through statistical analysis, defining a sufficiently large sample size to compute a stable ensemble-averaged flow field. In this work, the run-to-run variability was triggered by changing the so-called random seed parameter [89] used in the spray sub-models, as executed by [108] to introduce perturbations and mimic the spray-to-spray variability characterizing experimental injections.

Sample size

A total number of samples equal to 20 was considered for both free spray and DFI to carry out the LES statistical analysis. This value, in line with the scientific literature on the subject [123, 124], was chosen after a statistical convergence analysis based on the free spray configuration described with a minimum grid size equal to 62.5 μm (Fig. 3.5, left), given its good balance between accurate LES solution and computational effort in line with the scope of this task (Table 3.4). In particular, the ensemble average variability distribution ($\Delta\langle(r,Z)\rangle$) as a function of the considered number of samples (j) was evaluated for both the velocity magnitude ($|V|$) and the equivalence ratio (ϕ), as in equations 3.12 and 3.13.

$$\Delta\langle|V|(r,Z)\rangle_{j+1} = \langle|V|(r,Z)\rangle_{j+1} - \langle|V|(r,Z)\rangle_{j} \tag{3.12}$$

$$\Delta\langle\phi(r,Z)\rangle_{j+1} = \langle\phi(r,Z)\rangle_{j+1} - \langle\phi(r,Z)\rangle_{j} \tag{3.13}$$

In other words, the local variations between the ensemble average of $j+1$ samples and the ensemble average of j samples were computed for both ϕ and $|V|$ up to $j+1=20$, and the outcome for the ϕ field on five steps (i.e., every four samples) is reported in Fig. 3.8, together with the frequency distribution in logarithmic scale.

The regions of the spray with a $\Delta\langle\phi\rangle$ higher than 0.1 with respect to the previous averaging step are highlighted with a saturated grey color, while the regions which tend to stabilize to a final value (i.e., negligible variation considering a further sample for the average) are gradually whiter as the number of samples increases. The higher the number of samples, the whiter the whole spray picture. In particular, focusing on the first part of the spray (i.e, less than 30 mm distance from the nozzle), about 8-12 samples could be deemed sufficient to obtain stabilization of the average. Nevertheless, moving to the highly turbulent region (i.e., more than 30 mm distance from the nozzle), higher variability is present, and the saturated grey locations seem attenuated only after more than 16 samples, thus motivating the usage of 20 samples. This conclusion can be drawn also from the frequency distribution histograms (right): it is quite evident how the distribution becomes gradually more compact as the number of samples increases, moving towards 100% the bin related to the lowest error, and zeroing the bin $|\Delta\langle\phi\rangle| > 0.1$ only when 20 samples are considered.

To obtain a more quantitative and aggregate visualization of this variability for both ϕ and $|V|$, in Fig. 3.9, the average and the maximum values of the variability distributions as a function of the number of considered realizations are reported for

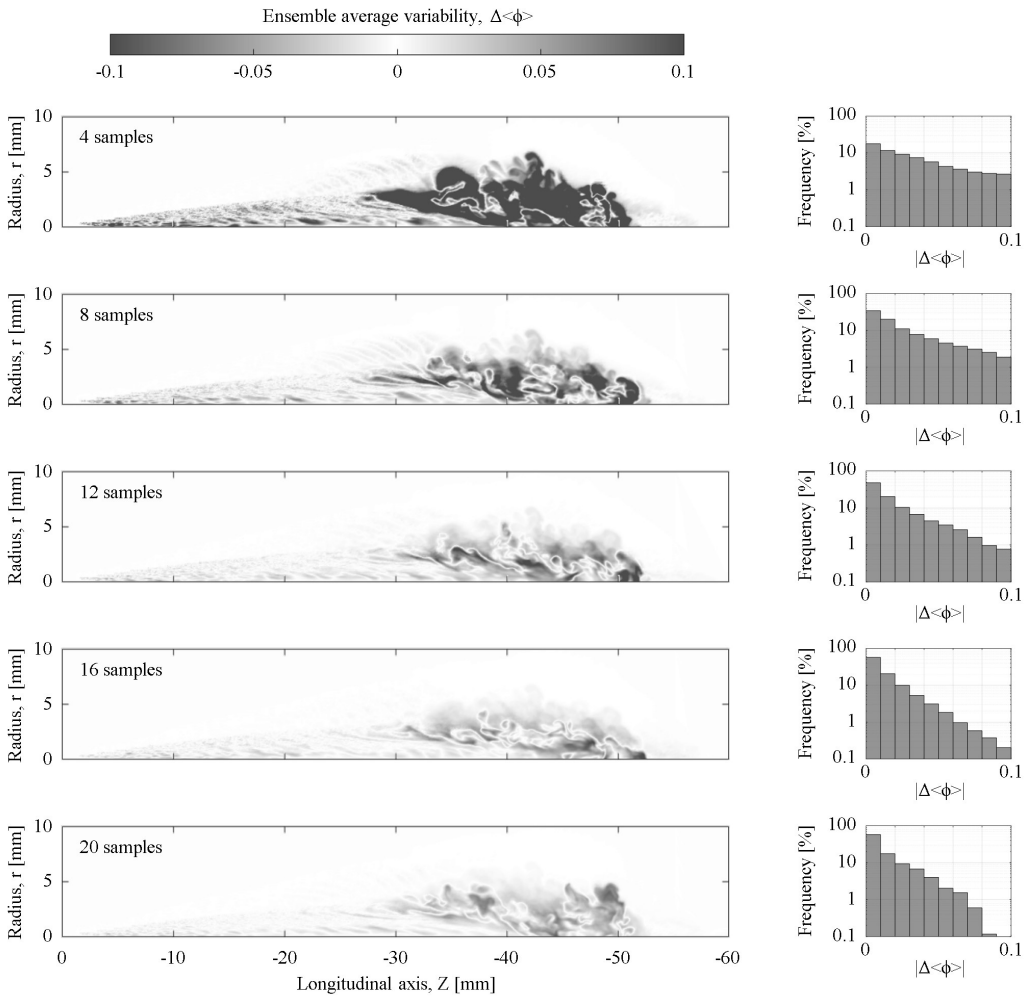

Fig. 3.8 Ensemble average variability for the equivalence ratio distribution on a section containing the spray axis at 0.3 ms aSOI as a function of the considered number of samples. Associated frequency distributions on the right.

transient (0.3 ms aSOI) and pseudo-stationary (0.7 ms aSOI) time instants. In this computation, only the computational cells belonging to the spray structure (based on a ϕ criterion) for the j and $j+1$ samples averages are taken into account. A logarithmic scale is employed for the data visualization.

Focusing on the $|\Delta\langle|V|\rangle|$ trends (Fig. 3.9, top), both the maximum and the average variability values are decreased by about an order of magnitude passing from 2 to 20 samples for the averaging process. In particular, the variability decreases almost linearly on the logarithmic scale at the beginning, while tends to plateau approaching 20 samples, suggesting that a much larger number of samples would be needed to obtain the variability reduction of another order of magnitude. This behaviour is

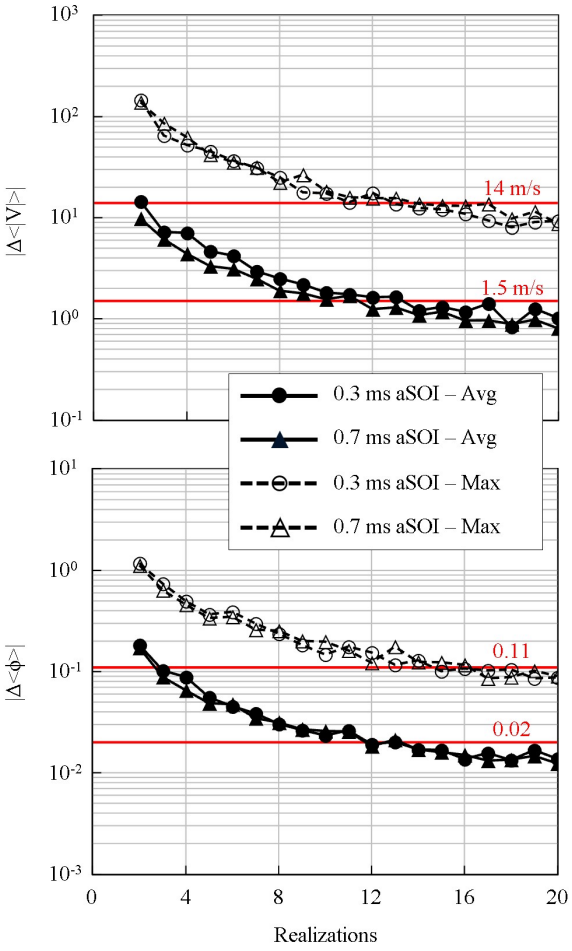

Fig. 3.9 Average (solid line) and maximum (dashed line) values of the variability distributions (Fig. 3.8) as a function of the considered number of realizations for both velocity magnitude (top) and equivalence ratio (bottom). Transient (0.3 ms aSOI – circle) and pseudo-stationary (0.7 ms aSOI – triangle) time instants are considered. Stability thresholds are highlighted in red.

similar during both the transient and the pseudo-stationary phases. Moving to the $|\Delta\langle\phi\rangle|$ trends (Fig. 3.9, bottom), similar conclusions can be drawn confirming the final choice of 20 realizations as statistical sample size.

Since, from a theoretical point of view, an infinite number of samples is needed to achieve statistical convergence (i.e., perfectly stable ensemble average), stability thresholds on both the average and the maximum values are herein evaluated to well-define the accuracy limits under which the adopted average on 20 samples is valid. These thresholds (red horizontal lines in Fig. 3.9) were defined, considering each time instant, as the approximated upper limit for the variability of the ensemble

average on 20 samples, capable of simultaneously including the previous four steps, for continuity and stability reasons. In the end, these thresholds represent the average and maximum error, due to the limited size of the statistical sample, that can be expected on the ensemble average if 20 realizations are considered. According to this computation, an average error of 1.5 m/s and a maximum error of 14 m/s is present for the $|V|$ ensemble average, while the ϕ ensemble average features an average error of 0.02 and a maximum error of 0.11. These errors were considered sufficiently low, especially considering the typical values of $|V|$ and ϕ reached by a diesel spray (e.g., see Fig. 3.5 for this case study). Furthermore, the maximum error is reached only in very few locations of the domain, as can be seen in Fig. 3.8 from both the spray picture and the histogram associated with the 20 samples average. Therefore, the defined accuracy limits were considered in line with the scope of the work.

Ensemble averaging process

The huge computational cost, associated with the chosen highly refined grid, was curtailed by means of the so-called Multi-Slice approach. This runtime saving ensemble average approach is occasionally proposed in the literature on LES spray simulations [125, 126] and the reliability of the final outcome for both free and DFI sprays is demonstrated in appendix A. It consists in exploiting the axial-symmetry characteristics of the case study by dividing a single simulation outcome in several semi-slices containing the spray axis and considering each of them as a different sample for the average. In particular, while the conventional approach (herein named Standard approach) consists in deriving a certain number of statistical samples (N) by running S=N simulations, the Multi-Slice approach considers a certain number (M) of semi-slices containing the spray axis and assumes that each semi-slice behaves as a different numerical experiment, ensuring statistical independence with a sufficient angular distance among semi-slices. In this way, the same number of statistical samples (N) can be achieved by S=N/M simulations. For the sake of clarity, a schematic representing the two considered ensemble average methods is reported in Fig. 3.10, considering M=4 for the multi-slice approach.

Keeping constant the required total number of samples, this methodology allows reducing the number of simulations by a factor equal to the number of semi-slices considered for each simulation, with the drawback of limiting results to a 2D representation, which is however generally used for axial symmetric problems.

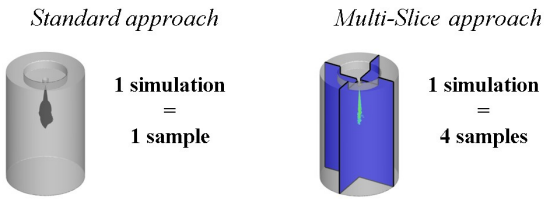

Fig. 3.10 Sketch of the Multi-Slice (4 slices) ensemble average approach compared with the Standard approach

The chosen number of semi-slices per simulation deals with two main aspects. On one hand, statistical independency among samples must be ensured by a sufficient angular distance among semi-slices: according to [125], a number of semi-slices lower than 10-12 enables sufficiently low spatial autocorrelation values for the azimuthal velocity, apart from the region close to the axis. On the other hand, the use of a cartesian grid for the resolution of the flow field can induce some numerical asymmetries, thus not caused by the physics of the problems. Hence, even though these grid-induced asymmetries are typically not taken into account for similar problems in literature, only orthogonal semi-slices, aligned with the resolution grid, were herein considered. Indeed, although the variations induced on the main physical quantities (e.g., absolute velocity values, pressure, etc.) can be considered neglectable, very slight non-physical deviations can instead largely affect the resolved TKE computation, being based on the RMS of the velocity fluctuations (equation 3.9). Therefore, a conservative value of 4 orthogonal semi-slices was considered for each simulation.

Thanks to this ensemble average approach, only 5 simulations for each configuration were necessary to achieve the targeted total number of samples (i.e., 20). For instance, about 447k core hours have been saved just for the DFI configuration, according to the data in Table 3.4.

3.2 Model validation for a single non-reacting condition

In order to provide robustness to the present analysis, a comparison of the liquid spray outcome obtained through experiments and LES is herein reported. However, it is an open point to consistently compare the liquid outcome of a Lagrangian 3D-CFD spray (showing all the parcels in the domain) with the pictures obtained

experimentally (e.g., via Schlieren imaging), based on light phenomena [127]. For this purpose, a methodology was developed to post-process the 3D-CFD parcels distribution, reported in Fig. 3.11 together with the post-processing procedure adopted for the experimental spray acquisitions.

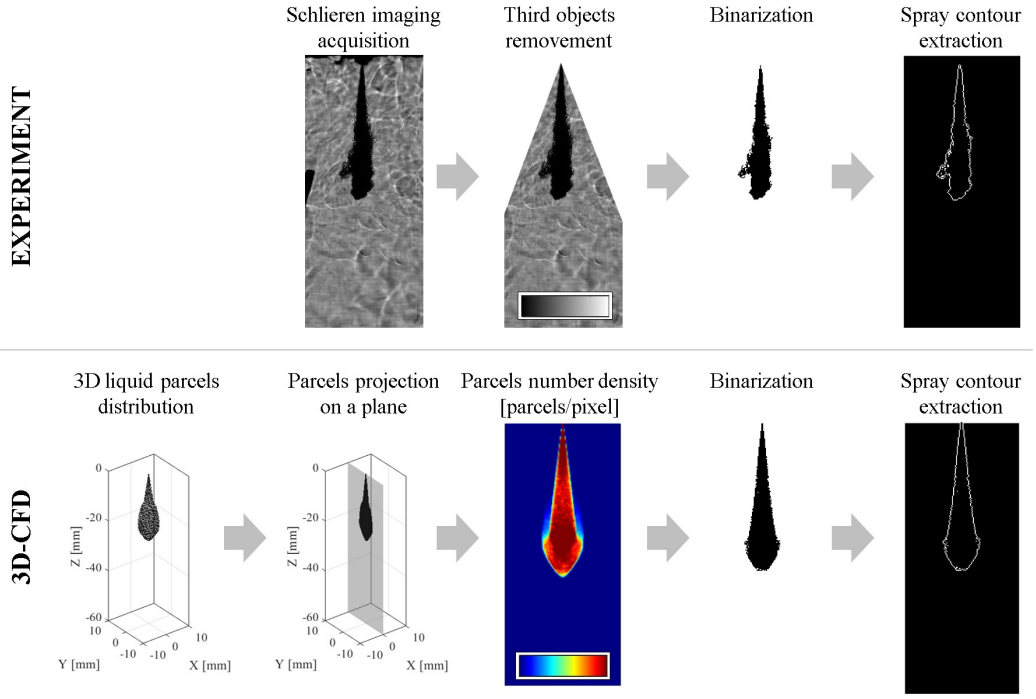

Fig. 3.11 Standardized and connected methodologies for the post-processing of the spray liquid data for both experiments applying Schlieren imaging analysis (top) and 3D-CFD simulations applying Lagrangian particle tracking (bottom).

Among the various techniques [128], the experiments have been postprocessed by binarizing [129] the spray picture to separate the liquid phase by the background colour. Then, the spray perimeter was extracted and reported on a proper reference system and all the aggregated spray quantities of interest (e.g., cone angle, penetration, etc.) can be obtained.

Focusing on the 3D-CFD, a procedure was developed under the hypothesis that the predominant effect of the absence of light in a certain pixel of the experimental spray picture is given by the droplets number density in the pixel itself. In other words, the higher the number of droplets in a certain region, the lower the light intensity. The effect on light intensity caused by other quantities (e.g., droplet diameter, liquid density, etc.) has been considered as of secondary importance. For doing that, firstly, the 3D parcels distribution was projected on a 2D plane, then, the parcels number density field was computed on a grid featuring the cell size equal

to the experimental pixel size. Once this field was available, binarization and spray contour extraction was conducted similarly to experiments.

This method was thus applied to compare the liquid spray outcome obtained through experiments and LES. In Fig. 3.12, the liquid spray contours are reported for both free spray and DFI configurations at four different time instants. The spray contours are associated to a single randomly chosen realization for both experiments and LES.

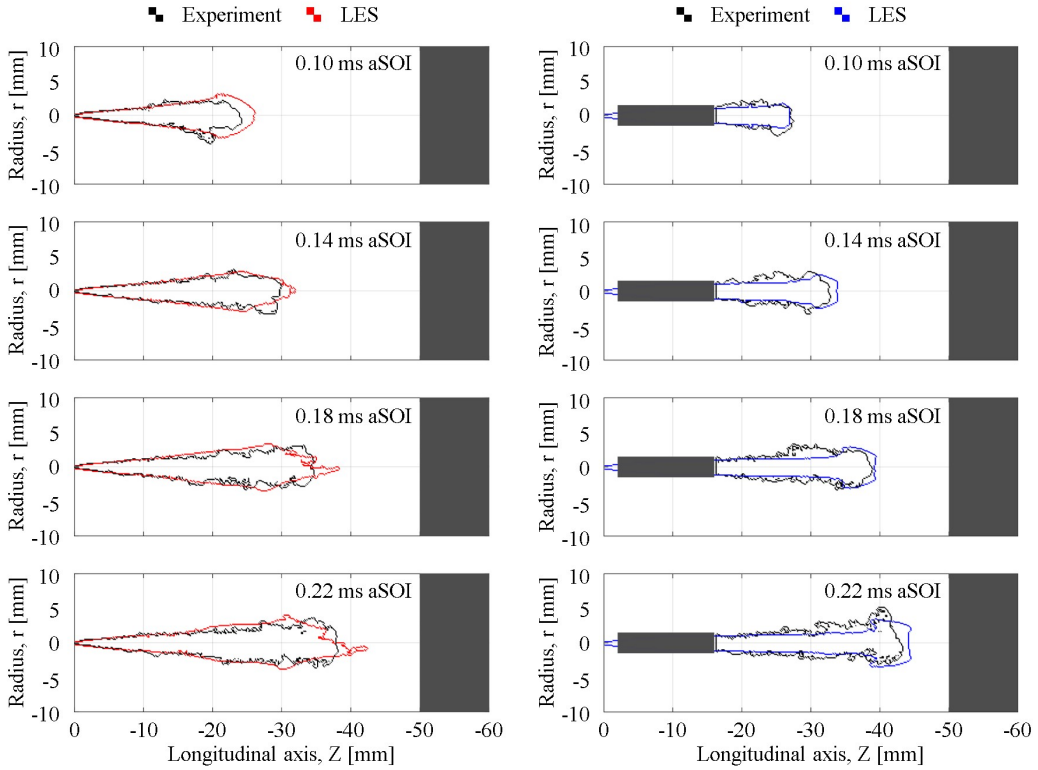

Fig. 3.12 Liquid spray contours extracted from experimental pictures (black) and LES simulations (red / blue) for both free spray (left) and DFI (right) configurations at four different time instants. Results obtained from a single randomly chosen realization for both experiment and LES.

Focusing on the free spray configuration (Fig. 3.12, left), at each time instant the experimental trace (black pixels) is correctly captured from an overall perspective by the LES (red pixels). In particular, the developed cone angle is almost overlapped and the penetration is very similar between the traces. Furthermore, a similar shape of the spray tip is predicted. Moving to the DFI configuration (Fig. 3.12, right), good predictions are obtained in terms of overall behaviour. In this case, the LES (blue

pixels) slightly underestimates the spray dispersion angle downstream of the duct, while accurately captures the penetration and the spray tip shape.

3.3 Results and discussion

First of all, the need for statistical analysis with LES is motivated by showing the run-to-run variability for both free spray and DFI. In Fig. 3.13, the ϕ fields on a plane containing the spray axis at 0.5 ms aSOI are depicted for both free spray and DFI for 5 randomly chosen realizations (R). The free spray is represented on the top side of each spray, while the DFI on the bottom side.

Although from an overall point of view the results do not undergo a dramatic change from realization to realization, a large variability is present with a pointwise approach starting from the Z at which vortices start to form. This location is advanced in space for the DFI, leading in general to a larger variability with respect to the free spray. For instance, the length of the rich pocket close to the wall at the duct exit varies in the range 20-24 mm, leading to significant differences in the downstream ϕ values.

To analyse these differences in variability from a more quantitative perspective, in Fig. 3.14, the standard deviation of the equivalence ratio (σ_ϕ) as a function of the spray radius is reported for both free spray and DFI at three different axial positions.

High standard deviation values are reached for the DFI configuration at the more advanced location, close to the duct exit, associated to the variability of the rich pockets previously mentioned, while low values are present for the free spray. A higher σ_ϕ is then maintained at the intermediate location, manifesting a higher relevance of the turbulence when the duct is present. Only for the farther location from the injector nozzle the free spray σ_ϕ becomes comparable to the DFI one.

In Fig. 3.15, the ϕ behaviour as a function of the spray radius is reported for both free spray and DFI at three different axial positions. In particular, a comparison across the entire dataset (i.e., 20 realizations per configuration) is reported together with the ensemble average behaviour. The free spray is on the right side, the DFI on the left side.

Focusing on the Z=-23 mm location (Fig. 3.15, top), it can be seen a peak for the DFI at r=1 mm, manifesting the presence of the abovementioned rich pocket. However, the magnitude of this peak is remarkably affected by run-to-run variability,

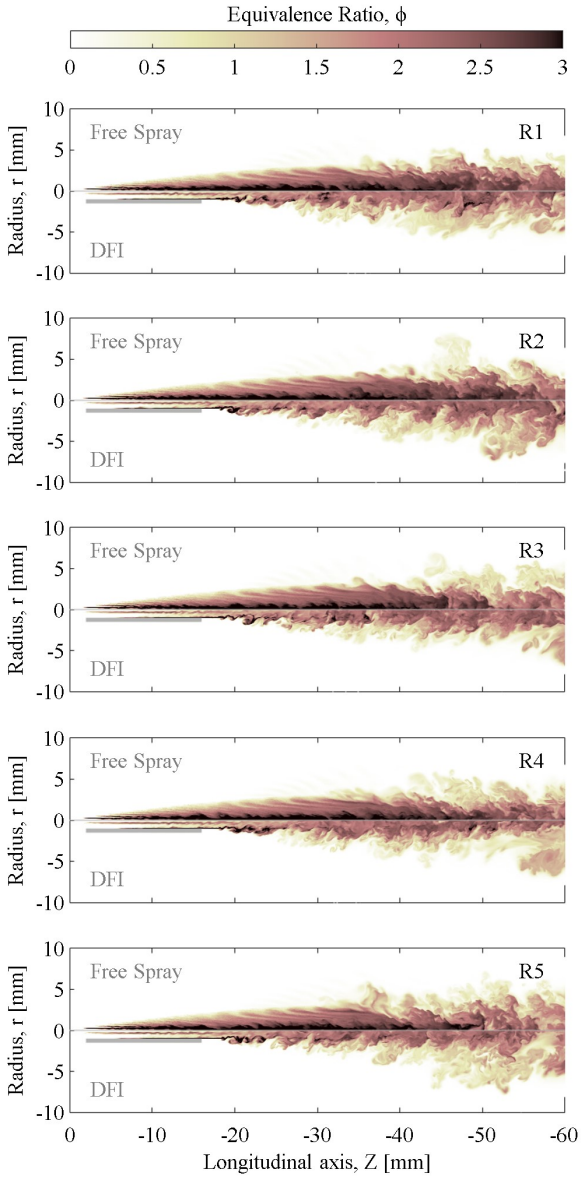

Fig. 3.13 Equivalence ratio fields on a semi-slice containing the spray axis at 0.5 ms aSOI for both free spray (top side) and DFI (bottom side) for five different randomly-chosen realizations (R).

falling in a ϕ window greater than 2. On the contrary, the maximum ϕ value is in the centreline for the free spray and shows a window of variability lower than 0.5. Moving to the Z=-32 mm location (Fig. 3.15, middle), the dispersion starts to increase for the free spray, especially towards the periphery, but the ensemble average is still representative of most of the realizations. For the DFI, the rich peak is smoothened and a homogenization process is evident within the centre of the

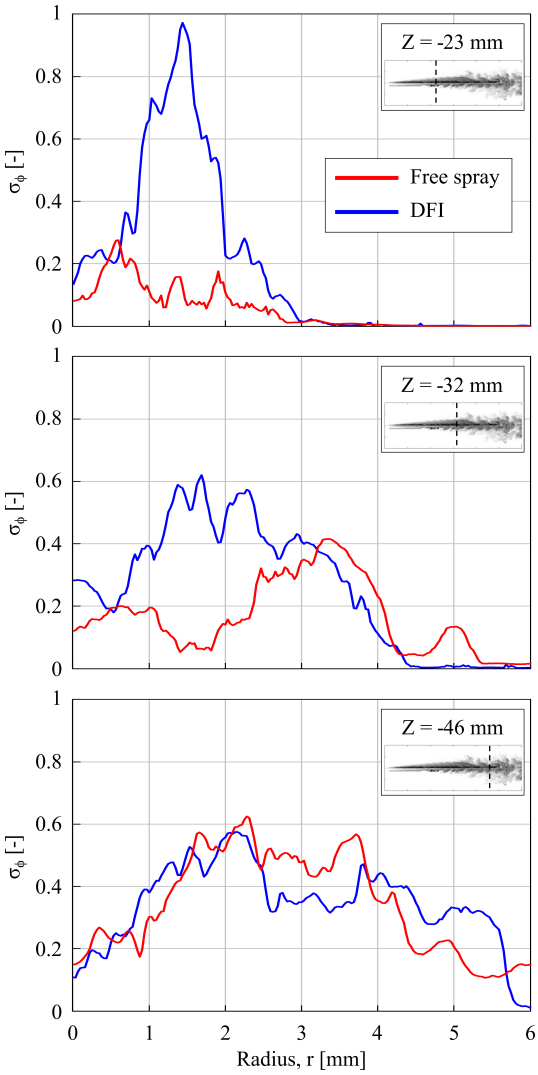

Fig. 3.14 Standard deviation of the equivalence ratio as a function of the spray radius at 0.5 ms aSOI for both free spray (red) and DFI (blue) at three different axial positions: Z=-23 mm (top); Z=-32 mm (middle); Z=-46 mm (bottom).

spray, showing almost constant ϕ value for a radius lower than 1 mm. Concerning the variability, a large dispersion is still present in the centre and becomes larger towards the periphery. Looking at Z=-46 mm (Fig. 3.15, bottom) location, the free spray features a variability which is comparable to the DFI. Focusing on the average curves, a similar bell-shape distribution is reached by both configurations, despite the values are significantly different. It is noteworthy that the ϕ average values do not show important reduction along the axis because the spray is still undertaking the evaporation process, since the liquid fraction is present at least in the first 50 mm under these injection conditions [39]. Finally, from a general view, comparing

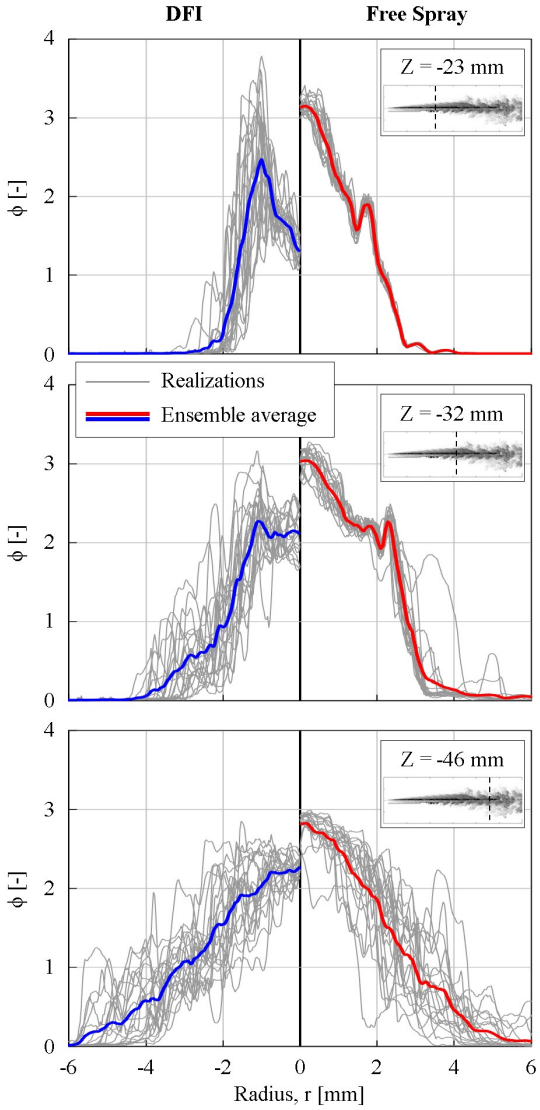

Fig. 3.15 Equivalence ratio as a function of the spray radius at 0.5 ms aSOI for both free spray (right side) and DFI (left side) at three different axial positions: Z=-23 mm (top); Z=-32 mm (middle); Z=-46 mm (bottom). Comparison between the ensemble averages (red and blue) and 20 different realizations (grey).

the average curves for DFI (blue) and free spray (red), an initial insight into the duct-enabled mixing effectiveness can be gained, since the DFI shows significantly lower ϕ average values at each considered axial distance. In particular, ϕ values lower than or very close to 2 are achieved by the DFI average curves, approaching mixture conditions necessary for a soot-free diesel combustion, or LLFC (see section 1.2).

In order to visualize and compare the average behaviour on the whole domain of interest, the ensemble-averaged ϕ fields on a plane containing the spray axis in both transient (0.3 ms aSOI) and pseudo-stationary (0.5 ms aSOI) phases are depicted in Fig. 3.16 for both free spray and DFI.

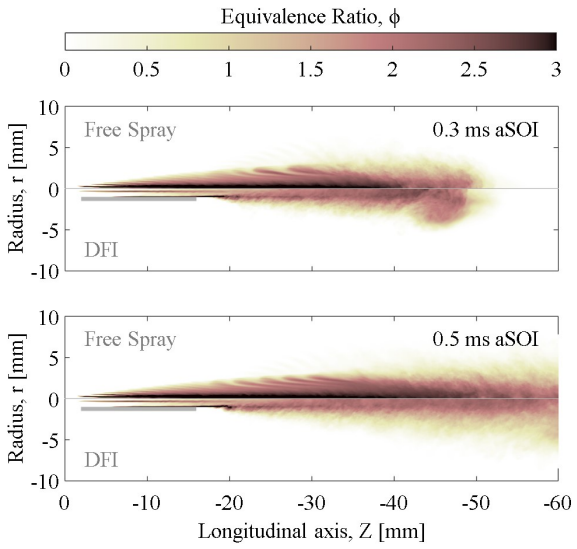

Fig. 3.16 Ensemble averaged equivalence ratio field on a semi-slice containing the spray axis at 0.3 ms aSOI (top) and 0.5 ms aSOI (bottom) for both free spray (top side) and DFI (bottom side).

First of all, the main differences in terms of spray shape between free spray and DFI can be clearly detected: the typical mushroom-shaped head for the DFI spray tip during the transient phase (Fig. 3.16, top) [36], as well the larger spray area downstream of the duct due to higher spray dispersion angle during the pseudo-stationary phase (Fig. 3.16, bottom) [34].

Focusing on the ϕ values, the average rich zone, highlighted with the saturated black colour, is completely different in terms of position, longitudinal extension and radial extension between free spray and DFI. In fact, the rich core in the centreline for the free spray is broken more than 20 mm later than the DFI pocket, located just downstream of the duct at r=1 mm. Furthermore, the spray core is almost lean for DFI, as already reported in Fig. 3.15. Therefore, a leaner and more homogeneous distribution is present for DFI, at least starting from about 20 mm axial distance.

In order to visualize the turbulent mixing behaviour and better understand the outcome in terms of ϕ, a similar representation is reported in Fig. 3.17 for the resolved TKE fields.

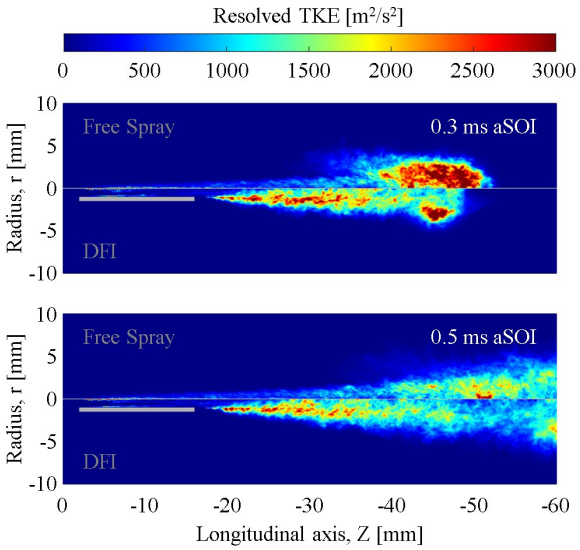

Fig. 3.17 Resolved Turbulent Kinetic Energy (TKE) field on a semi-slice containing the spray axis at 0.3 ms aSOI (top) and 0.5 ms aSOI (bottom) for both free spray (top side) and DFI (bottom side).

The energy cascade is spatially more advanced when the duct is adopted, shifting back TKE values higher than 2000 m^2/s^2 of more than 20 mm. In particular, the transient phase (Fig. 3.17, top) highlights that highly turbulent values are localized into the spray tip for the free spray, while they are widely distributed on the whole spray plume for the DFI, leading to a larger and longer area after the duct outlet characterized by high TKE values. This area is then maintained in terms of turbulent intensity and starting location during the injection (Fig. 3.17, bottom). Instead, for the free spray, the evolution of the initially formed turbulence into the spray tip leads to a reduction of TKE intensity at constant position.

The enhancement of the turbulent mixing after the duct outlet is caused by the flow detachment at the duct outlet: the spray is suddenly no more guided by the duct wall and strong velocity, density, and concentration gradients appear. This phenomenon triggers the formation of vortices, which remain also within the spray tip during the ducted spray evolution, determining its peculiar shape.

It is important to point out that, even though the maximum TKE value in the domain can be higher for the free spray, it is more important that DFI enables a wider and more advanced turbulent mixing, especially considering the limited dimension of a combustion chamber and the necessity to reduce the fuel-to-air ratio before the LOL, which is even extended by the duct adoption (see section 1.4.1).

To get an aggregated and quantitative view of the spray evolution along the axis in terms of TKE and ϕ, in Fig. 3.18, the maximum TKE and ϕ values for each cross-section of the spray at 0.5 ms aSOI are reported as a function of the spray axial distance for both the free spray and the DFI. To avoid taking into account values which are not statistically converged, axial values (i.e., values with r=0 mm) were excluded in the computation of the maximum TKE. Indeed, the used runtime saving ensemble average approach, discussed in section 3.1.3, fails close to the spray axis [125], where the semi-slices (assumed as different samples) tend to be statistically dependent for each simulation, due to the very small relative distance, tending to 0 for r=0 mm. This aspect, for highly fluctuating quantities (e.g., the RMS of the velocity fluctuations to compute the resolved TKE), can prevent the statistical convergence target, which is imperative for this kind of analysis.

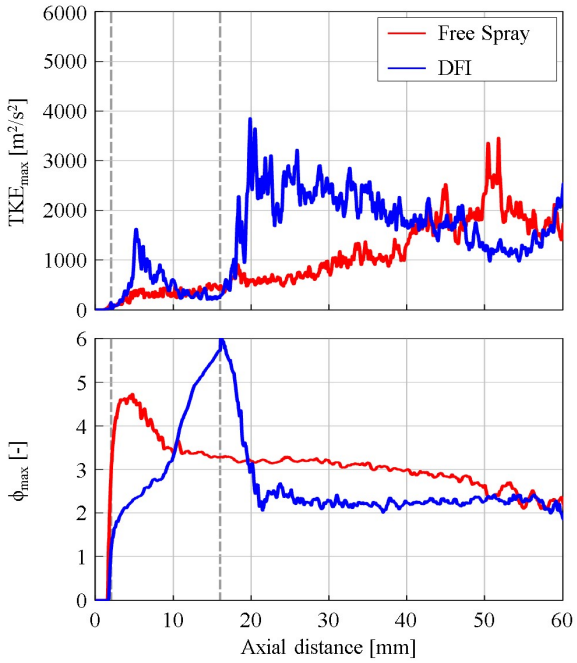

Fig. 3.18 Maximum values of the resolved TKE (top) and the equivalence ratio (bottom) on the spray cross section as a function of axial distance at 0.5 ms aSOI according to the ensemble-averaged LES. Results for both free spray (red) and DFI (blue) configurations.

The maximum TKE (Fig. 3.18, top) behaviour is completely different between free spray (red) and DFI (blue). The former shows an almost linear increment in turbulence when the axial distance increases, while the latter is characterized by two different phases, highlighted by two local peaks. The first turbulence increment occurs inside the duct, few mm after the duct entrance, manifesting a first mixing

enhancement related to the duct adoption. The second peak is larger in magnitude and occurs immediately downstream of the duct exit, leading to a second more intense mixing enhancement with respect to the free spray. Therefore, a two-stage turbulent mixing enhancement can be observed for the DFI. Actually, the turbulent vortices in the ducted-spray tip cause a third positive slope of the DFI curve which can be detected towards the end of the window of interest. Overall, a dramatic enhancement of the turbulent mixing is provided by the duct adoption across most of the spray plume. As a consequence, the free spray and DFI cases show a remarkably different behaviour also in terms of maximum ϕ (Fig. 3.18, bottom). At the duct entrance, while the ϕ curves feature a positive slope due to the beginning of fuel evaporation, the slope of the DFI curve reduces its slope due to the 1^{st} stage turbulent mixing enhancement and the pumping effect capable to increase the air entrainment upstream of the duct, dealt with later in the text. Thus, a local ϕ reduction is present for DFI. However, after the liquid spray starts to interact with the duct inner wall, the so-called collision length [36, 40] forms, leading to a dramatic ϕ increment close to the duct wall, from which originate the rich pockets observable at the duct exit in Fig. 3.16. The very fine grid adopted in this study is essential to capture the magnitude of the local ϕ increment. A maximum ϕ equal to 6 is reached for the DFI at the duct exit, which is much higher than the free spray value at equal location. Hence, this effect can explain better the abnormal DFI operation (i.e., much higher soot formation than free spray) observed in the literature [29, 53, 52] when the ignition occurs inside the duct (i.e., LOL shorter than the duct exit location), as commented in section 1.4.1. It is noteworthy that more evaporative injection conditions could mitigate the above-described collision length effect, due to reduced liquid/wall interaction. Finally, at the duct exit, the 2^{nd} stage turbulent mixing phenomenon occurs and the DFI curve falls down to maximum ϕ values much lower than the free spray in less than 5 mm. In particular, a maximum ϕ close to 2 is maintained for the ducted-spray whole extension.

To conclude the turbulence comparative analysis, the resolved TKE spectra related to both free spray and DFI configurations in two selected probe locations are reported in Fig. 3.19. The chosen locations are the duct outlet and half duct length after the duct outlet, namely, where vortices form due to the detachment of the flow. The different radius has been chosen to make the probe staying inside the duct, for the former, and in line with duct wall, for the latter.

At the end of the duct outlet (Fig. 3.19, top), it is not evident a turbulence enhancement in the energy containing range (i.e., just developed turbulence) by

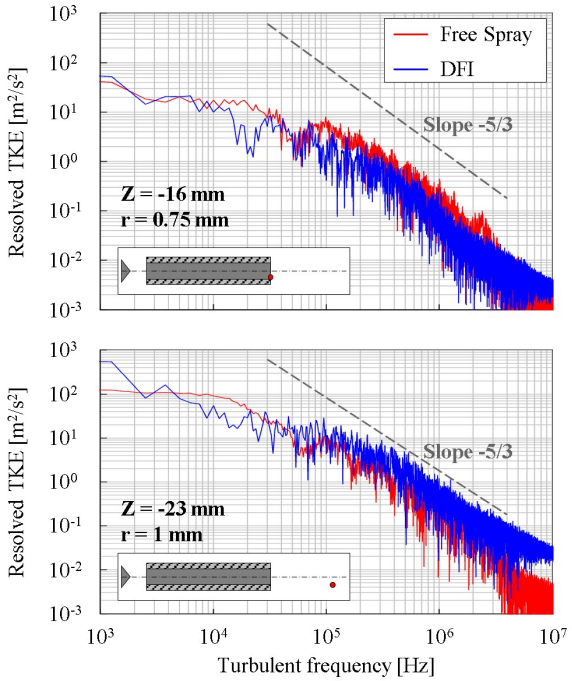

Fig. 3.19 Resolved Turbulent Kinetic Energy (TKE) spectra at selected locations (Z=-16 mm, r=0.75 mm and Z=-23 mm, r=1 mm) for both free spray (red) and DFI (blue).

using the duct. The first part of the inertial subrange presents even slightly higher TKE values for the free spray, while the final part of the resolved spectrum (i.e., smallest turbulent length scales) tends to be slightly higher, thus meaning that a higher amount of previously formed turbulence is evolving. Moving downstream of the duct (Fig. 3.19, bottom), the DFI spectrum is higher than the free spray one for almost each step of the turbulent energy cascade. This result supports the idea that, after the duct exit, turbulent mixing is enhanced due to vortices which are either just forming because of velocity and density gradients, or evolving according to the energy cascade.

In conclusion, the air entrainment into the fuel spray [130, 131, 50, 39] was evaluated for both free spray and DFI. In Fig. 3.20, from top to bottom, the axial velocity, the axial pressure, and the cumulated air entrainment at 0.5 ms aSOI are reported as a function of axial distance for both free spray and DFI. The cumulated air entrainment is the air mass flow rate crossing a cone lateral surface, having the vertex at the injector tip (with vertex angle slightly higher than the spray cone angle) and the height equal to the axial distance.

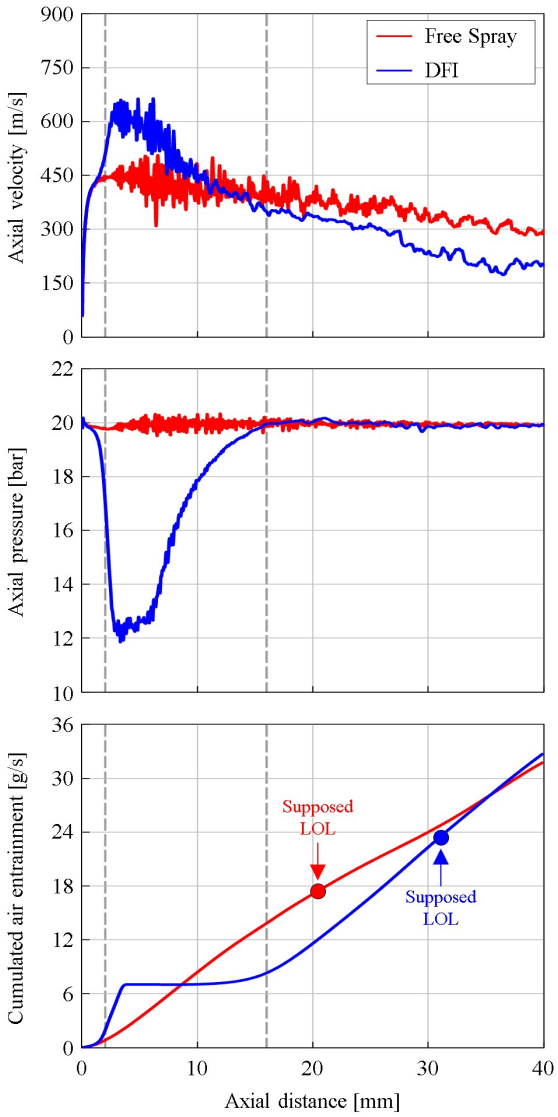

Fig. 3.20 Axial velocity (top), axial pressure (middle), and cumulated air entrainment (bottom) as a function of the axial distance at 0.5 ms aSOI according to the ensemble-averaged LES. Results for both free spray (red) and DFI (blue) configurations.

Focusing on the axial velocity (Fig. 3.20, top), free spray (red) and DFI (blue) curves diverge close to the duct inlet, due to the spray area restriction provided by the duct presence which results in higher velocities for the DFI spray. Then, a higher momentum transfer between spray and air is observable for DFI by looking at the negative slope of the curves after the peak. This leads to an inversion of the velocity trend between free spray and DFI close to the duct exit. Moving to the axial pressure (Fig. 3.20, middle), the difference in the velocity behaviour has consequences in terms of in-duct pressure: a reduction of about 8 bar is detectable, causing the

abovementioned pumping effect, whose influence is visible in terms of cumulated air entrainment (Fig. 3.20, bottom). In fact, the DFI dramatically enhances the air entrainment upstream of the duct, which is more than doubled with respect to the free spray. Then, after the collision length is established, DFI entrainment remains constant by increasing the axial distance until the flow at the duct exit affects again the surrounding air mass flow rate. Since the free spray behaviour is almost linear throughout the plotting window, the total entrainment immediately downstream of the duct is lower for DFI. However, the first derivative of the DFI curve in this region is higher, thus showing a higher entrainment rate. Therefore, the cumulated air entrainment becomes again equal between the two configurations at about 35 mm axial distance. Therefore, as already concluded in other studies [53], the duct presence does not necessarily enhance or reduce the air entrained into the fuel spray from a global point of view, but it changes the entrainment rate distribution across the spray plume, which is enhanced close to the injector. This characteristic can be very beneficial for a successful mixture preparation, because the region close to the injector tip was identified as the most relevant in terms of air entrainment intensity and subsequent air/fuel mixing rate [132, 133]. Furthermore, considering a combusting case, a longer LOL is expected for the DFI (e.g., the reacting simulations in [40] predicted a LOL equal to 21 mm for the free spray and 32 mm for the DFI, indicated by small circles on the plot), leading to a higher air entrainment also from a global point of view.

Chapter 4

Assessment of RANS-based DFI modelling using LES data

The LES turbulence modelling accurately describes turbulence phenomena, even taking into account the experimental variability, and thus it is a reliable tool to investigate and understand a turbulent mixing enhancement strategy like DFI, as dealt with in chapter 3. However, the present work aims at performing several sensitivity analyses of the DFI technology under different non-reacting and reacting conditions (see next chapters), thus the usage of the LES approach for the whole scope would have been prohibitive in terms of requested computational resources. RANS models are much more feasible for these purposes and, from a more general point of view, an increased need of this kind of models is expected if DFI is going to succeed in series production, to either simulate a wide range of operating conditions or perform geometrical optimizations. Therefore, the present chapter aims at assessing the performance of the RANS approach in modelling both free spray and DFI configurations, having as a reference the results obtained through LES combined with statistics in chapter 3. In particular, considering the same constant-volume non-reacting conditions, the mixing process predicted by the RANS model has been assessed in terms of turbulent kinetic energy and equivalence ratio fields, using the resolved portion of the LES turbulent energy spectrum (characterized by more than 80% of resolved turbulent length scales) as a target. Moreover, the assessed RANS model outcome is validated against experimental data in terms of liquid spray structure for the investigated non-reacting conditions, as done for the LES-based spray model.

4.1 Methodology

4.1.1 Operating conditions

Given the purpose of assessing the RANS-based prediction against the LES data provided in chapter 3, the same case study was considered, featuring the non-reacting operating conditions previously reported in Table 3.1 and the D2L14G2 duct geometry.

4.1.2 RANS 3D-CFD setup

The RANS non-reacting simulations were carried out on the commercially available software CONVERGE CFD 2.4 [134]. As discussed in section 3.1, the spray model validated in the LES framework was also used with RANS approach, whose characteristics are summarized in Table 3.2. The reliability of this spray model with RANS is shown in section 4.2. Since the spray sub-models are grid-convergent, as the mesh is refined the results approach a reasonably converged answer[1]. Therefore, a grid sensitivity analysis was performed to define the grid settings capable to reach convergence. Considering the nomenclature adopted in Fig. 3.2, a base grid size of 2 mm was adopted for the test vessel as in the LES case, the optical window was refined to 0.50 mm ($f = 2$) and the duct volume to 0.25 mm ($f = 3$) to guarantee a reasonable minimum number of cells along the duct diameter. In addition, the AMR technique (minimum grid size 0.25 mm) was applied in the chamber domain to automatically refine the grid based on local temperature and velocity gradients. Given the difference in terms of grid settings between LES and RANS, the number of injected parcels was reduced to 500k (against the 21M of LES, Table 3.4) to ensure a correct balance between liquid and gas phase in a single cell, referring to [95]. The chamber was initialized with an almost quiescent flow, with the same boundary conditions of the LES case. Regarding the wall treatment, the standard wall function was employed, guaranteeing the y_+ in its correct operating range.

Concerning the numerical aspects, the same settings of LES (section 3.1.2) were adopted apart from the temporal discretization, which was executed with the first-order implicit Euler scheme.

[1] Differently from LES which guarantees a better solution as the grid is refined, the fact that the RANS solution converges does not imply that this solution is correct.

4.1.3 RANS turbulence modelling

The concept behind the turbulence prediction through RANS models is to apply a time average process to the Navier-Stokes equations, eliminating the need to solve the turbulent structures of the flow field and modelling the diffusive effect of the mentioned structures on the time averaged flow. With this aim, the time averaging process should be sufficiently large in comparison with the turbulence time scale and small compared to the evolution of the mean flow. A much more economic approach with respect to LES is obtained but eliminating the turbulence-related physics from the equations and requiring the additional modelling of the resulting non-linear Reynolds stress term. This is necessary to obtain closure of the momentum transport equation and, thus, allow physically correct simulations [135]. From this perspective, it is not surprising that RANS computations are prone to not negligible modelling errors, and it is therefore essential to understand the strength and weaknesses of a certain RANS model for a given application.

The Reynolds stress tensor is typically related with the mean velocity gradient tensor by the usage of the turbulent eddy viscosity assumption, based on the idea that turbulent fluctuations have a dissipative effect on the mean flow, which can be modelled through a turbulent viscosity term. These models are called eddy viscosity models (EVMs). The main EVMs for industrial and confined flows are the two-equation models, where two transport equations are retrieved for two turbulent quantities, the TKE, κ, and the dissipation rate of TKE, ε, or the specific dissipation rate, ω, thus defining the so-called $\kappa-\varepsilon$ and $\kappa-\omega$ models respectively. Focusing on engine spray simulations, $\kappa-\varepsilon$ models have been widely implemented in the literature [85]. The standard $\kappa-\varepsilon$ model [136] defines the turbulent viscosity, μ_t, as in equation 4.1:

$$\mu_t = C_\mu \rho \frac{\kappa^2}{\varepsilon} \tag{4.1}$$

where C_μ is a constant and ρ is the density. The transport equations are expressed as in equations 4.2 and 4.3:

$$\frac{\partial(\rho\kappa)}{\partial t} + \frac{\partial(\rho u_j \kappa)}{\partial x_j} = \frac{\partial}{\partial x_j}\left[\left(\mu + \frac{\mu_t}{\sigma_\kappa}\right)\frac{\partial \kappa}{\partial x_j}\right] - \rho\overline{u'_i u'_j}\frac{\partial u_i}{\partial x_j} - \rho\varepsilon \tag{4.2}$$

$$\frac{\partial(\rho\varepsilon)}{\partial t} + \frac{\partial(\rho u_j \varepsilon)}{\partial x_j} = \frac{\partial}{\partial x_j}\left[\left(\mu + \frac{\mu_t}{\sigma_\varepsilon}\right)\frac{\partial \varepsilon}{\partial x_j}\right] - C_{\varepsilon 1}\frac{\varepsilon}{\kappa}\rho\overline{u'_i u'_j}\frac{\partial u_i}{\partial x_j} - C_{\varepsilon 2}\rho\frac{\varepsilon^2}{\kappa} \tag{4.3}$$

where $\overline{u'_i u'_j} = \tau_{ij}$ is the Reynolds stress tensor, while σ_κ, σ_ε, $C_{\varepsilon 1}$, $C_{\varepsilon 2}$ are model constants.

A modified version of the $\kappa - \varepsilon$ model is the re-normalization group (RNG) $\kappa - \varepsilon$ model [137] introduced to limit the over-prediction of the turbulence generation in case of strong local accelerations. The model has been developed using techniques from the RNG theory [138], using a modified model constant ($C_{\varepsilon 2}$) defined in equation 4.4:

$$C_{\varepsilon 2} = \widetilde{C_{\varepsilon 2}} + \frac{C_\mu \eta^3 \left(1 - \frac{\eta}{\eta_0}\right)}{1 + \beta \eta^3} \tag{4.4}$$

where $\widetilde{C_{\varepsilon 2}}$, η_0, β are additional model constants.

Given its widespread usage for internal combustion engine simulations [134, 139–141], the RNG $\kappa - \varepsilon$ model was adopted in this work for both free spray and DFI configurations, using the set of constants reported in Table 4.1. In particular, the standard values were employed except for the slightly different reciprocal Prandtl numbers (σ_κ, σ_ε) compared to the ones stemming from the RNG analysis [85, 138].

Table 4.1 Values of the constants used for the RANS RNG $\kappa - \varepsilon$ model

C_μ	$C_{\varepsilon 1}$	$\widetilde{C_{\varepsilon 2}}$	σ_κ	σ_ε	β	η_0
0.0845	1.42	1.68	1.39	1.39	0.012	4.38

4.2 Model validation: RANS vs LES vs experiment

In order to provide robustness to the present analysis, a comparison of the liquid spray outcome obtained through experiments, RANS and LES is reported in Fig. 4.1 in terms of liquid spray shape at different time instants for both free spray and DFI (similar representation to Fig. 3.12). The methodology presented in Fig. 3.11 was used for post-processing the RANS liquid parcels distribution.

It can be observed that the main improvement provided by the LES approach in terms of liquid parcels distribution is the shape of the free spray tip, whose enlargement seems overestimated by the RANS approach. On the contrary, considering the DFI configuration, almost identical predictions are obtained. In fact, both 3D-CFD approaches slightly underestimate the spray dispersion angle compared to the experiment, while accurately capture the penetration and the spray tip shape.

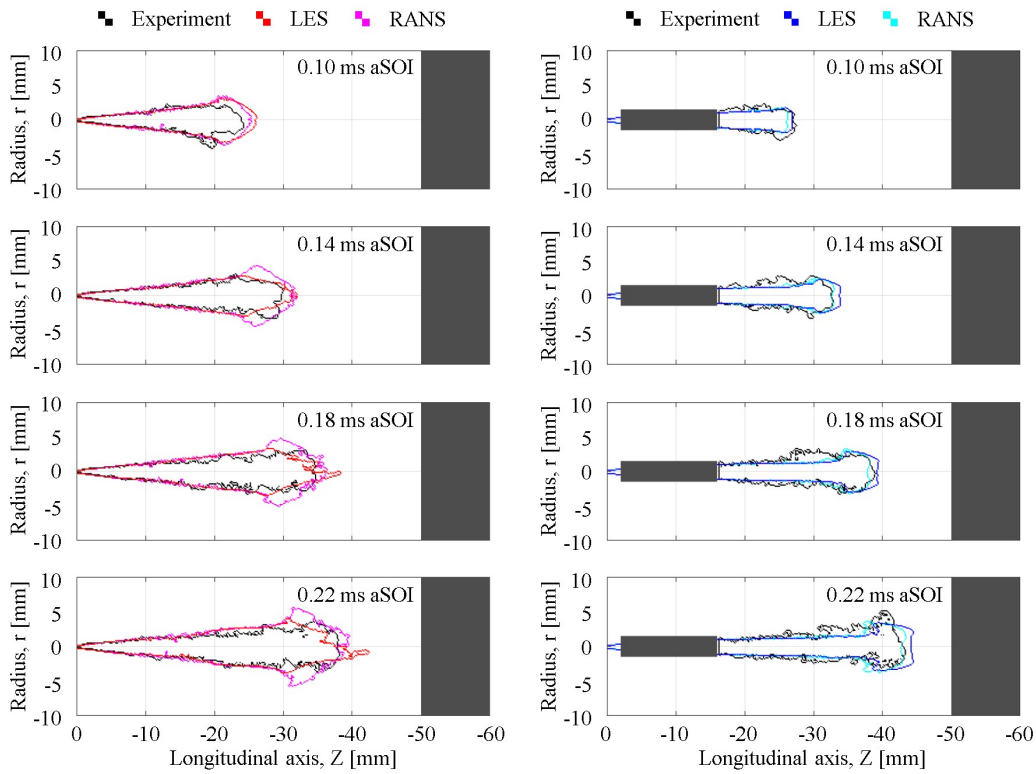

Fig. 4.1 Liquid spray contours extracted from experimental pictures (black), RANS simulations (magenta / cyan) and LES simulations (red / blue) for both free spray (left) and DFI (right) configurations at four different time instants. Results obtained from a single randomly chosen realization for both experiment and LES.

According to these results, even though some local differences emerge between RANS and LES, it can be concluded that both approaches are capable to capture the major characteristics of the experimental spray contours for both free spray and DFI. Therefore, a comparison of the local flow features calculated by RANS and LES can be consistently performed, without the need of spray sub-models re-calibration for the former.

4.3 Results and discussion: RANS vs LES

In Fig. 4.2, the ϕ fields on a plane containing the spray axis computed by RANS and ensemble-averaged LES are depicted in both transient (0.3 ms aSOI) and pseudo-stationary (0.5 ms aSOI) phases for both free spray and DFI.

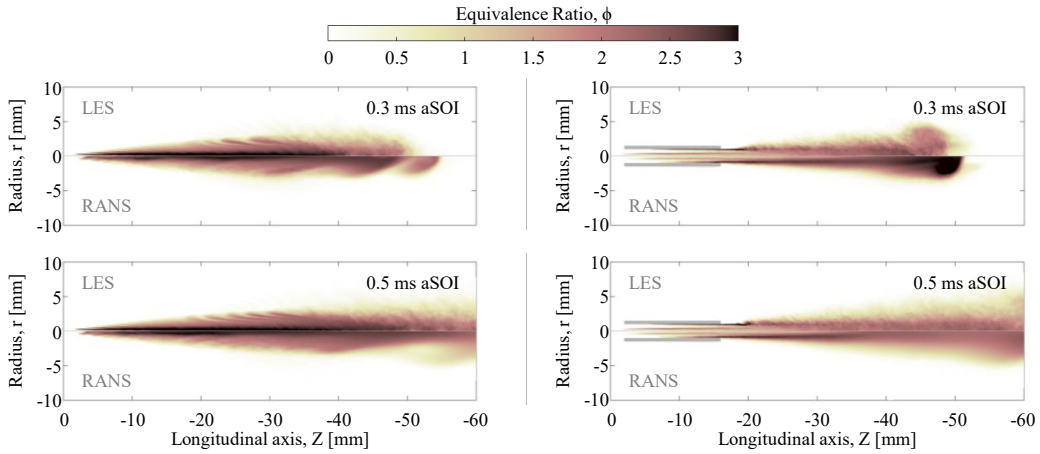

Fig. 4.2 Equivalence ratio field on a semi-slice containing the spray axis at 0.3 ms aSOI (top) and 0.5 ms aSOI (bottom) according to the ensemble-averaged LES (top side) and the RANS (bottom side) approaches. Results for both free spray (left) and DFI (right) configurations.

Focusing on the free spray configuration (Fig. 4.2, left), the macroscopic behaviour of the ϕ distribution is similar between RANS and LES, even though some differences emerge. During the transient phase (0.3 ms aSOI), the vapor phase spray tip is leaner, and its penetration is lower for the LES, while higher ϕ values are reached in the core of the spray, which seems slightly richer and longer than RANS. These characteristics remains valid during the pseudo-stationary phase (0.5 ms aSOI), when no significant differences are detected in terms of spray shape between RANS and LES.

Moving to the DFI configuration (Fig. 4.2, right), the differences are more evident. At 0.3 ms aSOI, the spray cone downstream of the duct is slightly larger, the tip penetration is shorter, and the ϕ values are qualitatively lower on average, when the turbulence is modelled with LES. The latter consideration is especially observable into the spray tip, which is highly rich for RANS and relatively lean for LES. At 0.5 ms aSOI, these differences are significantly reduced, even though LES leads to a shorter rich zone at the duct outlet, meaning that the flow detachment due to the solid discontinuity at the duct exit is predicted as more retarded with RANS. As a consequence, the DFI effectiveness in reducing the ϕ could be underestimated with RANS. It is important to point out that the major trends predicted by LES in terms of equivalence ratio reduction when DFI is introduced are still valid also with RANS approach, despite a different quantification.

Then, the TKE fields developed by the free and the ducted sprays according to the LES and the RANS models were evaluated. While for the former the resolved TKE was computed (equation 3.9), for the latter the TKE is entirely modelled by definition and is a turbulence model output. In this comparison, for the LES case the SGS modelled contribution to TKE was neglected, due to the high level of resolution achieved with the present computational setup (see Figure 3.7, bottom). In Fig. 4.3, the TKE fields on a plane containing the spray axis computed by RANS and ensemble-averaged LES are depicted in both transient (0.3 ms aSOI) and pseudo-stationary (0.5 ms aSOI) phases for both free spray and DFI.

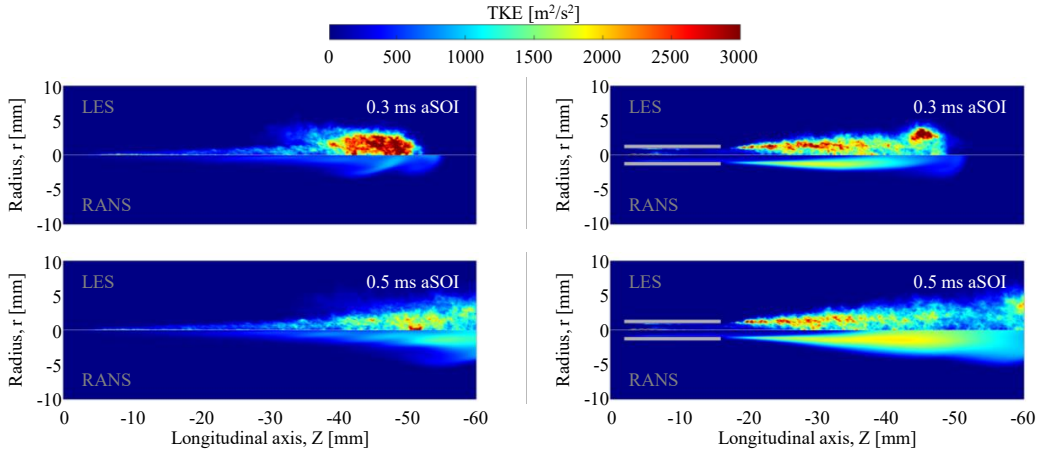

Fig. 4.3 Turbulent kinetic energy (TKE) on a semi-slice containing the spray axis at 0.3 ms aSOI (top) and 0.5 ms aSOI (bottom) according to the ensemble-averaged LES (top side) and the RANS (bottom side) approaches. Results for both free spray (left) and DFI (right) configurations.

Focusing on the transient phase (0.3 ms aSOI), the richer spray tip predicted by RANS for both free spray and DFI can be motivated by the less intense turbulence computed in that part of the spray. The lower mixing into the spray tip can also cause a lower momentum transfer from the spray to the surrounding air, thus increasing the penetration of the vapor phase at this time instant. Concerning the stabilized retarded flow detachment for the DFI observed in Fig. 4.2 (right) with the RANS approach at 0.5 ms aSOI, the location at which the turbulence starts to rise is actually very similar between RANS and LES, immediately after the duct exit. Nevertheless, the intensity of the turbulence is higher with LES, providing an efficient mixing which is underestimated with the RANS turbulence model, thus computing a different rich pocket length. More in detail, the maximum TKE values are reached about 20 mm farther upstream with LES, providing a great mixing advantage compared to

RANS, thus again the RANS-based results could underestimate DFI effectiveness in enhancing the air/fuel mixing. Nevertheless, the major physical trends observed with LES are respected with RANS also in terms of turbulent mixing, especially considering stabilized conditions, when the influence of the rich spray tip of the ducted spray reduces in importance. This would be particularly true under stabilized combusting conditions.

To get an aggregated view of spray evolution along the axis in terms of TKE and ϕ, their maximum value on the spray cross section was evaluated in Fig. 4.4, like in the LES-only analysis (Fig. 3.18).

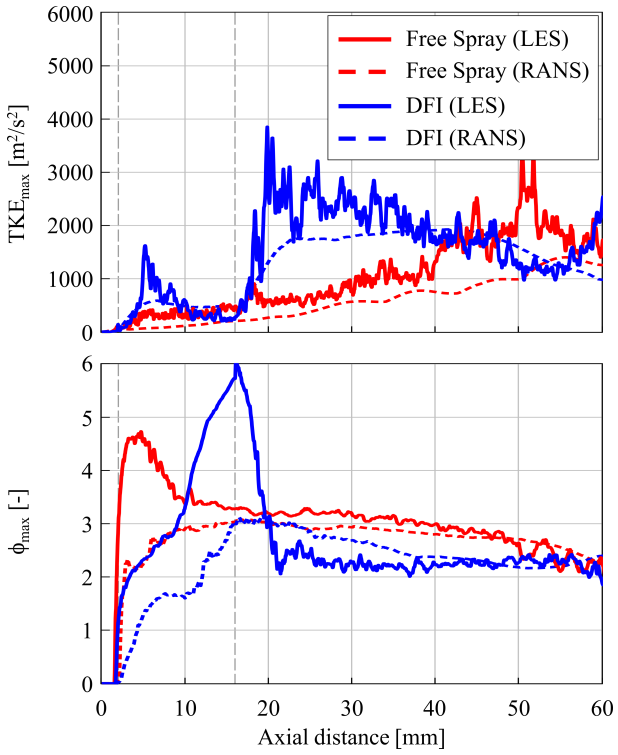

Fig. 4.4 Maximum values of the turbulent kinetic energy (top) and the equivalence ratio (bottom) on the spray cross section as a function of the longitudinal axis, Z, at 0.5 ms aSOI according to the ensemble-averaged LES (solid lines) and the RANS (dashed lines) approaches. Results for both free spray (red) and DFI (blue) configurations.

Focusing on the free spray (red), the maximum TKE (Fig. 4.4, top) shows a quite similar behaviour between RANS (dashed lines) and LES (solid lines) from a macroscopic perspective, despite significantly shifted towards higher values for LES. However, although higher turbulent mixing is present, the maximum ϕ curve (Fig. 4.4, bottom) is higher for LES when the axial distance is higher than 10 mm. This is probably due to the large difference close to the injector tip (i.e., Z<10 mm) between

RANS and LES which is mostly linked to the much more refined grid of the latter, enabling a more accurate prediction of the mixture conditions close to the injector, which tend to richer ϕ values.

Focusing on the DFI (blue), the two local enhancements predicted by LES are captured with RANS approach, despite some quantitative differences. Considering the in-duct turbulent mixing predicted by LES, identified as a 1st stage turbulent mixing enhancement in section 3.3, the local maximum is higher and closer to the duct inlet, while the curve slope is negative up to the duct outlet, differently from the almost constant value reached by RANS. The LES different dynamic could be more beneficial in terms of mixing length exploitation. In this region, the maximum ϕ is always higher for the LES because of two main reasons: on one hand, similar considerations to the free spray can be done for the first mm close to the injector tip; on the other hand, the effect of the collision length is much more evident, due to the finer grid at the duct wall, leading to the positive slope which peaks at the duct outlet section with $\phi_{max} = 6$. Considering the so-called 2nd stage turbulent mixing enhancement, immediately after the duct exit, the LES predicts a greater slope, reaching a higher turbulence intensity. This is in line with the comments to Fig. 4.3 (right) on turbulence anticipation with LES. The maximum ϕ curve reflects this greater turbulence enhancement which leads to lower values for axial distances higher than 20 mm when LES is adopted, although the starting point at the duct exit is 100% higher. Therefore, looking at this plots from an overall point of view, comparing free spray and DFI curves, some conclusions can be drawn on the DFI soot mitigation potential, which seems underestimated with a RANS approach, if a proper DFI working condition (i.e., LOL downstream of the duct) is considered. On the contrary, it is noteworthy that, if abnormal operation (i.e., in-duct combustion) is considered, underestimated soot formation is expected with RANS.

Deeping in the soot mitigation potential point of view, it is interesting to observe the radial distribution at the expected LOL. The LOL values for free spray and DFI are supposed from the reacting simulations in [40] (i.e., LOL=21 mm for free spray; LOL=32 mm for DFI), as previously done for Fig. 3.20. In Fig. 4.5, the TKE and ϕ behaviours at the LOL as a function of the spray radius at 0.5 ms aSOI, computed by RANS and ensemble-averaged LES, are reported for both free spray and DFI. The RANS is on the left side, the LES is on the right side. Close-to-axis TKE values computed with LES are obscured by a vertical grey band to avoid taking into account values which are not statistically converged, as commented in the explanation to Fig. 3.18.

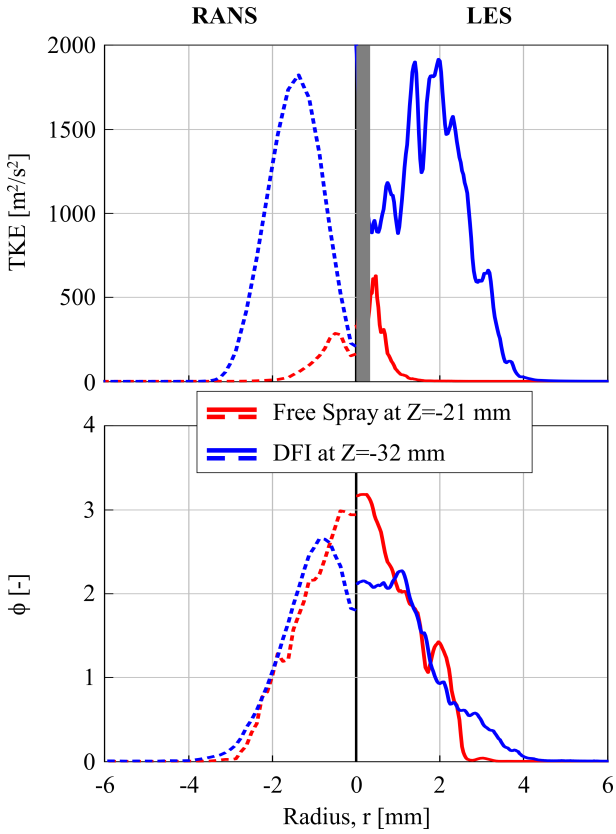

Fig. 4.5 Turbulent kinetic energy (top) and equivalence ratio (bottom) at the predicted lift-off lengths as a function of the spray radius at 0.5 ms aSOI according to the ensemble-averaged LES (right side, solid lines) and the RANS (left side, dashed lines) approaches. Results for both free spray (red) and DFI (blue) configurations.

Comparing the results at the LOL computed with RANS (dashed lines) and LES (solid lines), the TKE curves (Fig. 4.5, top) are relatively similar from a macroscopic point of view, despite the larger radial area involved by the DFI (blue lines) when the flow field is solved through LES, leading to a better homogenization process. Concerning the differences on the ϕ radial distribution (Fig. 4.5, top), the relative distance among free spray (red lines) and DFI curves is undervalued by the RANS simulations, if compared with LES. This is especially true in the core of the spray, where LES predicts, on one hand, a better homogenization for the DFI, smoothing the peak calculated with RANS (which even overcomes free spray values for r>1 mm), on the other hand, a slight increment of the free spray peak close to the axis.

In conclusion, according to the results of this assessment, the RANS with RNG $\kappa-\varepsilon$ model is capable to predict the main physical behaviours of both free spray and DFI configurations, thus capturing the major trends between them, in terms turbulent

mixing enhancement and mixture enleanment. This outcome is particularly relevant if analysed from the computational cost perspective (Table 4.2): the DFI configuration can be simulated with RANS requiring 3-4 orders of magnitude lower core hours on less performing processors compared to the ensemble-averaged LES. Similar values could be provided for the free spray configuration. These numbers immediately point out the importance of using the RANS approach for the affordability of the analyses presented in next chapters. However, it was also observed along this chapter that the RANS approach tends to underestimate the effect provided by the duct adoption in terms of absolute values, resulting in reduced mixing intensity and richer ϕ values at the LOL, if compared with the much more accurate LES approach. Therefore, it is Author's opinion that these RANS modelling settings can be reliably applied to perform sensitivity analyses on the DFI technology, but it must be always taken into account that the effectiveness of the duct adoption in terms of soot mitigation potential could be underestimated.

Table 4.2 Computational cost comparison between RANS and ensemble-averaged LES for the DFI configuration

	LES	RANS
Processors	x86 Intel Xeon Platinum 8276-8276L (2.4 GHz)	Intel Xeon E5-2680 v3 (2.50 GHz)
Nº simulations	5	1
Runtime (core hours)	149000	30

Chapter 5

DFI investigation with RANS: combustion and soot formation processes

Part of the work described in this chapter was previously published in:

- Cristiano Segatori, "Ducted Fuel Injection: a Computational Fluid Dynamics analysis of soot formation mitigation mechanisms," Rel . Federico Millo, Andrea Piano, Politecnico di Torino, Corso di laurea magistrale in Ingegneria Meccanica, 2020, http://webthesis.biblio.polito.it/id/eprint/14575
- Millo, F., Piano, A., Peiretti Paradisi, B., Postrioti, L., Pieracci, L., Bianco, A., Pesce, F.C. and Vassallo, A.L., "Ducted Fuel Injection: Experimental and numerical investigation on fuel spray characteristics, air/fuel mixing and soot mitigation potential," *Fuel*, Volume 289, 2021, doi:1016/j.fuel.2023.128110.

This chapter aims to study the final effect that enhanced turbulent mixing and entrainment mechanisms enabled by the duct adoption have on the combustion and soot formation / oxidation processes, if compared with the conventional diesel combustion. To do so, the definition of a high-fidelity RANS model was mandatory, due to the unfeasible computational cost required by a LES study coupled with detailed combustion models. This is especially related to the extremely refined grid required by the DFI case study for an accurate prediction, according to the grid sensitivity analysis reported and deeply discussed in chapter 3. Therefore, the

assessment of the RANS model for the numerical investigation of the DFI against the free spray, executed in chapter 4 by means of a local comparison with LES data, as well as the validation of the simulation results against the non-reacting experimental data were a step of paramount importance for the present purpose. Unfortunately, due to the absence of experimental data in reacting conditions for the herein injection case study, the results presented in this chapter must be considered as purely predictive. Nevertheless, a qualitative validation of the adopted combustion model, against well-known experimental data available in the scientific literature for different operating conditions, is reported at the end of the chapter to provide a perception of the reliability and robustness of the presented results.

5.1 Methodology

5.1.1 Operating conditions

The reacting numerical analysis was conducted under the operating conditions reported in Table 5.1, sweeping the air temperature and pressure within the CVV, keeping constant the vessel density. The values of oxygen concentration, vessel density and vessel temperature were close to the ECN Spray A ambient conditions [30], in order to allow a qualitative comparison with the data reported in [31], as dealt with in section 5.3. In addition, the highest available rail pressure value was selected to be as close as possible to typical engine operating conditions and to be consistent with previous non-reacting analysis. As in chapters 3 and 4, for the DFI configuration, the D2L14G2 geometry was used.

Table 5.1 Reference operating conditions for the combustion simulations

Oxygen concentration	%	21
Vessel density	kg/m^3	22.2
Vessel temperature	K	900÷1100
Rail pressure	bar	1200
Injection duration	ms	1.5
Injected mass	mg	11.85

5.1.2 RANS 3D-CFD setup

The reacting numerical simulations were carried out on the commercially available software CONVERGE CFD 2.4 [134]. The RANS RNG $\kappa-\varepsilon$ turbulence model was adopted for both free spray and DFI, while the spray model was exactly the same already successfully calibrated and validated in non-reacting conditions. As far as the volume discretization is concerned, similar grid settings to the RANS non-reacting analysis (chapter 4) were set, placing a fixed grid refinement in the region in which the spray evolves and in the duct region, obtaining a base grid size in the spray area of 0.50 mm and 0.25 mm inside the duct. In addition, AMR technique was applied to automatically adjust the grid resolution based on the curvatures of the velocity and temperature fields, obtaining a minimum grid size of 0.25 mm. Also in this case, the chamber was initialized with an almost quiescent flow. For other settings not cited in this section, please refer to the non-reacting 3D-CFD setup (chapters 3 and 4), on which they are entirely based.

5.1.3 Combustion and emissions modelling

The combustion was modelled by means of the SAGE detailed chemistry solver implementation, introduced by [142] and based on the well-stirred reactor (WSR) assumption [143]. Adopting this combustion modelling approach, chemistry and transport are decoupled, being the chemistry solved first. Indeed, given a generic chemical reaction mechanism, namely a set of elementary reactions describing the overall chemical reaction, the detailed chemistry solver calculates the reaction rates of each elementary reaction while the CFD solver solves the transport equations. In each time-step and cell, given a species m, SAGE solves for new species mass fractions (Y_m) immediately before the transport equations are solved, treating this net change ($d(\bar{\rho}\tilde{Y}_m)/dt$, equation 5.1) as an explicit source term (i.e., reaction rate $\dot{\omega}_m$) in the governing transport equation (equation 5.2). The bar ($\bar{}$) and the tilde ($\tilde{}$) indicate respectively Reynolds and Favre averaging for RANS[1], and Reynolds and

[1]According to the Reynolds average, each quantity Q is split into a mean $\bar{Q}$ and a deviation from the mean noted Q':

$$Q = \overline{Q} + Q' \quad \text{with} \quad \overline{Q} = 0$$

Since Reynolds averaging induces some difficulties in the modelling of turbulent flames, due to the density fluctuations, Favre (or mass-weitghted) averaging [144] is a mathematical formalism

Favre spatial filtering for LES.

$$\frac{d\bar{\rho}\tilde{Y}_m}{dt} = \widetilde{\dot{\omega}(Y_m, T)} \tag{5.1}$$

$$\frac{\partial \bar{\rho}\tilde{Y}_m}{\partial t} + \frac{\partial \bar{\rho}\tilde{u}_j\tilde{Y}_m}{\partial x_j} = \frac{\partial}{\partial x_j}\left(\bar{\rho}D_t\frac{\partial \tilde{Y}_m}{\partial x_j}\right) + \widetilde{\dot{\omega}(Y_m, T)} \tag{5.2}$$

where ρ is the density, T is the temperature temperature, $\partial/\partial t$ is the partial derivative with respect to time, $\partial/\partial x_j$ is the partial derivative with respect to space component j, and D_t is the turbulent diffusion coefficient.

The closure of the average reaction rate $\widetilde{\dot{\omega}_m}$ is the main focus of the turbulent combustion modelling studies [145, 143]. SAGE assumes that the average reaction rate in a cell commutes with the reaction rate of the average temperature and species concentration values, as in equation 5.3.

$$\widetilde{\dot{\omega}(Y_m, T)} \simeq \dot{\omega}(\tilde{Y}_m, \tilde{T}) \tag{5.3}$$

In this way, the reaction rate can be directly computed assuming the forward reaction rate coefficients (k_f) in the Arrhenius form as in equation 5.4.

$$k_f = AT^{\beta}\exp\left(\frac{-E_a}{RT}\right) \tag{5.4}$$

where A is the pre-exponential factor, β is the temperature exponent, E is the activation energy, and R is the ideal gas constant. The reverse reaction rate can be specified or calculated from the equilibrium coefficient (determined from thermodynamic properties). To ensure an accurate combustion simulation, it is critical that these data listed in the reaction mechanism for each reaction accurately represent laminar flame speed (for premixed combustion) and ignition delay (for non-premixed combustion).

The approach in equation 5.3 introduces the so-called *commutation error*, since fluctuations in temperature and species mass fraction, tending to increase or de-

decomposing any quantity into $Q = \widetilde{Q} + Q''$, where:

$$\widetilde{Q} = \frac{\overline{\rho Q}}{\overline{\rho}} \quad \text{with} \quad \widetilde{Q''} = 0$$

This averaging approach allows avoiding the explicit modelling of the velocity/density fluctuations correlation [143].

crease the reaction rate, are neglected[2]. In other words, the well-known turbulence-chemistry interaction (TCI) [146], typically affecting turbulent combusting flows, is taken into account only for what concerns the enhanced mixing physical effect (by modelling turbulent viscosity and turbulent diffusivity) and not for what concerns the chemical effect. Even though the presence of the commutation error could lead to a thin flame and cause an overestimation of the heat release rate [147], SAGE achieved very good predictions in several diesel combustion studies [142, 95, 148, 149] and the WSR assumption has been widely used in the scientific literature regarding DFI reacting simulations [44, 37, 65]. Furthermore, as executed in [150], given the absence of reacting experimental data for the herein case study, SAGE was deemed as the best option[3] to obtain predictive results in terms of combustion process and emissions, differently from other combustion models (e.g., those based on the flamelet assumption [152, 153]) requiring a dedicated calibration of the constants to match the experimental data.

For the predictivity purpose, an appropriate combustion mechanism must be used, valid for the simulated operating conditions. In this work, the Skeletal Zeuch chemical mechanism based on the N-C_7H_{16} oxidation scheme [154], with additional soot reactions from Mauss's work [155] and compiled of thermal NO_x reactions (for both NO and NO_2), was adopted. It consists of 121 species and 593 reactions; the inclusion of poly-cyclic aromatic hydrocarbons (PAHs) as soot precursors enables the detailed Particulate Mimic model [156, 157] for more accurate soot estimation. This detailed soot model applies comprehensive mathematical description for the soot particle size distribution function (PSDF) and solve the complex soot formation and oxidation with detailed chemistry. It is based on the so-called *method of moments*

[2]It is worth noting that with LES the commutation error limits to zero as the cell size is reduced, thus becomes negligible with sufficient grid resolution. On the contrary, for RANS, the commutation error does not limit to zero as the cell size is reduced. In many combusting flows, this error is relatively small, and predictive results can be produced without accounting for it. In other flows (especially highly turbulent combustion with local extinction or re-ignition), it should be modelled. In these cases, turbulent Schmidt and Prandtl numbers can be adjusted to enhance or reduce the mixing effect on combustion.

[3]It is noteworthy that the choice of modelling combustion with SAGE comes with the drawback of a much higher computational cost with respect to other combustion models. In order to expedite the detailed chemistry calculations, the kinetics was not solved in cells falling below a minimum cell temperature (i.e., 600 K), and reaction rate coefficients are not updated if the cell temperature changes less than 2 K between two subsequent time steps. Furthermore, the adaptive zoning [151] was exploited to solve together all the cells characterized by similar temperature and equivalence ratio values, gathering them in a reduced number of groups featuring a single average temperature and composition. In particular, the computational domain was divided in equally-spaced bins, considering a bin size of 5 K for the temperature and of 0.05 for the equivalence ratio.

[158], a statistical approach of estimation of population parameters, and only the first few moments are taken into account[4]. This soot model assumes that the following basic physical and chemical processes are important for the soot formation: particle inception [155], coagulation [159], condensation (modeled as the coagulation of PAH molecules with soot particles [159]), and heterogeneous surface reactions (i.e., surface growth) and oxidation by OH and O2. The soot mass growth and loss of soot particles due to reactions with gas phase species on their surface are described by the Hydrogen Abstraction Acetylene Addition Ring Closure (HACARC) mechanism [155]. From an overall point of view, the Particulate Mimic model features good capability over wide ranges of operating conditions [89], thus being considered as the best option when comprehensive soot formation analyses are needed, enabling the investigation of different test conditions without losing results reliability. Furthermore, its capability to provide accurate quantitative soot predictions under diesel engine conditions has been reported in the scientific literature [160].

Regarding NO_x emissions and other pollutants, such as CO and unburned hydrocarbons HC, they were estimated relying on the outcome of the detailed chemistry, based on the reactions included in the combustion mechanisms. Hence, no further modelling effort was performed. In particular, the included reactions for the NO formation are based on the extended Zel'dovich mechanism, as presented by [5], while further series of reactions are present for the NO_2 formation.

In table 5.2, combustion and emissions modelling details are summarized.

Table 5.2 Summary of combustion and emissions modelling details

Combustion	SAGE detailed chemistry solver
Fuel surrogate	N-C_7H_{16}
Chemical kinetics	Skeletal Zeuch mechanism
Nº species	121
Nº reactions	593
Soot precursor	A_3R_5- (PAH)
Soot formation / oxidation	Particulate Mimic model
NO_x, HC, CO emissions	Detailed chemistry output

[4]This approach assumes that integral properties, such as the mean particle number density, the mean mass or the mean particle diameter, are the main focus of soot modelling outcomes.

5.2 Combustion and emissions results

The numerical results in terms of heat release rate and soot emission mass are shown in Fig. 5.1 for the tested operating conditions.

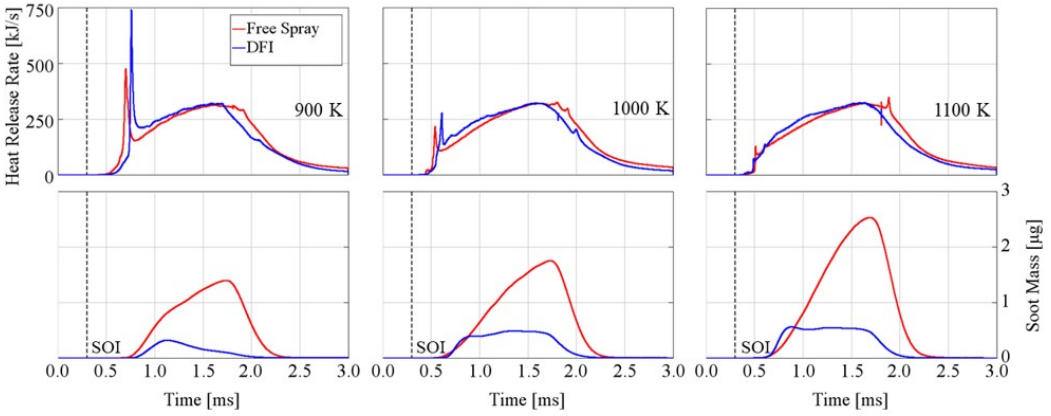

Fig. 5.1 Heat release rate (top) and soot mass (bottom) comparison between free spray (red) and DFI (blue) configurations. Test conditions: vessel temperatures = 900 K (left), 1000 K (center), 1100 K (right); rail pressure = 1200 bar, vessel density = 22.2 kg/m^3.

The heat release rate comparison shows an extension of the ID due to the duct adoption except for the 1100 K case (Fig. 5.1, right), in which the SOC occurs inside the duct. In fact, the higher temperature of the latter case leads to a short-enough ID to have a pre-ignition happening inside the duct for the DFI, almost at the same time instant of the free spray. This demonstrates that the detachment of the flow at the duct exit, suddenly reducing the local equivalence ratio values, can play a role in the ID increment due to the duct adoption. As an example, according to [161], the low ϕ values increase the chemical ID. Nevertheless, after few instants, the MC flame stabilizes after the duct exit, thus making the DFI properly work, similarly to the other vessel temperature levels. The delayed SOC at 900 and 1000 K causes a more intense DFI premixed combustion phase and a quasi-steady combustion slightly higher with respect to the free spray, causing a faster burnout at the EOI, as experimentally observed in [29, 31, 32]. The higher MC combustion phase and the faster burnout for DFI are present also in the 1100 K case, even though the premixed phase intensity is similar to the free spray due to the abovementioned similar ID. Therefore, despite the pre-ignition inside the duct, the DFI combustion emerges as more premixed even at this latter temperature level.

Looking at the total soot mass predicted by the Particulate Mimic model, it is evident that the DFI configuration is able to substantially abate soot emissions with

respect to the free spray, with a complete attenuation at 1.8 ms aSOI for all the tested conditions. More in detail, the DFI soot mass is close-to-zero for the whole time window at 900 K, while slightly increases as the vessel temperature is higher. For the free spray, the soot mass at 900 K is noticeably higher than DFI and the trend with the vessel temperature is even more emphasized. It is noteworthy that the DFI soot mass at 1100 K is even lower than the free spray one at 900 K, leading to the conclusion that the duct presence enables more than 200 K higher air temperature levels without any deterioration in terms of soot emission behaviour. Contour plots of the evolution of the local soot mass distributions are shown in Fig. 5.2 for vessel temperature equal to 1100 K case, comparing the free spray and the DFI configurations.

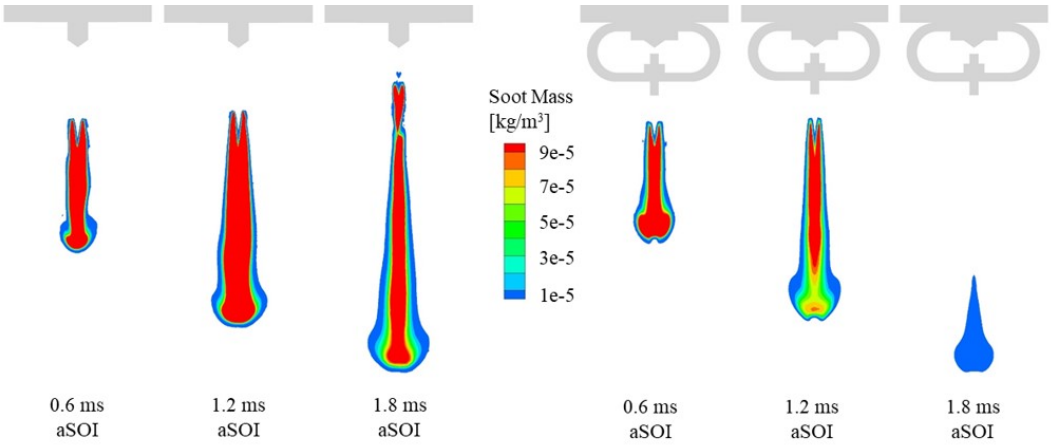

Fig. 5.2 Evolution of the soot mass distribution comparing free spray and the DFI configurations. Test conditions: rail pressure = 1200 bar, vessel temperature = 1100 K, vessel density = 22.2 kg/m^3.

At the beginning (0.6 ms aSOI) the total soot mass quantities are comparable for the two configurations as well as the spatial extents of soot mass distribution. Going ahead in the combustion process (1.2 ms aSOI), the soot formation in the free spray jet is still rising, showing a larger area of high soot mass density with respect to the previous frame. On the contrary, the DFI configuration highlights a reduction of soot mass density at the jet front. Finally, towards the end of combustion (1.8 ms aSOI), the soot mass is almost completely oxidized in the DFI configuration, while an extensive area of high soot mass density remains still visible in the free spray configuration.

In order to provide insights also on the other pollutant emissions, results concerning NO_x, CO and HC emissions evaluated at the end of combustion are presented in Fig. 5.3.

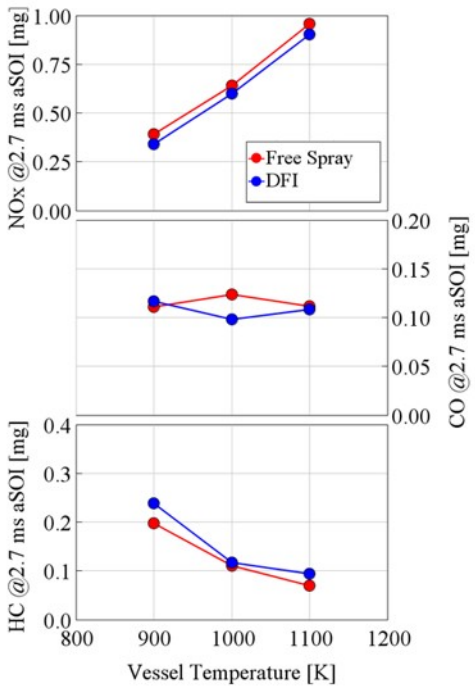

Fig. 5.3 NO_x, CO and HC emissions as a function of the vessel temperature for free spray (red) and DFI (blue) configurations.

A slight decrease in terms of NO_x emissions can be detected for DFI, thus suggesting the DFI ability to break the traditional soot/NO_x trade-off as experimentally investigated in [57, 66] (Fig. 1.11), allowing high EGR rates to attenuate NO_x formation without any drawbacks on soot emissions. Moreover, similar CO and HC emissions values are obtained for free spray and DFI configurations. Concluding, the preliminary results obtained for all gaseous pollutant emissions are promising, without showing any detrimental effect of DFI.

5.3 Qualitative combustion model validation

In order to understand the reliability of the predicted 3D-CFD results in reacting conditions, qualitative validations against scientific literature experimental data are reported in the next subsections.

5.3.1 Comparison against *Gehmlich et al.* experimental data

The first validation was carried out against the *Gehmlich et al.* work [31], in which the same vessel temperature sweep (900-1100 K) was executed with the same oxygen concentration level (21%) and a very similar vessel density, equal to 22.8 kg/m^3. Nevertheless, the comparison must be mainly considered in terms of trends between free spray and DFI configurations, rather than in terms of quantitative values, since several differences are still present in the injection setup. Similarities and differences in the injection setups are summarized in Table 5.3.

Table 5.3 Comparison of the injection setup between this work and the experiments carried out by *Gehmlich et al.* [31]

		This work	*Gehmlich et al.*
Vessel temperature	K	900÷1100	900÷1100
Vessel density	kg/m^3	22.2	22.8
O_2 concentration	%	21	21
Rail pressure	*bar*	1200	1500
Injection duration	*ms*	1.5	4.0
Injected mass	*mg*	11.85	10.7
Fuel		Diesel #2 (liquid) N-Heptane (vapor)	99% N-Dodecane
Nozzle diameter	μm	180	90
Duct geometry		D2L14G2	D2L16G1.4δ[5]

As can be seen, although a similar amount of fuel mass is injected and the rail pressure is higher for *Gehmlich et al.*, a more than doubled DOI is needed in the latter case, due to the smaller injector nozzle hole, featuring a half diameter. The significantly smaller nozzle diameter is expected to be the major difference among the considered setups, due to the influence on the atomization and evaporation behaviour of the injected fuel spray.

In Fig. 5.4, a comparison between the results obtained in this work and the experimental data coming from *Gehmlich et al.* is reported in terms of pressure derivative and soot mass traces for the three different vessel temperatures. The temporal axis is reported in a normalized form, by dividing the time aSOI with the correspondent DOI, to obtain a clear comparison regardless of the different time window.

[5]The δ symbol indicates a duct shape proposed by [31], previously reported in Fig. 1.13.

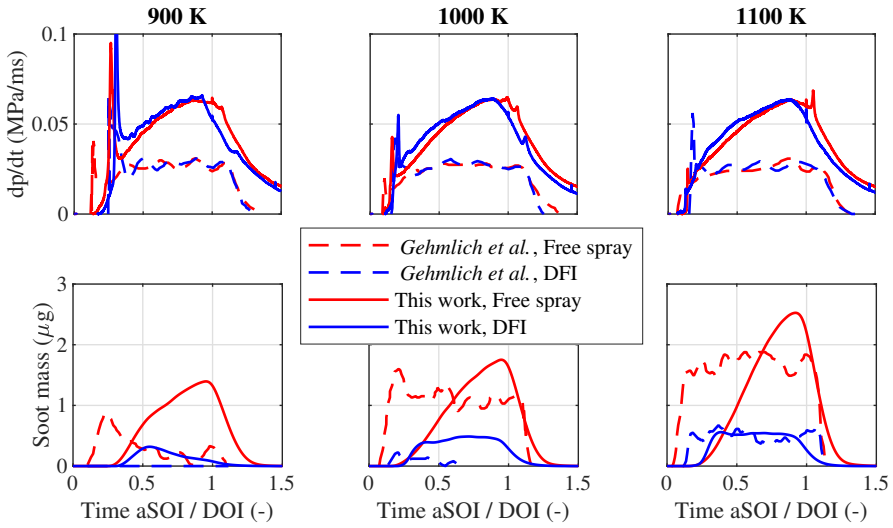

Fig. 5.4 Pressure derivative (top) and soot mass (bottom) as a function of the non-dimensional time for three different vessel temperatures (900 K, 1000 K, 1100 K) for both free spray (red) and DFI (blue). Comparison among this work (solid line) and *Gehmlich et al.* [31] experimental data (dashed line).

The 3D-CFD results are in good agreement, featuring the main trends observed experimentally moving from the free spray to the DFI configuration. Indeed, on the one hand, the pressure traces are characterized by similar characteristics (i.e., longer ID, more intense premixed burn, slightly higher MC combustion phase, and faster burnout for the DFI), with some differences in the absolute value of the ID and of the pressure derivative associated with the MC phase, due to the different injector characteristics and fuel (i.e., chemical energy) mass flow rate. On the other hand, the soot mass traces capture very well the impressive soot formation abatement due to the duct adoption, predicting similar percental reduction and even very close absolute values to the experiments for both free spray and DFI, confirming the reliability of the Particulate Mimic model [156], chosen for this numerical activity.

These comments are even more evident looking to the comparison in terms of average combustion and soot formation parameters, reported in Fig. 5.5 as a function of the vessel temperature for both free spray and DFI. The numerical ID was calculated according to the well-known ECN modeling standards [162], namely, by identifying the SOC as the instant at which the OH* radicals formation rate exceeded a preset threshold. The CD was computed as the difference between the end of combustion (EOC) and the SOC, where the EOC was detected as the instant at which the 90% of the mass fraction burned is reached, and is reported normalized with respect to the DOI. The average soot mass throughout the combustion event was

calculated as the integral of the soot mass trace over time divided by the injection duration.

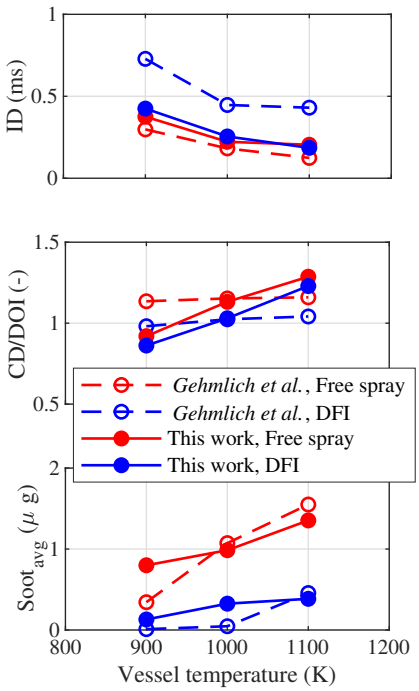

Fig. 5.5 Ignition delay (top), non-dimensional combustion duration (middle) and average soot mass (bottom) values as a function of the vessel temperature for both free spray (red) and DFI (blue). Comparison among this work (solid line) and *Gehmlich et al.* [31] experimental data (dashed line).

Focusing on the ID (Fig. 5.5, top), except for the 1100 K case, the experimental trend between free spray and DFI is respected by the 3D-CFD model, despite the much lower ID increment provided by the duct adoption. At the highest vessel temperature, the ID is almost identical between free spray and DFI for this work, due to the abovementioned pre-ignition occuring inside the duct. The trend is even better captured for the normalized CD (Fig. 5.5, middle), featuring a reduction with DFI of a similar amount at each temperature level. In other words, this work confirms for a different injection configuration that a higher combustion efficiency can be achieved by the DFI due to its faster combustion, presumably related to the more intense premixed phase. Interestingly, in this work, a higher sensitivity of the CD to the vessel temperature can be observed for both spray configurations. Finally, looking at the average soot mass values (Fig. 5.5, bottom), trends and absolute values are very similar between this work and Gehmlich et al. experimental data.

The larger difference can be observed at 900 K, where the free spray case manifests that the herein injection conditions are more sooting, presumably due to the slower evaporation process related the larger orifice diameter. However, even in this case, the duct presence is capable to impressively attenuate soot formation at a value close-to-zero, approaching the zero-soot experimentally observed.

5.3.2 Comparison against *Fitzgerald et al.* experimental data

The second validation was carried out against the *Fitzgerald et al.* work [32]. Among the operating conditions tested in their extensive experimental campaign, the most similar were selected for comparison with the present numerical results. The two injection setups are compared in Table 5.4.

Table 5.4 Comparison of the injection setup between this work and the experiments carried out by *Fitzgerald et al.* [32]

		This work	*Fitzgerald et al.*
Vessel temperature	K	900	900
Vessel density	kg/m^3	22.2	$\simeq$23.0
O_2 concentration	$\%$	21	21
Rail pressure	bar	1200	2500
Injection duration	ms	1.5	5.0
Injected mass	mg	11.85	43.5
Fuel		Diesel #2 (liquid) N-Heptane (vapor)	U.S. Certification ULSD
Nozzle diameter	μm	180	138
Duct geometry		D2L14G2	D2L14G2

The injection setups in this case are relatively more similar compared to the previous comparison. Indeed, apart from the almost identical ambient conditions, the nozzle diameter size is closer to the herein employed one and the same duct geometry was adopted. However, the injected fuel mass is almost 4 times higher for *Fitzgerald et al.* work despite the smaller injector nozzle hole, given the more than doubled rail pressure and the more than three times higher DOI. As in the previous validation, the smaller nozzle diameter and the significantly higher injection pressure are expected to provide major differences in terms of atomization and evaporation, and thus on the resulting combustion process. Therefore, a systematic comparison cannot again be executed from a rigorous, quantitative point of view, but only qualitative assessments can be performed.

In Fig. 5.6, a comparison between the results obtained in this work and the experimental data coming from *Fitzgerald et al.* is reported in terms of average combustion and soot formation parameters that can be extracted from the article. In particular, ID, LOL, and soot values are reported. It is noteworthy that, for the latter parameter, no soot mass measurement was available in the article, thus average spatial integral NL values are reported instead. Since not only the soot concentration but also local temperatures and optical issues (e.g., soot spatial distribution along the line-of-sight) affect the NL signal, the correlation between soot mass and NL cannot be considered linear [163]. Therefore, this uncertainty should be taken into account during comparisons in terms of soot.

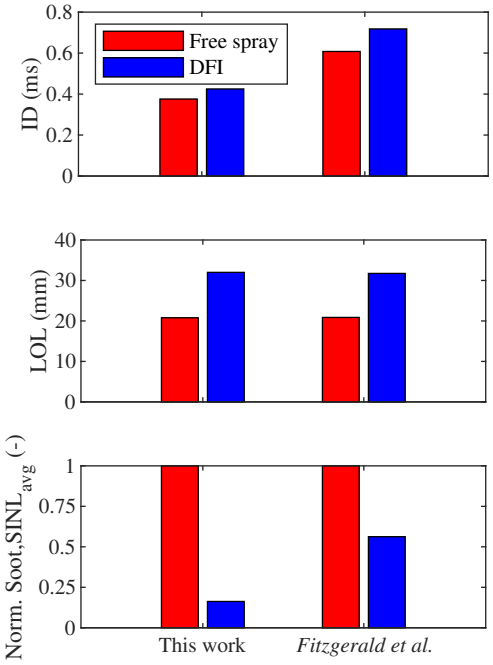

Fig. 5.6 Ignition delay (top), lift-off length (middle) and normalized average soot mass or spatial integral natural luminosity (bottom) values for both free spray (red) and DFI (blue). Comparison among this work and *Fitzgerald et al.* [32] experimental data.

Even though the ID (Fig. 5.6, top) absolute values are different for the two injection setups, the increment between free spray and DFI predicted by the present CFD model is relatively similar to the shown experimental data. Considering the LOL (Fig. 5.6, middle), this close match is even more evident, since the increment between free spray and DFI is almost the same for both injection setups. Moreover, the herein predicted absolute values are almost the same of the experimental data, probably due

to a physical balance between the lower rail pressure (tending to decrease the LOL) and the larger nozzle diameter (tending to increase the LOL). Finally, both works predict a significant reduction in terms of soot (Fig. 5.6, bottom) when the duct is adopted, even though it is higher for the present work from a percentage point of view, reaching more than 80% reduction against the almost 50% of *Fitzgerald et al.* These differences, apart from the different injection characteristics, could arise from the different physical quantity under evaluation, which is a mass value for the present CFD model while an optical luminosity measurement for the experimental work.

In conclusion, according to the validations against two experimental dataset available in the scientific literature [31, 32], the combustion and soot emissions modelling approach adopted in this work can be deemed reliable in predicting DFI physical characteristics and, thus, can be robustly applied for the sensitivity and optimization analyses presented in next chapters.

Chapter 6

DFI investigation with RANS: impact of the duct design

Part of the work described in this chapter was previously published in:

- Millo, F., Piano, A., Peiretti Paradisi, B., Segatori, C., Postrioti, L., Pieracci, L., Bianco, A., Pesce, F.C. and Vassallo, A.L., "Ducted Fuel Injection: A Numerical Soot-Targeted Duct Geometry Optimization," *SAE Int. J. Engines* 15(2):2022, doi:10.4271/03-15-02-0014.

After that the main DFI-enabled physical mechanisms have been highlighted through LES (chapter 3), and that a relatively low-cost RANS 3D-CFD model has been validated in both non-reacting (chapter 4) and reacting (chapter 5) conditions, the latter can be reliably applied for a practical investigation of the DFI technology, based on the former ones. In light of this, the present chapter aims to investigate the influence of the main geometrical features (stand-off distance, duct length and diameter, inlet and outlet shape) on the ducted spray characteristics, on the combustion and emissions formation processes. For this purpose, since only the D2L14G2 duct geometry (Table 2.3) has been numerically investigated so far, the developed virtual test rig is preliminary subject to a further validation against experimental liquid penetration considering different duct geometries, proving its capability to predict the effects of duct geometrical variations. Then, the impact of each geometrical characteristic is analysed though an extensive test matrix, towards an optimal soot-targeted duct design based on the tested operating conditions.

6.1 Methodology

The parametric analysis of the duct geometrical features was carried out on the commercially available software CONVERGE CFD 2.4 [134]. The same RANS-based model previously defined and investigated in non-reacting and reacting conditions has been employed. Please, refer to chapters 4 and 5 for details on the 3D-CFD setup not mentioned throughout this section.

6.1.1 Model validation for different duct geometries

First of all, a further spray validation against the experimental data available in chapter 2 was carried out. Fig. 6.1 shows the liquid penetration comparison between free spray and DFI configurations for the three different duct geometries highlighted in Table 2.3.

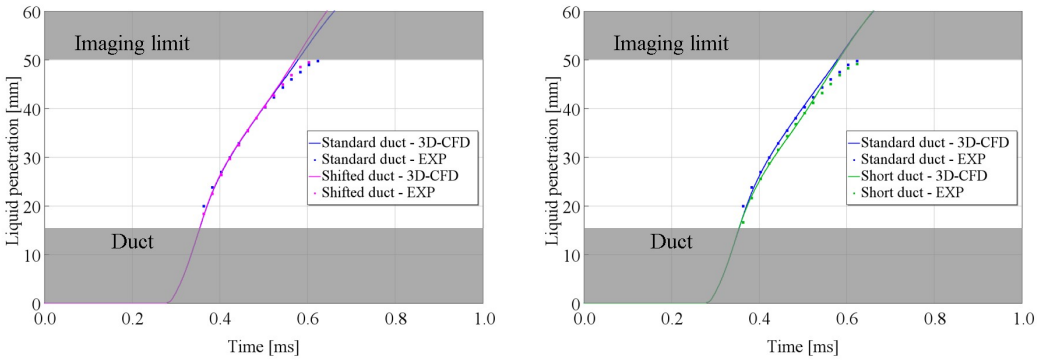

Fig. 6.1 Liquid penetration curves for standard duct (blue) and shifted duct (magenta) configurations on the left and for standard duct (blue) and short duct (green) configurations on the right: comparison between numerical results (solid lines) and experimental data (square dots). Test conditions: vessel pressure = 20 bar; vessel temperature = 773 K; rail pressure = 1200 bar.

The spray model is able to replicate the experimental spray evolution with a more than satisfactory accuracy in the prediction of the liquid penetration for the tested duct geometries. More specifically, standard duct and shifted duct (Fig. 6.1, left) show a similar penetration thus confirming that the liquid spray evolution is not remarkably affected by the different entrance distance. In addition, the developed spray model can correctly predict the experimental spray behavior. Moving to Fig. 6.1 (right), as highlighted in chapter 2, the short duct shows a lower spray velocity with respect to the standard duct. This result is also visible in the numerical simulation outcomes,

confirming the high predictive capabilities of the calibrated spray model. Given the good agreement between available experimental data and simulation results varying the duct geometry, the spray model was considered robust enough for parametric analysis of DFI towards a preliminary geometrical optimization.

6.1.2 Test matrix and operating conditions

The simulation activity was carried out with the purpose of understanding the influence of the main duct geometrical features on the ducted spray characteristics and on the combustion and soot emissions formation processes. With this aim, the DFI spray was analyzed in both non-reacting and reacting conditions, varying consecutively the following geometrical features:

- stand-off distance (G) and duct length (L)
- duct diameter (D)
- duct inlet and outlet shape (Fig. 6.2).

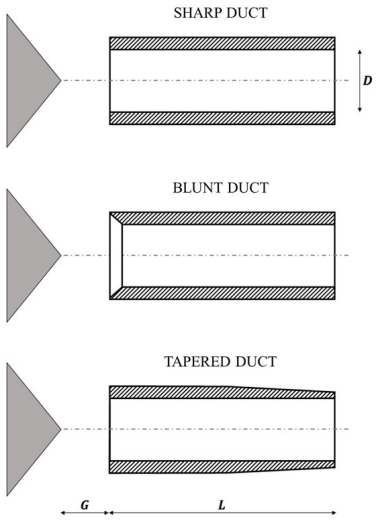

Fig. 6.2 Tested duct shapes and fundamental duct geometric parameters (D, L and G).

The sharp duct is the simplest configuration featuring a sharp inlet and outlet. This is the reference geometry for the herein study, thus, if not indicated differently, the duct must be intended as sharp. When the inlet shape is modified with a 45°-chamfer along the whole duct thickness, the duct shape is defined blunt duct; while,

when the outlet shape is characterized by a convergent outer diameter (configuration similar to the δ configuration, Fig. 1.13), the duct shape is defined tapered duct. Moving to the different duct geometries evaluated, the test matrix is illustrated in Fig. 6.3.

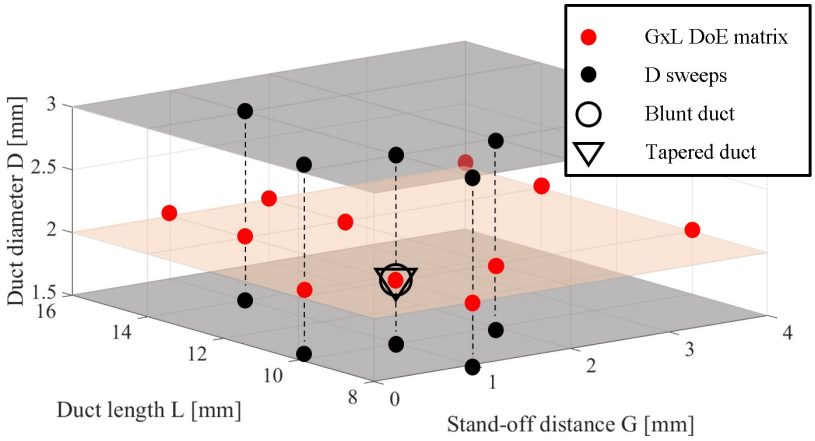

Fig. 6.3 Matrix of the tested duct geometries: GxL DoE matrix (red dots), D-sweep (black dots), blunt inlet shape (circle) and tapered outlet shape (triangle).

Firstly, the G and L effect was analyzed by means of a design of experiments (DoE) technique keeping D equal to 2 mm. As a result, a full-factorial 9-element matrix was enlarged to cover two additional combinations of G and L representative of extremely low G and L values (i.e. G=0.1 mm; L=8 mm). The whole GxL matrix is highlighted with red dots in Fig. 6.3. Afterward, the duct diameter was varied around the optimal combinations of stand-off distance and duct length ranging between 1.5 mm and 3 mm, as shown by the black dots. Finally, blunt and tapered duct configurations (triangle and circle, respectively) were tested on the optimal (D, L, G) combination. A total of 23 different duct geometries were analyzed, following the naming convention previously established (Table 2.3).

Each duct geometry was tested in both non-reacting and reacting conditions. On one side, non-reacting simulations had the aim of understanding the influence on air entrainment into the fuel spray and turbulent mixing without taking into account further effects derived from the combustion process. On the other side, both the analysis of the influence of the combustion process on the air entrainment and mixing, and the quantification of LOL and soot formation were evaluated through simulations in reacting conditions. The operating conditions of both the non-reacting and reacting simulations are reported in Table 6.1.

Table 6.1 Non-reacting and reacting operating conditions for the parametric analysis to the duct design

		Non-reacting	Reacting
Oxygen concentration	%	0	21
Vessel pressure	bar	20	57.3
Vessel temperature	K	773	900
Rail pressure	bar	1200	1200
Injection duration	ms	1.5	1.5
Injected mass	mg	11.85	11.85

6.2 Results

6.2.1 Effect of stand-off distance (G) and duct length (L)

Non-reacting analysis

Thanks to the LES-based investigation, enhanced upstream air entrainment (Fig. 3.20) and turbulent mixing (Fig. 3.17) were detected as DFI soot formation mitigation mechanisms, and the combination of this phenomena resulted in a remarkable equivalence ratio reduction in the core of the jet with respect to the free spray (Fig. 3.16). Starting from these outcomes, a detailed analysis on the upstream air entrainment was carried out for the GxL matrix at D = 2 mm, measuring the air mass flow rate ($\dot{m}_{air}$) across the spray iso-surface at a properly set value of overall equivalence ratio (i.e. fuel to air ratio including fuel liquid phase), until the spray impinges the duct inner wall. Given the asymptotic behavior of the phenomenon [39], the mass flow rate was calculated only at 0.3 ms aSOI, when pseudo-stationary conditions are reached inside the duct. The results are reported in Fig. 6.4.

At constant duct diameter, the longer G and L, the higher the upstream air entrainment. In particular, the G parameter seems to have more influence with respect to L. To better analyze this aspect, the pressure distribution along the spray axis (Z) is reported in Fig. 6.5 considering four different duct geometries (D2L10G1; D2L10G4; D2L16G1; D2L16G4). The pressure distribution is depicted at 0.3 ms aSOI when air flow stationary conditions are reached inside the duct. For the sake of clarity, the duct axial placement for each geometry is illustrated at the bottom.

Taking the D2L10G1 geometry (red) as a reference, it can be observed that a G increase (D2L10G4, blue) causes a slightly lower minimum pressure, shifted along

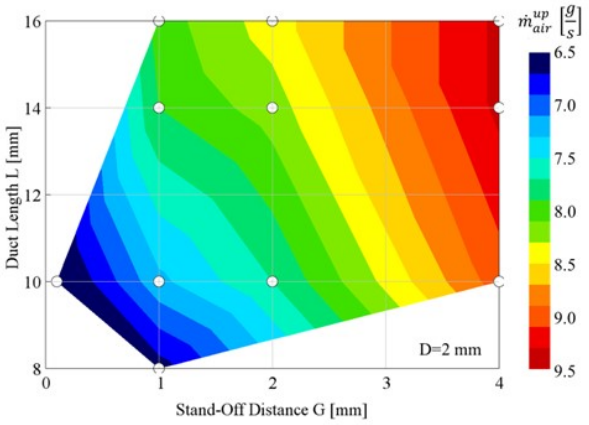

Fig. 6.4 Contour plot of the air entrainment into the fuel spray upstream the duct inlet as a function of G and L (D=2 mm) at 0.3 ms aSOI. Test conditions: vessel pressure = 20.0 bar; vessel temperature = 773 K; rail pressure = 1200 bar.

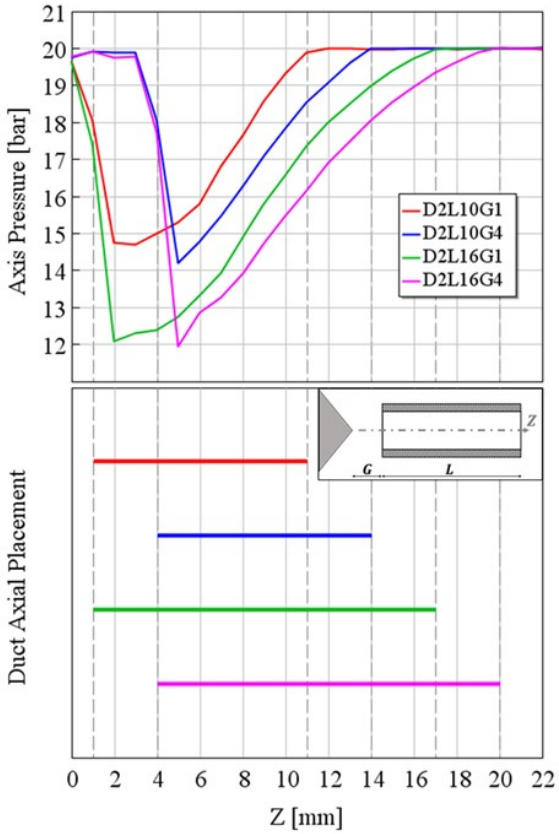

Fig. 6.5 Pressure evolution (top) along the Z-axis of the spray at 0.3 ms aSOI for the following duct geometries: D2L10G1 (red); D2L10G4 (blue); D2L16G1 (green); D2L16G4 (magenta). The location of the ducts for each configuration is illustrated at the bottom. Test conditions: vessel pressure = 20.0 bar; vessel temperature = 773 K; rail pressure = 1200 bar.

the axis according to the duct inlet location. On the other side, at constant G, an L increment leads to a more significant influence on the pressure drop (D2L16G1, green). Moreover, as expected, the simultaneous variation of G and L (D2L16G4, magenta) causes a combined effect on the pressure in terms of absolute drop value and its position along the duct axis.

The huge impact of duct length on the in-duct pressure drop could be explained considering the flow evolution within the duct. In the DFI configuration, the entraining air, driven by the jet momentum, increases its velocity since it is constrained to pass through a much smaller flow area with respect to the free spray. According to the energy conservation, neglecting in first approximation the air density variations, the increase in kinetic energy is reached by means of a decrease in pressure energy, thus, the pressure inside the duct drops down. Thereby, the higher the duct length, the longer the space in which the pressure energy can be converted into kinetic energy before rising again for continuity reasons at the duct exit, where the pressure must be equal to the CVV condition.

However, the upstream air entrainment distribution is not only a function of pressure drop in the duct volume but also of available minimum flow area. In fact, comparing the D2L10G4 (blue) and D2L16G1 (green) configurations in Fig. 6.5, it can be easily visualized that the longer duct shows a much higher pressure variation with respect to the shorter geometry; however, the longer duct results in lower upstream air entrainment (Fig. 6.4) with respect to the configuration with short duct but with duct inlet location farther from the injector tip. In other words, the amount of upstream air entrainment depends not only on the static pressure stratification in the duct, but also on the minimum flow area, A_{min}, highlighted in Fig. 6.6, that is strictly dependent on the duct configuration (i.e. G, D, inlet shape).

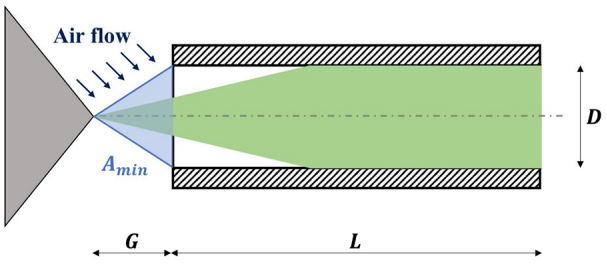

Fig. 6.6 Sketch of the minimum flow area for the upstream entraining mass flow rate ("Air flow").

As far as the G is concerned, since it linearly affects the minimum flow area, it has a strong influence on the upstream air entrainment. To quantify this dependency, Fig.

6.7 shows the correlation between minimum flow area and upstream air entrainment, normalized with respect to the maximum, for the tested GxL matrix.

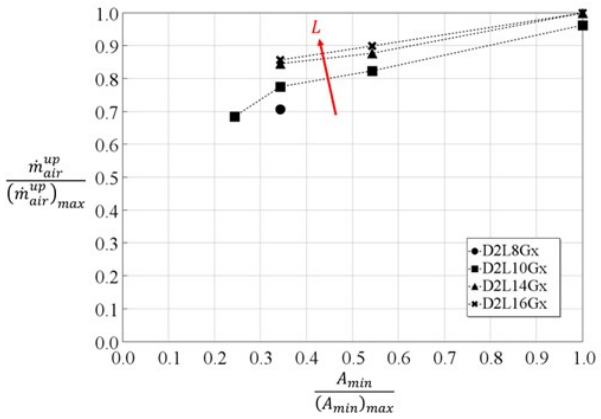

Fig. 6.7 Normalized upstream air entrainment as a function of normalized minimum flow area at different G at 0.3 ms aSOI. Test conditions: vessel pressure = 20.0 bar; vessel temperature = 773 K; rail pressure = 1200 bar.

Once assessed the geometry influence on the upstream air entrainment, the focus was moved to the enhanced turbulent mixing that, in section 3.3, was highlighted as a two-stage process for DFI: on one hand, a highly turbulent regime is reached inside the duct; on the other hand, the velocity gradient between the high-momentum jet and the surrounding quiescent air at the duct exit creates a high turbulent zone downstream of the duct. To quantitatively evaluate the turbulent mixing, the maximum TKE value for each cross-section of the spray at 0.3 ms aSOI was selected as a turbulence index for the whole 3D TKE field. The TKE index is reported in Fig. 6.8 (top) as a function of the spray axis, for the four different duct geometries previously analyzed and for the free spray configuration for comparison purposes. Furthermore, the maximum equivalence ratio (ϕ_{max}) for each cross-section of the spray is also reported (Fig. 6.8, middle) to directly evaluate the effect of turbulence on air/fuel mixing. It is worth noting that the maximum values instead of the average quantities were selected for both TKE and ϕ to avoid the noisy effect of evaporation and breakup processes on the mean quantities. In addition, with the aim of isolating the spray volume from the surrounding air in the CVV, the maximum values were computed only in a defined region by adopting an equivalence ratio filter to consider exclusively the computational cells in which $\phi > \phi_{threshold}$. As previously reported, Fig. 6.8 (bottom) shows the duct axial placement for each geometry.

Starting from the free spray versus DFI comparison in terms of maximum TKE distribution (Fig. 6.8, top), the abovementioned two stages of the mixing process

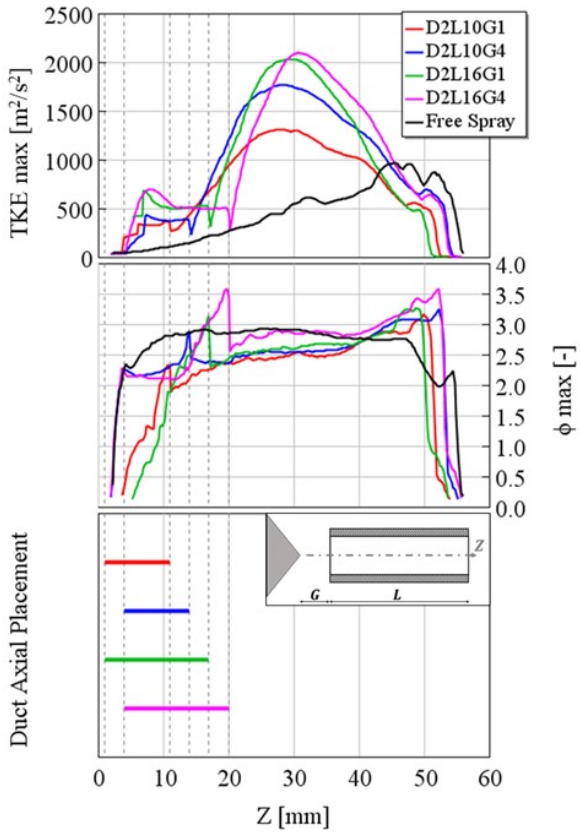

Fig. 6.8 Maximum TKE (top) and maximum ϕ (middle) on the spray cross-section as a function of the Z-axis at 0.3 ms aSOI for the free spray (black) and the following duct geometries: D2L10G1 (red); D2L10G4 (blue); D2L16G1 (green); D2L16G4 (magenta). The location of the ducts for each configuration is illustrated at the bottom. Test conditions: vessel pressure = 20.0 bar; vessel temperature = 773 K; rail pressure = 1200 bar.

can be clearly identified along the Z-axis. The first stage (i.e., in-duct turbulent regime) is evident by focusing on the TKE enhancement with respect to free spray (black) from the injector tip to the duct exit. This stage is characterized by a steep TKE increment at the beginning followed by a quasi-constant value characteristic of the geometry for a certain operating condition. In particular, this is verified for 3 geometries out of 4 (i.e., excluding the D2L10G1), in which a fully developed in-duct turbulent regime is established. Then, starting from the duct exit, the TKE significantly increases due to the high velocity gradient (i.e., the second stage of the process). Evaluating in detail the different duct geometries, it can be concluded that the farther the duct exit from the injector tip, the higher the maximum TKE, or, in other words, the second stage turbulent mixing retard is proportional to its intensity. This relation seems associated with the turbulence level reached inside the duct and

with the related establishment of fully developed turbulent conditions at the duct exit. Indeed, the abovementioned D2L10G1 (red) geometry shows a remarkably lower TKE slope at the duct exit than the remaining three, whose maximum TKE intensity is comparable despite the further increment in duct exit location.

Focusing on the equivalence ratio maximum (Fig. 6.8, middle), it is noteworthy that each considered duct configuration shows more promising results in terms of air-fuel mixing than the free spray, for most of the spray domain. The analysis of the ϕ_{max} distribution (gas phase) needs to take into account the impact of the evaporation process especially in the region close to the injector tip. In fact, at constant duct length, the difference between the D2L10G1 (red) and D2L10G4 (blue) geometries can be attributed to the lower spray contact with the surrounding air thus reducing the evaporation rate. The minimum ϕ_{max} after the duct exit is achieved with the duct geometry in which the second stage turbulent mixing is advanced and therefore less intense (D2L10G1, red line), suggesting that the equivalence ratio reduction is a trade-off between the intensity and the timing of the mixing. In fact, the shorter the duct exit location, the higher the capability of the spray of entraining air downstream of the duct, which is totally inhibited along the duct collision length. More specifically, although the turbulent mixing is enhanced inside the duct, the ϕ_{max} distribution close to the duct exit for the longest tested ducts (D2L16G1, green and D2L16G4, magenta) rises more than the one obtained in free spray configuration, due to the steep increment along the duct collision length. In other words, the maximum turbulent mixing is not enough to determine the most effective duct geometry in reducing ϕ, because the turbulent motion has to be combined with a sufficient amount of entraining air [58].

Combustion analysis

When combustion is enabled, the air entrainment and turbulent mixing mechanisms can be remarkably affected, thus changing the effectiveness of a certain duct configuration in soot mitigation. Therefore, for the purpose of defining the optimal duct geometry, the LOL is used as an axial threshold to quantify the capability of a certain spray configuration (both free spray and DFI) in entraining air and mixing it with fuel vapors before the combustion zone. First of all, the stabilized LOL contour plot at 1.2 ms aSOI for each GxL combination is reported in Fig. 6.9. As defined in the literature [164, 165] and in the ECN modeling standards [162], the LOL was

evaluated using the OH* radicals concentration, identifying the computational cell closest to the injector tip overcoming a suitable OH* threshold.

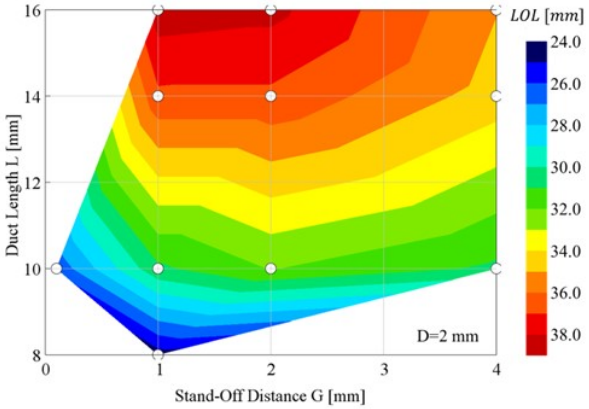

Fig. 6.9 Contour plot of the Lift-Off Length as a function of G and L (D=2 mm) at 1.2 ms aSOI. Test conditions: vessel pressure = 57.3 bar; vessel temperature = 900 K; rail pressure = 1200 bar.

It emerges that the LOL increases with the duct length due to the faster liquid penetration [33]. On the other side, the stand-off distance variation, which changes only the duct exit location keeping constant the axial spray confinement, leads to a maximum of the LOL for 1-2 mm value. Once defined the LOL in reacting conditions, the air entrainment was evaluated both upstream and downstream of the duct. The upstream air flow was computed as in the non-reacting simulation, while a similar methodology was adopted for the evaluation at the duct exit. In this case, the air mass flow rate was measured considering as cross-section the iso-surface at a ϕ value, properly set to contour the whole fuel spray in the axis range between the duct exit location and the LOL. A descriptive sketch of both the upstream and downstream iso-surfaces, $A_{upstream}$ and $A_{downstream}$, is reported in Fig. 6.10.

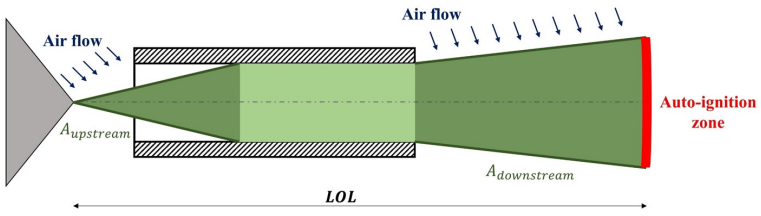

Fig. 6.10 Sketch of the isosurfaces for the calculation of the entraining mass flow rate ("Air flow") upstream and downstream of the duct in reacting conditions.

Since the upstream air entrainment is not affected by the combustion due to the large chamber volume, its contour plot is not reported. Same trends with G and L

variations of non-reacting analysis were obtained (Fig. 6.4) with the mass flow rate absolute values properly scaled due to the different CVV air density. The absolute downstream entrained mass flow rate, as well, is not here reported since it mainly depends on the net LOL (i.e. LOL minus collision length): the longer the net LOL, the higher the surface over which the mass flow rate is computed. In addition, the comparison between upstream and downstream air entrainment in terms of absolute values would have been misleading due to the difference in terms of flow area with $A_{downstream} > A_{upstream}$ for the evaluated duct geometries, thus not reflecting the real entrainment intensity. Therefore, the entrained mass flux was considered dividing the air flow per spray area unit. The upstream and downstream mass flux contour plots at 1.2 ms aSOI, when the air flow stationary conditions are reached, are reported in Fig. 6.11, left and right respectively.

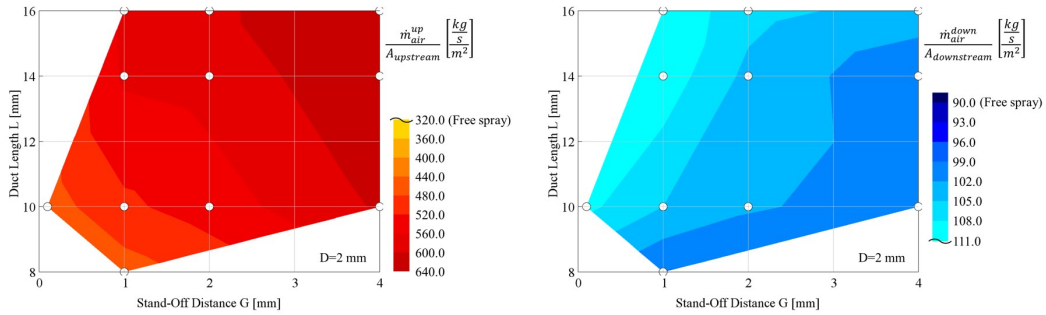

Fig. 6.11 Contour plots of the entrained mass flux into the fuel spray upstream (left) and downstream (right) of the duct as a function of G and L (D=2 mm) at 1.2 ms aSOI. Test conditions: vessel pressure = 57.3 bar; vessel temperature = 900 K; rail pressure = 1200 bar.

It is clear that the upstream entrainment mass flux is largely higher than the downstream one. Given that the Free Spray values (indicated in brackets in Fig. 6.11) are much lower than DFI for the upstream entrainment mass flux while they are quite similar to DFI for the downstream one, it could be drawn that the duct adoption enhances the air entrainment where is most beneficial, as concluded in the comments to Fig. 3.20. As far as the geometry dependency is concerned, the upstream air entrained mass flux shows a similar trend highlighted in non-reacting conditions (Fig. 6.4), being $A_{upstream}$ not remarkably affected by the different CVV thermodynamic conditions and by the duct geometry variation. On the other side, the downstream air entrained flux tends to grow reducing G and increasing L, highlighting its maximum with the D2L16G1 configuration.

Afterward, the turbulent mixing was evaluated considering the same methodology defined in non-reacting conditions for maximum TKE and equivalence ratio but

reducing the domain of interest at 0<Z<LOL. The maximum TKE and ϕ at 1.2 ms aSOI are depicted in Fig. 6.12 (top and middle, respectively) for the free spray and the four different duct geometries already analyzed in the non-reacting analysis. In addition, the LOL is highlighted at the bottom, with dashed line and indicators, in which the duct axial placement for each geometry is reported as well.

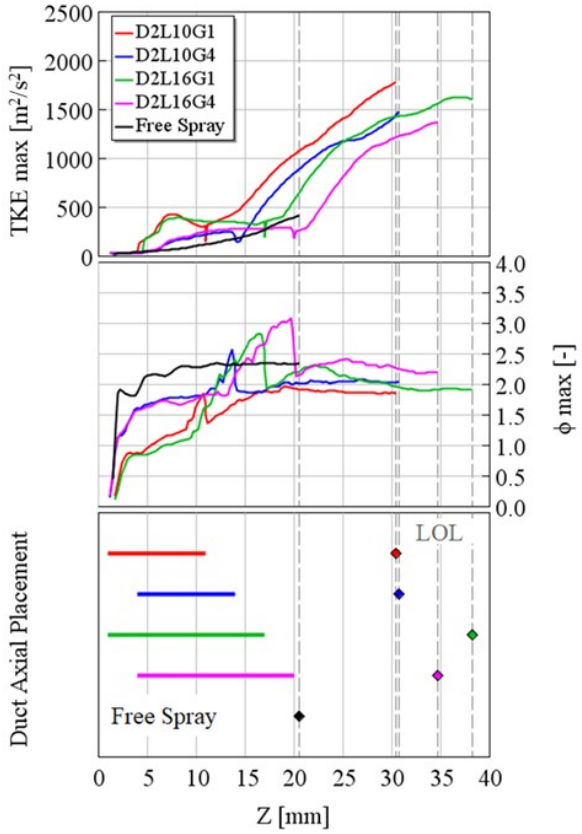

Fig. 6.12 Maximum TKE (top) and maximum ϕ (middle) on the spray cross-section as a function of the Z-axis at 1.2 ms aSOI for the free spray (black) and the following duct geometries: D2L10G1 (red); D2L10G4 (blue); D2L16G1 (green); D2L16G4 (magenta). The location of the ducts and the LOL are illustrated at the bottom. Test conditions: vessel pressure = 57.3 bar; vessel temperature = 900 K; rail pressure = 1200 bar.

As expected, the LOL plays a crucial role in determining the best balance between turbulent mixing and air entrainment, since it is an index for both available time and spray surface for the air/fuel mixing. More in detail, taking the free spray as a reference, DFI geometries feature a definitely longer LOL, highlighting an increment of about 10-18 mm, depending on the duct configuration. On the other side, free spray shows a maximum TKE lower than each DFI configuration for most of the analyzed domain, even considering a reduction of the gap between

free spray and in-duct TKE with respect to non-reacting simulation case (Fig. 6.8, top). Lower turbulence and shorter LOL, highlighted in the free spray configuration, lead to a not optimal air/fuel mixing, increasing the maximum ϕ at the LOL with respect to each duct geometry. Moving to the tested DFI configurations, several differences can be observed compared to the non-reacting simulations (Fig. 6.8) concerning the maximum TKE (Fig. 6.12, top): firstly, the in-duct TKE value is strongly dependent on the G value rather than the L; secondly, the second stage turbulent mixing steep increment is less dependent on the duct exit location, showing a similar slope among the different duct geometries and making the timing more relevant. In reacting conditions, the distance between LOL and duct exit tends to be a controlling parameter for DFI turbulent mixing effectiveness. In fact, D2L10G1 (red) and D2L10G4 (blue) configurations show a similar TKE intensity at the duct exit, but the advanced duct exit location, at LOL approximately equal, guarantees higher TKE values for the D2L10G1 geometry. In other words, the duct geometry second phase turbulent mixing capability has to be evaluated considering more than one aspect: the timing (i.e., duct exit location), the intensity (i.e., the slope) and the second phase mixing length (i.e., LOL minus duct exit location). These considerations on maximum TKE, along with the evaluation of the abovementioned duct collision length, can be mirrored in the maximum ϕ distributions (Fig. 6.12, middle). Indeed, the D2L10G1 geometry, which features the best turbulent mixing properties and the shorter collision length (due to the advanced duct exit), shows the lowest ϕ_{max} at the LOL and for most of the domain, apart from Z<12 mm (where the higher D2L16G1 upstream air entrainment prevails at similar evaporating conditions, Fig. 6.11). Comparing the D2L10G4 and the D2L16G1, the latter shows a lower ϕ_{max} after the axial distance from the tip (Z = 25-30 mm) in which its maximum TKE value overcomes the former one. The difference is, then, enhanced due to the longer LOL. Finally, the D2L16G4 (magenta) geometry, characterized by the longest collision length and by the most retarded duct exit location, reduces the DFI potential in terms of ϕ_{max} reduction.

After the evaluation of the main soot mitigation mechanisms, the combustion process and soot emissions were evaluated with the aim of selecting the optimal combination of G and L for the operating conditions defined in Table 6.1. In Fig. 6.13, the heat release rate (HRR) and soot mass traces related to the free spray and the already analyzed four duct geometries are reported.

As far as the combustion process is concerned, each duct geometry shows a retarded combustion start and, consequently, a more intense premixed combustion

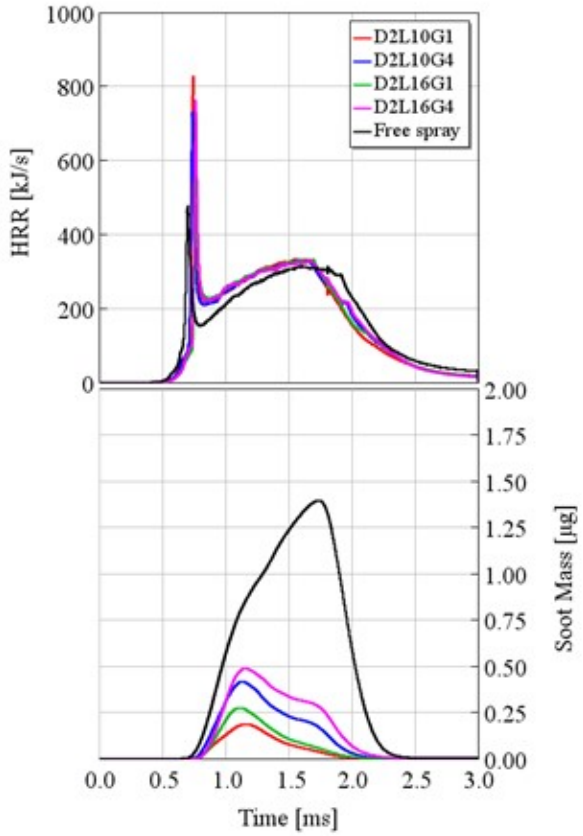

Fig. 6.13 Heat release rate (top) and soot mass in the CVV (bottom) for the free spray (black) and the following duct geometries: D2L10G1 (red); D2L10G4 (blue); D2L16G1 (green); D2L16G4 (magenta). Test conditions: vessel pressure = 57.3 bar; vessel temperature = 900 K; rail pressure = 1200 bar.

compared with free spray, confirming the outcomes of chapter 5. Moreover, the impressive soot reduction achieved by the duct adoption is worth to be noted. More specifically, D2L10G1 (red) geometry highlights the best performance in soot reduction, due to the higher mixing rate at LOL enabled by a combination of a longer available mixing duration and higher turbulence, as previously highlighted in Fig. 6.12. The analysis concerning the soot mass was then extended to the whole GxL DoE matrix. The scalar soot mass ($Soot_{avg}$) was calculated as the integral of the time-dependent soot trace divided for the injection duration (1.5 ms) and the contour plot of the soot mass percentage reduction with respect to free spray is reported in Fig. 6.14.

As it can be clearly noted, the DFI confirms its remarkable soot formation mitigation potential, in fact, all the considered geometries show a drastic soot mass reduction of more than 70.0%. In particular, the D2L10G1 configuration allows the

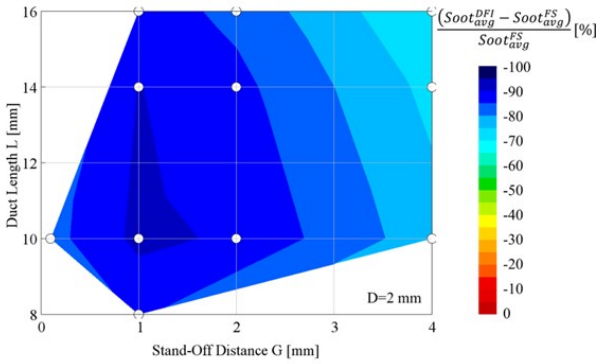

Fig. 6.14 Contour plot of the average soot mass in the CVV as a function of G and L (D=2 mm) in the form of percentage reduction with respect to free spray. Test conditions: vessel pressure = 57.3 bar; vessel temperature = 900 K; rail pressure = 1200 bar.

maximum soot attenuation achieving a reduction of 91.4% with respect to free spray. In conclusion, the optimal GxL combination is achieved by reducing the length of the duct and by placing it close to the injector tip until the air entrainment and LOL reductions overcome the benefits derived from the turbulent mixing. Indeed, taking the optimal configuration (D2L10G1) as a reference, the reduction of both L and G (8 mm and 0.1 mm, respectively) leads to a slightly higher soot mass due to the lower upstream air entrained mass flux (Fig. 6.11) and shorter LOL (Fig. 6.9).

6.2.2 Effect of duct diameter (D)

Non-reacting analysis

When the duct diameter varies according to the matrix in Fig. 6.3 (black dots), the air entrainment and mixing can drastically change. In Fig. 6.15, from top to bottom, the upstream air entrainment, the maximum in-duct velocity, the minimum in-duct pressure and the minimum flow area are reported at 0.3 ms aSOI (i.e. pseudo-stationary conditions reached inside the duct) as a function of the duct diameter, considering constant stand-off distance (G=1 mm) and duct length (L=10 mm).

Starting from Fig. 6.15(b), the in-duct velocity is reduced considering a larger duct cross-sectional area. Therefore, with a bigger duct diameter, the conversion from pressure energy to kinetic energy is reduced, causing a less intense in-duct pressure drop as shown in Fig. 6.15(c): for instance, D=3 mm leads to about 2 bar of in-duct pressure reduction with respect to the CVV (20 bar), while a decrease of more than 8 bar is achieved with D=1.5 mm. Nonetheless, this pressure variation

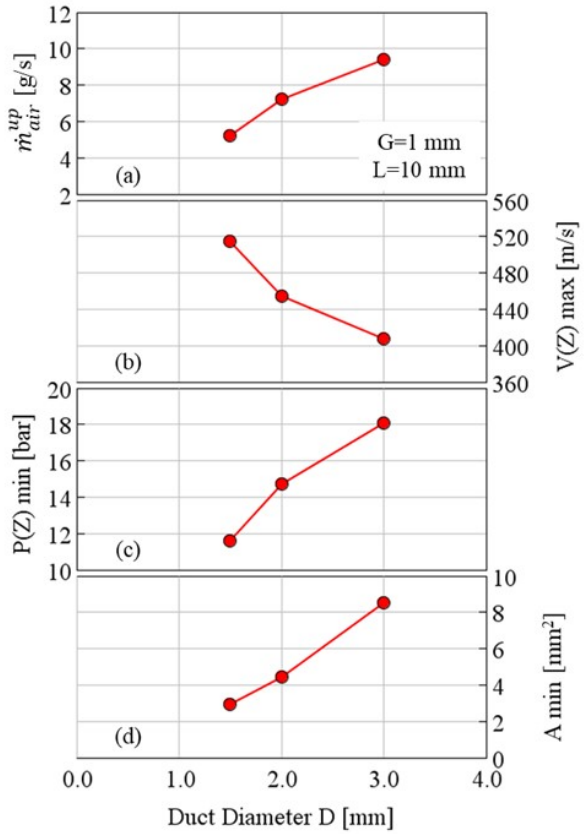

Fig. 6.15 Upstream air entrainment (a), maximum velocity (b) and minimum pressure (c) on the Z-axis at 0.3 ms aSOI and entraining air minimum flow area (d) as a function of the duct diameter (G=1 mm; L=10 mm). Test conditions: vessel pressure = 20.0 bar; vessel temperature = 773 K; rail pressure = 1200 bar.

is not directly reflected in the upstream air entrainment values (Fig. 6.15(a)) which rises for larger D. This is consistent with the already discussed outcomes: in fact, the pressure drop is one driver for the air entrainment enhancement in the duct along with the minimum flow area, that act as the control parameter for the mass flow rate, since the increment in A_{min} (Fig. 6.15(d)) counterbalances the reduced pressure drop.

As far as the turbulent mixing is concerned, Fig. 6.16 shows the cross-section maximum TKE (top) and maximum ϕ (middle) as a function of the Z-axis at 0.3 ms aSOI considering the same duct configurations (D-sweep, G=1 mm; L=10 mm) and the free spray for comparison. At the bottom, the duct axial placement is reported highlighting the collision length with a grey line for each considered duct geometry.

As already pointed out, each considered duct configuration improves both TKE and air-fuel mixing with respect to the free spray. Focusing on the top graph, the

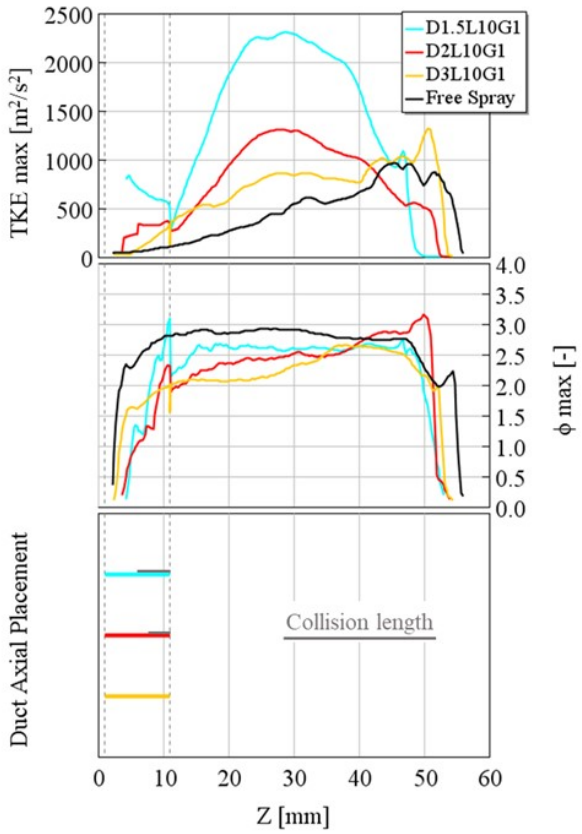

Fig. 6.16 Maximum TKE (top) and maximum ϕ (middle) on the spray cross-section as a function of the Z-axis of the spray at 0.3 ms aSOI for the free spray (black) and the following duct geometries: D1.5L10G1 (cyan); D2L10G1 (red); D3L10G1 (yellow). The location of the ducts and the collision length (grey) are illustrated at the bottom. Test conditions: vessel pressure = 20.0 bar; vessel temperature = 773 K; rail pressure = 1200 bar.

in-duct maximum TKE is higher for the smallest diameter (D1.5L10G1, cyan), highlighting a dependency on the in-duct velocity, which increases the Reynolds number and, thus, the strength of the turbulent regime through the small pipe. Consequently, the higher in-duct spray velocity leads to a more intense second turbulent mixing phase since a larger amount of kinetic energy after the duct exit is converted in TKE. Moving to the maximum ϕ distribution, it is noteworthy that the D3L10G1 does not show the steep increment close to the duct exit, since the collision length, where the entrainment process is almost zeroed, tends to disappear. On the contrary, the D1.5L10G1 configuration even overcomes the free spray ϕ in that phase. From a general point of view, in non-reacting conditions the lower ϕ_{max} values are reached with the largest D, thus suggesting that the improved entrainment

rate due to both flow area increment and collision length reduction influences more than the enhanced turbulence.

Combustion analysis

The combustion results, in terms of HRR and soot mass traces, for the same spray configurations already analyzed in Fig. 6.16, are reported in Fig. 6.17.

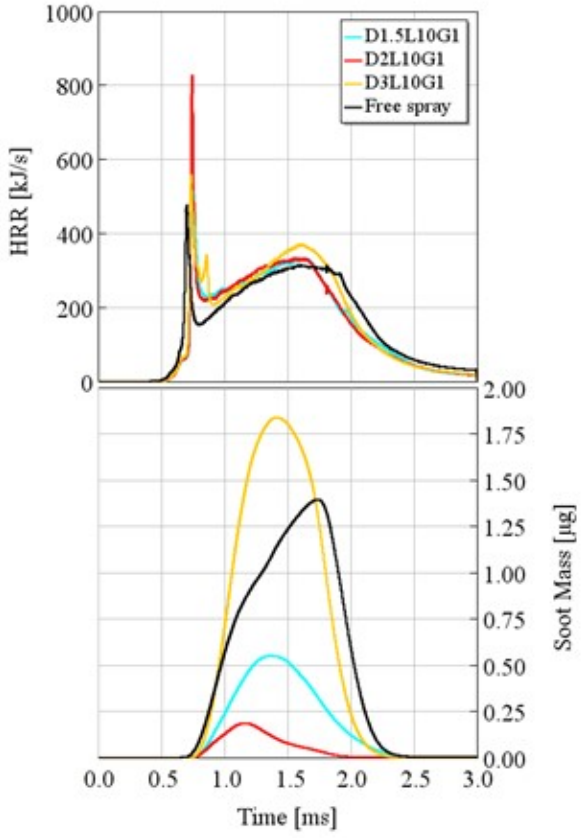

Fig. 6.17 Heat release rate (top) and soot mass in the CVV (bottom) as a function of time for the free spray (black) and the following duct geometries: D1.5L10G1 (cyan); D2L10G1 (red); D3L10G1 (yellow). Test conditions: vessel pressure = 57.3 bar; vessel temperature = 900 K; rail pressure = 1200 bar.

Differently from the abovementioned results, the D3L10G1 duct (yellow) leads to a remarkable higher soot mass not only with respect to the other duct geometries but also to the free spray (black). In particular, it features an average soot mass in the CVV throughout the combustion event about 1.2 times the free spray and even 13.6 times the D2L10G1 (red). On the other hand, the soot mass obtained with the D1.5L10G1 geometry (cyan) is significantly lower than the free spray but more than

twice with respect to the D2L10G1. This result is in line with the reduction of the upstream air entrainment (Fig. 6.15(a)) which inhibits the soot formation mitigation process.

To better understand the soot mass outcomes in Fig. 6.17(bottom), the temperature and soot distribution on a section of the spray flame for the three duct geometries at 1.2 ms aSOI are reported in Fig. 6.18.

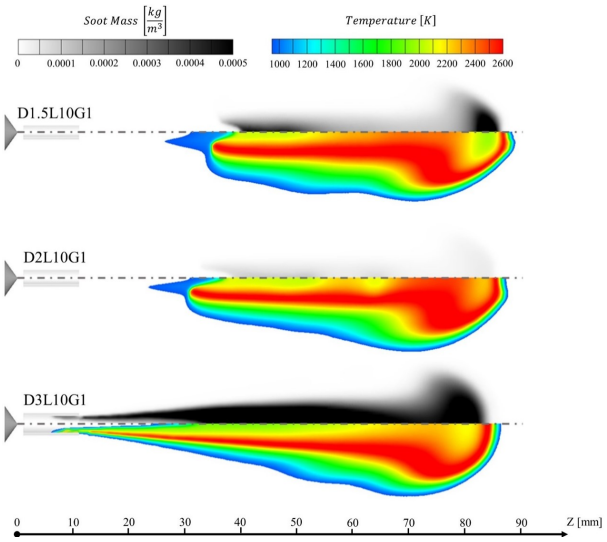

Fig. 6.18 Soot mass and temperature distribution on a section of the spray flame at 1.2 ms aSOI for the following duct geometries: D1.5L10G1 (top); D2L10G1 (middle); D3L10G1 (bottom). Test conditions: vessel pressure = 57.3 bar; vessel temperature = 900 K; rail pressure = 1200 bar.

Comparing the D1.5L10G1 (top) and D2L10G1 (middle), it can be noticed the different soot mass distribution along the spray axis. More specifically, considering Z<70 mm the soot mass is slightly higher for the smallest diameter, confirming that the lower upstream air entrainment leads to higher soot formation, even considering the favorable effect of the longer LOL achieved with the reduced diameter. Focusing on the flame tip (Z>70 mm), the temperature distribution differs: the smallest diameter leads to a temperature in the core of the spray tip below 2000 K, about 300 K lower than the D2L10G1 configuration, thus resulting in a lower oxidation capability. Increasing the duct diameter, D3L10G1 (bottom), the combustion starts within the duct volume as shown by the temperature contour plot, preventing any additional entrainment and mixing at the duct outlet, causing a remarkable soot increment. Furthermore, the premature combustion deteriorates both the first stage turbulent mixing, due to the shorter in-duct mixing length linked to the LOL reduction, and the upstream air entrainment, due to the in-duct pressure rise given by combustion

[52]. This result confirms the outcomes highlighted in [29], where the drawbacks associated with an in-duct combustion event were experimentally demonstrated. A possible explanation of the in-duct combustion onset for the D3L10G1 geometry is illustrated in Fig. 6.19, in which the pressure field, the liquid drops distribution and the streamlines at the duct inlet and outlet on a spray longitudinal section are reported at 1.2 ms aSOI, for the previously shown three duct configurations.

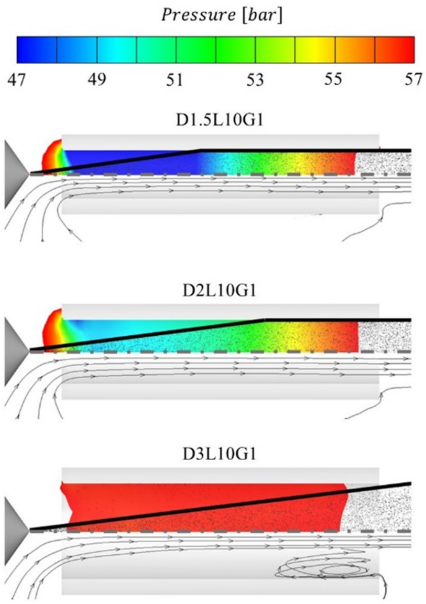

Fig. 6.19 Pressure field, liquid drops distribution and streamlines at duct inlet and outlet on a section of the spray at 1.2 ms aSOI for the following duct geometries: D1.5L10G1 (top); D2L10G1 (middle); D3L10G1 (bottom). Test conditions: vessel pressure = 57.3 bar; vessel temperature = 900 K; rail pressure = 1200 bar.

As said before (Fig. 6.15(c)), the in-duct pressure distributions are definitely affected by the duct diameter variation but the in-duct pressure remains always lower than the CVV one. Focusing on Fig. 6.19(bottom), it can be observed that the collision length of the D3L10G1 case tends to zero, thus the expected DFI dynamic changes, being absent the spray/wall interaction. In particular, the gap between spray and wall at the duct outlet leads to a reverse air flow pumped downstream of the duct. This backflow causes the formation of some eddies inside the duct, leading to the stagnation of fuel vapors which, once depleted the ignition delay, burn and establish a spray flame starting upstream of the duct exit.

In Fig. 6.20, the scalar soot mass GxL contour plots are reported for D=1.5 mm, D=2 mm (zoomed in from Fig. 6.14) and D=3 mm in the form of percentage reduction with respect to free spray.

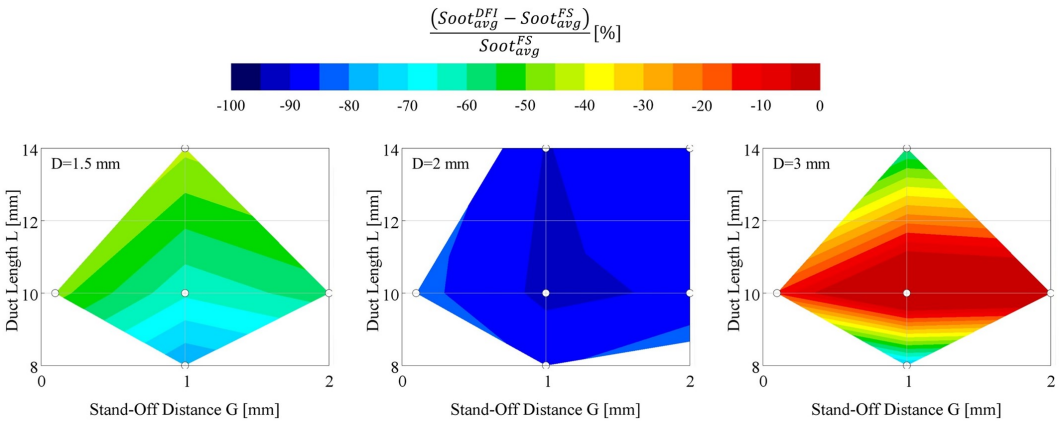

Fig. 6.20 Contour plots of the average soot mass in the CVV as a function of G and L in the form of percentage reduction with respect to free spray for ducts with D=1.5 mm (left), D=2 mm (middle) and D=3 mm (right). Test conditions: vessel pressure = 57.3 bar; vessel temperature = 900 K; rail pressure = 1200 bar.

Starting from D=1.5 mm (Fig. 6.20, left), although the soot reduction is less pronounced than the D=2 mm configuration (Fig. 6.20, middle), DFI remains effective in breaking down the soot formation, leading to an average soot mass reduction of more than 40% for each duct configuration. As for the whole D=2 mm contour plot (Fig. 6.14), DFI becomes more effective reducing G (until the upstream air entrainment starts to drastically reduce) and L (to advance the turbulent mixing and the air entrainment downstream of the duct). In this case, the optimal configuration features L=8 mm reaching approximately 80% of soot mass reduction with respect to free spray. Focusing on the D=3 mm case (Fig. 6.20, right), 3 configurations out of 5, featuring L=10 mm, show the combustion event inside the duct volume. As already pointed out, the DFI entrainment and mixing benefits are lost leading to an overall air-fuel mixing process worse than the free spray configuration. Varying L, DFI is again effective in reducing soot emission, with an abatement of about 80% for L=8 mm configuration, and 60% for L=14 mm. Referring to Fig. 6.19, the former case even further prevents the collision length establishment, manifesting that DFI could also work without spray/wall interaction; the latter instead newly establishes the collision length due to the longer L and DFI can work as expected.

6.2.3 Effect of duct shape

Non-reacting analysis

Different inlet (blunt duct) and outlet (tapered duct) geometries were tested exclusively on the optimal duct configuration of previous results based on a sharp geometry (i.e. D2L10G1). The upstream air entrainment results at 0.3 ms aSOI for the three analyzed duct shapes are reported as a bar chart in Fig. 6.21.

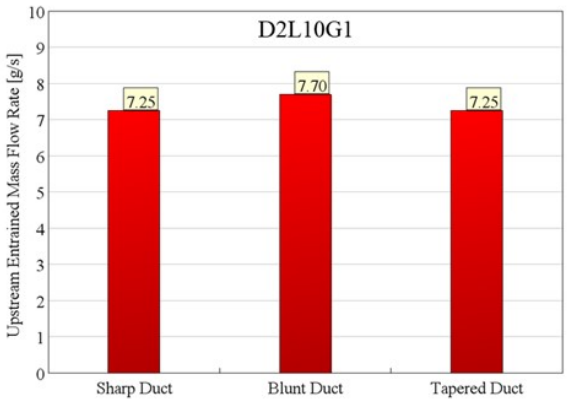

Fig. 6.21 Upstream air entrainment at 0.3 ms aSOI for three different duct shapes (D2L10G1 geometry), defined in Fig. 6.2: sharp duct (left); blunt duct (middle); tapered duct (right). Test conditions: vessel pressure = 20.0 bar; vessel temperature = 773 K; rail pressure = 1200 bar.

The blunt duct improves the air entrainment upstream of the duct by about 6% with respect to the sharp duct, while the tapered duct does not affect it at all, as expected. In particular, the blunt inlet shape does not significantly change the in-duct pressure distribution but, on one hand, increases the minimum flow section and, on the other hand, improves the incoming flow directionality. As far as the turbulent mixing is concerned, no substantial differences were detected in non-reacting conditions changing the duct shape, thus, the results are not reported.

Combustion analysis

The LOL and the maximum and average ϕ at LOL at 1.2 ms aSOI are reported in Fig. 6.22 to evaluate the three duct shapes in reacting conditions. The blunt duct geometry extends the LOL with respect to the other two (Fig. 6.22, top), thereby improving the downstream air entrainment as well (Fig. 6.22, top). On the other side, the tapered

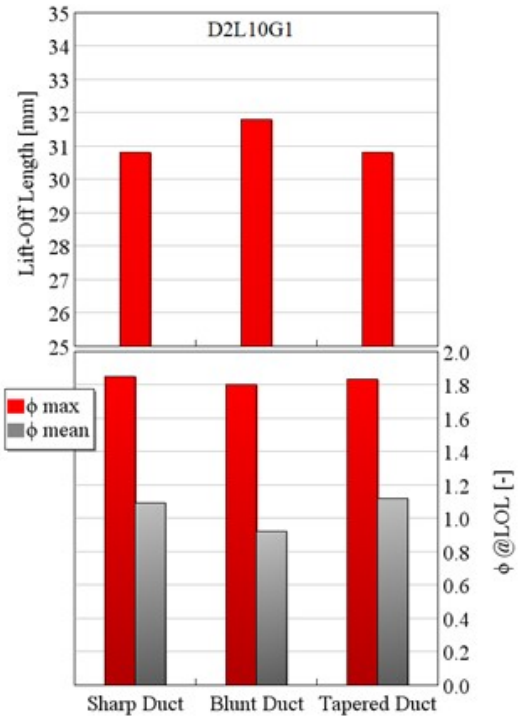

Fig. 6.22 Lift-off length (top) and equivalence ratio (bottom) at the LOL at 1.2 ms aSOI for three different duct shapes (D2L10G1 geometry), defined in Fig. 6.2: sharp duct (left); blunt duct (middle); tapered duct (right). Both maximum (red) and average (grey) equivalence ratios are illustrated. Test conditions: vessel pressure = 57.3 bar; vessel temperature = 900 K; rail pressure = 1200 bar.

duct features no significant variation with respect to the sharp one. To evaluate the effect of the different ϕ at LOL caused by the duct geometry modification, the HRR and soot mass traces related to the three duct shapes and free spray are reported in Fig. 6.23. Even if the HRR traces (Fig. 6.23, top) are practically overlapped for each duct configuration, some differences can be highlighted in terms of soot (Fig. 6.23, bottom). Because of the higher upstream air entrainment, the extended LOL and the consequent ϕ reduction, the blunt duct (red dotted line) leads to a further improvement in soot mitigation with respect to the sharp duct (red continuous line), reaching 94% of average soot mass reduction in comparison with conventional injection. On the contrary, the tapered duct (red dashed line) does not significantly modify the results already obtained with the sharp shape.

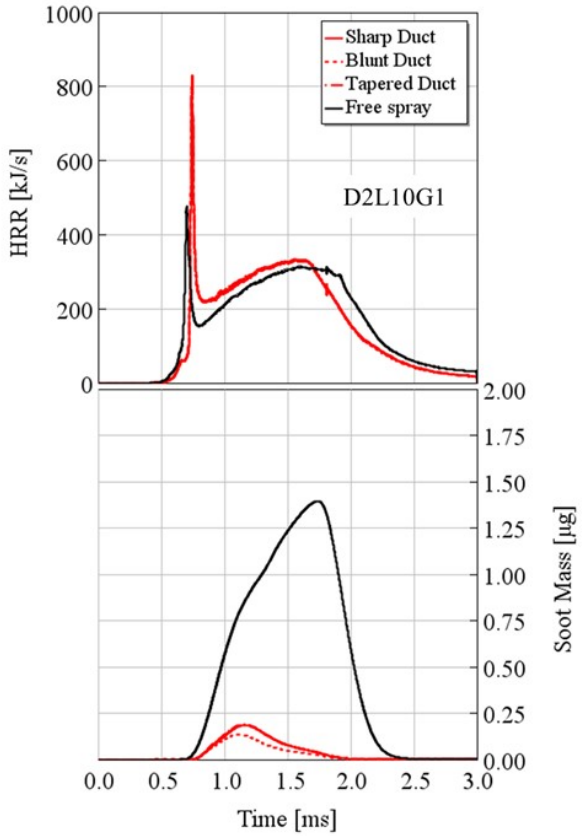

Fig. 6.23 Heat release rate (top) and soot mass in the CVV (bottom) as a function of time for the free spray (black) and three different duct shapes (D2L10G1 geometry), defined in Fig. 6.2: sharp duct (red continuous line); blunt duct (red dotted line); tapered duct (red dashed line). Test conditions: vessel pressure = 57.3 bar; vessel temperature = 900 K; rail pressure = 1200 bar.

6.3 Optimal DFI configuration

A comparison between free spray and optimal DFI configuration (D2L10G1 – Blunt) in terms of equivalence ratio and TKE distribution on a spray longitudinal section in non-reacting conditions is reported in Fig. 6.24. Looking at the bottom side of each spray, DFI features a significant TKE enhancement not only inside the duct volume but also downstream of the duct exit in which the established high recirculating turbulent mixing zone more than doubles the TKE with respect to the free spray. Moving to the top side of each spray, DFI strongly affects the equivalence ratio distribution inside the duct: on one hand, the upstream air entrainment (improved through the chamfer at the duct inlet) reduces the maximum value; on the other hand, the higher mixing leads to an overall homogeneity, also avoiding the radial

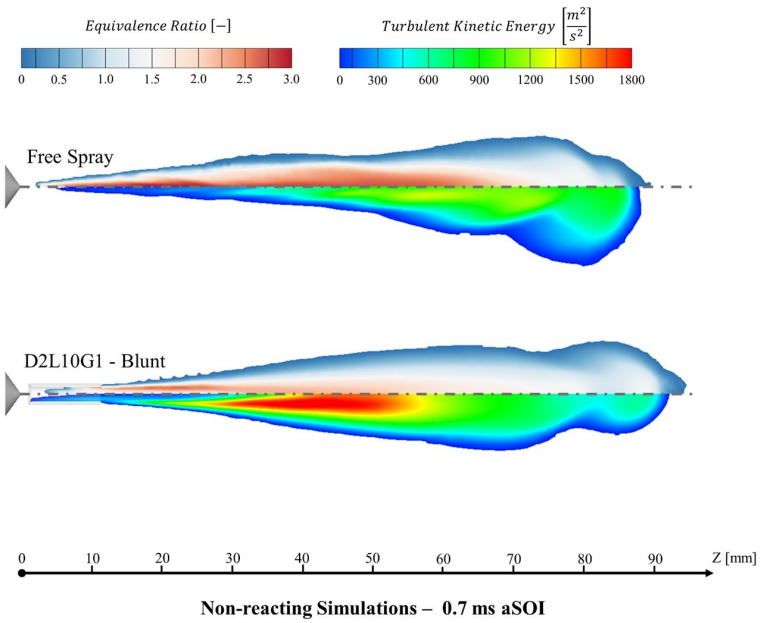

Fig. 6.24 Equivalence ratio and TKE distribution on a section of the spray at 0.7 ms aSOI for free spray (top) and DFI (bottom) featuring the optimized duct configuration (D2L10G1; blunt inlet). Test conditions: vessel pressure = 20.0 bar; vessel temperature = 773 K; rail pressure = 1200 bar.

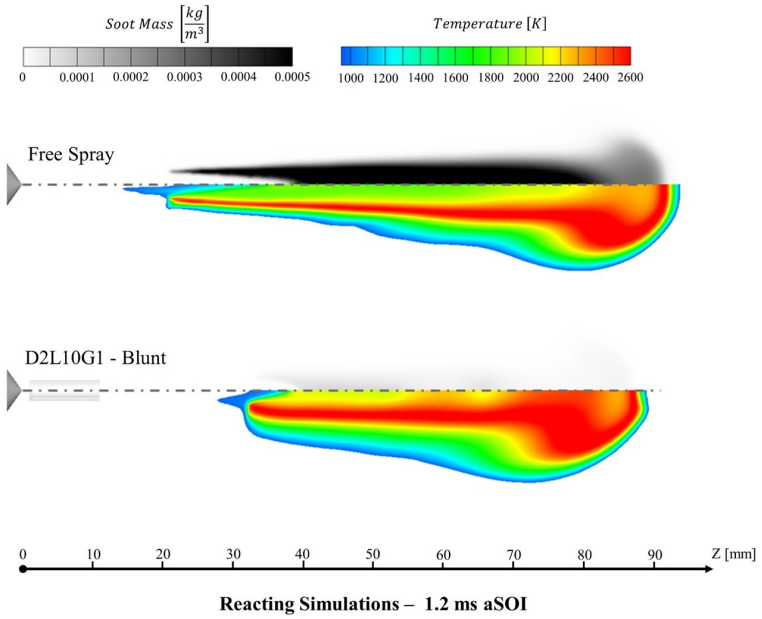

Fig. 6.25 Soot mass and temperature distribution on a section of the spray flame at 1.2 ms aSOI for free spray (top) and DFI (bottom) featuring the optimized duct configuration (D2L10G1; blunt inlet). Test conditions: vessel pressure = 57.3 bar; vessel temperature = 900 K; rail pressure = 1200 bar.

ϕ distribution typical of the free spray. The relatively short collision length of this duct geometry limits the drawbacks on the equivalence ratio associated with the temporary air entrainment inhibition. At the duct exit, the second turbulent mixing phase continues to homogenize the equivalence ratio field, leading to much lower ϕ values than the free spray.

In Fig. 6.25, a comparison between free spray and optimal DFI configuration (D2L10G1 – Blunt) in terms of temperature and soot distribution on a section of the flame is reported. By using this duct geometry, DFI features a definitely longer LOL, a more compact and high-temperature flame, which allow almost zero-soot diesel combustion compared to the high-soot free spray flame.

Chapter 7

DFI investigation with RANS: engine operating parameter sensitivity analysis

Part of the work described in this chapter was previously published in:

- Millo, F., Piano, A., Peiretti Paradisi, B., Postrioti, L., Pieracci, L., Bianco, A., Pesce, F.C. and Vassallo, A.L., "Ducted Fuel Injection: Experimental and numerical investigation on fuel spray characteristics, air/fuel mixing and soot mitigation potential," *Fuel*, Volume 289, 2021, doi:1016/j.fuel.2023.128110.
- Millo, F., Segatori, C., Piano, A., Peiretti Paradisi, B. and Bianco, A., "An Engine Parameters Sensitivity Analysis on Ducted Fuel Injection in Constant-Volume Vessel Using Numerical Modeling," *SAE Technical Paper* 2021-24-0015, 2021, doi:10.4271/2021-24-0015.

The present chapter aims at analysing the influence of several engine operating parameters on DFI combustion, having free spray results as a reference, by employing the developed RANS turbulence model and by using the optimized duct geometry defined in chapter 6. For this purpose, since the model has been validated only on a single operating condition so far (Table 3.1), the developed virtual test rig is preliminary subject to an extensive validation against experimental liquid penetration considering most of the operating conditions examined in the experimental campaign (Table 2.4). In this way, it has been proven the capability of the RANS model

in predicting the effects of rail pressure, temperature and density variations, at least in non-reacting conditions. Then, the impact of rail pressure, air density, oxygen concentration is analysed through several sweeps in reacting conditions, defining some preliminary DFI calibration requirements. Furthermore, the duct wall temperature influence is investigated in order to preliminary explore the needs in terms of duct thermal management.

7.1 Methodology

The engine operating parameter sensitivity analysis was carried out on the commercially available software CONVERGE CFD 2.4 [134]. The same RANS-based model previously defined and investigated in non-reacting and reacting conditions has been employed. Please, refer to chapters 4 and 5 for details on the 3D-CFD setup not mentioned throughout this section.

7.1.1 Model validation for different operating conditions

Since the model was validated against experimental data considering only one test reference condition so far, the validation in the RANS framework was extended to most of the experimental test matrix (Table 2.4), for both free spray and DFI. Only the experimental data at 400 bar rail pressures were excluded, since less relevant for diesel engine applications. In Figs. 7.1, 7.2, 7.3 and 7.4, the liquid penetration curves comparison between experiments and simulation results for free spray and ducted jet, considering two rail pressure levels (800 and 1200 bar), two vessel pressures (10 and 20 bar) and two vessel temperatures (573 and 773 K), is shown. The experimental liquid penetration curve is presented in terms of averaged values of twenty scans. Two different grey boxes were added on each plot: on one side, since the duct was not optically accessible, no comparison can be made within it; on the other side, the experimental imaging window length limits the comparison at 50.0 mm.

A more than satisfactory agreement between experiments and simulations could be highlighted for both free spray and DFI configurations. A slight discrepancy can be observed close to the imaging limit, especially at higher vessel temperatures (Figs. 7.2 and 7.4); however the error was considered as acceptable for engine applications taking into account the typical piston bore size. In addition, the DFI ability to increase the liquid penetration rate is experimentally confirmed in all the

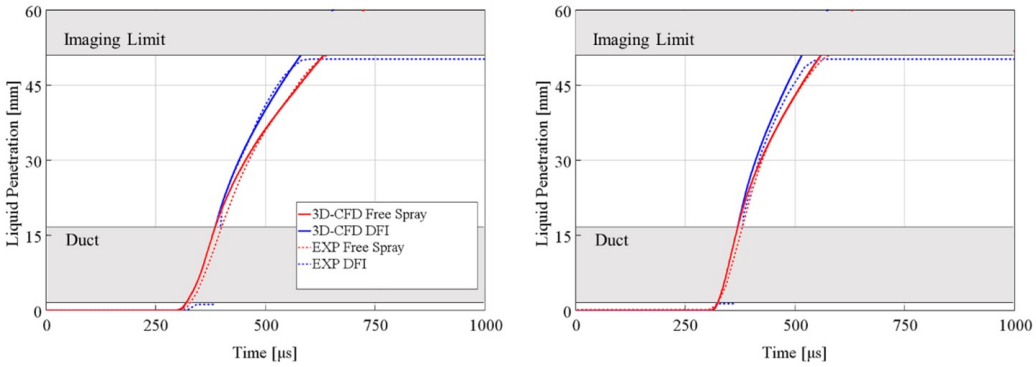

Fig. 7.1 Liquid penetration curve for the free spray (red) and DFI (blue) configurations: numerical results (solid lines) compared with experimental data (dotted lines). Test conditions: rail pressure = 800 bar (left) – 1200 bar (right); vessel pressure = 10 bar, vessel temperature = 573 K.

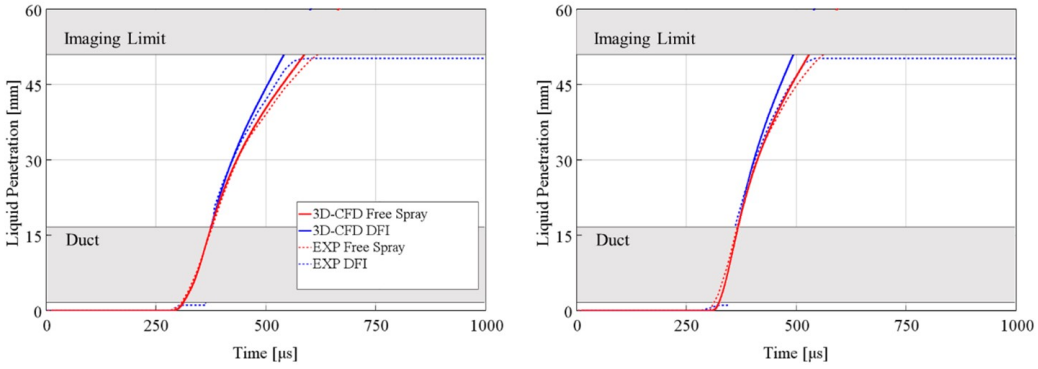

Fig. 7.2 Liquid penetration curve for the free spray (red) and DFI (blue) configurations: numerical results (solid lines) compared with experimental data (dotted lines). Test conditions: rail pressure = 800 bar (left) – 1200 bar (right); vessel pressure = 10 bar, vessel temperature = 773 K.

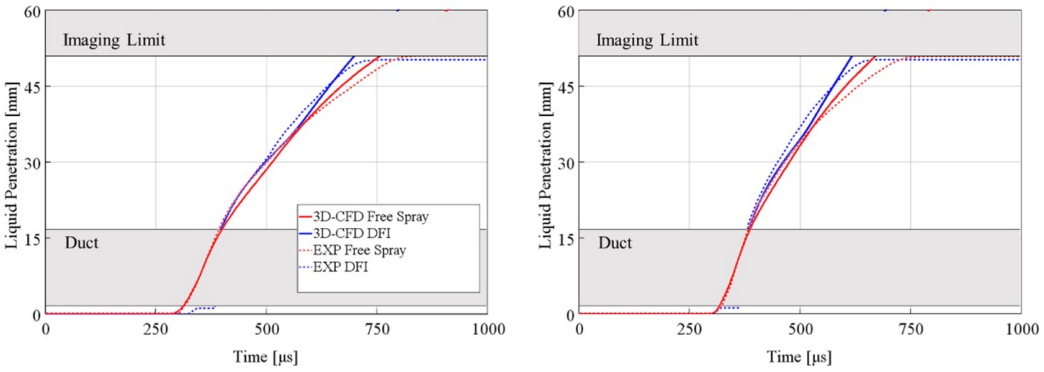

Fig. 7.3 Liquid penetration curve for the free spray (red) and DFI (blue) configurations: numerical results (solid lines) compared with experimental data (dotted lines). Test conditions: rail pressure = 800 bar (left) – 1200 bar (right); vessel pressure = 20 bar, vessel temperature = 573 K.

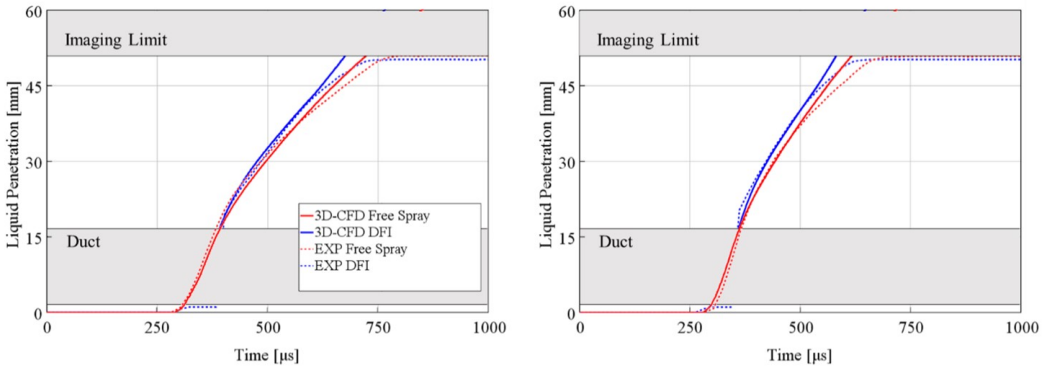

Fig. 7.4 Liquid penetration curve for the free spray (red) and DFI (blue) configurations: numerical results (solid lines) compared with experimental data (dotted lines). Test conditions: rail pressure = 800 bar (left) – 1200 bar (right); vessel pressure = 20 bar, vessel temperature = 773 K.

tested conditions, and correctly reproduced by the developed 3D-CFD numerical model. Given these conclusions, the spray model was considered robust enough to parametrically analyse the DFI technology under different operating conditions, towards the definition of preliminary calibration requirements.

7.1.2 Test matrix and duct design

For the present analysis, the optimal duct geometry (D2L10G1) resulted from chapter 6 was employed, with the idea of assessing the robustness of the design optimization process when working conditions are varied. For the sake of clarity, the optimized duct geometry is represented in Fig. 7.5.

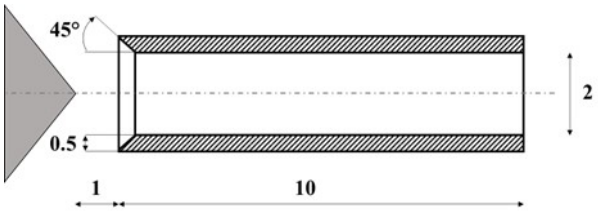

Fig. 7.5 Duct design employed for the engine operating parameter sensitivity analysis (distances in [mm]).

Several operating parameters sweeps were performed for investigating their effect on DFI combustion, always having the free spray results as a reference. The sweeps object of the analysis are summarized in Table 7.1.

The reference baseline condition, indicated in the first line, was the same employed for the reacting simulations in chapters 5 and 6. The simulation activity was then carried out evaluating the effect of the variation of every single parameter (primary variable variation, highlighted in yellow), while keeping constant and equal to the baseline value all the others when possible (if not, the secondary variable variation is highlighted in red). More in detail, the rail pressure (P_{rail}) sweep was performed varying the mass flow rate according to the rail pressure level and keeping constant the injection duration, thus changing the injected mass. Focusing on the dilution sweep, the reduction in oxygen (O_2) concentration with respect to the baseline value of 21% was achieved by substituting the O_2 fraction with CO_2 and H_2O, to simulate the EGR system of a CI engine burning N-C_7H_{16}. As far as the vessel density (ρ_{vessel}) is concerned, its variation was obtained acting on ambient pressure (ranging between 57.3 bar and 129.2 bar) while maintaining the vessel temperature

Table 7.1 Engine operating parameters sweeps. Primary variable highlighted in yellow, secondary variable highlighted in red.

Test name	O_2 %	ρ_{vessel} kg/m^3	T_{vessel} K	P_{rail} bar	DOI ms	m_{inj} mg	T_{duct} K
Baseline	21.0	22.2	900	1200	1.5	11.85	900
P_{rail} sweep	21.0	22.2	900	800 1600 2000	1.5	9.65 13.50 15.09	900
O_2 sweep	16.5 18.0 19.5	22.2	900	1200	1.5	11.85	900
ρ_{vessel} sweep	21.0	30.0 40.0 50.0	900	1200	1.5	11.85	900
T_{duct} sweep	21.0	30.0 40.0 50.0	900	1200	1.5	11.85	700 1100

equal to 900 K. Finally, the impact of duct temperature (T_{duct}), maintained homogeneous and constant, was assessed for each vessel density condition. In particular, the duct temperature was both increased and lowered by 200 K starting from the baseline value of 900 K. The lowest duct temperature (700 K) was evaluated to simply mimic a duct temperature decreased by a proper cooling system, while the highest duct temperature (1100 K) was chosen to be representative of an injection immediately subsequent to a combustion event, without enough time to stabilize again the duct temperature to the ambient value, as in an engine combustion chamber case.

7.2 Results

7.2.1 Effect of rail pressure

The impact of rail pressure on combustion and soot formation was studied by comparing DFI and free spray for four different rail pressure levels, ranging from 800 bar to 2000 bar. In Fig. 7.6 the ID, the CD, the LOL and the average soot mass are reported for both free spray and DFI configurations, as a function of rail pressure.

These parameters were computed according to same modeling standards explained in chapters 5 and 6.

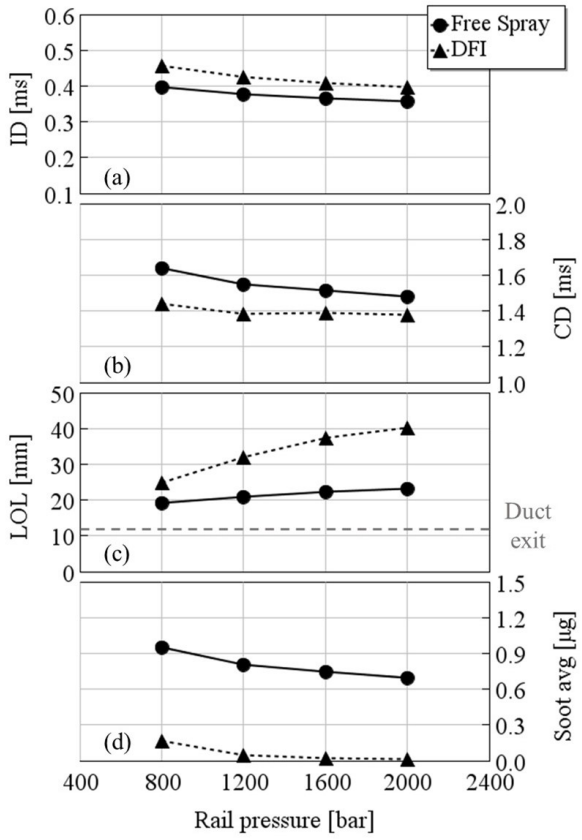

Fig. 7.6 Ignition delay (a), combustion duration (b), lift-off length (c) and average soot mass (d) as a function of rail pressure level for free spray (dots – solid line) and DFI (triangles – dashed line). Test conditions: vessel temperature = 900 K; vessel density = 22.2 kg/m^3; oxygen concentration = 21%.

Focusing on the ID (Fig. 7.6(a)), DFI (triangles – dashed line) shows a slightly longer ID with respect to free spray (circles – solid line), maintaining a quite constant difference for all the rail pressure range. As expected, both free spray and DFI tend to reduce the ID for a rail pressure increase, thanks to the accelerated vaporization process.

Moving to the CD (Fig. 7.6(b)), the higher the rail pressure, the shorter the combustion duration for both free spray and DFI. However, for high rail pressures, the CD tends to stabilize, as a trade-off among the higher injected mass, shorter ID and more intense mixing. DFI shows more rapid combustion for the whole rail pressure range, well-correlated with the higher premixing level associated with

longer ID. Free spray and DFI curves are weakly converging when the rail pressure increases for both the ID and the CD.

Concerning the flame LOL (Fig. 7.6(c)), DFI features a longer LOL with respect to free spray, showing a gap increment at a higher level of rail pressure. Indeed, the curves show a relatively low difference (about 5 mm) at 800 bar and then almost double the LOL with the duct adoption at 2000 bar. Therefore, although the rail pressure increment leads to significant benefits in terms of LOL extension for both cases, the DFI configuration remarkably enhances this behavior.

Moving to the soot mass in the CVV (Fig. 7.6(d)), DFI impressively reduces the soot mass for the whole rail pressure range, achieving practically zero soot at 1600 bar and 2000 bar. In general, the DFI soot reduction with respect to free spray ranges between about 85% at 800 bar and 100% at 2000 bar. It is noteworthy that also the DFI@800 bar case features a soot mass reduction of approximately 80% with respect to the free spray@2000 bar case, suggesting that the duct adoption impacts much more than the rail pressure on the soot mitigation performance. Furthermore, since both the abovementioned cases show the same LOL (approximately 24-25 mm), the simple LOL extension provided by DFI cannot completely explain the observed soot reduction by itself, but other mechanisms must contribute and need to be clarified.

To analyse the air entrainment and the turbulent mixing as in previous chapters, the former was again quantified as the air mass flow rate crossing an iso-surface contouring the spray plume and longitudinally dividing the spray into two zones as in Fig. 6.10: “upstream” is referred to the air entering the spray area between the injector tip and the axial point of contact between spray and duct wall; “downstream” is referred to the air entering the spray area between the duct exit and the LOL. It is noteworthy that for the free spray configuration, being absent the duct solid wall, the downstream air entrainment begins exactly where the upstream ends. Regarding the turbulent mixing, it was evaluated using as an index the maximum TKE in the spray plume before the LOL. In Fig. 7.7 the upstream air entrainment, the downstream air entrainment and the maximum TKE for the whole spray before reaching the LOL are reported as a function of the rail pressure level for both free spray and DFI. The results are illustrated at 1.2 ms aSOI, namely in the middle of the MC combustion phase, when pseudo-stationary conditions are reached.

The upstream air entrainment (Fig. 7.7, top) rises when the rail pressure increases for both free spray (circles – solid line) and DFI (triangles – dashed line), due to the higher jet velocity which retrieves a larger amount of air. However, the difference

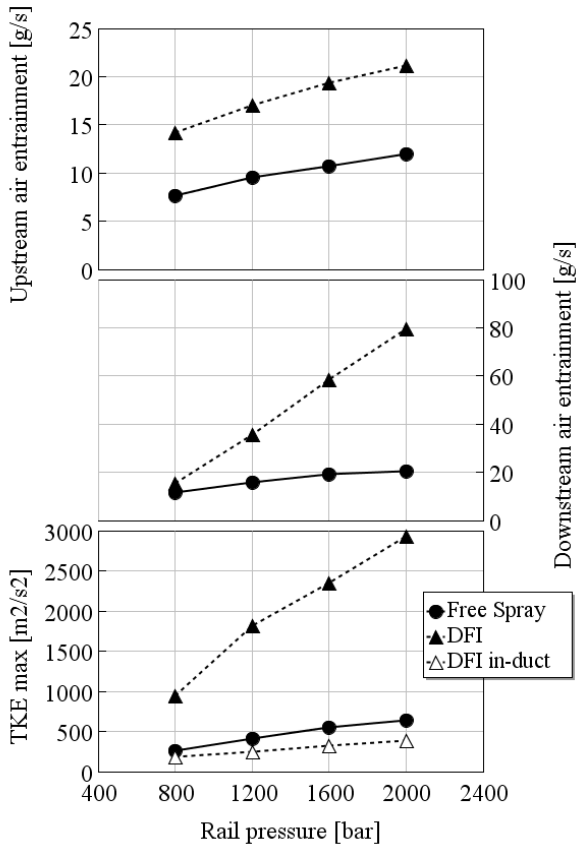

Fig. 7.7 Upstream (top) and downstream (middle) air entrainment into the fuel spray and maximum turbulent kinetic energy (bottom) at 1.2 ms aSOI as a function of rail pressure level for free spray (dots – solid line) and DFI (triangles – dashed line). Test conditions: vessel temperature = 900 K; vessel density = 22.2 kg/m^3; oxygen concentration = 21%.

between DFI and free spray increases with the rail pressure: in fact, DFI upstream air entrainment effectiveness is driven by the conversion of pressure energy in kinetic energy inside the duct which causes the formation of the in-duct low-pressure zone. This conversion is enhanced with faster jets, which are obtained thanks to higher rail pressure levels, thus leading to lower in-duct pressure. Focusing on the DFI@800 bar case, it shows upstream air entrainment even higher than the free spray at 2000 bar, partially justifying the huge soot reduction observed in Fig. 7.6(d).

The downstream air entrainment (Fig. 7.7, middle) shows similar values for both free spray and DFI at 800 bar but strongly diverges when rail pressure is increased. In Fig. 6.11, the mass flux (i.e. mass flow rate per spray area unit) downstream of the duct was evaluated and no large differences were observed between free spray and DFI; therefore, the gap is mainly linked to the different LOL reached. In particular, at 800 bar the air mass flow rates coincide despite the different LOL extension,

because of the presence of the collision length with DFI (i.e., fuel spray impinges on internal duct wall) which initially inhibits the air entrainment. Then, increasing the rail pressure from 800 bar, the axial distance of air entrainment prevention inside the duct becomes negligible, compared to the LOL extension. As a consequence, a four times higher downstream air entrainment is obtained for DFI at 2000 bar than in the corresponding free spray case.

Focusing on the mixing process, Fig. 7.7 (bottom) shows the TKE max index for free spray and DFI both in the whole domain (filled circles and triangles, respectively) and inside the duct (empty triangles), to provide also an indication of the first stage of DFI turbulent mixing process. DFI maximum TKE values are remarkably higher than the free spray ones, and the difference increases with the rail pressure: DFI about triples the maximum TKE at 800 bar, while achieves 5 times higher values at 2000 bar. Indeed, the free spray maximum TKE increases with rail pressure mainly due to the LOL extension; on the contrary, DFI second stage turbulent mixing is also strongly enhanced by the higher velocity gradients at the duct exit (main drivers for the formation of intense vortices downstream of the duct), which extensively rise with higher injection velocities. Furthermore, an additional contribution to the maximum TKE is given by the first stage turbulent mixing at high rail pressure levels: the in-duct maximum TKE (empty triangles – dashed line) about linearly increase with rail pressure, due to the higher jet velocity which raises the Reynolds number and causes the establishment of a more intense in-duct turbulent regime. It is noteworthy that the maximum level of TKE reached inside the duct is similar to the level reached in the correspondent free spray configuration, although the former is referred to a much more advanced spray axis location. In other words, the DFI first stage turbulent mixing process alone would be almost enough to reach the same mixing levels of the free spray, while the second stage turbulent mixing (which is the most beneficial DFI mixing phase) becomes the real driver of the mixing enhancement. Also in this case, comparing the DFI at 800 bar and the free spray at 2000 bar, it can be observed that the former features a maximum TKE almost doubled with respect to the latter, thus explaining the soot formation outcome shown in Fig. 7.6(d).

Finally, the equivalence ratio (ϕ) distribution at LOL on a longitudinal section of the spray is reported as a function of radial distance from spray axis in Fig. 7.8 for both free spray and DFI at each evaluated rail pressure level.

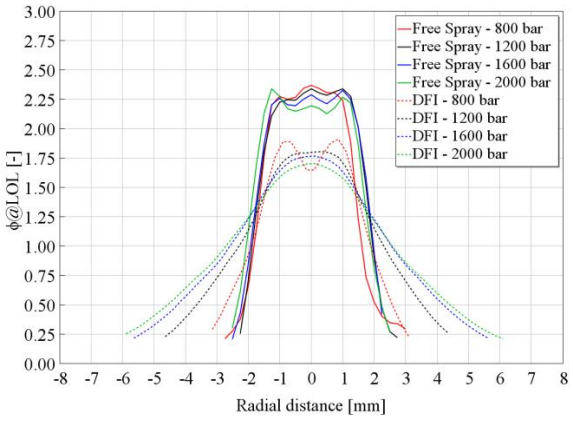

Fig. 7.8 Equivalence ratio distribution at the lift-off length on a longitudinal section of the spray at 1.2 ms aSOI for free spray (solid line) and DFI (dashed line) at different rail pressure levels: 800 bar (red), 1200 bar (black), 1600 bar (blue), 2000 bar (green). Test conditions: vessel temperature = 900 K; vessel density = 22.2 kg/m^3; oxygen concentration = 21%.

Focusing on the free spray configurations (solid lines), the rail pressure increment tends to decrease the ϕ in the core of the jet at the LOL, maintaining a similar distribution on the peripheries with approximately equal spray confinement (the longer LOL counterbalances the effect of higher confinement when the rail pressure is increased). On the other side, the DFI sprays (dashed lines) are affected by the rail pressure variation in terms of equivalence ratio both at the core and periphery of the jet. Indeed, the higher rail pressure results, on one hand, in a lower ϕ into the spray core and, on the other hand, to a wider spray distribution due to a much longer LOL which tends to enlarge the spray section. When the LOL is quite close to the duct exit, as for the 800 bar case (red dashed line), the distribution features a peculiar shape with a double peak, because it is still affected by the presence of the duct wall, along which the air entrainment is inhibited (i.e. along the duct collision length). It is noteworthy how each DFI distribution is lower and wider with respect to the free spray ones, consistently with the soot formation outcome of Fig. 7.6(d). In conclusion, DFI is characterized by ϕ values at the LOL always lower than 2, which lead to a close-to-zero soot mass thanks to the enabling of the LLFC.

7.2.2 Effect of oxygen concentration

The oxygen volumetric concentration in the test vessel was varied from 21.0% (ambient air) to 16.5%. No further oxygen reduction was tested to avoid the enabling of different combustion regimes (e.g. low temperature combustion [18]), given

that DFI is conceived to work in MC combustion mode [29]. In Fig. 7.9 the ID, the CD, the LOL and the average soot mass are reported as a function of oxygen concentration, comparing free spray and DFI.

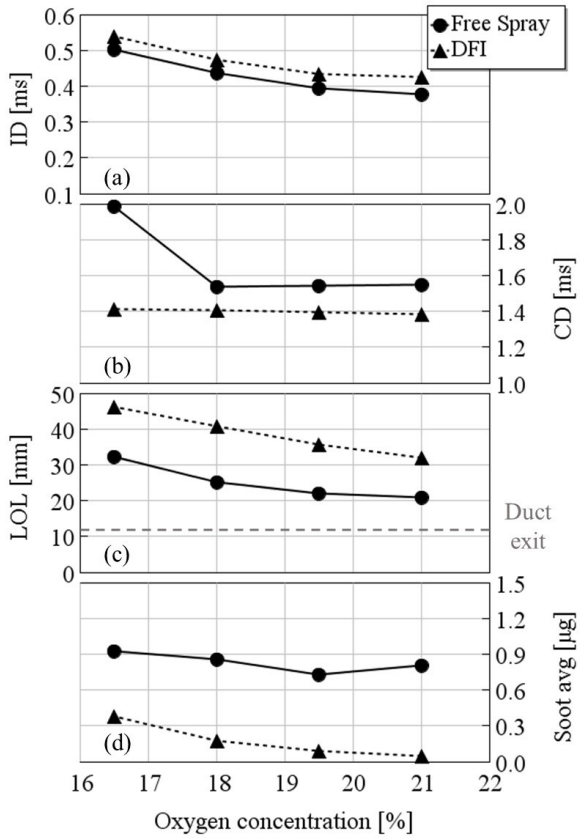

Fig. 7.9 Ignition delay (a), combustion duration (b), lift-off length (c) and average soot mass (d) as a function of oxygen volumetric concentration for free spray (dots – solid line) and DFI (triangles – dashed line). Test conditions: vessel temperature = 900 K; vessel density = 22.2 kg/m^3; rail pressure = 1200 bar.

The ID (Fig. 7.9(a)), which is longer for lower oxygen availability, is higher for DFI (triangles – dashed line) with respect to free spray (circles – solid line) for the whole tested range; the ID values tend to approach each other for lower oxygen concentrations.

The CD (Fig. 7.9(b)), apart from the free spray – 16.5% case, is quite constant varying the oxygen concentration for both free spray and DFI. Indeed, the slowdown of the combustion process given by the shortage of oxygen is counterbalanced by the higher premixing level guaranteed by longer IDs. For the free spray at 16.5%, the increase in the speed of the combustion process due to the more intense premixed combustion phase is not sufficient to counterbalance the slowing effect due to the

lack of oxygen and the CD remarkably increases. Contrarily, with the duct adoption, efficient combustion is ensured also at a low level of O_2. This DFI robustness to dilution could be a crucial aspect for its success on a CI engine, as already highlighted by [66]. In general, as observed for the rail pressure sweep, DFI features faster combustion across the entire tested range.

In terms of LOL (Fig. 7.9(c)), the lower the oxygen availability, the more distant the auto-ignition zone from the injector tip for both free spray and DFI, consistently with the ID trend (spray penetration characteristics not affected by the oxygen variation). Comparing free spray and DFI, the latter is shifted to higher values of LOL for each oxygen concentration, maintaining an almost constant gap of about 10-14 mm with respect to free spray. It is worth pointing out that DFI features a LOL at 21% O_2 which is comparable with the free spray one at 16.5% O_2.

Moving to the average soot mass (Fig. 7.9(d)), the free spray presents a non-linear behavior with dilution. In particular, a minimum of soot mass is reached at 19.5% O_2; then, as expected, it features a higher soot mass when the oxygen concentration is further reduced, despite the longer LOL. Similar considerations can be drawn if the duct is applied, with the soot mass which monotonically increases when oxygen decreases, showing that the longer LOL is not enough to counterbalance the lower oxygen availability. In general, DFI features a largely lower soot mass than free spray for the whole range, with the gap partially reduced at 16.5%. Nonetheless, this case for DFI is characterized by 55% lower soot mass than the free spray at ambient air (21%), highlighting the possibility to employ high EGR rate for NO_x reduction without a significant detrimental effect on soot formation, as already shown by the breakage of the soot/NO_x trade-off with dilution reported in [66].

Upstream and downstream air entrainment and maximum TKE at 1.2 ms aSOI are reported in Fig. 7.10 as a function of the volumetric oxygen concentration for both free spray and DFI. Concerning the upstream air entrainment, the calculated values (reported in black) are not affected by the different oxygen concentrations, air density being equal. To take into account the different oxygen availability, equivalent air entrainment (reported in cyan) is introduced multiplying the resulting mass flow rate for the ratio between the oxygen mass fraction and the ambient air oxygen mass fraction (0.23); the outcome is an effective mass flow rate as if the air was characterized by 21% oxygen concentration. The same considerations were performed for downstream air entrainment.

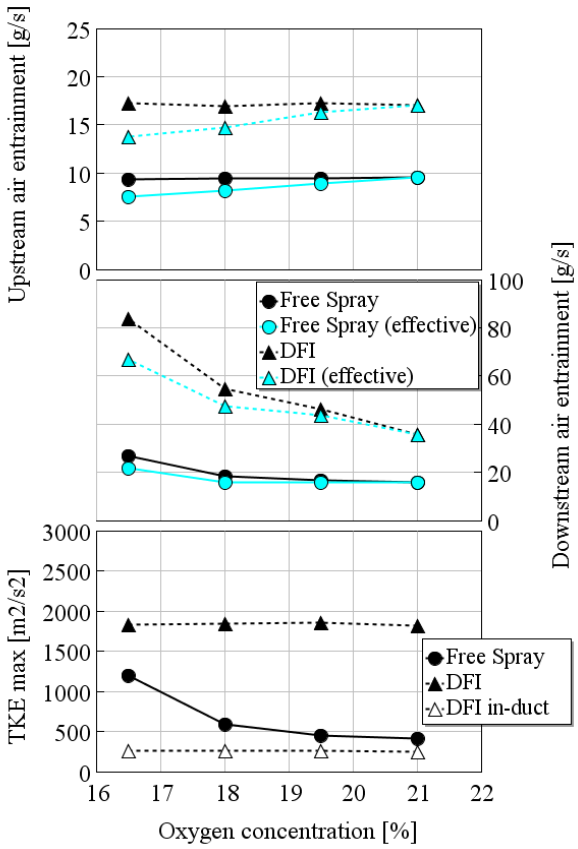

Fig. 7.10 Air entrainment into the fuel spray upstream (top) and downstream (middle) of the duct and maximum turbulent kinetic energy (bottom) at 1.2 ms aSOI as a function of oxygen volumetric concentration for free spray (dots – solid line) and DFI (triangles – dashed line). Test conditions: vessel temperature = 900 K; vessel density = 22.2 kg/m^3; rail pressure = 1200 bar.

As already stated, the upstream air entrainment (Fig. 7.10, top) shows an almost constant trend at different oxygen levels for both free spray (circles – solid line) and DFI (triangles – dashed line). In fact, the air density remains constant together with the spray velocity and the suction effect in the duct is not influenced. However, when the effective values (cyan) are considered, the lower oxygen concentration means a smaller amount of effective air entrainment in the upstream zone. In particular, DFI and free spray slightly converge towards 16.5% but DFI entrainment remains always higher than each free spray value, partially justifying the abovementioned soot mass outcome.

The downstream air entrainment (Fig. 7.10, middle) increases for lower oxygen concentrations due to the longer LOL and the consequent enlargement of the spray cone. Focusing on the effective oxygen availability in free spray configuration,

the downstream air entrainment is approximately constant between 21% and 18%, while slightly increases at 16.5%. Instead, DFI maintains increasing downstream air entrainment with lower oxygen concentration, given the stronger original slope guaranteed by longer LOLs. In general, DFI features higher downstream air entrainment values than free spray for the whole tested range, thus strongly mitigating the soot formation process.

Considering the maximum TKE graph (Fig. 7.10, bottom), the free spray turbulent mixing is higher for lower oxygen concentrations. Indeed, the longer LOL ensures a longer-lasting spray evolution before the ignition. Reducing oxygen concentration, the slight increase in TKE combined with similar air entrainment conditions, can cause a limited reduction in soot mass observed passing from 21% to 19.5% (Fig. 7.9(d)). Moving to DFI, it can be observed that both curves are quite constant across the oxygen concentration range: on one hand, the in-duct behavior (empty triangle) does not manifest any difference in terms of velocity field inside the duct, on the other hand, the overall maximum TKE values (filled triangles) are constant due to the very extended LOLs. Indeed, the maximum TKE behavior as a function of the spray axis in non-reacting conditions features a maximum after a certain distance from the injector tip and, then, falls again towards the spray tip region. Therefore, if the LOL in reacting conditions is higher than the axial location of the maximum TKE, a further LOL extension does not lead to a greater maximum TKE value in the domain. From an overall point of view, DFI features a more intense turbulent mixing over the whole tested oxygen concentration range. However, the TKE difference between DFI and free spray significantly reduces at 16.5% O_2, thus leading to a less pronounced soot mitigation effect. Nevertheless, the still higher turbulence, combined with the more beneficial air entrainment conditions, continue to guarantee an impressive soot mass reduction of about 60% (Fig. 7.9(d)).

In Fig. 7.11 the equivalence ratio distribution at LOL on a longitudinal section of the spray is reported as a function of radial distance from spray axis for both free spray and DFI at each oxygen concentration level tested in this work.

Considering the free spray cases (solid lines), a lower oxygen concentration (from the black to the green line) leads to a wider ϕ distribution (due to the longer LOL) but higher absolute values (due to lower oxygen availability), especially within the spray core. Moving to the DFI cases (dashed lines), the longer LOL at low oxygen concentration causes a wider distribution as well, and higher radial-average ϕ values. However, the higher homogenization capability of DFI (due to the intense

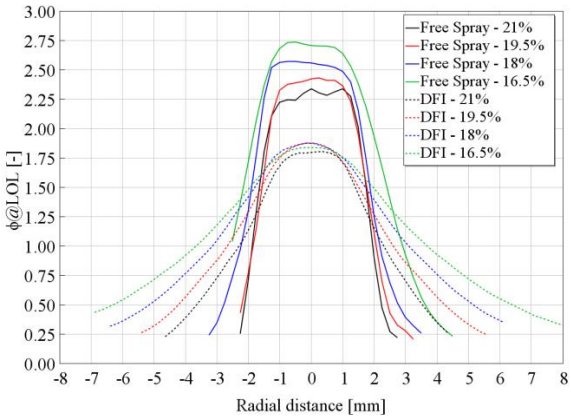

Fig. 7.11 Equivalence ratio distribution at the lift-off length on a longitudinal section of the spray at 1.2 ms aSOI for free spray (solid line) and DFI (dashed line) at different oxygen volumetric concentrations: 21.0% (black), 19.5% (red), 18.0% (blue), 16.5% (green). Test conditions: vessel temperature = 900 K; vessel density = 22.2 kg/m^3; rail pressure = 1200 bar.

turbulent mixing) and the strongly growing downstream air entrainment ensure similar maximum ϕ values (i.e. in the spray core), thus maintaining relatively low soot mass even at 16.5% (Fig. 7.9(d)).

7.2.3 Effect of air density

The air density in the CVV was gradually increased from the baseline conditions (22.2 kg/m^3) up to 50 kg/m^3 (representative of high load engine conditions) to understand if and how it affects DFI operation comparatively to free spray. In Fig. 7.12 the ID, the CD, the LOL and the average soot mass are reported for both free spray and DFI as a function of the vessel density.

The ID (Fig. 7.12(a)) is highly influenced by the air density increment, showing a significant reduction for both free spray (circles – solid line) and DFI (triangles – dashed line) due to the evaporation and mixing enhancements. DFI curve is shifted upward for the whole tested range but the gap decreases when the density increases, reaching an ID almost equal to free spray at 50 kg/m^3.

The CD (Fig. 7.12(b)) monotonically increases for DFI, while stabilizes at about 1.6 ms for free spray from 30 kg/m^3 and above. In general, DFI combustion is always faster, even though it approaches free spray duration when the air density increases, well correlating with the premixing intensity due to ID variations.

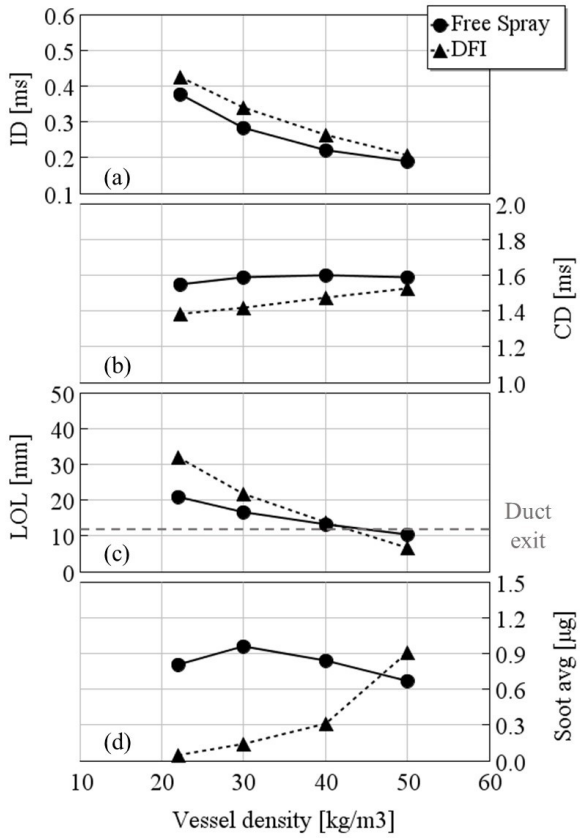

Fig. 7.12 Ignition delay (a), combustion duration (b), lift-off length (c) and average soot mass (d) as a function of vessel density for free spray (dots – solid line) and DFI (triangles – dashed line). Test conditions: vessel temperature = 900 K; rail pressure = 1200 bar; oxygen concentration = 21%.

Focusing on the LOL (Fig. 7.12(c)), the air density increment leads to shorter LOL, but the slope of the curves is much different between free spray and DFI. The latter is more affected by the density increment in terms of LOL shortening: at 22.2 kg/m^3, DFI shows 11 mm longer LOL, while reaching ignition location equal to free spray at 40 kg/m^3. When the density is further increased (50 kg/m^3), DFI features a shorter LOL than free spray. In this latter condition, the ignition is located inside the duct, which should be avoided as widely discussed in previous chapters. Therefore, the duct adoption could limit the density operating range due to the high LOL sensitivity. At 40 kg/m^3, a limit condition is reached for DFI, with the combustion occurring immediately after the duct exit (illustrated with the grey horizontal dashed line). It is noteworthy that DFI LOL in this case is equal to free spray one, despite the longer ID and the well-known faster penetration [33]. Furthermore, at 50 kg/m^3 DFI features even a shorter LOL than free spray at very

similar ignition conditions. It suggests that, when the ignition occurs near or inside the duct, the stabilized LOL tends to progressively shorten, anchoring to the duct region.

Moving to the average soot mass (Fig. 7.12(d)), free spray shows a quite stable behavior across the density range, with a slightly reduced soot mass at 50 kg/m^3 with respect to the baseline. Instead, for DFI the higher the air density, the more sooting the combustion, even overcoming (i.e. +28%) the free spray at 50 kg/m^3, when the combustion occurs inside the duct. In the other density conditions, DFI maintains lower soot mass than free spray ranging from -94% at 22.2 kg/m^3 to -63% at 40 kg/m^3. In this latter operating condition, it is interesting to observe that DFI leads to a strong soot reduction even though the LOL is equal to free spray and anchored to the duct exit, proving once again that the duct adoption cannot be simply classified as a LOL extender technology, but other soot mitigation mechanisms play a crucial role.

Upstream and downstream air entrainment and maximum TKE at 1.2 ms aSOI are reported in Fig. 7.13 as a function of vessel air density for both free spray and DFI.

Leaving aside the in-duct combustion case (DFI at 50 kg/m^3), the upstream air entrainment (Fig. 7.13, top), increases for both free spray and DFI when the air density increases, according to the definition of the mass flow rate. However, the air entrainment increment does not scale exactly with the air density, but the relative variation is damped. Indeed, the higher air density reduces the velocity of the spray, decreasing its capability to retrieve air within the spray. This damping with the density increase is more evident for DFI, whereby the pumping effect enabled by the duct presence plays a role. In particular, this aspect is analyzed in Fig. 7.14, where the in-duct velocity magnitude and the pressure field at 1.2 ms aSOI are reported for the DFI configuration at 30 kg/m^3, 40 kg/m^3 and 50 kg/m^3. Given the different initial vessel pressures, the pressure field is reported in the form of relative difference with respect to the CVV initial conditions.

Considering the velocity magnitude fields (Fig. 7.14, top side), the higher vessel density reduces the in-duct spray velocity; therefore, the related in-duct pressure drop (Fig. 7.14, bottom side) is mitigated, damping the air entrainment increase due to higher density. Focusing on the DFI@50 kg/m^3 case, also the combustion occurring inside the duct (as highlighted by the LOL marker) raises the pressure, thus strongly reducing the delta with respect to the chamber. Therefore, the upstream

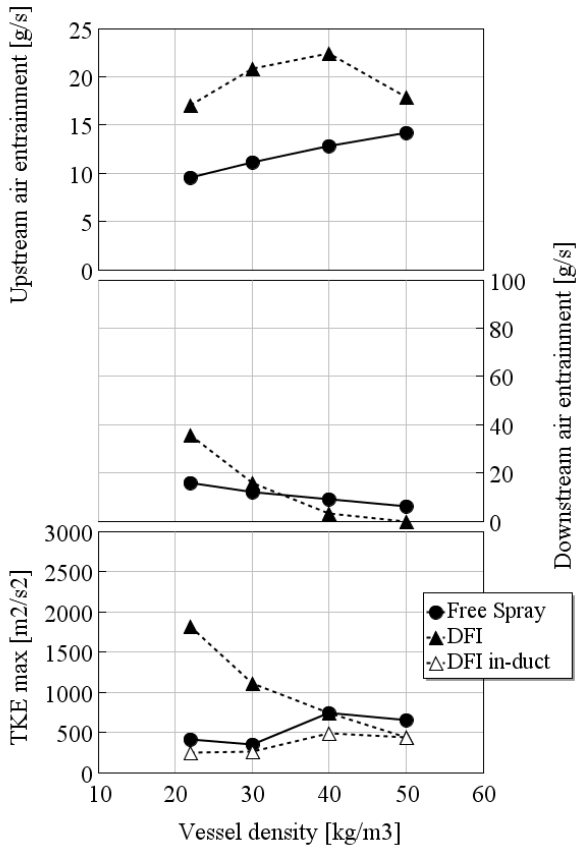

Fig. 7.13 Air entrainment into the fuel spray upstream (top) and downstream (middle) of the duct and maximum turbulent kinetic energy (bottom) at 1.2 ms aSOI as a function of vessel density for free spray (dots – solid line) and DFI (triangles – dashed line). Test conditions: vessel temperature = 900 K; rail pressure = 1200 bar; oxygen concentration = 21%.

air entrainment (Fig. 7.13, top) breaks the trend and falls to a value similar to the baseline, despite the more than doubled air density.

Moving to the downstream air entrainment (Fig. 7.13, middle), both free spray and DFI show a continuous reduction when the air density increases: the LOL shortening and the lower spray velocity are predominant with respect to the positive effect provided by a higher air density value. The overall trend between free spray and DFI is similar to the LOL one (Fig. 7.12(c)) but the breakeven point is reached in advance because in this case, as mentioned above, DFI operation is worsened due to air entrainment inhibition along the duct collision length. From 40 kg/m^3 onwards, DFI features an almost zero downstream air entrainment because of the LOL near the duct exit or inside the duct. However, the downstream air entrainment is expected to have a marginal role also for the free spray, given the low values achieved for these air density levels.

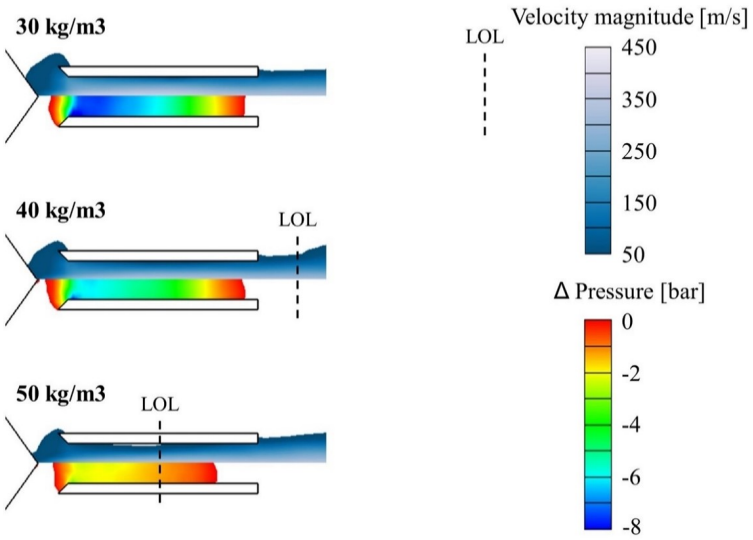

Fig. 7.14 In-duct velocity magnitude field (top side) and relative pressure field (bottom side) with respect to the test vessel at 1.2 ms aSOI for the DFI configuration at different air density values: 30 kg/m^3 (top), 40 kg/m^3 (middle), 50 kg/m^3 (bottom). Lift-Off Length (LOL) location indicated with a transversal dashed line. Test conditions: vessel temperature = 900 K; rail pressure = 1200 bar; oxygen concentration = 21%.

Focusing on the maximum TKE (Fig. 7.13, bottom), the higher vessel density tends to promote the mixing for free spray, although the LOL is shorter (thus, lower mixing length for the spray to develop). However, the rise is not continuous and a balance between LOL and TKE enhancement has to be reached to maximize the turbulent mixing capability of the free spray. Instead, for the DFI, although the higher density promotes the in-duct mixing as well (empty triangles), the overall TKE (filled triangles) monotonically decreases because the LOL shortening has a predominant effect. At 40 kg/m^3, free spray and DFI have the same maximum TKE at equal LOL, highlighting that the mixing enhancement related to the air density increase has a much larger influence on free spray, while the spray confinement within the duct could attenuate this beneficial effect. In this operating condition, the upstream air entrainment (almost 2 times higher than with free spray) plays a crucial role as a soot formation mitigation mechanism, as shown in Fig. 7.12(d). At 50 kg/m^3, the in-duct LOL leads to a maximum TKE that is reached within the duct volume, which is lower than the free spray one. As justified above, the in-duct combustion comes also with upstream air entrainment quite similar to the free spray one, thus resulting in a larger soot mass for DFI (Fig. 7.12(d)).

Summarizing, on one hand, for free spray an increment in terms of air density enhances mixing and air entrainment with a limited LOL variation; on the other

hand, the duct adoption limits the typical mixing benefits offered by a higher air density, since DFI combustion has shown high sensitivity in terms of LOL reduction. Therefore, DFI works better at lower air densities relatively to free spray and a limitation of the density range could be suggested for successful employment of DFI on a CI engine, to avoid undesirable operating conditions.

7.2.4 Effect of duct temperature

Finally, the impact of duct temperature was assessed reducing and increasing it by 200 K with respect to the CVV temperature for each vessel density condition. The duct temperature, as in previous analyses, was held constant during the entire simulation time and homogeneous over the wall. Fig. 7.15 shows the ID, the CD, the LOL and the average soot mass for both free spray and DFI as a function of the vessel density. Differently from Fig. 7.12, additional results related to the analyzed wall temperatures are provided, grouping DFI outcomes according to their duct temperature.

Focusing on the ID (Fig. 7.15(a)), a slight reduction is observed when the duct temperature increases, since the hotter wall raises the temperature of the mixture.

As far as the CD (Fig. 7.15(b)) is concerned, the variations among the different duct temperatures tested are almost negligible.

The stabilized LOL (Fig. 7.15(c)) shows a more evident variation: it shortens by more than 3 mm at 22 kg/m^3 when the duct wall temperature increases from 700 K (blue) to 1100 K (red). It results from the combined effect of the lower ID and of the enhanced evaporation rate which reduces the liquid penetration. The LOL reduction for the 1100 K case is further enhanced at 40 kg/m^3, when a limited mixture fraction pre-ignites inside the duct. Nevertheless, given the relatively low released heat, it cannot be considered as a stabilized in-duct combustion event, thus leading only to partial degradation of DFI benefits. The LOL further ahead stabilizes in proximity to the duct outlet. Moving to the highest density (50 kg/m^3), the LOL values converge for the different temperatures to about 5 mm, manifesting that the high-density conditions are predominant on the duct temperature variation, and the combustion stabilizes inside the duct.

The LOL variations with duct temperature are reflected on the average soot mass curves (Fig. 7.15(d)). More in detail, excluding the 50 kg/m^3 cases for which the in-duct combustion zeroes the soot differences, the effect of the wall temperature on

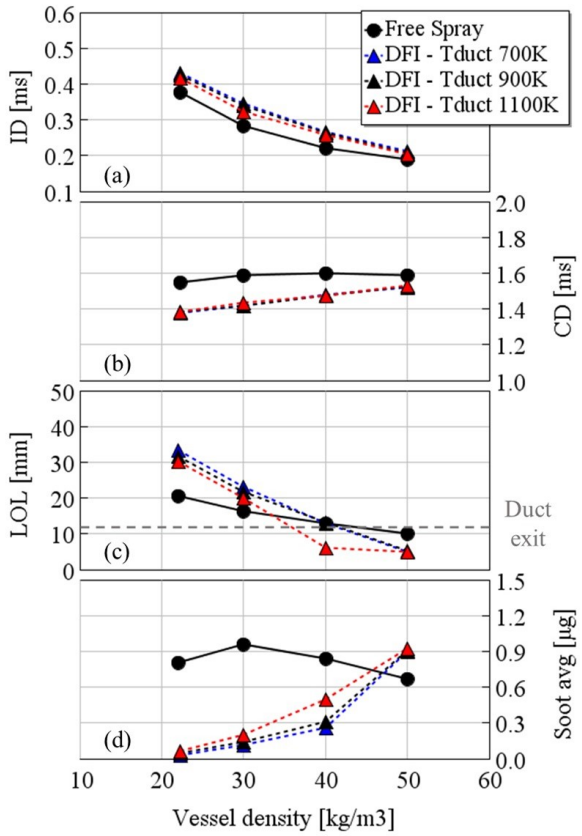

Fig. 7.15 Ignition delay (a), combustion duration (b), lift-off length (c) and average soot mass (d) as a function of vessel density for free spray (dots – solid line) and DFI (triangles – dashed line). DFI results grouped according to their duct temperature: 700 K (blue); 900 K (black); 1100 K (red). Test conditions: vessel temperature = 900 K; rail pressure = 1200 bar; oxygen concentration = 21%.

the average soot mass is amplified when the density increases, showing diverging curves moving from 22.2 kg/m^3 to 40 kg/m^3. Comparing the present sweeps in CVV with the conditions encountered inside the CI engine combustion chamber, the increase in density can be linked to a load increment. Therefore, according to these results, the thermal management of the duct wall becomes increasingly important when the load rises, also because the temperature conditions inside the combustion chamber tend to be more critical. Focusing on the 40 kg/m^3 case, moving from 1100 K to 700 K wall temperature enables a further average soot mass reduction of about 28% with respect to the free spray, while the variation is only 4.1% at 22.2 kg/m^3.

To summarize, the adoption of a proper cooling system to cool down the duct wall can improve DFI performances. These benefits are amplified when the air

density increases, suggesting that the wall temperature control could be a crucial parameter for a proper DFI operation at high loads.

7.2.5 Discussion

In Fig. 7.16, the results presented so far are summarized in four different soot/NO_x plots, each of them related to an engine parameter sweep previously analyzed. The NO_x emissions were evaluated as the NO_x mass value in the CVV at 2.7 ms aSOI, namely when nitrogen oxidation reactions can be considered frozen.

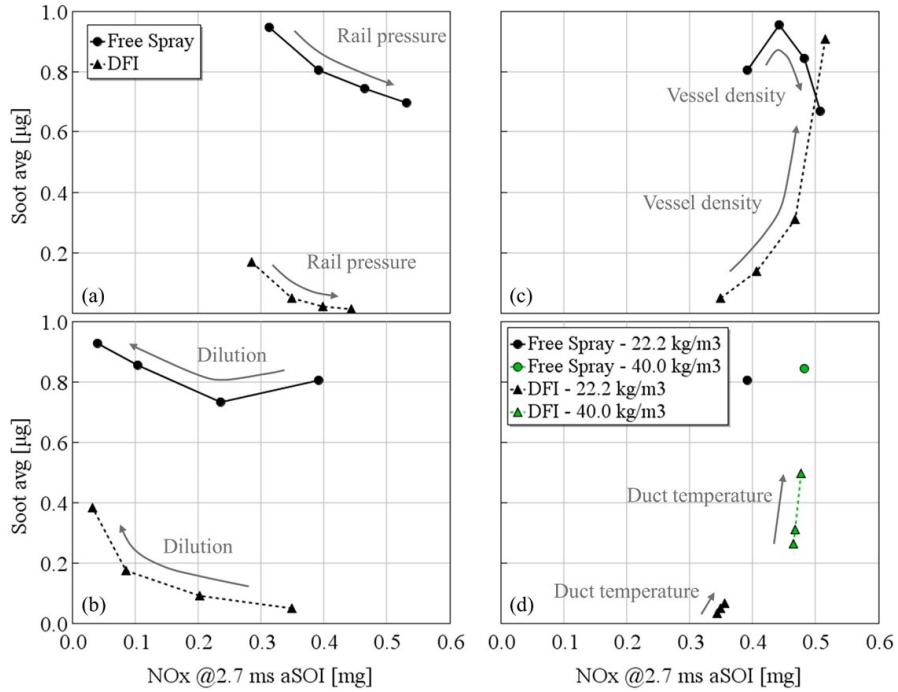

Fig. 7.16 Trade-offs between average soot mass and *NOx* at 2.7 ms aSOI for the rail pressure sweep (a), the oxygen concentration sweep (b), the vessel density sweep (c) and the duct temperature sweep (d) for both free spray (dots – solid line) and DFI (triangles – dashed line).

The rail pressure sweep (Fig. 7.16(a)) leads to a similar slope for free spray (circles – solid line) and DFI (triangles – dashed line) but the curve is shifted towards zero-soot values for DFI. Also NO_x emissions are slightly reduced with the duct adoption, enlarging the gap at higher rail pressure levels.

Moving to the oxygen concentration sweep (Fig. 7.16(b)), the higher dilution drastically reduces the NO_x emissions in a similar way between free spray and DFI,

while it increases the soot mass faster for DFI. Therefore, the soot/NO_x trade-off with dilution is shifted towards largely lower values of soot mass. Comparing this result with the outcomes from the optical engine investigation shown by Nilsen et al. in [66], it emerges that the soot oxidation phase could play a crucial role in the soot/NO_x trade-off breakage with dilution operated by DFI. In fact, the present plot is a valid indication of the soot mass formed during the DFI combustion but, given the significant differences between the CVV and the engine combustion chamber (e.g. constant-volume conditions and much lower global equivalence ratio), it is not able to describe the engine oxidation phase, which largely impacts the engine-out soot emissions balance.

Regarding the air density sweep (Fig. 7.16(c)), the lower the density, the more beneficial the DFI in terms of both soot and NO_x. In fact, as abovementioned, the soot mass trend is different between free spray and DFI. The NO_x emissions are slightly lower for DFI but, as density increases, the gap with respect to the free spray decreases. At 50 kg/m^3, when the combustion occurs inside the duct for DFI, not only higher soot mass but also more NO_x emissions are observed for DFI.

As far as the duct temperature sweep (Fig. 7.16(d)), its impact is reported at both 22.2 kg/m^3 (black) and 40 kg/m^3 (green). It can be observed that a lower wall temperature is beneficial in terms of both soot and NO_x, especially at high-density conditions. Therefore, a well-designed cooling system for the duct and duct holder, besides the requirements in terms of duct thermal management (e.g. avoid hot temperature spots in the combustion chamber), could yield additional emissions advantages to DFI and smooth its employment at higher engine loads. It is noteworthy that NO_x emissions for DFI remain lower than the equal-density free spray even when the duct temperature is 200 K higher than the CVV temperature.

In conclusion, from an overall point of view, each working condition shows an impressive less amount of soot for DFI and a simultaneous slight NO_x emissions reduction compared to the free spray, excluding the in-duct combustion case (50 kg/m^3 density), when both soot and NO_x are higher for DFI. Therefore, according to the present results, DFI technology not only curtails soot formation across a wide range of operating conditions but also maintains NO_x emissions under control, even showing some potential synergic benefit in this direction.

Chapter 8

DFI implementation on a light-duty CI engine

Part of the work described in this chapter was previously published in:

- Piano, A., Segatori, C., Millo, F., Pesce, F.C. and Vassallo, A.L., "Investigation of Ducted Fuel Injection Implementation in a Retrofitted Light-Duty Diesel Engine through Numerical Simulation," *SAE Int. J. Engines* 16(5):2023, doi:10.4271/03-16-05-0038.

In the context of a project in collaboration with *PUNCH Torino S.p.A.*, the DFI implementation on a series-production light-/medium-duty engine has been explored through RANS numerical simulations. The aim of this activity was the evaluation of potential benefits coming from the usage of DFI technology with a direct-retrofit approach, understanding the factors which can limit or facilitate its integration in existing engine combustion chambers. After the development of this preliminary knowledge, *PUNCH Torino S.p.A.* moved forward on the topic by means of optical engine analyses performed in the facilities of *CMT - Clean Mobility & Thermofluids* of *Universitat Politècnica de València* [166]. These optical engine analyses were executed to experimentally demonstrate the soot reduction potential of DFI technology on a similar engine case study implementing a series-production 8-holes injector. Given the close connection among the two analyses, a selection of outcomes coming from both projects are reported throughout this chapter.

8.1 Case study

Even though a similar case study was considered for both the numerical and the experimental analyses, some differences were present due to the particular necessities of the optical investigation. The main specifications are reported in Table 8.1.

Table 8.1 Case studies for the numerical and optical engine analysis

		Numerical analysis	Optical analysis
Displacement	l	0.8	
Bore / Stroke		1	
Nº holes		8	
Holes diameter	μm	140	
Inj. pressure	bar	1500	1200
Inj. rate shape		2 pilots + main (+ post)	Pilot + main
O_2 conc.	$mol\%$	18	15, 18, 21
Engine speed	rpm	1800	1200
Engine load	bar	6 (BMEP)	7.6 (IMEP)
Cylinder head		Series-production	
Piston bowl		Sharp-step omega-shape re-entrant	Flat re-entrant
Duct designs		D2L14G3	D2L8G3.3 D2L(8,10)G4.3 D3L10G4.3
Duct holder		Not	Yes

As can be seen, the same engine displacement and bore-to-stroke ratio were used, as well as the same injector characteristics. The injection pressure was slightly lower for the optical analysis and the injection pattern was simplified, composed by a single pilot and a main injection. The same oxygen concentration was tested, despite the sweep was extended during the optical analysis. Approximately the same load was achieved but at a lower engine speed for the optical analysis. An additional difference is that the optical engine was operated in skip fire mode, with 1 combustion over 20 cycles. Concerning the engine design, both engines employed the series-production cylinder head and a re-entrant piston bowl. However, in the optical analysis the sharp step in the squish area was removed and the piston dome was flattened with respect to the metal engine numerically studied. This modification led to about 2 points lower compression ratio for the optical engine. Different ducts design were experimentally investigated, not coincident with the one used in the numerical analysis. These ducts were easily exchangeable thanks to a developed duct holder prototype shown in Fig. 8.1 (taken from [166]), which was designed with the

following constraints: avoiding interaction with valves by limiting the duct radial extension; accommodating 8 ducts for the 8-holes injector by avoiding duct-to-duct interaction; ensuring alignment between spray and duct; overcoming manufacturing issues with conventional technologies by using additive manufacturing; avoiding interaction with omega-shape high compression ratio piston bowl.

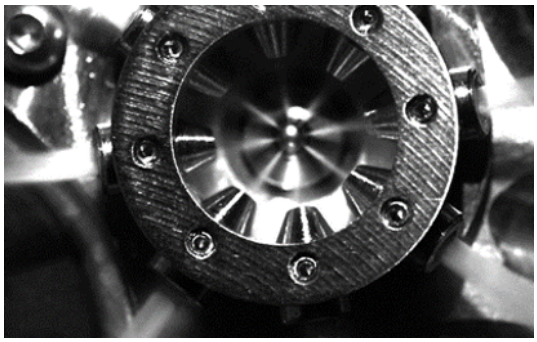

Fig. 8.1 Reproduced from [166]. Photo of the duct holder prototype for the 8-holes injector of the optical engine analysis.

8.2 Numerical analysis

For the sake of brevity, only the main results of the numerical analysis are reported in this section. They were obtained by means of the SAGE detailed chemistry solver and the particulate mimic model for detailed soot modelling, deeply discussed in chapter 5. For details on the 3D-CFD modelling and the validation against experimental data (for CDC only, given the absence of experimental data related to DFI at the time of the analysis), please refer to [53].

In Fig. 8.2, the fuel injection rate, the burn rate and the in-cylinder pressure, the in-cylinder soot mass trace, and its first derivative (i.e., soot formation/oxidation rate) are reported for both free spray and DFI as a function of crank angle (CA).

The injection rate (Fig. 8.2(a), grey) is characterized by two small pilot, one main and one post injections. Considering only the amount of fuel injected after the pilot injections, the main and post injections feature a fuel mass share of about 75% and 25%, respectively. Comparing free spray (red) and DFI (blue) in terms of burn rate (Fig. 8.2(b)), most of the typical trends characterizing DFI combustion can be detected. In fact, the duct adoption leads to a longer ID and, consequently, a more intense premixed combustion, as shown by the higher and retarded burn rate

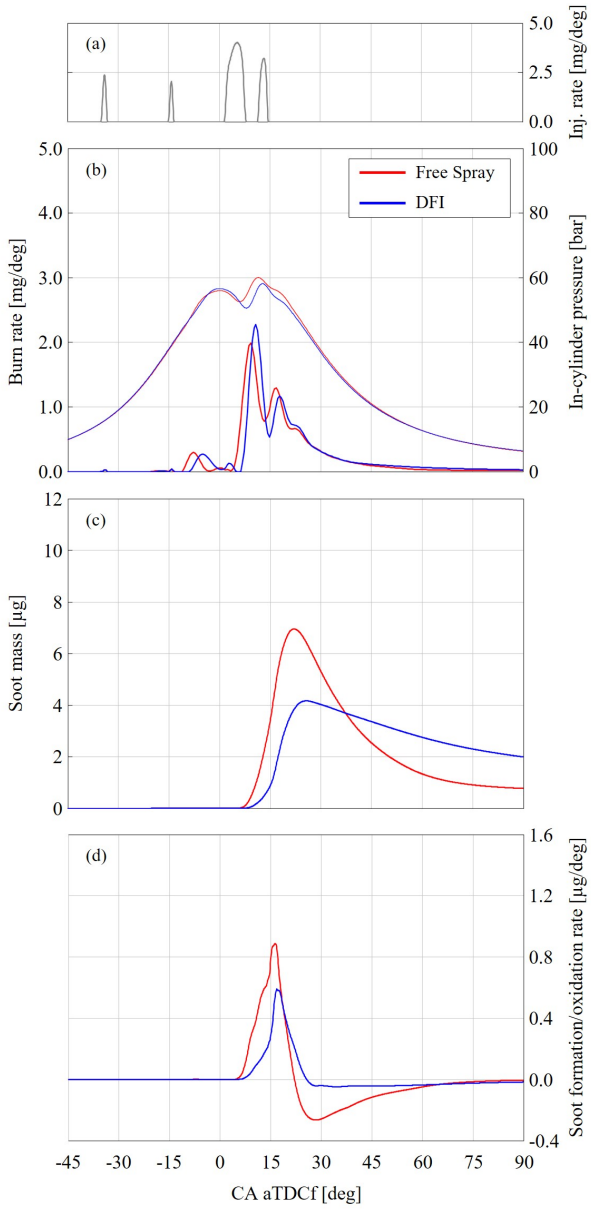

Fig. 8.2 Fuel injection rate (a), burn rate and in-cylinder pressure (b), in-cylinder soot mass (c), and soot formation/oxidation rate (d) for both free spray (red) and DFI (blue).

peak. On the contrary, the burn rate associated with the post injection combustion is lower than the free spray, despite the retarded ignition. This leads to a slower end of combustion, unusual for DFI technology which typically features a much faster burn out, as analysed in chapter 5. In the end, the abovementioned variations are reflected on the in-cylinder pressure traces (Fig. 8.2(b)), causing a load decrease of about 3% with DFI, injected fuel mass being equal. The in-cylinder soot mass

(Fig. 8.2(c)) shows a retarded rise in the curve and a significantly lower soot mass peak for DFI, highlighting a remarkable reduction of soot formation during the main combustion phase. This is also clear by looking at the soot formation rate curve (Fig. 8.2(d)), which shows much lower values than free spray for the whole injection duration and most of the combustion associated with the main injection. However, moving to the late combustion phase, higher in-cylinder soot mass is present for DFI, due to a strong reduction of soot oxidation rate compared to the free spray curve. Focusing on the soot formation phase, the duct presence in the combustion chamber is effective in reducing soot with respect to the free spray, despite this mitigation is less impressive with respect to most of the literature on the subject (section 1.4.2). This difference can be related to several aspects, among them:

- the size of the herein combustion chamber, designed for light-duty applications, which could mitigate the DFI soot mitigation mechanisms with respect to test vessel studies and heavy-duty CI engines;
- the shape of the combustion chamber which is again optimized for the free spray configuration and does not take into account the characteristics (e.g., higher penetration) of the ducted spray;
- the engine calibration which is optimized for free spray configuration since a direct retrofit methodology was adopted with DFI, thus no effort was spent in trying to maximize DFI benefits.

The first two points, being related to geometrical aspects, are not herein investigated but were object of the experimental analysis on optical engine. The third point is preliminarily analysed in terms of injection rate shape in a later section. Focusing on the soot oxidation phase, the negative impact of similar aspects seems even more evident. In fact, the oxidation rate for DFI is much lower than the free spray, as highlighted by the first derivative curves (e.g., DFI soot oxidation rate only a bit lower than 0), leading to higher soot mass towards the exhaust valve opening (EVO), despite the advantage in terms of soot formation.

In order to better understand the soot mass behavior, a local analysis of the 3D results is proposed below, focusing, at first, on the soot formation phase only, then, on the soot mass temporal evolution up to the late oxidation phase. First of all, the DFI soot formation mitigation is investigated, illustrating the ϕ results during the main injection for both the free and the ducted sprays on two different combustion

chamber sections (Fig. 8.3). The frame is taken at 6 deg aTDCf, thus, near the maximum of the main injection rate.

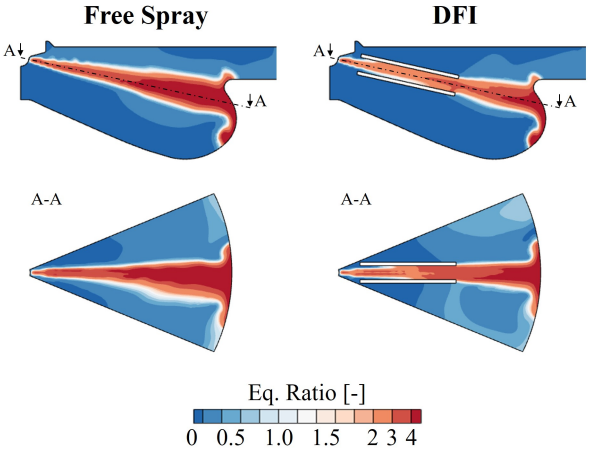

Fig. 8.3 Equivalence ratio distribution during the main injection (6 deg aTDCf) on a vertical section (top) and a respective orthogonal section (A-A, bottom) of the combustion chamber for both free spray (left) and DFI (right).

The first section is a vertical plane containing the nozzle and the cylinder axes (Fig. 8.3, top), while the second one is the respective orthogonal plane containing the nozzle axis (Fig. 8.3, bottom), indicated with the A-A segment. From both the sections, it emerges that DFI attenuates the ϕ values, both inside and downstream of the duct. Similar values are only reached where the spray impinges on the piston wall, but the rich area is less extended for DFI. However, this ϕ rising after the duct exit was not present in the test vessel simulations, suggesting that the spray/bowl interaction could deteriorate the mixing benefits coming from duct adoption, particularly intense after the duct exit. In light of this, the relatively low size of this light-duty combustion chamber could be a crucial aspect and a proper optimization of its design should be considered to fully exploit DFI soot formation mitigation mechanisms. Despite this, from an overall point of view, DFI leads to a significant advantage in terms of air-fuel mixing, motivating the soot formation reduction observed in Fig. 8.2, which however shows that higher engine-out soot emissions are caused by the duct adoption due to its negative impact on soot oxidation in this case study. To better understand the underlying reasons behind this outcome, a time-varying local analysis is needed. Therefore, in Fig. 8.4 and Fig. 8.5 respectively, the temperature and soot mass distributions on a section of the combustion chamber, containing cylinder and nozzle axes, are reported for both free spray and DFI at different selected time instants.

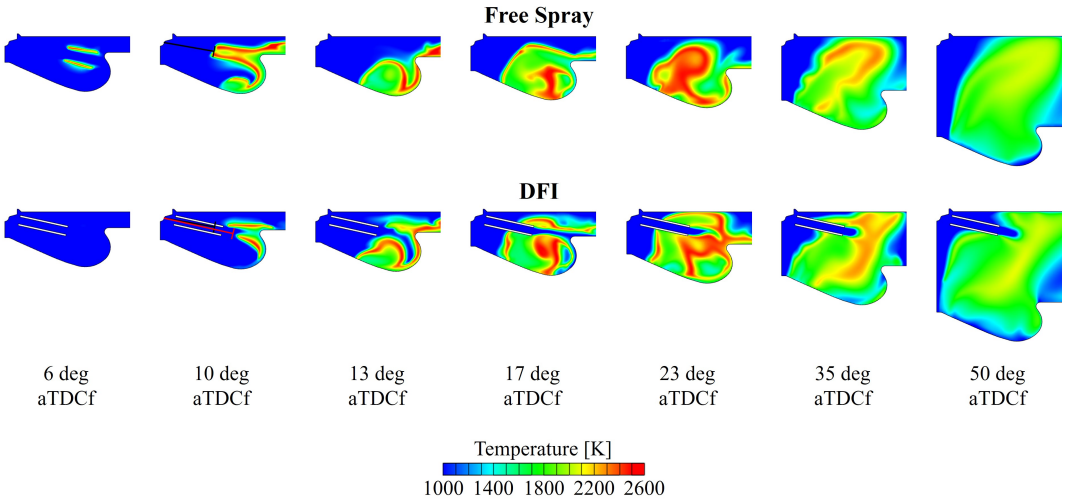

Fig. 8.4 Temperature distribution on a vertical section of the combustion chamber for both free spray (top) and DFI (bottom) at different time instants (from left to right).

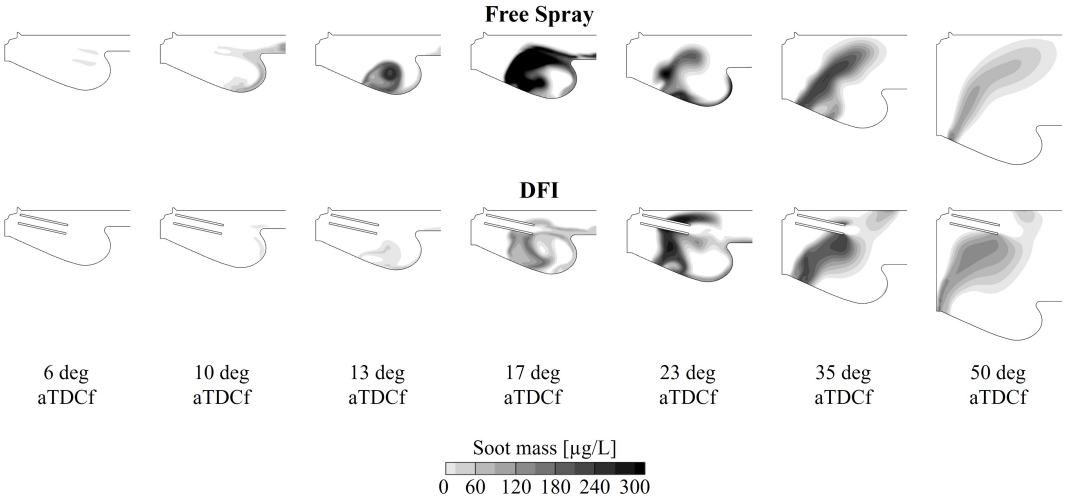

Fig. 8.5 Soot mass distribution on a vertical section of the combustion chamber for both free spray (top) and DFI (bottom) at different time instants (from left to right).

- **6 deg aTDCf**: this time instant is related to the main injection at its maximum fuel mass flow rate, previously analysed. For the free spray case, a temperature increase due to ignition can be observed on the periphery of the spray, while the abovementioned longer ID is confirmed for DFI, where no ignition is highlighted. The soot has practically not yet formed in both configurations, as confirmed in Fig. 8.2.

- **10 deg aTDCf**: this time instant is related to the combustion of the main injection, during the dwell time between main injection and post injection. Stabilized spray flames can be observed, featuring the LOLs highlighted with black and red segments for free spray and DFI, respectively. The duct adoption leads to a significant extension of the LOL, ensuring DFI works properly, without in-duct combustion. From an overall perspective, the flame area is less extended and the temperatures lower for DFI. In terms of soot mass, soot pockets can be noted inside the bowl and near the step region for the free spray, while quasi zero soot is depicted for DFI.

- **13 deg aTDCf**: this time instant is related to the post injection at its maximum fuel mass flow rate. This fuel mass is injected during the main injection-related combustion. It is immediate to note that the post injection must react in a colder environment for DFI due to both the slower combustion development of the main and the colder gas inside the duct retrieved by the tail of the main spray and pushed out by the tip of the post spray. In terms of soot mass, the soot formation mitigation provided by the duct, motivated in previous paragraphs, is evident: the difference between the two configurations is amplified in the bowl region, indeed the soot is forming at a higher rate for free spray, as confirmed in Fig. 8.2.

- **17 deg aTDCf**: this time instant is related to the combustion of the post injection. A cold path can be observed from the injector to the piston rim for DFI, making more evident the temperature reduction. This relatively cold gas brought from the duct into the combustion region further increases the ID associated with the post injection for DFI and tends to deteriorate the late combustion process, as shown in Fig. 8.2 where the typical DFI faster burnout is not present. This slow-down of the post injection combustion is expected to also have a negative impact on soot oxidation. Looking at the soot mass distribution, the DFI's positive impact on the soot formation related to the main combustion is again evident. However, the soot pockets are moving back towards the duct region, where soot oxidation can be more difficult. The soot formation due to post injection-related combustion can also be observed close to the bowl lip for both free spray and DFI, with lower values of soot mass for DFI.

- **23 deg aTDCf**: this time instant is associated with the maximum in-cylinder soot mass. A temperature increase near the bowl lip can be observed for DFI,

due to the post injection combustion occurring later than free spray. On the contrary, the temperatures are generally lower for DFI in the rest of the volume, especially in the region occupied by the duct. These low-temperature areas (i.e., at about 1600-1800 K) are reflected as high soot pockets on the soot distributions, due to the reduced oxidation rate.

- **35 deg aTDCf**: this time instant is associated with the breakeven point between the soot traces in Fig. 8.2, thus free spray and DFI are characterized by an equal soot mass in the cylinder, but a different soot oxidation rate. Again, DFI features lower combustion temperature values, especially for the gases surrounding the duct volume, and a blue cold region inside the duct, where combustion is not occurring. Therefore, the volume involved in the combustion process is smaller. As above said, the lower combustion temperature values work as a sort of tracer of high soot concentration regions, due to the reduced oxidation. In fact, the highest soot mass values for DFI are reached close to the duct. The oxidation is inhibited in that region due to three main effects: first, the temperatures are lower; second, the soot on the duct wall cannot comes in direct contact with the oxidizing air; third, the duct presence acts as a sort of container, removing part of the available fresh air, essential to oxidize the formed soot mass. Therefore, the free spray case has a larger amount of air available for soot oxidation purposes. This aspect is particularly critical due to the reduced dimension of the chamber and due to the piston bowl design, which directs the spray towards the center, where the duct occupies most of the available space. This consideration suggests that a geometrical optimization of the combustion chamber could be of paramount importance for DFI implementation in light-duty diesel engines.

- **50 deg aTDCf**: this time instant is related to the late soot oxidation phase, when DFI is characterized by a higher soot mass than free spray. DFI shows lower temperatures in the center of the chamber, where the duct is present, confirming that it is hindering the soot oxidation process. Both free spray and DFI feature a residual soot pocket near the bowl dome, where a possible interaction could occur with the other sprays, especially for the DFI, due to the higher spray velocity. While the soot mass progressively reduces moving from the bowl to the cylinder head, another large soot pocket is present for DFI near the duct, due to the mechanisms analysed at the previous time instants.

It is important to point out that also the different swirl level between free spray and DFI, due to the interaction of the ducts with the bulk flow motions [53], can have a negative impact on the soot oxidation phase. The reduced swirl level for the DFI in the present engine configuration is confirmed in Fig. 8.6, where the DFI swirl ratio normalized with respect to the free spray one is represented as a function of the CA. From a percentage point of view, this effect becomes more evident moving towards the expansion phase, where a 10% reduction in late-cycle mixing is observed for DFI. This gap can affect the late-cycle soot oxidation phase, whose enhancement is typically the specific purpose of a high-swirl combustion chamber design. Therefore, this aspect should be taken into account among the possible adverse effects of DFI on the soot oxidation.

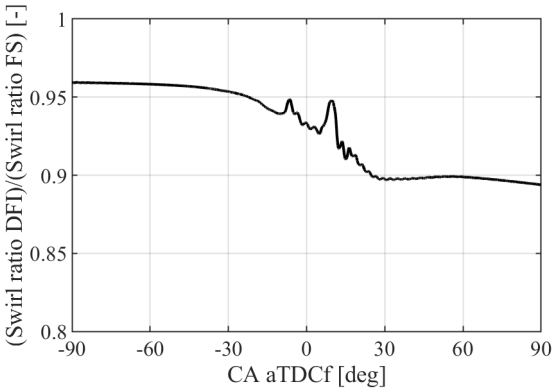

Fig. 8.6 DFI swirl ratio normalized with respect to the free-spray one.

8.2.1 Impact of post injection

According to the analysis on the part load working point, the direct retrofit approach for DFI seems not a viable solution for both engine calibration and engine design aspects. Indeed, although a soot reduction was observed during the formation phase, soot oxidation was strongly inhibited for DFI, leading to higher engine-out soot emissions. The purpose of this section is to preliminary investigate if a variation of the engine calibration, without any modification of the engine design, could be beneficial for DFI. In particular, a simple variation of the injection pattern was considered, based on the previous results. The post injection is typically involved in CDC for both enhancing soot oxidation, due to enhanced mixing and temperature effects, and reducing soot formation, due to the lower main injection duration [167]. In this case, the post injection seemed not beneficial for DFI due to the very slow

reaction rate, leading to late-combustion degradation and no beneficial effect on soot oxidation. Therefore, a test with a simplified injection was executed, suppressing the post injection and increasing the main injection duration, in order to maintain equal total injected fuel mass. In Fig. 8.7, the fuel injection rate, the burn rate and the in-cylinder pressure, the in-cylinder soot mass, and the soot formation/oxidation rate are reported for both free spray and DFI as a function of CA. For the soot mass trace, the results associated with the previous analysis, involving the post injection, are illustrated again with dashed lines to facilitate the comparison.

Focusing on the burn rate (Fig. 8.7(b)), it is immediate to note that the impact of the longer main injection on the premixed combustion phase is much higher for DFI (blue), which shows a larger increment of the peak. In fact, a larger amount of fuel mass is involved in the premixed combustion regime with respect to the free spray (red), thus affected more by the higher amount of fuel mass injected during the main. The late combustion is more rapid for both configurations when post injection is excluded, leading to an increment in load, which is higher for DFI (+2.2% on IMEP) than free spray (+1.4% on IMEP), leading to only a less-than-1% reduction in IMEP for DFI. However, also in this case, DFI does not feature the typical faster burnout, present in constant-volume conditions.

Looking at the in-cylinder soot mass (Fig. 8.7(c)), in the free spray case the post injection removal (solid line) causes an in-cylinder soot mass peak increment, due to a higher soot formation rate, as highlighted in Fig. 8.7(d). Therefore the presence of the post injection (dashed line) seems to reduce the jet fuel-rich regions, according to the split-flame and jet replenishment concepts [167–169], thus reducing the soot formation. Since the DFI case reduces the soot mass enabling different mechanisms, the well-known effects of post injection on soot formation cannot be considered. Only a slight increment in the soot mass slope can be detected, with a similar peak of the soot mass curve. In other words, during the soot formation phase, the removal of the post injection worsens the free spray configuration, while almost does not affect the DFI one. As far as the soot oxidation phase is concerned, the absence of post injection in the free spray case causes a slightly steeper slope of the soot mass curve. However, the removal of the post injection leads to higher engine-out soot emissions at EVO, as expected. Different is the outcome related to the DFI configuration: starting from a similar amount of soot mass formed, the slope of the curve associated with the injection strategy without post injection is remarkably steeper than the main plus post injection one. Hence, the engine-out soot emissions are reduced when the post injection is removed for the DFI case. In particular,

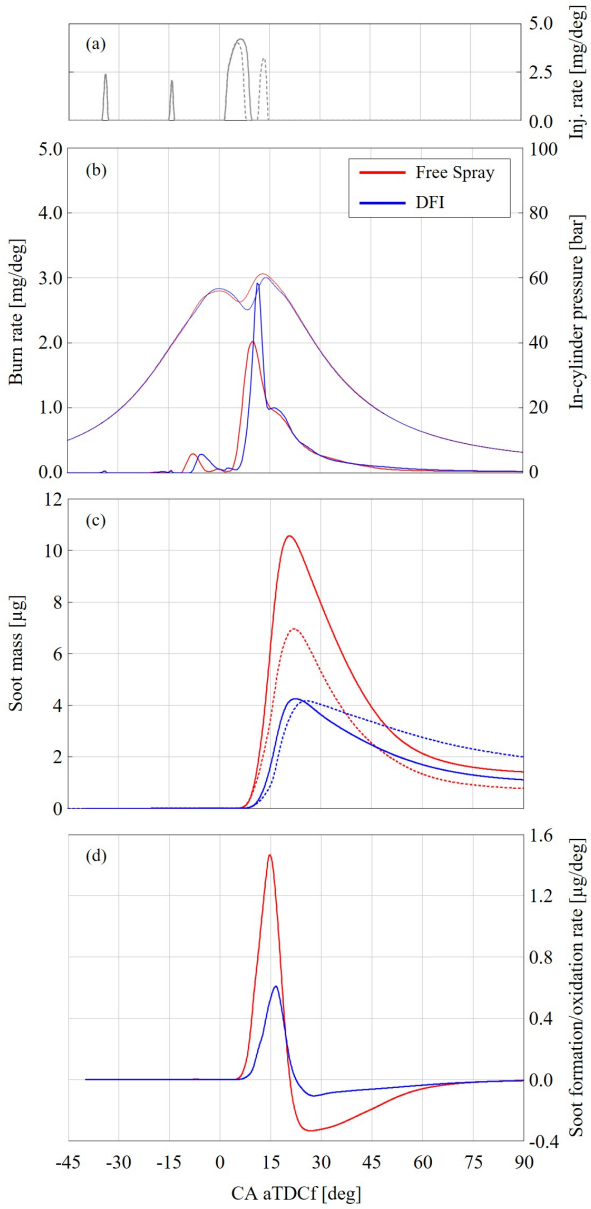

Fig. 8.7 Fuel injection rate (a), burn rate and in-cylinder pressure (b), in-cylinder soot mass (c), and soot formation/oxidation rate (d) for both free spray (red) and DFI (blue). Injection patterns without post injection (solid lines) and with post injection (dashed lines) are compared.

comparing free spray and DFI without post injection, a 22% engine-out soot mass reduction can be observed with the duct adoption. It is noteworthy, that this outcome is achieved despite the limitation associated with the combustion chamber size and design, which are detrimental to soot oxidation with DFI, eroding its benefits in terms of soot formation.

Even though the suppression of the post injection was revealed to be very beneficial for DFI, at the current state the lowest engine-out soot mass is still reached by the free spray with the initial calibration. However, from the present analysis, good potentialities emerge from DFI technology, which is capable to achieve much lower soot formation and only slightly higher engine-out soot emissions, compared to the free spray reference curve. In fact, it has to be taken into account that no real effort was spent in optimizing the DFI combustion system and related calibration, maintaining a bowl design that has been demonstrated to partially deteriorate the DFI benefits. On the contrary, the free spray case is the result of a time-consuming engine design and calibration optimization. In other words, a DFI-oriented calibration could lead to very interesting results for the DFI configuration, even in a light-duty retrofitted combustion chamber design. In addition, a DFI-oriented geometrical optimization of the chamber would further pave the way to its success as soot-curtailing technology for diesel combustion.

8.3 Optical engine analysis

For the sake of brevity, only the main results qualitatively comparable with ones of the numerical analysis are reported in this section. For more details on the experimental setup, other results of the optical analysis related to different bowl designs, and engine-out soot emissions measured through opacimeter, please refer to [166].

Two techniques were used throughout the optical analysis: the OH* chemiluminescence measurement and the 2-color pyrometry. The former aims to identify the near-stoichiometric high-temperature reaction region by capturing the radiation emitted by the excited-state of the OH molecule, named OH*. The latter aimed to evaluate the optical soot density (or thickness, since denotes all the soot along the optical path), named KL, by capturing the thermal radiation emitted by soot clouds at two different wavelengths. In Figs. 8.8 and 8.9 (adapted from [166]), respectively, the OH* chemiluminescence and the KL distributions in the combustion chamber observed from the optical access piston are reported for both free spray and DFI at different selected time instants, comparable to the ones chosen for the numerical analysis in Figs. 8.4 and 8.5. Since in this case the post injection was not adopted, the time instants related to the post injection and its combustion event are absent.

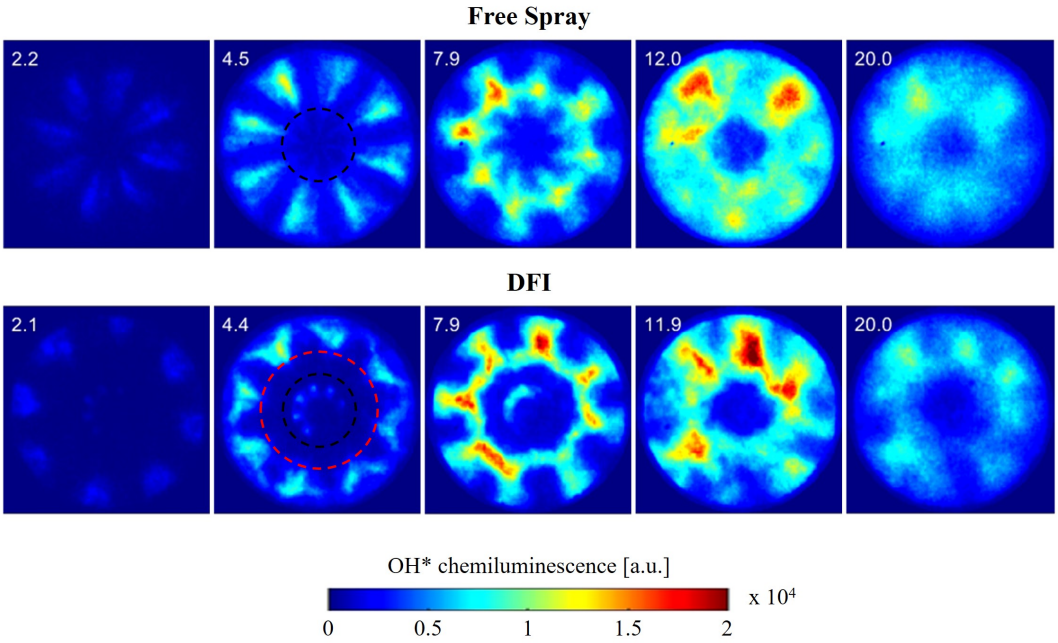

Fig. 8.8 Adapted from [166]. OH* chemiluminescence distribution in the optical engine combustion chamber for both free spray (top) and DFI (bottom) at different CA, indicated at the top-left of each image. O_2=21 mol%; duct geometry: D2L8G4.3.

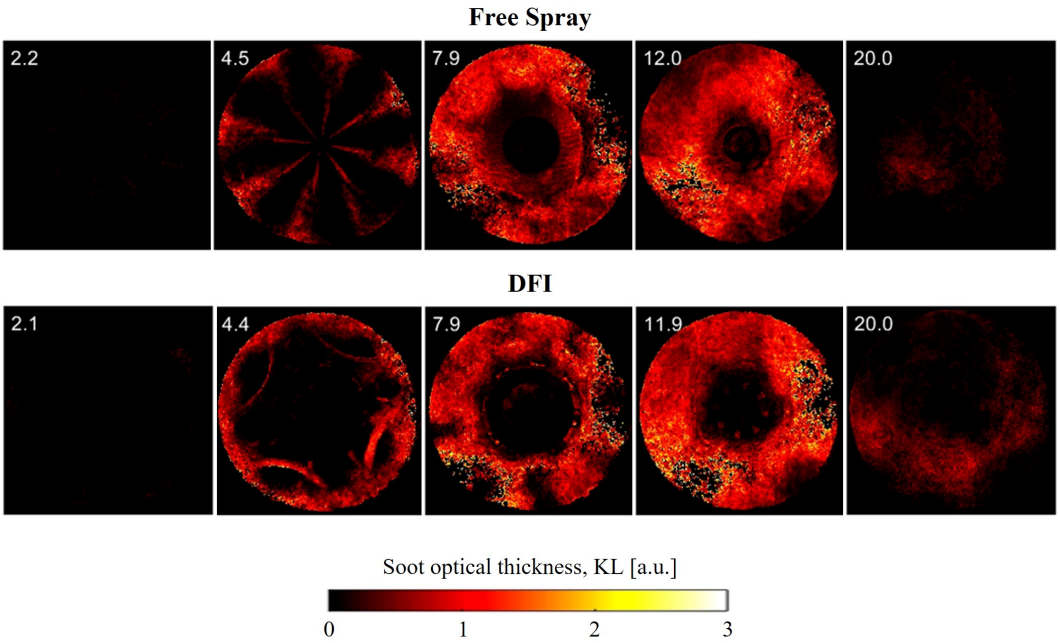

Fig. 8.9 Adapted from [166]. Soot optical thickness (KL) distribution in the optical engine combustion chamber for both free spray (top) and DFI (bottom) at different CA, indicated at the top-left of each image. O_2=21 mol%; duct geometry: D2L8G4.3.

- **∼2.2 deg aTDCf**: this time instant is related to the main injection and the SOC. For both configurations, a OH* chemiluminescence increase can be observed due to ignition, which covers a wider area for the free spray. The soot has practically not yet formed in both configurations, despite some very small red clouds can be spotted.

- **∼4.5 deg aTDCf**: this time instant is related to the combustion of the main injection. Stabilized spray flames can be observed, featuring the LOLs highlighted with black and red dashed circles for free spray and DFI, respectively. The duct adoption leads to a significant extension of the LOL, consistently with the lower soot optical thickness. For the free spray the high KL values are achieved both in the spray structure and in the bowl periphery, while only in the bowl periphery for the DFI. In general, a stronger interaction between spray and piston bowl is visible for the DFI.

- **∼7.9 deg aTDCf**: this is the time instant in which free spray and DFI approximately achieve the maximum in-cylinder soot optical thickness. High values of OH* chemiluminescence are achieved for both configurations in similar regions of the bowl, despite much lower values are present in the center for the DFI, suggesting that lower temperature regions could be present, probably linked to the additional ducts and duct holder walls. The soot optical thickness features a similar distribution between free spray and DFI, but generally lower values are observable for the latter.

- **∼12 deg aTDCf**: this is the time instant in which free spray and DFI are characterized by an almost equal soot optical thickness. Even higher OH* chemiluminescence values are achieved for the DFI but a central possible low-temperature area persists. The effect of this area seems visible also in terms of soot, since very low KL values are achieved in the center for the DFI, indicating that no soot is burning there. Even though a similar soot optical thickness is present at this time instant for free spray and DFI on average, the very low KL values in the center could indicate a degraded oxidation due to low temperatures and/or ducts plus duct holder presence, reducing the available air for oxidation and the swirl motion.

- **∼20 deg aTDCf**: this time instant is related to the late soot oxidation phase. In general, lower OH* chemiluminescence values and higher KL values can be observed for the DFI, indicating that the soot oxidation phase was less effective

than free spray. The lower temperatures, the reduced amount of available air for oxidation, the reduced swirl level, and the stronger interaction between spray and piston bowl could all have played a role.

In order to provide an aggregated view of the soot optical thickness as a function of CA, also when duct geometry and oxygen concentration vary, in Fig. 8.10 (taken from [166]) the mean accumulated KL traces are reported for the free spray and the DFI considering four different duct geometries and three different oxygen concentration levels.

As can be seen, each duct geometry at each oxygen concentration level, on the one hand, reduces soot formation compared to the free spray, on the other hand, worsens the late soot oxidation phase, resulting in the end in higher mean accumulated KL values towards the end of the combustion process. Indeed, each DFI curve features a lower KL peak with a less intense downward sloping phase. Therefore, the present optical measurements are in line with the outcome from the preliminary numerical analysis, suggesting an improved soot formation phase but a degraded soot oxidation phase with DFI. Furthermore, the underlying reasons behind this deteriorated soot oxidation phase, such as lower temperatures, air subtraction due to ducts plus duct holder presence, and enhanced spray/bowl interaction are visible in both the numerical and optical analyses. Another reason could also be the reduced late-cycle swirl level that emerged from the numerical results.

The duct geometry affects the mean accumulated KL trace, improving the soot results when the duct is shorter, closer to the injector nozzle and with a larger diameter. Hence, duct geometrical modifications which tend to reduce the interaction between spray and bowl seem beneficial for this engine combustion system. This is in line with additional optical results discussed in [166] which suggest that the usage of an open bowl design instead of a re-entrant bowl design, reducing spray/bowl interaction and flow re-circulation towards the duct holder, can improve DFI performance for this kind of engine applications. Nevertheless, the discussion of such results are considered out of the scope for the present PhD work.

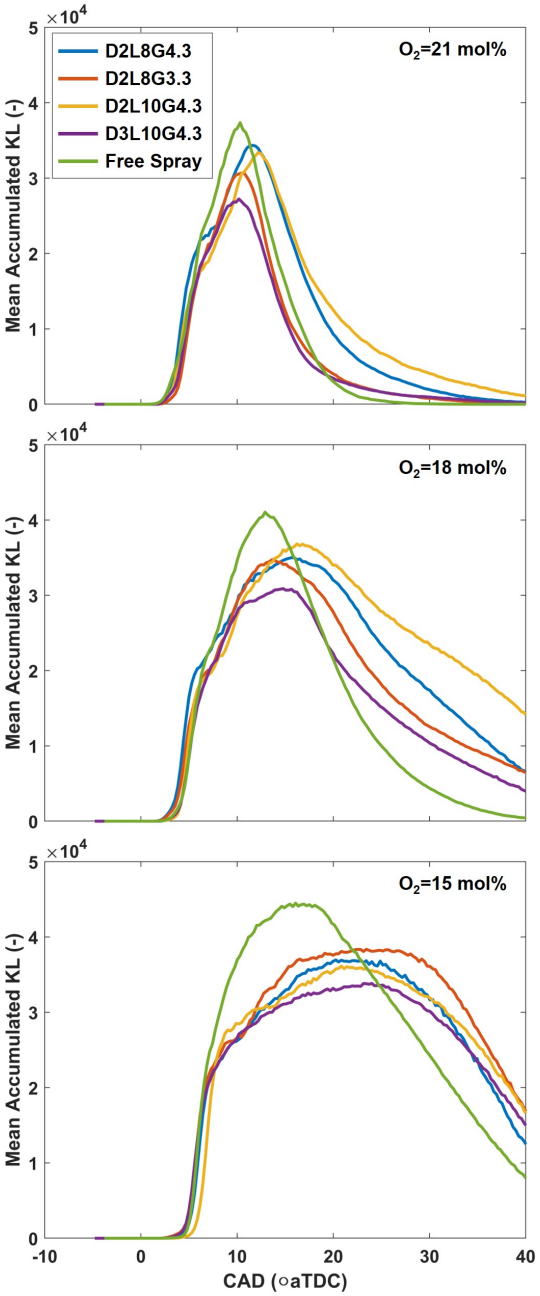

Fig. 8.10 Reproduced from [166]. Mean accumulated soot optical thickness (KL) as a function of CA for the free spray and four different duct configurations at different oxygen concentration levels.

8.4 Discussion: adverse effects of DFI on oxidation in a retrofitted CI engine

As largely discussed throughout this chapter, the implementation of the DFI technology in an existing spray-guided CDC combustion system with a direct retrofit approach, even though could provide some benefits in terms of soot formation, could also lead to adverse effects in terms of soot oxidation. Several reasons have been highlighted by both the numerical and the optical engine analyses herein presented:

- lower temperatures due to the DFI system walls;
- lower available air for oxidation due to the ducts plus duct holder volume;
- enhanced spray/bowl interaction;
- lower late-cycle swirl level due to flow-ducts interaction.

Though not identical to these results, a study recently published by Caterpillar researchers [170] confirmed most of these outcomes for a wall-guided CDC combustion system by means of optical analyses in a high-temperature-pressure vessel implementing a 3D sector piston geometry created to mimic the same spray/wall interactions present in the metal engine under examination. Ambient pressure and temperature values, as well as the injection parameters, reproduced the conditions at the SOI of the correspondent metal engine on a full load working point. By looking at the CH^*[1] evolution inside the combustion chamber, the investigators claimed that the longer LOL and the higher jet velocity make the DFI configuration more influenced by jet-jet interactions, jet-wall interactions, and re-entrainment of hot combustion products. In particular, they stated that "the more rapid turning of the DFI flame back on itself can lead to hot product re-entrainment, subsequent shortening of the lift-off length, and potential for flame-holding within the duct" [170], thus partially curtailing the soot formation advantage. Moreover, regarding the soot oxidation phase, they concluded that, for their wall-guided geometry, "the counterclockwise vortex observed downstream of the duct is characterized by reduced reactions at its center," which "may be indicative of under-utilization of in-cylinder air and relatively slower oxidation reactions during late-injection periods and burnout" [170]. It is Author's opinion that the marked similarity of these findings further confirms the

[1] Radical species tracking the flame evolution.

reliability and the relevance of present results concerning the implementation of DFI technology in a retrofitted CI engine.

Conclusions and outlook

Conclusions

Ducted fuel injection (DFI) is a promising concept, based on the implementation of a small duct in front of the injector tip, to abate soot emissions from diesel combustion by enhancing the air/fuel mixture preparation upstream of the auto-ignition region, or lift-off length (LOL). Although several experiments in the literature showed its remarkable effectiveness in both constant-volume and compression-ignition (CI) engine conditions, many questions remain unanswered about the mechanisms through which DFI suppresses soot formation and its real feasibility on the whole engine operating map. The full comprehension of these mechanisms is of paramount importance for the success of this new concept, especially when duct geometry optimization and DFI-related engine calibration requirements are concerned. In light of this, the present PhD study aimed to cover several key knowledge gaps in the understanding of DFI, analysing in detail the entrainment and mixing mechanisms, the combustion and emissions formation processes, as well as the impact that duct geometrical features and/or operating conditions have on them. Free and ducted sprays evolving along the axis of a cylindrical test vessel caused by the injection of diesel fuel from a 0.180 mm single-hole common rail injector were taken as case studies, relevant for heavy duty applications. For this purpose, 3-dimensional computational fluid dynamics (3D-CFD) can be a powerful tool, since it can provide additional insights on concepts that cannot be analyzed though experiments, like in the DFI-case. Therefore, a high-fidelity 3D-CFD spray model, based on the Lagrangian particle tracking approach, was developed as a means to investigate the DFI-related physics. Model calibration and validation was executed against spray characterization data collected during an extensive experimental campaign in constant-volume non-reacting conditions, considering both the free spray and the DFI configurations with several duct geometries. In particular, spray structure pictures obtained through Schlieren technique, liquid

penetration curves as a function of time, and droplet size and velocity measurements were available.

DFI physical understanding through large eddy simulation

As a first approach, considering that the turbulence plays a dominant role in DFI mixing process, the highly accurate but computationally expensive large eddy simulation (LES) approach, coupled with statistical analysis, was adopted for describing the turbulence on a single non-reacting condition, comparing the free and ducted spray flow fields. The main outcomes related to the DFI physics coming from this part of analysis can be summarized as follows.

- The turbulent energy cascade is spatially more advanced when duct is adopted, and the enhanced turbulent mixing areas are generally wider. Farther upstream mixing is of particular importance considering the limited dimension of a combustion chamber and the necessity to reduce the equivalence ratio before the LOL.
- DFI increases the entrained air in the near-nozzle region due to the reduced pressure within the duct, causing a sort of pumping effect. However, given the presence of the duct wall that inhibits air entrainment for a certain length of the spray, DFI does not necessarily enhance the globally entrained air into the whole fuel spray. In other words, the duct presence changes the entrainment rate distribution across the spray plume, enhancing it close to the injector. This characteristic can be very beneficial for a successful mixture preparation.
- The spray equivalence ratio distribution is completely modified by the duct adoption in comparison with the standard free spray distribution. The rich central core typical of the free spray configuration is not present, leading to leaner and more homogeneous areas. Rich pockets are present only at the duct exit close to the wall, but they are broken in small lean vortices by the flow detachment and the associated turbulent mixing enhancement occurring downstream of the duct exit.

Moreover, some other conclusions can be drawn regarding simulation accuracy and feasibility in the context of DFI modelling through LES, as follows.

- The grid settings were properly examined, highlighting the need for an extremely refined grid for accurate DFI prediction in the LES framework, never

achieved so far in the current literature on the subject because of the huge computational cost.

- Moreover, the run-to-run variability typical of LES is larger when the duct is adopted, manifesting a higher relevance of the turbulence for DFI. Therefore, it emerges the need for statistical analysis when DFI is investigated through LES, even rising the already high investement of computational resources to obtain a sufficiently large sample size.

- To curtail the almost prohibitive computational cost, the number of simulations needed to obtain a certain sample size can be reduced by adopting the runtime saving ensemble average method, termed *Multi-Slice approach*, exploiting axial symmetry characteristics of the domain. The reliability of this ensemble average methodology has been proven for both spray configurations, highlighting a dramatic runtime saving (i.e., approx. -75%) without any worsening of the accuracy level.

RANS turbulence and combustion modelling assessment

A large set of high-fidelity data was thus produced by the LES analysis at a computational cost not affordable for other kind of investigations within the objectives of this work, especially if chemical kinetics must be included for combustion simulations. Therefore, the research activity was carried on relying on the modelling of turbulence instead of directly solving it, namely using the low-cost Reynolds-averaged Navier-Stokes (RANS) turbulence model instead of directly solving the largest turbulent length scales as LES does. Nevertheless, it is well-known how, for highly turbulent case studies, a LES capable to satisfy the quality criteria guarantees much more accurate and reliable results with respect to the corresponding RANS simulation, whose models' performance is typically case-dependent. Therefore, the accuracy of the RANS predictions, obtained with the RNG $\kappa - \varepsilon$ model, were primarily assessed for both free spray and DFI configurations having as a reference the LES data. In particular, considering the same constant-volume non-reacting conditions, the mixing process predicted by the RANS model has been assessed in terms of turbulent kinetic energy and equivalence ratio fields, using the resolved portion of the LES turbulent energy spectrum (characterized by more than 80% of resolved turbulent length scales) as a target. The RANS approach, applied as in this work, was capable to predict the main physical behaviours, capturing the

major trends between free spray and DFI in terms turbulent mixing enhancement and mixture enleanment, reducing at the same time the computational cost of more than 3 orders of magnitude compared to the ensemble-averaged LES. However, a general underestimation of the effect provided by the duct adoption was also present, resulting in reduced mixing intensity and richer equivalence ratio values at the LOL, if compared with flow field computed by the LES for DFI. Therefore, the RANS modelling settings were reliably applied for the subsequent investigations, keeping in mind that the resulting effectiveness in terms of soot mitigation potential could be always slightly underestimated.

The RANS-based 3D-CFD model was thus employed to evaluate the DFI potential for soot emissions abatement, considering reacting conditions. Results have shown that thanks to the DFI adoption, an impressive soot reduction could be effectively achieved without any drawbacks on the other pollutants, in good agreement with the main outcomes emerging from the non-reacting analysis and with the combustion evolution trends already reported in the literature. This latter aspect was considered as an important pillar of this combustion analysis since, due to the lack of experimental data in reacting conditions for the herein injection case study, these results were purely predictive. Nevertheless, thanks to a side-by-side comparison with well-known experimental combustion data available in the scientific literature, a qualitative validation of the adopted combustion model (based on detailed chemical kinetics) was obtained, ensuring robustness to the subsequent investigations under reacting conditions.

Impact of the duct design

The 3D-CFD RANS model, assessed in both non-reacting and reacting conditions, was exploited to investigate the influence of the main geometrical features (stand-off distance, duct length and diameter, inlet and outlet shape) on the DFI performance, resulting in the following outcomes.

- The reduction of both stand-off distance and duct length improves the soot mitigation performance due to the higher turbulent mixing effectiveness and the lower collision length until the upstream air entrainment enhancement becomes negligible and the LOL is quite close to the duct exit.

- Large duct diameters could change DFI operation leading to ignition within the duct volume, while small duct diameters tend to reduce the upstream air entrainment, decreasing DFI benefits. A trade-off is therefore necessary.
- A chamfer at the duct inlet can improve DFI performances, promoting higher upstream air entrainment and extending the LOL. On the other side, the tapered outlet does not lead to significant improvements, according to the present results[2].
- Each evaluated duct geometry results in lower soot emissions than free spray configuration, ranging between 43% and 94% of relative reduction, apart from the case of in-duct combustion. In this latter case, the DFI benefits are completely deleted making DFI combustion more sooting than free-spray one.
- From a general point of view, results have shown that DFI combustion and soot formation are very sensitive to duct geometrical variations; therefore, duct geometry optimization in engine application is mandatory.

Impact of engine operating parameters

After that, the optimal duct geometry was used to study the impact of rail pressure, air density, oxygen concentration, defining some preliminary DFI-oriented engine calibration requirements. Furthermore, the duct wall temperature influence was investigated in order to preliminary explore the needs in terms of duct thermal management. The main findings are reported below.

- The DFI impressively reduces soot formation over a wide range of engine-like operating conditions, achieving always more than 60% of relative reduction with respect to the free spray when the LOL is located beyond the duct exit.
- LOL extension led by duct adoption is not sufficient to explain the corresponding soot results, but enhanced mixing intensity and air entrainment amount have a crucial role in soot mitigation.
- The rail pressure rise over 1200 bar with DFI leads to almost undetectable values of soot mass, thus suggesting that a full leaner lifted-flame combustion regime can be achieved adopting this technology.

[2]More detailed numerical analyses, using a finer grid and/or a more accurate turbulence modelling approach, are probably needed to confirm the present findings related to the tapered duct geometry.

- DFI low-soot combustion is resistant to dilution, maintaining much lower soot formation with respect to the free spray, as well as efficient combustion also at low oxygen concentration values. However, the soot/NO_x trade-off breakage with dilution, described in the literature for a CI engine implementing DFI, is not captured by the present work since the soot oxidation process, which could play a crucial role, cannot be reproduced in test vessel simulations.
- DFI works better at lower ambient air densities, especially to avoid in-duct combustion events.
- Duct temperature has a marginal effect on the result at low air density, while becomes a relevant parameter when high-density conditions are considered.

DFI implementation on a light-duty CI engine

Finally, in the context of a project in collaboration with an industrial partner, the potential benefits coming from DFI implementation on a light-/medium-duty series-production CI engine were explored through RANS-based numerical analyses. After that, the industrial partner performed an optical engine experimental campaign on a similar case study. The comparison among the main outcomes of these two projects led to the following conclusions.

- According to the numerical results, the DFI was capable of attenuating soot formation due to the equivalence ratio reduction.
- According to the numerical results, the re-entrant bowl shape caused a degraded soot oxidation phase for DFI, since the formed soot mass was directed toward the duct region where lower temperatures and lower air availability drastically reduced the oxidation potential. Moreover, a lower swirl level was also observed for DFI, especially during the late-cycle mixing.
- According to the numerical results, DFI worked better without post injection. In fact, the slower reaction rate associated with the post injection led to the degradation of DFI late combustion. This step made it emerge a great potential of a DFI-oriented engine calibration.
- The main numerical outcomes were experimentally confirmed through optical analyses. OH* chemiluminescence and soot optical thickness measurements indicated that the DFI extended the LOL, reduced the soot formation, but

worsened the soot oxidation phase due to the ducts plus duct holder presence and the stronger interaction between spray and piston bowl.

- In general, this project highlighted that the direct retrofit of existing light-duty CI engines, employing a similar spray-targeted combustion chamber design, seems not a viable solution for DFI, at least if an engine calibration optimized for conventional diesel combustion is considered. On the contrary, a proper optimization of the combustion system is strongly suggested.

Prospects and future works

Overlaying the new information obtained from this PhD thesis with that found to date in the literature, although a large knowledge gaps on DFI concept has been covered, several questions are still unanswered and must be investigated for the success of this technology at an industrial level.

Concerning the understanding of the DFI working principles, even though most or all of them have been highlighted, it is still not clear the importance of each one when injection and/or ambient conditions change. The clarification of this aspect is of paramount importance to develop a unified and commonly accepted theory on DFI physics. To achieve these goals, the entire information available in the literature must be analysed thoroughly and critically, as well as the amount of conditions on which these mechanisms are highlighted must be amplified, providing both experimental data and 3D-CFD high-level results.

Regarding the effective implementation of DFI on CI engines, there is pretty large evidence that the duct presence can reduce the soot at low and medium loads, poor evidence that this can happen in high load conditions, and almost no evidence that this is feasible on the whole engine operating map. Moreover, most of the available data refers to conditions which are realistic for research purposes (i.e., optical engines in skip fire modes equipped with few orifices injector, ≤ 4, and simplified injection strategies) and less realistic for real world ones. Therefore, the dataset regarding DFI experimental tests on series production metal engines must be amplified, considering injector with high number of orifices (≥ 6) and more complex multi-injection strategies, like the ones typically used for commercial diesel engines.

In addition, the number of engine sizes on which DFI has been tested is limited, despite the understanding of its performance when engine size scales can be of

interest. Indeed, if DFI implementation on light-duty engines can be harder due to packaging limits and much more variable engine operating modes, it becomes easier for heavy-duty engine sizes typical of diesel trucks[3]. As a consequence, since heavy-duty transport powered by diesel engines is a vast field, it can be very interesting the testing of DFI on even bigger engines, like the ones used for maritime shipping. In this kind of applications, packaging limits reduce of importance, the bulk flow motions are less complex with conditions more similar to the test vessel ones, for which DFI has been largely demonstrated as effective and, last but not least, the main operating modes on which the engine typically run are fewer. Indeed, the optimization of the DFI combustion for soot abatament on few high power working points could already justify its usage, given the long time spent on cruise mode for this kind of applications.

Framing perspective in this context, CFD modelling will be a game changer, on the one hand, to increase and facilitate the understanding thanks to its capability to compute where the experiment cannot readily measure, on the other hand, to boost the amount of conditions tested thanks to its usage as virtual test rig, without the cost and complexity associated to the development of experimental setups. Therefore, it is Author's opinion that the extension of the CFD analysis presented throughout this work could be important. It follows a list of possible next steps.

- The highly accurate DFI physics investigation by means of LES can be extended under reacting conditions, by adopting detailed chemistry solver and soot modelling, to understand the impact that the resolved turbulent flow field has on the combustion process. Furthermore, a high-quality LES, with a limited impact of the sub-grid scale model as in this work, improves also the quality of the prediction of this kind of combustion model, based on the well-stirred reactor assumption, since turbulence-chemistry interaction is naturally considered in the resolved turbulent scales. Therefore, the final results would be highly accurate and usable for both improved understanding and benchmark of RANS combustion simulations. Of course, proper computational resources must be available for this kind of activity.

- Other RANS models, different from RNG $\kappa - \varepsilon$, can be assessed targeting the LES data, and their constants calibrated to understand the best way to model the turbulence caused by the interaction between the diesel spray and

[3]Most of the data today available in the literature are collected on this kind of engines, featuring a displacement lower than 2L.

the duct. An optimized RANS model, with improved and accurate predictions, would result in a low cost very high-reliability 3D-CFD model, thus extremely interesting at an industrial level.

- The engine operating parameter sensitivity analysis can be extended to the study of the interaction between DFI and more complex injection strategies, characterized by multiple injection events.

Moreover, the developed expertise in the CFD modelling of DFI technology and similar numerical methodologies could be exploited for other possible future activities, as listed below.

- Studying other injectors, characterized by different nozzle hole diameters, to understand the impact of their selection on the DFI soot formation mitigation mechanisms. Furthermore, the enlargement of the dataset could be used to develop 0D correlations[4] for preliminary optimization of DFI combustion system. For this purpose, the experimental data available on the Engine Combustion Network website [174] for conventional diesel injection could be preliminary used for model validation purposes before extension to the DFI configuration.

- Creating a virtual test rig of a heavy-duty CI engine implementing ducts, exploiting the data available in the literature and/or building partnership with other researchers working on this topic. Once validated, this virtual test rig could be used to numerically explore physical mechanisms in engine-conditions and to gain additional insights regarding coupling of DFI with more complex injection strategies, defining DFI-oriented engine calibration requirements in general. Moreover, by solving the solid wall temperature through conjugate heat tranfer simulations, fundamental information about duct and duct holder thermal management could be extracted.

- Preliminary studying with numerical simulation the performance of DFI on large bore engines, typical of maritime shipping, by scaling the engine size.

[4]For instance, correlations similar to the ones developed for conventional diesel combustion [171, 172, 164, 173] could be developed, by taking into account the duct geometrical characteristics. Some examples follow:

$$Penetration, Ignition\ delay, LOL, \phi_{LOL}, Soot = f(duct\ geometry, injector, operating\ conditions)$$

Given the much larger computational domain, proper high power computing resources must be available also in this case.

- Gaining more insights on the coupling of DFI with renewable diesel-like fuels (e.g., hydrotreated vegetable oil, HVO [175, 176]; renewable diesel [177], etc.), if proper chemical reaction mechanisms are developed for combustion modelling. According to the Author's opinion, this kind of analyses would be extremely interesting, since the coupling of these technologies can be a game changer for heavy-duty CI engine-based transportation, providing a simultaneous low-soot low-lifecycle-CO_2 emissions solution.

References

[1] V. Smil. *Prime movers of globalization: The history and impact of diesel engines and gas turbines*. MIT press, 2010.

[2] ACEA. New eu truck sales by power source, 2023. https://www.acea.auto/figure/trucks-eu-fuel-type/.

[3] IEA. World energy outlook 2022. IEA Paris, France, 2022.

[4] T. Zhou, M.J. Roorda, H.L. MacLean, and J. Luk. Life cycle GHG emissions and lifetime costs of medium-duty diesel and battery electric trucks in Toronto, Canada. *Transportation Research Part D: Transport and Environment*, 55:91–98, 2017.

[5] J.B. Heywood. *Internal combustion engine fundamentals*. McGraw-Hill Education, 2018.

[6] J.E. Dec. A conceptual model of DI diesel combustion based on laser-sheet imaging. *SAE transactions*, pages 1319–1348, 1997.

[7] T. Kamimoto and M. Bae. High combustion temperature for the reduction of particulate in diesel engines. *SAE transactions*, pages 692–701, 1988.

[8] M.A. Patterson, S.C. Kong, G.J. Hampson, and R.D. Reitz. Modeling the effects of fuel injection characteristics on diesel engine soot and NOx emissions. *SAE transactions*, pages 836–852, 1994.

[9] A. Joshi. Review of vehicle engine efficiency and emissions. *SAE Technical Paper*, 2021-01-0575, 2021.

[10] P.M. Villafuerte. AECC-IPA Ultra-low Emissions Heavy-duty Demo Vehicle – Data Analysis in view of Euro 7, 2022. https://www.aecc.eu/event/aecc-ipa-euro-7-technical-seminar-and-driving-event/.

[11] J. Miller and L. Jin. Global progress toward soot-free diesel vehicles in 2019. *ICCT-International Council on Clean Transportation*, 2019.

[12] Z. Klimont, K. Kupiainen, C. Heyes, P. Purohit, J. Cofala, P. Rafaj, J. Borken-Kleefeld, and W. Schöpp. Global anthropogenic emissions of particulate matter including black carbon. *Atmospheric Chemistry and Physics*, 17(14):8681–8723, 2017.

[13] S.C. Anenberg, J. Schwartz, D. Shindell, M. Amann, G. Faluvegi, Z. Klimont, G. Janssens-Maenhout, L. Pozzoli, R. Van Dingenen, E. Vignati, et al. Global air quality and health co-benefits of mitigating near-term climate change through methane and black carbon emission controls. *Environmental health perspectives*, 120(6):831–839, 2012.

[14] S. Anenberg, J. Miller, D. Henze, and R. Minjares. A global snapshot of the air pollution-related health impacts of transportation sector emissions in 2010 and 2015. *International Council on Clean Transportation: Washington, DC, USA*, 2019.

[15] N.A.H. Janssen, M.E. Gerlofs-Nijland, T. Lanki, R.O. Salonen, F. Cassee, G. Hoek, P. Fischer, B. Brunekreef, and M. Krzyzanowski. *Health effects of black carbon*. World Health Organization. Regional Office for Europe, 2012.

[16] T.C. Bond, S.J. Doherty, D.W. Fahey, P.M. Forster, T. Berntsen, B.J. DeAngelo, M.G. Flanner, S. Ghan, B. Kärcher, D. Koch, et al. Bounding the role of black carbon in the climate system: A scientific assessment. *Journal of geophysical research: Atmospheres*, 118(11):5380–5552, 2013.

[17] International Council on Clean Transportation. Vision 2050: a strategy to decarbonize the global transport sector by mid-century. 2020.

[18] M.P.B. Musculus, P.C. Miles, and L.M. Pickett. Conceptual models for partially premixed low-temperature diesel combustion. *Progress in energy and combustion science*, 39(2-3):246–283, 2013.

[19] F. Zhao, T.N. Asmus, D.N. Assanis, J.E. Dec, J.A. Eng, and P.M. Najt. Homogeneous charge compression ignition (HCCI) engines. 2003.

[20] L.M. Pickett and D.L. Siebers. Non-sooting, low flame temperature mixing-controlled DI diesel combustion. *SAE transactions*, pages 614–630, 2004.

[21] C.J. Polonowski, C.J. Mueller, C.R. Gehrke, T. Bazyn, G.C. Martin, and P.M. Lillo. An experimental investigation of low-soot and soot-free combustion strategies in a heavy-duty, single-cylinder, direct-injection, optical diesel engine. *SAE International Journal of Fuels and Lubricants*, 5(1):51–77, 2012.

[22] R.K. Gehmlich, C.E. Dumitrescu, Y. Wang, and C.J. Mueller. Leaner lifted-flame combustion enabled by the use of an oxygenated fuel in an optical CI engine. *SAE International Journal of Engines*, 9(3):1526–1543, 2016.

[23] C.J. Mueller. Ducted fuel injection, March 6 2018. US Patent 9,909,549.

[24] R. Bunsen and H.E. Roscoe. Photo-chemical researches. Part I. Measurement of the chemical action of light. *Philosophical Transactions of the Royal Society of London*, (147):355–380, 1857.

[25] J.L. Porter and R.A. Squyers. A summary/overview of ejector augmentor theory and performance, Phase II–Technical Report. *Vought Corporation Advanced Technology Center Report No*, pages 0704–0188, 1979.

[26] G. Flugel. The design of jet pumps. national advisory committee for aeronautics, report: technical memorandum no. 982. Technical report, 1941.

[27] M.T. Kandakure, V.C. Patkar, and A.W. Patwardhan. Characteristics of turbulent confined jets. *Chemical engineering and processing: Process intensification*, 47(8):1234–1245, 2008.

[28] C.J. Mueller, C.W. Nilsen, D.E. Biles, and B.F. Yraguen. Effects of fuel oxygenation and ducted fuel injection on the performance of a mixing-controlled compression-ignition optical engine with a two-orifice fuel injector. *Applications in Energy and Combustion Science*, 6:100024, 2021.

[29] C.J. Mueller, C.W. Nilsen, D.J. Ruth, R.K. Gehmlich, L.M. Pickett, and S.A. Skeen. Ducted fuel injection: A new approach for lowering soot emissions from direct-injection engines. *Applied energy*, 204:206–220, 2017.

[30] ECN Engine Combustion Network. Spray A&B. https://ecn.sandia.gov/diesel-spray-combustion/target-condition/spray-ab/.

[31] R.K. Gehmlich, C.J. Mueller, D.J. Ruth, C.W. Nilsen, S.A. Skeen, and J. Manin. Using ducted fuel injection to attenuate or prevent soot formation in mixing-controlled combustion strategies for engine applications. *Applied energy*, 226:1169–1186, 2018.

[32] R. Fitzgerald, K.I. Svensson, G.C. Martin, Y. Qi, and C. Koci. Early investigation of ducted fuel injection for reducing soot in mixing-controlled diesel flames. *SAE International Journal of Engines*, 11(6):817–834, 2018.

[33] K.I Svensson and G.C. Martin. Ducted fuel injection: effects of stand-off distance and duct length on soot reduction. *SAE International Journal of Advances and Current Practices in Mobility*, 1(2019-01-0545):1074–1083, 2019.

[34] F. Li, C.F. Lee, H. Wu, Z. Wang, and F. Liu. An optical investigation on spray macroscopic characteristics of ducted fuel injection. *Experimental Thermal and Fluid Science*, 109:109918, 2019.

[35] F. Li, C. Lee, Z. Wang, H. Wu, and G. Lu. Schlieren investigation on impacts of duct size on macroscopic spray characteristics of ducted fuel injection. *Applied Thermal Engineering*, 176:115440, 2020.

[36] F. Li, C.F. Lee, Z. Wang, F. Liu, and G. Lu. Optical investigation on impacts of ambient pressure on macroscopic spray characteristics of ducted fuel injection under non-vaporizing conditions. *Fuel*, 268:117192, 2020.

[37] X. Liu, B. Mohan, and H.G. Im. Numerical investigation of the free and ducted fuel injections under compression ignition conditions. *Energy & Fuels*, 34(11):14832–14842, 2020.

[38] F. Li, C. Lee, Z. Wang, Y. Pei, and G. Lu. Impacts of duct inner diameter and standoff distance on macroscopic spray characteristics of ducted fuel injection under non-vaporizing conditions. *International Journal of Engine Research*, 22(5):1702–1713, 2021.

[39] F. Millo, A. Piano, B.P. Paradisi, L. Postrioti, L. Pieracci, A. Bianco, F.C. Pesce, and A. Vassallo. Ducted fuel injection: Experimental and numerical investigation on fuel spray characteristics, air/fuel mixing and soot mitigation potential. *Fuel*, 289:119835, 2021.

[40] F. Millo, A. Piano, B. Peiretti Paradisi, C. Segatori, L. Postrioti, L. Pieracci, A. Bianco, F.C. Pesce, and A. Vassallo. Ducted fuel injection: A numerical soot-targeted duct geometry optimization. *SAE International Journal of Engines*, 15(03-15-02-0014):297–317, 2021.

[41] C.W. Nilsen, D.E. Biles, B.M. Wilmer, and C.J. Mueller. Investigating the effects of duct length and diameter and fuel-injector orifice diameter in a compression-ignition engine equipped with ducted fuel injection. *Applications in Energy and Combustion Science*, 7:100030, 2021.

[42] F. Li, Z. Wang, C. Lee, F. Ma, and W. Yang. Visualization and simulation study on impacts of wall roughness on spray characteristics of ducted fuel injection. *Applied Thermal Engineering*, 211:118380, 2022.

[43] A. Pandal, F. Rahantamialisoa, N. Sahranavardfard, L. Postrioti, and M. Battistoni. Numerical simulation of non-reacting ducted fuel injection by means of the diffuse-interface Σ-Y atomization model. *SAE Technical Paper*, 2022-01-0491, 2022.

[44] J.C. Ong, M. Zhang, M.S. Jensen, and J.H. Walther. Large eddy simulation of soot formation in a ducted fuel injection configuration. *Fuel*, 313:122735, 2022.

[45] T. Lucchini, Q. Zhou, G. D'Errico, and D. Severgnini. Modeling fuel-air mixing, combustion and soot formation with ducted fuel injection using tabulated kinetics. *SAE Technical Paper*, 2022-01-0403, 2022.

[46] J. Guo, D. Brouzet, W.T. Chung, and M. Ihme. Analysis of ducted fuel injection at high-pressure transcritical conditions using large-eddy simulations. *International Journal of Engine Research*, 2023.

[47] T. Chen, Y. An, S. Shen, H. Shi, Y. Pei, and K. Wang. Large eddy simulation of fuel-air mixing process in a convergent-divergent duct spray under non-vaporizing conditions. *Fuel*, 353:129176, 2023.

[48] T. Chen, Y. An, S. Shen, H. Shi, Y. Pei, and K. Wang. Experimental investigation of the effect of duct structure geometry on macroscopic spray characteristics and air entrainment of duct fuel spray. *Fuel*, 339:127459, 2023.

[49] Y. Zhang, Z. Wang, C. Lee, F. Li, and H. Wu. Analysis of mechanism of ducted fuel injection under non-vaporizing condition. *Fuel*, 305:121496, 2021.

[50] C.W. Nilsen, B.F. Yraguen, C.J. Mueller, C. Genzale, and J.P. Delplanque. Ducted fuel injection vs. free-spray injection: A study of mixing and entrainment effects using numerical modeling. *SAE International Journal of Engines*, 13(5):705–716, 2020.

[51] C. Segatori, A. Piano, B. Peiretti Paradisi, A. Bianco, and F. Millo. Exploiting the potential of large eddy simulations (les) for ducted fuel injection investigation in non-reacting conditions. *International Journal of Multiphase Flow*, page 104686, 2023.

[52] F. Millo, C. Segatori, A. Piano, B. Peiretti Paradisi, and A. Bianco. An engine parameters sensitivity analysis on ducted fuel injection in constant-volume vessel using numerical modeling. *SAE Technical Paper*, 2021-24-0015, 2021.

[53] A. Piano, C. Segatori, F. Millo, F.C. Pesce, and A.L. Vassallo. Investigation of ducted fuel injection implementation in a retrofitted light-duty diesel engine through numerical simulation. *SAE International Journal of Engines*, 16(03-16-05-0038), 2022.

[54] R. Pritchard, J.J. Guy, and N.E. Connor. Handbook of industrial gas utilization: engineering principles and practice. 1977.

[55] Y. Feng, T. Shang, J. Cai, K. Sun, and T. Wang. Leaner lifted-flame combustion with ducted fuel injection: The key role of forced two-stage mixing. *Fuel*, 347:128431, 2023.

[56] D.R. Haylett, D.F. Davidson, and R.K. Hanson. Ignition delay times of low-vapor-pressure fuels measured using an aerosol shock tube. *Combustion and Flame*, 159(2):552–561, 2012.

[57] C.W. Nilsen, D.E. Biles, and C.J. Mueller. Using ducted fuel injection to attenuate soot formation in a mixing-controlled compression ignition engine. *SAE International Journal of Engines*, 12(3):309–322, 2019.

[58] S. Tanno, J. Kawakami, K. Kitano, and T. Hashizume. Investigation of a novel leaner fuel spray formation for reducing soot in diffusive diesel combustion-homogenizing equivalence ratio distribution in the lift-off region. *SAE Technical Paper*, 2019-01-2273, 2019.

[59] C.W. Nilsen, D.E. Biles, B.F. Yraguen, and C.J. Mueller. Ducted fuel injection vs. conventional diesel combustion: Extending the load range in an optical engine with a four-orifice fuel injector. *SAE International Journal of Engines*, 14(1):47–58, 2021.

[60] K. Svensson, R. Fitzgerald, and G. Martin. Ducted fuel injection: An experimental study on optimal duct size. *SAE Technical Paper*, 2022-01-0450, 2022.

[61] R Şener. Ducted fuel injection: Numerical study of soot formation and oxidation using detailed soot modeling approach in a compression ignition engine at different loads. *Journal of the Brazilian Society of Mechanical Sciences and Engineering*, 44(1):45, 2022.

[62] R. Şener. Numerical investigation of ducted fuel injection strategy for soot reduction in compression ignition engine. *Journal of Applied Fluid Mechanics*, 15(2):475–489, 2022.

[63] R. Şener, C.W. Nilsen, D.E. Biles, and C.J. Mueller. A computational investigation of engine heat transfer with ducted fuel injection. *International Journal of Engine Research*, page 14680874221149321, 2023.

[64] H. Barths, C. Hasse, and N. Peters. Computational fluid dynamics modelling of non-premixed combustion in direct injection diesel engines. *International Journal of Engine Research*, 1(3):249–267, 2000.

[65] X. Liu, H.G. Im, C.J. Mueller, and G. Nyrenstedt. A computational parametric study of ducted fuel injection implementation in a heavy-duty diesel engine. *Fuel*, 2023.

[66] C.W. Nilsen, D.E. Biles, B.F. Yraguen, and C.J. Mueller. Ducted fuel injection versus conventional diesel combustion: An operating-parameter sensitivity study conducted in an optical engine with a four-orifice fuel injector. *SAE International Journal of Engines*, 13(3):345–362, 2020.

[67] K. Svensson, C. Kim, P. Seiler, G. Martin, and C. Koci. Performance and emission results from a heavy-duty diesel engine with ducted fuel injection. *SAE Technical Paper*, 2021-01-0503, 2021.

[68] Fábio Jairo Dias, Pedro Teixeira Lacava, Caio Rufino, Ezio Castejon Garcia, and Raphael Lomonaco. Load variation using ducted fuel injection-dfi, with different compression ratio in ic engine. *SAE Technical Paper*, 2022-36-0089, 2023.

[69] N.J. Buurman, G. Nyrenstedt, and C.J. Mueller. Ducted fuel injection provides consistently lower soot emissions in sweep to full-load conditions. 17(1), 2023.

[70] B.F. Yraguen, A.M. Steinberg, C.W. Nilsen, D.E. Wengrove, and C.J. Mueller. Parametric evaluation of ducted fuel injection in an optically accessible mixing-controlled compression-ignition engine with two-and four-duct assemblies. *International Journal of Engine Research*, 2023.

[71] B.M. Wilmer, C.W. Nilsen, D.E. Biles, C.J. Mueller, and W.F. Northrop. Solid particulate mass and number from ducted fuel injection in an optically accessible diesel engine in skip-fired operation. *International Journal of Engine Research*, 23(7):1226–1236, 2022.

[72] G. Nyrenstedt, C.W. Nilsen, D.E. Biles, and C.J. Mueller. Ducted fuel injection with low-net-carbon fuels as a solution for meeting future emissions regulations. *Fuel*, 338:127167, 2023.

[73] F. Li, Z. Wang, C.F. Lee, W. Yang, and F. Ma. Visualization and simulation study on the impacts of conical duct geometry on the spray characteristics of ducted fuel injection. *International Journal of Engine Research*, 24(5):2187–2205, 2023.

[74] F. Li, Z. Wang, and C.F. Lee. Investigation on impacts of elliptical ducts on macroscopic spray characteristics of ducted fuel injection. *Atomization and Sprays*, 33(6), 2023.

[75] D. Oke, L. Sittler, H. Cai, A. Avelino, E. Newes, G.G. Zaimes, Y. Zhang, L. Ou, A. Singh, J.B. Dunn, et al. Energy, economic, and environmental impacts assessment of co-optimized on-road heavy-duty engines and bio-blendstocks. *Sustainable Energy & Fuels*, 7(18):4580–4601, 2023.

[76] ECN Engine Combustion Network. Spray D Nozzle Geometry. https://ecn.sandia.gov/diesel-spray-combustion/target-condition/spray-d-nozzle-geometry/.

[77] W.T. Chung, P.C. Ma, and M. Ihme. Examination of diesel spray combustion in supercritical ambient fluid using large-eddy simulations. *International Journal of Engine Research*, 21(1):122–133, 2020.

[78] W. Zeuch. Neue verfahren zur messung des einspritzgesetzes und der einspritzregelmäßigkeit von diesel-einspritzpumpen. *MTZ*, 22(9):415–420, 1961.

[79] L. Postrioti, G. Buitoni, F.C. Pesce, and C. Ciaravino. Zeuch method-based injection rate analysis of a common-rail system operated with advanced injection strategies. *Fuel*, 128:188–198, 2014.

[80] A. Piano, F. Millo, L. Postrioti, G. Biscontini, A. Cavicchi, and F.C. Pesce. Numerical and experimental assessment of a solenoid common-rail injector operation with advanced injection strategies. *SAE International Journal of Engines*, 9(1):565–575, 2016.

[81] C. Segatori. *Ducted Fuel Injection: a Computational Fluid Dynamics analysis of soot formation mitigation mechanisms*. Master's thesis, Politecnico di Torino, 2020.

[82] D.L.S. Hung, D.L. Harrington, A.H. Gandhi, L.E. Markle, S.E. Parrish, J.S. Shakal, H. Sayar, S.D. Cummings, and J.L. Kramer. Gasoline fuel injector spray measurement and characterization–a new SAE J2715 recommended practice. *SAE International Journal of Fuels and Lubricants*, 1(1):534–548, 2009.

[83] G. Brizi, L. Postrioti, and N. van Vuuren. Experimental analysis of SCR spray evolution and sizing in high-temperature and flash boiling conditions. *SAE International Journal of Fuels and Lubricants*, 12(2):87–108, 2019.

[84] L. Postrioti, A. Cavicchi, G. Brizi, F. Berni, and S. Fontanesi. Experimental and numerical analysis of spray evolution, hydraulics and atomization for a 60 mpa injection pressure gdi system. *SAE Technical Paper*, 2018-01-0271, 2018.

[85] S.B. Pope. *Turbulent flows*. Cambridge university press, 2000.

[86] I. Celik, I. Yavuz, and A. Smirnov. Large eddy simulations of in-cylinder turbulence for internal combustion engines: a review. *International Journal of Engine Research*, 2(2):119–148, 2001.

[87] N. Van Dam, M. Sjöberg, and S. Som. Large-eddy simulations of spray variability effects on flow variability in a direct-injection spark-ignition engine under non-combusting operating conditions. *SAE Technical Paper*, 2018-01-0196, 2018.

[88] S.B. Pope. Ten questions concerning the large-eddy simulation of turbulent flows. *New journal of Physics*, 6(1):35, 2004.

[89] K.J. Richards, P.K. Senecal, and E.D. Pomraning. *CONVERGE 3.0**. Convergent Science, Madison, WI (United States), 2023.

[90] Mathworks, Natick, MA (United States). *MATLAB, Release 2021a*, 2021.

[91] A.A. Amsden and M. Findley. KIVA-3V: A block-structured KIVA program for engines with vertical or canted valves. Technical report, Lawrence Livermore National Lab. (LLNL), Livermore, CA (United States), 1997.

[92] R.I. Issa. Solution of the implicitly discretised fluid flow equations by operator-splitting. *Journal of computational physics*, 62(1):40–65, 1986.

[93] C.M. Rhie and W.L. Chow. Numerical study of the turbulent flow past an airfoil with trailing edge separation. *AIAA journal*, 21(11):1525–1532, 1983.

[94] R.D Reitz and R. Diwakar. Structure of high-pressure fuel sprays. *SAE transactions*, pages 492–509, 1987.

[95] P.K. Senecal, E. Pomraning, K.J. Richards, and S. Som. Grid-convergent spray models for internal combustion engine computational fluid dynamics simulations. *Journal of Energy Resources Technology*, 136(1):012204, 2014.

[96] R.D. Reitz. Mechanism of breakup of round liquid jets. *Encyclopedia of fluid mechanics*, 10, 1986.

[97] A.B. Liu, D. Mather, and R.D. Reitz. Modeling the effects of drop drag and breakup on fuel sprays. *SAE Transactions*, pages 83–95, 1993.

[98] A.A. Amsden, P.J. O'Rourke, and T.D. Butler. KIVA-II: A computer program for chemically reactive flows with sprays. Technical report, Los Alamos National Lab. (LANL), Los Alamos, NM (United States), 1989.

[99] H. Chaves, M. Knapp, A. Kubitzek, F. Obermeier, and T. Schneider. Experimental study of cavitation in the nozzle hole of diesel injectors using transparent nozzles. *SAE transactions*, pages 645–657, 1995.

[100] J.D. Naber and R.D. Reitz. Modeling engine spray/wall impingement. *SAE transactions*, pages 118–140, 1988.

[101] M.A. Gonzalez D., G.L. Borman, and R.D. Reitz. A study of diesel cold starting using both cycle analysis and multidimensional calculations. *SAE transactions*, pages 189–208, 1991.

[102] P.J. O'Rourke and A.A. Amsden. A spray/wall interaction submodel for the kIVA-3 wall film model. *SAE transactions*, pages 281–298, 2000.

[103] D. Kuhnke. *Spray/wall-interaction modelling by dimensionless data analysis*. PhD thesis, Technischen Universität Darmstadt, 2004. ISBN 3-8322-3539.

[104] G.P. Celata, M. Cumo, A. Mariani, and G. Zummo. Visualization of the impact of water drops on a hot surface: effect of drop velocity and surface inclination. *Heat and mass transfer*, 42(10):885–890, 2006.

[105] S.C. Yao and K.Y. Cai. The dynamics and leidenfrost temperature of drops impacting on a hot surface at small angles. *Experimental Thermal and Fluid Science*, 1(4):363–371, 1988.

[106] M. Germano, U. Piomelli, P. Moin, and W.H. Cabot. A dynamic subgrid-scale eddy viscosity model. *Physics of Fluids A: Fluid Dynamics*, 3(7):1760–1765, 1991.

[107] E.D. Pomraning and C.J. Rutland. Dynamic one-equation nonviscosity large-eddy simulation model. *AIAA journal*, 40(4):689–701, 2002.

[108] P.K. Senecal, E.D. Pomraning, K.J. Richards, and S. Som. An investigation of grid convergence for spray simulations using an LES turbulence model. *SAE Technical Paper*, 2013-01-1083, 2013.

[109] E.D. Pomraning. *Development of large eddy simulation turbulence models*. PhD thesis, The University of Wisconsin-Madison, 2000.

[110] J. Martínez, F. Piscaglia, A. Montorfano, A. Onorati, and S.M. Aithal. Influence of spatial discretization schemes on accuracy of explicit LES: Canonical problems to engine-like geometries. *Computers & Fluids*, 117:62–78, 2015.

[111] D.R. Chapman. Computational aerodynamics development and outlook. *AIAA journal*, 17(12):1293–1313, 1979.

[112] U. Piomelli. Wall-layer models for large-eddy simulations. *Progress in aerospace sciences*, 44(6):437–446, 2008.

[113] H. Werner and H. Wengle. Large-eddy simulation of turbulent flow over and around a cube in a plate channel. In *Turbulent Shear Flows 8: Selected Papers from the Eighth International Symposium on Turbulent Shear Flows*, pages 155–168, Munich (Germany), September 9–11 1991. Springer.

[114] P.R. Spalart. Detached-eddy simulation. *Annual review of fluid mechanics*, 41:181–202, 2009.

[115] C. Mockett, M. Fuchs, and F. Thiele. Progress in DES for wall-modelled LES of complex internal flows. *Computers & Fluids*, 65:44–55, 2012.

[116] A.K. Travin, M.L. Shur, P.R. Spalart, and M.K. Strelets. Improvement of delayed detached-eddy simulation for LES with wall modelling. In *ECCOMAS CFD 2006: Proceedings of the European Conference on Computational Fluid Dynamics*, Egmond aan Zee (The Netherlands), September 5–8 2006. Delft University of Technology; European Community on Computational Methods ....

[117] S. Slimon. Computation of internal separated flows using a zonal detached eddy simulation approach. In *ASME International Mechanical Engineering Congress and Exposition*, volume 37165, pages 423–433, 2003.

[118] P.K. Senecal, K.J. Richards, E.D. Pomraning, T. Yang, M.Z. Dai, R.M. McDavid, M.A. Patterson, S. Hou, and T. Shethaji. A new parallel cut-cell cartesian CFD code for rapid grid generation applied to in-cylinder diesel engine simulations. *SAE Technical Paper*, 2007-01-0159, 2007.

[119] C. Segatori, A Piano, B. Peiretti Paradisi, F. Millo, and A. Bianco. Ensemble average method for runtime saving in large eddy simulation of free and ducted fuel injection (DFI) sprays. *Fuel*, 344:128110, 2023.

[120] C.J. Mueller. The quantification of mixture stoichiometry when fuel molecules contain oxidizer elements or oxidizer molecules contain fuel elements. *SAE transactions*, pages 1243–1252, 2005.

[121] F. Piscaglia, A. Montorfano, and A. Onorati. Towards the LES simulation of IC engines with parallel topologically changing meshes. *SAE International Journal of Engines*, 6(2):926–940, 2013.

[122] P. Sagaut. *Large eddy simulation for incompressible flows: an introduction*. Springer Science & Business Media, 2005.

[123] B. Hu, S. Banerjee, K. Liu, D. Rajamohan, J.M. Deur, Q. Xue, S. Som, P.K. Senecal, and E.D. Pomraning. Large eddy simulation of a turbulent non-reacting spray jet. In *Internal Combustion Engine Division Fall Technical Conference*, volume 57281, page V002T06A007. American Society of Mechanical Engineers, 2015.

[124] Y. Pei, S. Som, P. Kundu, and G.M. Goldin. Large eddy simulation of a reacting spray flame under diesel engine conditions. *SAE Technical Paper*, 2015-01-1844, 2015.

[125] D. Farrace, R. Panier, M. Schmitt, K. Boulouchos, and Y.M. Wright. Analysis of averaging methods for large eddy simulations of diesel sprays. *SAE International Journal of Fuels and Lubricants*, 8(3):568–580, 2015.

[126] H. Pitsch and H. Steiner. Large-eddy simulation of a turbulent piloted methane/air diffusion flame (Sandia flame D). *Physics of fluids*, 12(10):2541–2554, 2000.

[127] S. Wang, J. Cao, S. Yang, X. Li, D.L.S. Hung, and M. Xu. Post processing method for lagrangian spray field based on mie scattering theory. In *International Conference on Liquid Atomization and Spray Systems (ICLASS)*, volume 1, 2021.

[128] M. Linne. Imaging in the optically dense regions of a spray: A review of developing techniques. *Progress in Energy and Combustion Science*, 39(5):403–440, 2013.

[129] T. Tzanetakis, J. Johnson, H. Schmidt, W. Atkinson, and J. Naber. Non-reacting spray characteristics of gasoline and diesel with a heavy-duty single-hole injector. *Frontiers in Mechanical Engineering*, 8:887657, 2022.

[130] G.E. Cossali, A. Gerla, A. Coghe, and G. Brunello. Effect of gas density and temperature on air entrainment in a transient diesel spray. *SAE transactions*, pages 1293–1303, 1996.

[131] C. Gong, M. Jangi, T. Lucchini, G. D'Errico, and X.S. Bai. Large eddy simulation of air entrainment and mixing in reacting and non-reacting diesel sprays. *Flow, turbulence and combustion*, 93:385–404, 2014.

[132] D.R. Rhim and P.V. Farrell. Characteristics of air flow surrounding non-evaporating transient diesel sprays. *SAE transactions*, pages 1916–1932, 2000.

[133] G. Bruneaux. Mixing process in high pressure diesel jets by normalized laser induced exciplex fluorescence part I: Free jet. *SAE transactions*, pages 1444–1461, 2005.

[134] K.J. Richards, P.K. Senecal, and E.D. Pomraning. *CONVERGE 2.4**. Convergent Science, Madison, WI (United States), 2018.

[135] D.C. Wilcox. *Turbulence Modeling for CFD (Third Edition)*. DCW Industries, 2006.

[136] B.E. Launder and D.B. Spalding. The numerical computation of turbulent flows. In *Numerical prediction of flow, heat transfer, turbulence and combustion*, pages 96–116. Elsevier, 1983.

[137] V. Yakhot and S.A. Orszag. Renormalization group analysis of turbulence. I. Basic theory. *Journal of scientific computing*, 1(1):3–51, 1986.

[138] S.A. Orszag, I. Staroselsky, W.S. Flannery, and Y. Zhang. Introduction to renormalization group modeling of turbulence. *Simulation and Modelling of Turbulent Flows*, pages 155–183, 1996.

[139] Z. Han and R.D. Reitz. Turbulence modeling of internal combustion engines using RNG κ-ε models. *Combustion science and technology*, 106(4-6):267–295, 1995.

[140] R. Scarcelli, T. Wallner, N. Matthias, V. Salazar, and S. Kaiser. Numerical and optical evolution of gaseous jets in direct injection hydrogen engines. *SAE Technical Paper*, 2011-01-0675, 2011.

[141] F. Perini, K. Zha, S. Busch, and R. Reitz. Comparison of linear, non-linear and generalized RNG-based k-epsilon models for turbulent diesel engine flows. *SAE Technical Paper*, 2017-01-0561, 2017.

[142] P.K. Senecal, E. Pomraning, K.J. Richards, T.E. Briggs, C.Y. Choi, R.M. McDavid, and M.A. Patterson. Multi-dimensional modeling of direct-injection diesel spray liquid length and flame lift-off length using CFD and parallel detailed chemistry. *SAE transactions*, pages 1331–1351, 2003.

[143] T. Poinsot and D. Veynante. *Theoretical and numerical combustion*. RT Edwards, Inc., 2005.

[144] A. Favre. Statistical equations of turbulent gases. *Problems of hydrodynamics and continuum mechanics*, pages 231–266, 1969.

[145] D. Veynante and L. Vervisch. Turbulent combustion modeling. *Progress in energy and combustion science*, 28(3):193–266, 2002.

[146] L. Zhou, W. Zhao, K.H. Luo, H. Wei, and M. Xie. Spray–turbulence–chemistry interactions under engine-like conditions. *Progress in Energy and Combustion Science*, 86:100939, 2021.

[147] G. D'Errico, T. Lucchini, F. Contino, M. Jangi, and X.S. Bai. Comparison of well-mixed and multiple representative interactive flamelet approaches for diesel spray combustion modelling. *Combustion Theory and Modelling*, 18(1):65–88, 2014.

[148] P.K. Senecal, E. Pomraning, J.W. Anders, M.R. Weber, C.R. Gehrke, C.J. Polonowski, and C.J. Mueller. Predictions of transient flame lift-off length with comparison to single-cylinder optical engine experiments. *Journal of Engineering for Gas Turbines and Power*, 136(11):111505, 2014.

[149] F. Millo, A. Piano, B. Peiretti Paradisi, M.R. Marzano, A. Bianco, and F.C. Pesce. Development and assessment of an integrated 1D-3D CFD codes coupling methodology for diesel engine combustion simulation and optimization. *Energies*, 13(7):1612, 2020.

[150] F. Millo, A. Piano, L. Rolando, F. Accurso, F. Gullino, S. Roggio, A. Bianco, F.C. Pesce, A. Vassallo, and R. Rossi. Synergetic application of zero-, one-, and three-dimensional computational fluid dynamics approaches for hydrogen-fuelled spark ignition engine simulation. *SAE International Journal of Engines*, 15(03-15-04-0030):561–580, 2021.

[151] A. Babajimopoulos, D.N. Assanis, D.L. Flowers, S.M. Aceves, and R.P. Hessel. A fully coupled computational fluid dynamics and multi-zone model with detailed chemical kinetics for the simulation of premixed charge compression ignition engines. *International journal of engine research*, 6(5):497–512, 2005.

[152] N. Peters. Laminar diffusion flamelet models in non-premixed turbulent combustion. *Progress in energy and combustion science*, 10(3):319–339, 1984.

[153] H. Pitsch. Large-eddy simulation of turbulent combustion. *Annu. Rev. Fluid Mech.*, 38:453–482, 2006.

[154] T. Zeuch, G. Moréac, S.S. Ahmed, and F. Mauss. A comprehensive skeletal mechanism for the oxidation of n-heptane generated by chemistry-guided reduction. *Combustion and Flame*, 155(4):651–674, 2008.

[155] F. Mauß. *Entwicklung eines kinetischen Modells der Rußbildung mit schneller Polymerisation*. PhD thesis, RWTH Aachen University, 1998. ISBN 3-89712-152-2.

[156] A. Kazakov and M. Frenklach. Dynamic modeling of soot particle coagulation and aggregation: Implementation with the method of moments and application to high-pressure laminar premixed flames. *Combustion and flame*, 114(3-4):484–501, 1998.

[157] M. Frenklach. Reaction mechanism of soot formation in flames. *Physical chemistry chemical Physics*, 4(11):2028–2037, 2002.

[158] M. Frenklach and S.J. Harris. Aerosol dynamics modeling using the method of moments. *Journal of colloid and interface science*, 118(1):252–261, 1987.

[159] M. Smoluchowski. Versuch einer mathematischen theorie der koagulationskinetik kolloider lösungen. *Zeitschrift für physikalische Chemie*, 92(1):129–168, 1918.

[160] J. Eismark, M. Andersson, M. Christensen, A. Karlsson, and I. Denbratt. Role of piston bowl shape to enhance late-cycle soot oxidation in low-swirl diesel combustion. *SAE International Journal of Engines*, 12(3):233–250, 2019.

[161] H.J. Curran, P. Gaffuri, W.J. Pitz, and C.K. Westbrook. A comprehensive modeling study of n-heptane oxidation. *Combustion and flame*, 114(1-2):149–177, 1998.

[162] ECN Engine Combustion Network. Modeling standards. https://ecn.sandia.gov/diesel-spray-combustion/computational-method/modeling-standards/.

[163] R. Hessel, Z. Yue, R. Reitz, M. Musculus, and J. O'Connor. Guidelines for interpreting soot luminosity imaging. *SAE International Journal of Engines*, 10(3):1174–1192, 2017.

[164] D. Siebers and B. Higgins. Flame lift-off on direct-injection diesel sprays under quiescent conditions. *SAE Transactions*, pages 400–421, 2001.

[165] B. Higgins and D. Siebers. Measurement of the flame lift-off location on di diesel sprays using oh chemiluminescence. *SAE Transactions*, pages 739–753, 2001.

[166] F. Accurso, F.C. Pesce, A.L. Vassallo, G. Belgiorno, A. Garcia, C. Micó, F. Lewiski, and U. Bin-Khalid. Investigation of the ducted fuel injection concept applied to a 8-hole nozzle in a medium duty optical engine. In *16th International Conference on Engines & Vehicles for Sustainable Transport*, Capri (Italy), September 2023.

[167] J. O'Connor and M. Musculus. Post injections for soot reduction in diesel engines: a review of current understanding. *SAE International Journal of Engines*, 6(1):400–421, 2013.

[168] J.M. Desantes, J. Arrègle, J.J. López, and A. García. A comprehensive study of diesel combustion and emissions with post-injection. *SAE Transactions*, pages 542–550, 2007.

[169] Z. Han, A. Uludogan, G.J. Hampson, and R.D. Reitz. Mechanism of soot and NOx emission reduction using multiple-injection in a diesel engine. *SAE transactions*, pages 837–852, 1996.

[170] K. Svensson, R. Fitzgerald, and G. Martin. Ducted fuel injection: Confirmed re-entrainment hypothesis. *SAE Technical Paper*, 2024-01-2885, 2024.

[171] J.D. Naber and D.L. Siebers. Effects of gas density and vaporization on penetration and dispersion of diesel sprays. *SAE transactions*, pages 82–111, 1996.

[172] D.L. Siebers. Scaling liquid-phase fuel penetration in diesel sprays based on mixing-limited vaporization. *SAE transactions*, pages 703–728, 1999.

[173] L.M. Pickett, D.L. Siebers, and C.A. Idicheria. Relationship between ignition processes and the lift-off length of diesel fuel jets. *SAE transactions*, pages 1714–1731, 2005.

[174] ECN Engine Combustion Network. Diesel Data Search. https://ecn.sandia.gov/ecn-data-search/.

[175] ENI | enioilproducts. HVOLUTION. https://oilproducts.eni.com/it_IT/prodotti/carburanti-e-combustibili/trazione/hvolution/hvolution.

[176] L. Pellegrini, C. Beatrice, and G. Di Blasio. Investigation of the effect of compression ratio on the combustion behavior and emission performance of HVO blended diesel fuels in a single-cylinder light-duty diesel engine. *SAE Technical Paper*, 2015-01-0898, 2015.

[177] U.S. Department of Energy | Energy Efficiency & Renewable Energy. Alternative Fuels Data Center - Renewable Diesel. https://afdc.energy.gov/fuels/renewable_diesel.html.

[178] M.M. Ameen, Y. Pei, and S. Som. Computing statistical averages from large eddy simulation of spray flames. *SAE Technical Paper*, 2016-01-0585, 2016.

Appendix A

Validation of the multi-slice ensemble average method for LES of free and DFI sprays

Part of the work described in this chapter was previously published in:

- Segatori, C., Piano, A., Peiretti Paradisi, B., Millo, F. and Bianco, A., "Ensemble average method for runtime saving in Large Eddy Simulation of free and Ducted Fuel Injection (DFI) sprays," *Fuel*, Volume 344, 2023, doi:1016/j.fuel.2023.128110.

The multi-slice ensemble average method used for the LES statistical analysis was assessed for both free spray and DFI configurations by comparison with the standard ensemble average approach, referring to the nomenclature of Fig. 3.10. In other words, the underlying hypothesis that the effect on turbulent fluctuations induced by a different initialization is comparable with the one induced by a different angular position was verified, and the main outcomes are reported in this appendix.

In order to consistently compare the standard and the multi-slice approaches, the same number of realizations (equal to 20) has been considered, where, in this context, a single realization is represented by a statistically independent semi-slice, passing through and tangential to the symmetry axis. This target number of realizations was achieved by means of 20 simulations for the standard approach and 5 simulations for the multi-slice one. As done for the statistical convergence analysis reported in section 3.1.3, this assessment is based on the LES setup featuring the minimum

grid size of 62.5 μm, for curtailing the computational cost (see Table 3.4) with respect to the final setup used for the LES physical analysis. These grid settings satisfy the TRI restriction for the free spray configuration as observable in Fig. A.1, while are not sufficient for the DFI one, as already illustrated in Fig. 3.7. Even though this aspect makes the DFI setup fall into the very large eddy simulation (VLES) field, the investigation on the DFI configuration must be only intended as an additional verification, while most of the analysis is carried out on the free spray setup. Therefore, the resulting VLES-related error of DFI was considered in line with the scope of this investigation. For both free spray and DFI, a 1 ms simulation duration (0.7 ms of injection event) has been considered, longer than the LES physical analysis (0.5 ms of injection event, 0.8 ms in total; section 3.1).

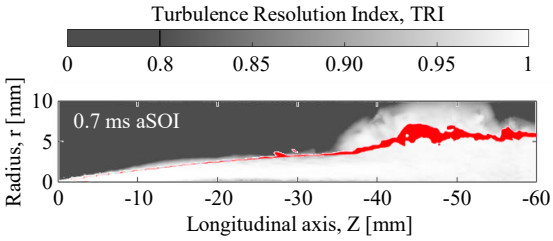

Fig. A.1 Turbulence resolution index (TRI) distribution on a section containing the spray axis at 0.7 ms aSOI for the free spray with 62.5 µm grid size, considering an ensemble average among 20 statistical samples. The area with an equivalence ratio value between 0.1 and 0.2 is overlapped in red.

A.1 Free spray

In Table A.1, the details related to the considered number of simulations, number of realizations, and resulting computational costs are reported. The computational cost is based on the utilization of Intel Xeon Scalable Processors Gold 6130 2.10 GHz.

As reported, the multi-slice ensemble average approach, as set in this work, involves running just 25% of the original number of simulations, if a 2D representation of the results is sufficient. However, in dealing with LES spray simulations, the statistics of several macroscopic parameters (e.g., spray tip penetration or SMD), which are intrinsically related to the 3D distribution of the liquid parcels, can be affected by the lower number of samples, in this case passing from 20 of the standard approach to 5 of the multi-slice approach. Therefore, it is important to verify that this

Table A.1 Number of simulations, number of realizations, and total runtime considered for the standard and the multi-slice ensemble average approaches. Processors: Intel Xeon Scalable Processors Gold 6130 2.10 GHz.

Ensemble average	Simulations	Semi-slices / simulation	Realizations	Total runtime *coredays*
Standard	20	1	20	$\simeq 1520$
Multi-slice	5	4	20	$\simeq 380$

lower number of samples can be acceptable for these parameters, from a statistical convergence point of view.

In Fig. A.2, the ensemble-averaged liquid and vapor penetrations as a function of time are illustrated for both 20 samples and 5 samples statistics, together with the associated standard deviation (σ). The simulated liquid penetration is herein defined as the radius of a sphere centred in the nozzle hole which contains 95% of the total liquid mass at each time instant, while the vapor penetration is the largest distance between the nozzle hole and the cells which feature a fuel vapor mass fraction higher than 0.1%. Moreover, experimental liquid penetration is depicted with empty circles to easily evaluate the accuracy level of the calibrated spray model.

Focusing on the penetration curves (Fig. A.2, bottom), it can be observed that the LES ensemble averages (solid lines) are almost identical considering 20 samples (black) or 5 samples (red). This is confirmed also for the standard deviation bands, which are almost overlapped, highlighiting a similar variability, despite the different sample size. It is worth noting the high predictive capability of the 3D-CFD spray model in terms of liquid penetration, if compared with the experimental data (grey circles).

The influence of the number of samples on the average drop sizing was also evaluated, measuring the SMD value across a certain temporal window in several evenly spaced locations, placed on a segment orthogonal to the spray axis (named Y Traverse) at 50 mm axial distance from the nozzle, as experimentally executed in Fig. 2.14 for a different operating condition. In Fig. A.3, these average SMD values are illustrated for both 20 samples and 5 samples statistics. As above, the variability among the different cases is also reported in terms of standard deviation bands.

The SMD average values (solid lines) are almost overlapped between 20 samples (black) and 5 samples (red) statistics for most of the spatial window, with a slight

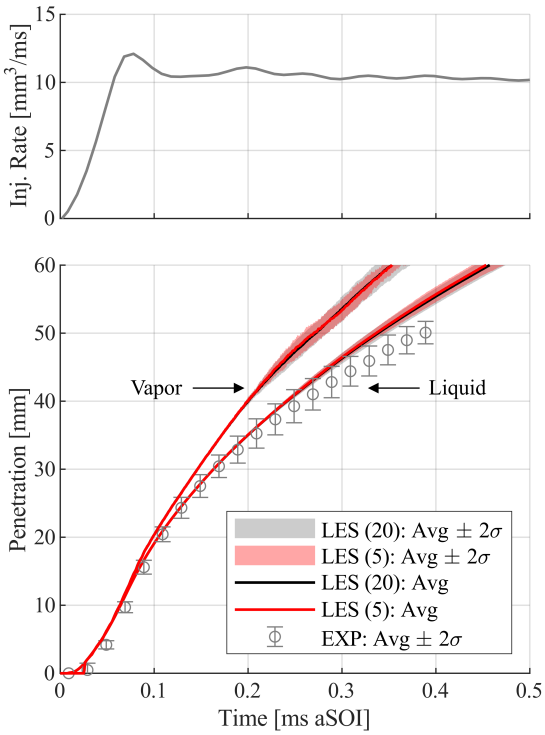

Fig. A.2 Spray liquid and vapor penetrations (bottom) as a function of time for the LES, both 20 samples (black) and 5 samples (red) statistics, and the experiment (grey circles). The average (solid lines) and the standard deviation (shaded bands) are both represented. The injection rate is reported on the top.

deviation when the spray periphery is approached for negative Y traverse values. Concerning the standard deviation bands, when only 5 samples are considered, the dispersion on the average values seems slightly underestimated or overestimated by looking at positive or negative Y traverse values, respectively.

In general, from both Figs. A.2 and A.3, it emerged that in the LES framework the average spray macroscopic characteristics are only slightly affected by the number of samples considered for the average, due to a relatively low event-to-event dispersion. Therefore, the employment of the multi-slice ensemble average approach, targeted at a 2D representation of the simulation results at a lower computational cost, does not affect the quality of the average spray global parameters, despite the lower number of statistical samples. These results are in line with the LES results in [108], in which Senecal et al. concluded that even a single injection event can be run when looking at spray global parameters since the predictions among different injections are very similar.

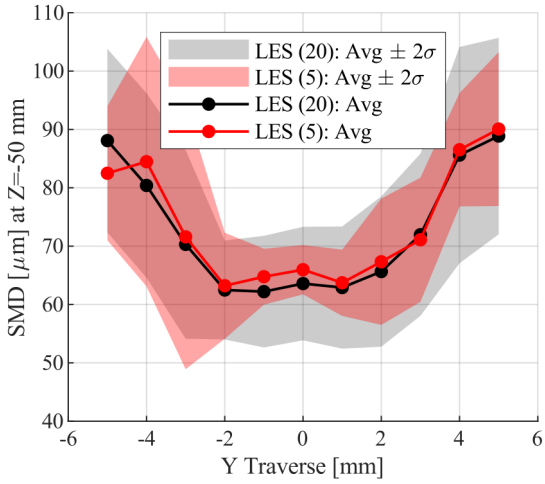

Fig. A.3 SMD values, for both 20 samples (black) and 5 samples (red) statistics, at 50 mm axial distance from the injector nozzle in different locations placed on a segment orthogonal to the spray axis (i.e., Y Traverse). The average (solid line, filled circle) and the standard deviation (shaded bands) are both reported.

Given this basis, the standard approach and the multi-slice approach outcomes can be compared in terms of spray structure on the average longitudinal semi-slice. In Fig. A.4, the ensemble-averaged velocity magnitude and ϕ fields at various time instants are depicted for both the standard and the multi-slice approaches. The injector nozzle is located at r=0 mm, Z=0 mm.

From an overall point of view, the ensemble averages approaches provide very similar results in terms of both velocity magnitude (Fig. A.4, left) and ϕ (Fig. A.4, right) field. In particular, the outcome is almost identical until the spray breakup process begins, at about 30 mm axial distance. When the spray reaches the highly turbulent region, some local differences emerge, despite not being significant from a macroscopic perspective. To systematically quantify the impact of these local differences on the full picture, two similarity indices are introduced: the structure similarity index (SSI) and the magnitude similarity index (MSI), reported in equations A.1 and A.2, respectively.

$$SSI = \frac{(m_j, n)}{\|m_j\| \cdot \|n\|} \tag{A.1}$$

$$MSI = 1 - \frac{\|m_j - n\|}{\|m_j\| + \|n\|} \tag{A.2}$$

According to their definition [123], m_j and n represent vectors collecting the data related to two different pictures that must be compared: m_j is the picture under test,

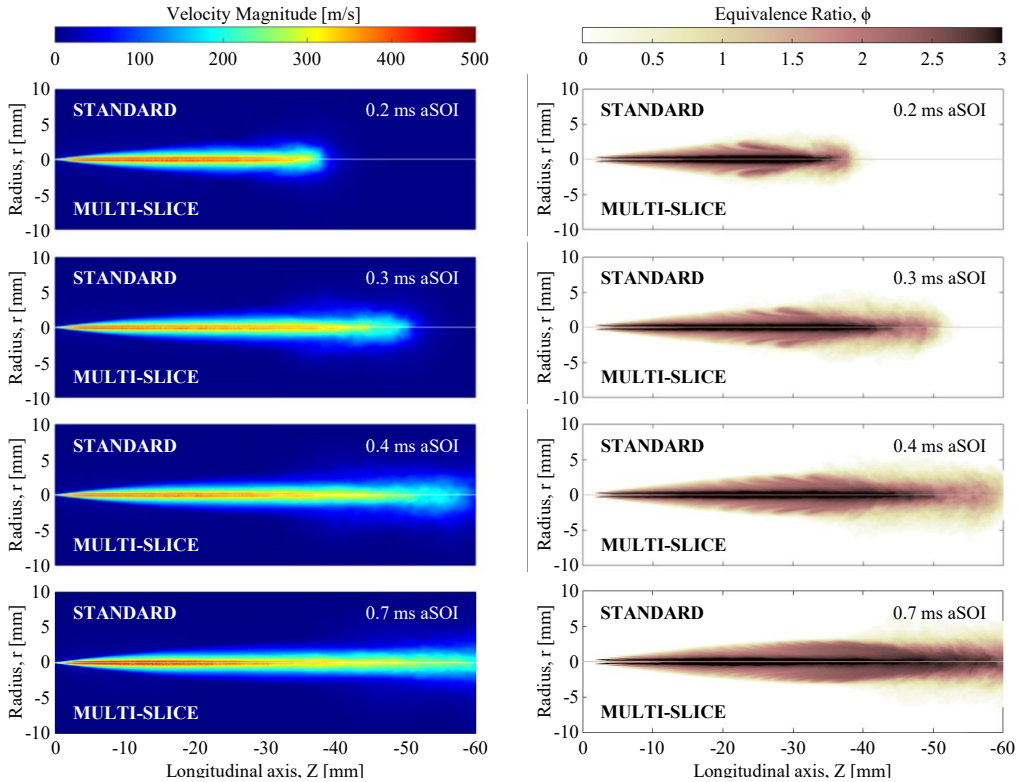

Fig. A.4 Ensemble-averaged velocity magnitude (left) and equivalence ratio (right) distributions on a section containing the spray axis at several time instants: 0.2 ms aSOI, 0.3 ms aSOI, 0.4 ms aSOI, 0.7 ms aSOI. Comparison between Standard (top side) and Multi-Slice (bottom side) ensemble average approaches.

and n is the target picture. In this case, n is the ensemble average computed with standard approach on all the 20 available samples (equation A.4), while m_j is the ensemble average computed with standard or multi-slice approach considering only a certain number of samples (j) lower than 20 (equation A.3):

$$m_j = \langle |V|, \phi \rangle_{Std/MS}(jsamples) \tag{A.3}$$

$$n = \langle |V|, \phi \rangle_{Std}(20samples) \tag{A.4}$$

Therefore, the behaviour of m can be studied as j increases, and thus the similarity with n, comparing the standard and the multi-slice approaches. It is important to underline that, when j is equal to 20, m and n represent by definition the same vector, if m is computed with the standard approach. The parenthesis, ( ), denotes the inner product of the two vectors, and the symbol $\| \ \|$ denotes the magnitude of the vector. If the similarity indices reach values close to 1, it means that the ensemble averages

m and *n* are close to being identical in terms of direction (i.e., for the SSI) and magnitude (i.e., for the MSI). On the contrary, a value approaching zero means that the two flow fields are extremely different from each other.

Differently from previous studies [178], these similarity indices are not herein employed to justify the chosen number of samples as statistically sufficient, since the target vector would not be known a priori. In fact, given a certain number of realizations, as said above, these indices tend to reach a final value equal to 1 by definition if the standard approach is considered, without providing information on the nature of the curve if a larger number of samples would be employed in the averaging process (thus, changing the target vector). In this case, the number of samples to reach statistical convergence has been chosen with a different criterion, together with the definition of its accuracy limits (section 3.1.3). Once defined that 20 samples are statistically representative of the present case study, the similarity index method is, instead, exploited to assess the validity of the multi-slice ensemble average approach with respect to the standard one, thus the target vector is well-established and fixed. In Fig. A.5, the SSI and the MSI as a function of the number of considered realizations for the average are reported for both the |V| and ϕ fields, comparing the computation with standard and multi-slice approaches. The results are referred to a time instant (0.7 ms aSOI) in which pseudo-stationary conditions are reached within the window under analysis.

From an overall point of view, the results show very high values of similarity indices, above 0.93 even considering just two samples for the ensemble average. This manifests that, comparing the entire window with respect to the target picture, the differences are not remarkable due to the limited run-to-run variability in this case study. This is in line with the observation in Fig. A.4. Therefore, the typical criterion based on fixed-value (0.9-0.95) thresholds to establish a good similarity between target and under-test pictures cannot be employed in this study. Subsequently, the graphs in Fig. A.5 should be analysed from a comparative point of view, understanding the real speed-up ensured by the multi-slice approach compared to the standard approach, if an equal variability with respect to the target picture must be guaranteed.

The SSI curves (circles) are almost overlapped after 5 realizations for both the |V| field (Fig. A.5, top) and the ϕ field (Fig. A.5, bottom), achieving a value close to 1. Therefore, highly parallel vectors originate from the data collected with both ensemble average processes. For a fair comparison of the MSI curves (triangles), the

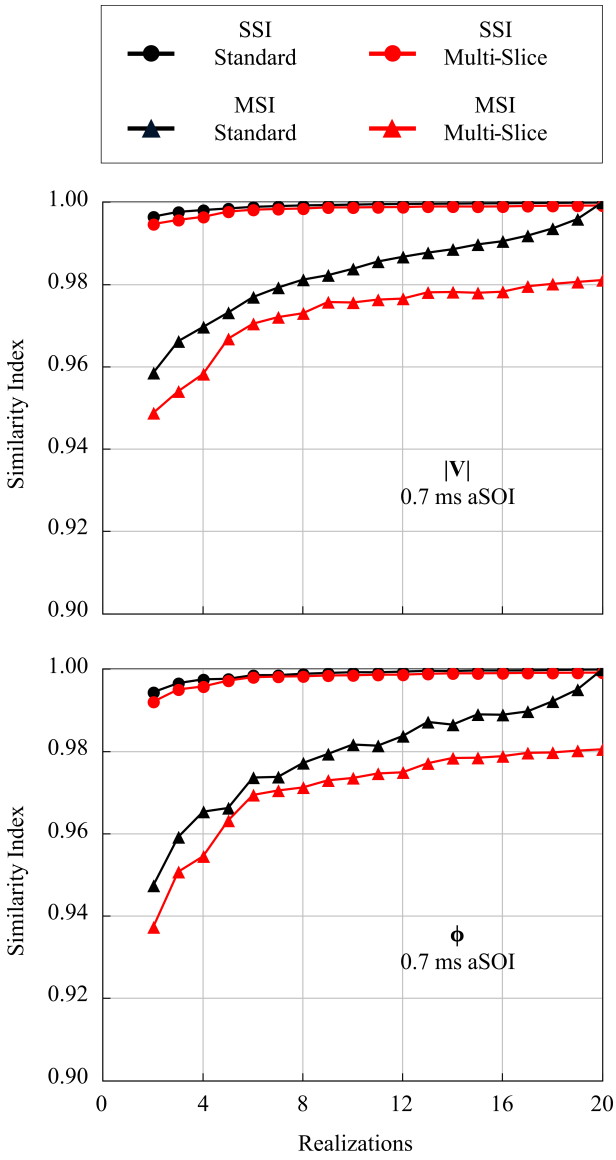

Fig. A.5 Structure Similarity Index (SSI, circles) and Magnitude Similarity Index (MSI, triangles) as a function of the number of realizations for the velocity magnitude (top) and equivalence ratio (bottom) fields at 0.7 ms aSOI. Comparison between standard approach (black) and multi-slice approach (red).

last steps in which the standard curve (black) suddenly changes its slope moving towards 1 should be neglected. In fact, as above said, this value is reached by definition, thus the difference in that region cannot be used as an eligibility criterion. Hence, the MSI value achieved by the multi-slice approach (red) at 16 realizations is considered for the analysis (namely, immediately before that the slope artificially increases for the standard curve): an MSI equal to about 0.98 is achieved by the multi-slice approach for both fields. The same similarity to the target is achieved by

the standard approach after 7-9 realizations. In other words, since 16 realizations are obtained using only 4 simulations with the multi-slice approach applied as in this work (i.e., 4 slices per simulation), a 50% effective reduction of the computational cost is ensured, if an equal variability with respect to the target picture is an eligibility criterion. Therefore, according to this point of view and these results, the effective speed-up (i.e., x2) operated by the multi-slice approach is lower than the theoretical one (i.e., x4). It is noteworthy that this speed-up remains still very significant, especially considering the large computational cost associated with a well-resolved LES employing statistical analyses (i.e., approximately 1520 core days for the present case study simulating the described 3D-CFD setup on the available computational resources, according to Table A.1).

Given the importance of the resolved TKE distribution, correlated to the high-mixing regions of the spray, it was computed for both ensemble average approaches (equation 3.9) and results are depicted in Fig. A.6 at various time instants.

According to this computation, the resolved TKE mainly raises in the spray tip and along the spray axis, with high-TKE regions increasing in size as the spray progresses. This behaviour is captured by the multi-slice approach, confirming that the macroscopic characteristics are almost identical by adopting both ensemble average approaches. At each time instant, the high-TKE regions are similar in terms of shape and values, with only slight local variations mainly after the spray begins the breakup process. These are especially visible in the middle of the transient phase (0.3 ms aSOI), when the multi-slice approach predicts a less turbulent leading edge of the spray and slightly lower TKE values on the back part of the spray tip, however without losing the main outcomes. These slight differences are strongly attenuated moving to the other time instants, especially when pseudo-stationary conditions are achieved in the window of interest. To analyse these results from a more local perspective and to understand the most affected turbulent length scales by averaging with the multi-slice approach, in Fig. A.7, the resolved TKE spectrum at Z=-23 mm, r=1 mm (location close to the expected LOL for the free spray, 6.12, and already employed before, 3.19) is reported for both standard and multi-slice approaches.

From a global perspective, the multi-slice curve (red) captures well the behaviour of the standard curve (black) for both low frequencies (larger turbulent structures) and high frequencies (smaller turbulent structures). In particular, the curves are almost overlapped throughout the resolved portion of the inertial sub-range (i.e., approximately between 100 kHz and 1000 kHz), and for most of the energy-containing

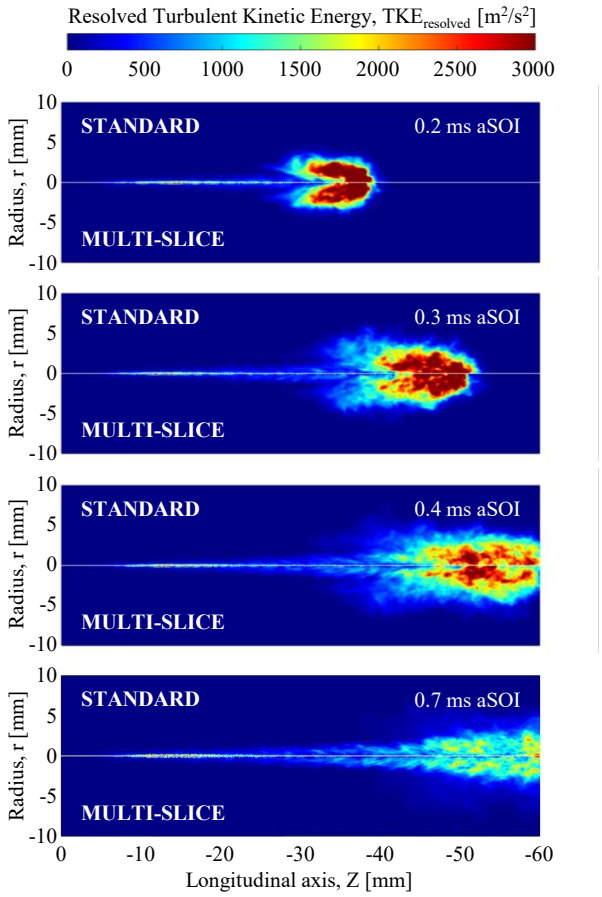

Fig. A.6 Resolved Turbulent Kinetic Energy distribution on a section containing the spray axis at several time instants: 0.2 ms aSOI, 0.3 ms aSOI, 0.4 ms aSOI, 0.7 ms aSOI. Comparison between Standard (top side) and Multi-Slice (bottom side) ensemble average approaches.

range (i.e., the lowest frequencies). The maximum deviation between the spectra is instead achieved in the range of 10-100 kHz, where a periodic behaviour described by two local peaks with the standard approach is not captured by the multi-slice one. In other words, this periodic behaviour is probably linked to a larger variability of the sample's initial conditions, which seems not representable by varying its angular position. However, since this deviation at intermediate frequencies is very short in terms of duration and occurs towards the end of the energy-containing range, thus having a limited impact on the final TKE outcome, it can be considered negligible for the purpose of this kind of evaluation.

In conclusion, in the context of free spray CFD simulation, the differences between the ensemble average approaches are very low in terms of both spray main physical quantities and turbulence characteristics, both globally and locally.

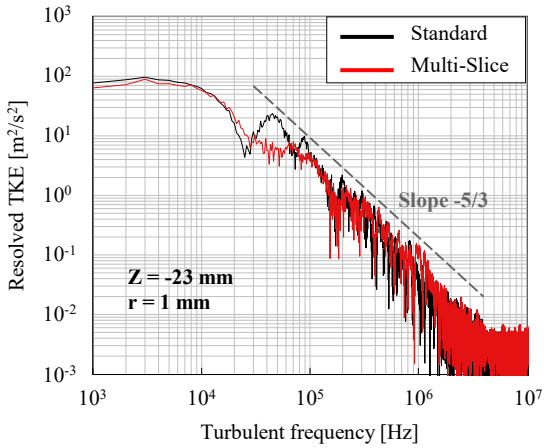

Fig. A.7 Resolved Turbulent Kinetic Energy spectrum at a selected location (Z=-23 mm; r=1 mm), computed with both Standard (black) and Multi-Slice (red) ensemble average approaches.

Therefore, the herein assessed multi-slice approach, as applied in this work, can be a valid tool to strongly reduce the computational cost by 50-75% (i.e., according to the prescribed requirements) while still maintaining a high level of results accuracy, as mandatory for research investigations applying LES combined with statistics.

A.2 Application of the method to the DFI configuration

In Fig. A.8, the ensemble-averaged velocity magnitude field is depicted for both the standard and the multi-slice approaches at 0.7 ms aSOI, namely in pseudo-stationary conditions considering the spatial window of interest.

It can be observed that the multi-slice picture (bottom) is almost identical to the standard one (top), correctly describing the behaviour of the duct inflow and outflow, the velocity increment inside the duct, and the gradual velocity reduction after the duct exit due to the momentum transfer from the spray to the surrounding air. The radial enlargement of the spray shape after the duct exit, highlighted by computational cells with velocity values higher than the test vessel, is almost specular between the standard approach and the multi-slice one.

As carried out for the free spray case, the SSI and the MSI indices (equations A.1 and A.2) were employed to understand the impact of the local differences on the

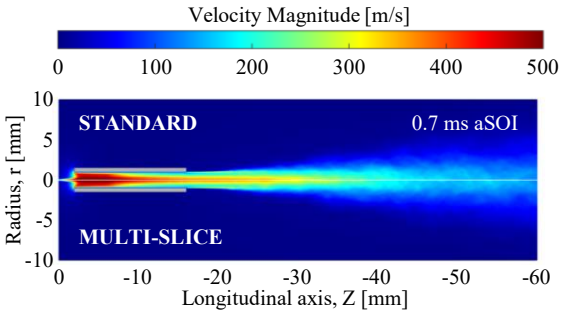

Fig. A.8 Ensemble-averaged velocity magnitude distribution on a section containing the spray axis at 0.7 ms aSOI. Comparison between Standard (top side) and Multi-Slice (bottom side) ensemble average approaches in the DFI configuration.

full ensemble average picture. In Fig. A.9, the SSI and the MSI as a function of the number of considered realizations for the average are reported for both the |V| and ϕ fields at 0.7 ms aSOI, comparing the computation with standard and multi-slice approaches.

As in the free spray case, the SSI curves (circles) are very close to 1 after a few realizations for both the |V| (Fig. A.9, top) and the ϕ (Fig. A.9, bottom) fields, and almost overlapped between standard (black) and multi-slice (blue) approaches. Therefore, the associated vectors are highly parallel also with the DFI configuration. Focusing on the MSI results (triangles), it is evident how the final slope of the standard curve has a much higher final slope (i.e., immediately before reaching a value equal to 1, by definition) than the free spray case (Fig. A.5). This manifests that the more intense turbulent fluctuations present in the DFI case, enlarging the variability between different samples (Fig. 3.15), makes the statistical convergence less forthcoming by adopting the same number of samples (i.e., 20 in this case). This effect makes harder the comparison between the multi-slice approach and the standard one by using these graphs since even the standard curve is less stable. The difference could be thus linked to either the application of the multi-slice approach or the not sufficiently stable average. However, considering the ensemble-averaged |V| distribution, which is less affected by the stronger turbulent fluctuations, and referring to the maximum number of realizations before the sudden slope increase of the standard curve (i.e., 12 realizations), it is still possible to examine the simulation speed-up introduced by the multi-slice approach, in the DFI case. In particular, an MSI equal to about 0.97 is achieved by the multi-slice approach after 12 realizations (i.e., 3 simulations). The same similarity to the target is achieved by the standard approach after 6 realizations (i.e., 6 simulations). In other words, the multi-slice

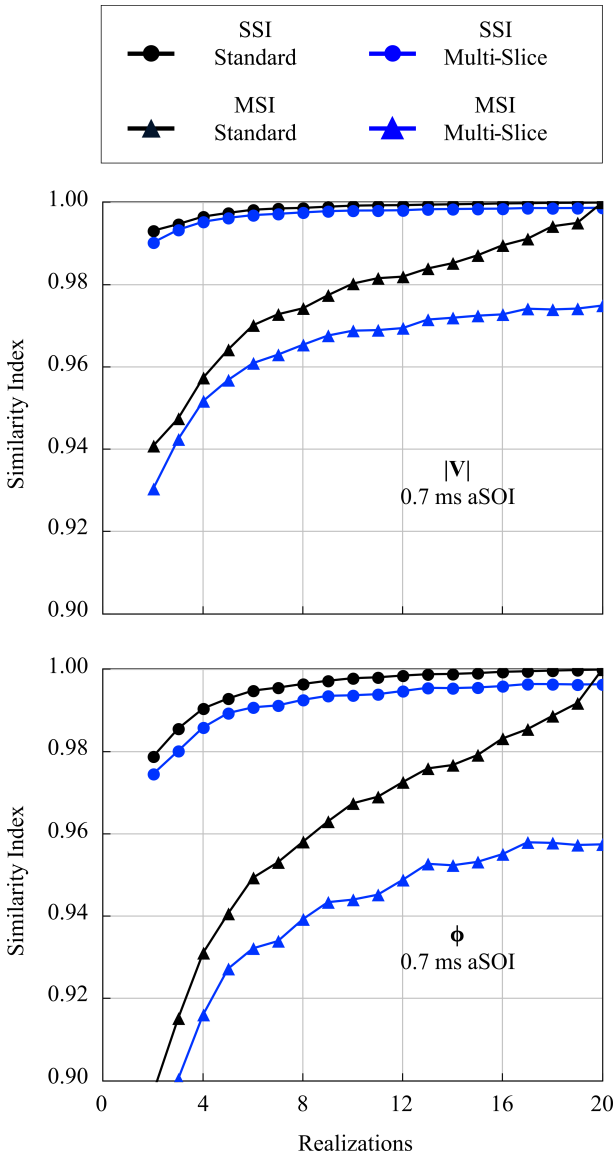

Fig. A.9 Structure Similarity Index (SSI, circles) and Magnitude Similarity Index (MSI, triangles) as a function of the number of realizations for the velocity magnitude (top) and equivalence ratio (bottom) fields at 0.7 ms aSOI. Comparison between standard approach (black) and multi-slice approach (blue) in the DFI configuration.

approach, as applied in this work, guarantees a 50% effective reduction of the computational cost also in the DFI case, if equal variability with respect to the target picture is an eligibility criterion.

In Fig. A.10, the resolved TKE in the selected location (Z=-23 mm; r=1 mm) as a function of the turbulent frequency is reported in logarithmic scale for both the standard approach and the multi-slice approach. This location is of particular interest

due to the triggering of the so-called second stage turbulent mixing enhancement, computed for the DFI technology with RANS simulations [15,16,19]. In fact, in that region, characterized by high-velocity gradients between spray and test vessel, the flow detachment occurs since the spray is no longer guided by the duct wall. Therefore, in this location, the accuracy of the resolved TKE computed with multi-slice ensemble average approach is of paramount importance for the DFI investigation.

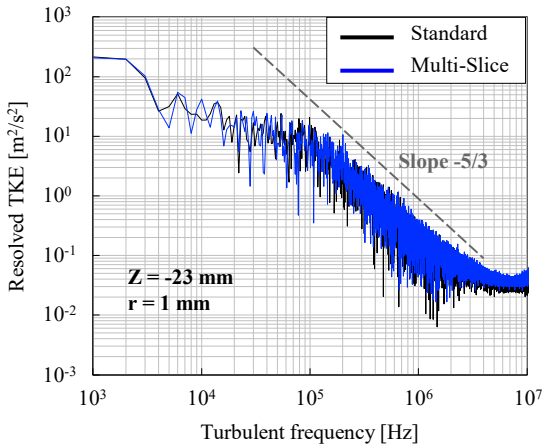

Fig. A.10 Resolved Turbulent Kinetic Energy spectrum in the DFI configuration at a selected location (Z=-23 mm; r=1 mm), computed with both Standard (black) and Multi-Slice (blue) ensemble average approaches.

The resolved TKE computed with the multi-slice approach (blue) accurately reproduces the standard curve (black) throughout both the energy-containing range and resolved portion of the inertial sub-range. Compared to the TKE spectrum associated with the free spray case in the same location (Fig. A.7), the multi-slice approach behaves even better in the DFI configuration, not showing any significant variation in the entire spectrum.

Finally, according to the present results, similar conclusions can be drawn for the multi-slice approach applied to a DFI case study. Indeed, the differences between the ensemble average approaches are very low in terms of both ducted spray main physical quantities and turbulence characteristics, both globally and locally, paving the way for a larger utilization of the multi-slice approach for DFI investigation through LES, as done in the present research activity. Indeed, the multi-slice approach, if applied as in this work, enables a reduction of the computational cost by 50-75%, still maintaining a high level of results accuracy.